COLLEGES SCIENCES
BRETAGNE POUR L'INGENIEUR
LOIRE ET LE NUMERIQUE

ENSTA INSTITUT POLYTECHNIQUE DE PARIS

STELLANTIS

PHD THESIS

L'ECOLE NATIONALE SUPERIEURE
DE TECHNIQUES AVANCEES
INSTITUT POLYTECHNIQUE DE PARIS – CAMPUS DE BREST

DOCTORAL SCHOOL N°648
Sciences pour l'Ingénieur et le Numérique
Specialty: Solid Mechanics, Materials Science, Structures and Surfaces

By
Leandro Maurício da Silva

Control of appearance defects generated by differential thermal expansion on an aluminum alloy roof assembled in a multi-material body-in-white

Thesis presented and defended in Rennes on January 16, 2025
Research unit: Dupuy de Lôme Research Institute – UMR CNRS 6027

Reviewers before the defense:

Lucas da Silva	Professor, University of Porto (FEUP), Porto, Portugal
Till Vallée	Doctor-Researcher, Fraunhofer Institute, Bremen, Germany

Composition of the jury:

President and examiner:	Armelle Chabot	Research Director, Gustave Eiffel University, MAST-LAMES, Bouguenais, France
Thesis director:	Romain Créac'hcadec	Associate Professor (HDR), ENSTA-Bretagne, IRDL – UMR CNRS 6027, Brest, France
Thesis co-supervisors:	Christophe Cellard	Associate professor, UBO, IRDL – UMR CNRS 6027, Brest, France
	Laurent Sohier	Associate professor, UBO, IRDL – UMR CNRS 6027, Brest,France

Guest / Industrial partners:

Olivier P.-Felgueiras	Doctor-Engineer, Company Supervisor, Stellantis, Poissy, France
Patrick Briend	Project assistant, Stellantis, Rennes, France

Aos meus pais,

a cada pessoa da minha família que me apoiou e apoia.

To my parents,

to each member of my family who has supported me.

Acknowledgments

These thesis studies symbolize years of dedication, during which I gained profound knowledge and honed both my professional and personal skills. I immersed myself in this challenging journey, garnering enriching experiences across various facets of life. Recognizing this as a long-term endeavor, I extend my heartfelt gratitude to those who collaborated and supported me.

Firstly, I express my gratitude to the members of my thesis advisory committee for their unwavering presence throughout. Christophe Cellard, thank you for infusing our scientific and personal debates with positivity. Laurent Sohier, your calm demeanor and effective teaching methods were invaluable. And of course, I would like to warmly thank my thesis director Romain Créac'hcadec for his guidance and the numerous discussions we had, both scientific and friendly. From my first project at ENSTA-Bretagne in 2017 to the final year of the thesis, you always pushed me to achieve higher scientific standards, and you certainly have a huge influence on who I am professionally today.

I also want to thank my colleagues at Stellantis, Patrick Briend (for industrial tests), Pascal dos Santos (for conversations in Portuguese), Pierre Colin (for management), and all the ATRP-Rennes team members who followed the progress of my work and advised me when needed. I particularly want to thank Olivier Ponte-Felgueiras for his scientific support on the industrial side throughout my thesis years. Olivier, always in a very charismatic way, you have been very present in scientific and personal moments, and I am immensely grateful for that.

I also want to thank my colleagues at ENSTA Bretagne, as well as the other doctoral students. I have a special thought for Gwladys Belone, my office partner who gradually became a great friend for life. Paulo Guimaraes, for bringing a Brazilian atmosphere to ENSTA-Bretagne. Pierre-Yves Corbel, always with his jokes to lift everyone's spirits. Thomas Fkyerat, with whom I shared advisory committee members but also very funny adventures (the Nantes - Carvoeiro adventure would not have been the same without you).

I would like to express my sincere gratitude to the jury members who graciously accepted to evaluate the work completed during this thesis journey. My heartfelt thanks go to Professor Lucas da Silva from the University of Porto (FEUP) in Portugal, and Dr. Till Vallée, Doctor-Researcher at the Fraunhofer Institute in Germany, for their thorough reviews and insightful feedback. I also extend my deep appreciation to Research Director Armelle Chabot from Gustave Eiffel University, France, for her invaluable contributions as an examiner. Thank you all for your time, effort, and expertise in guiding and assessing this work.

Lastly, but most importantly, I want to thank my family immensely, especially my parents, for supporting, encouraging, and motivating me, not only during the thesis but also during all other stages of my life (even with an ocean of distance between us). Know that I feel very privileged every day to have you as parents. Everyone I meet always speaks highly of my principles, but they don't know that I learned all of this from you. Your guidance has shaped my principles, for which I am deeply thankful.

Abstract

The new EU regulations on CO_2 emissions, Industry 4.0 advancements, and emerging energy sources are prompting the automotive sector to explore lightweight materials for future vehicles. In this context, Stellantis launched a project called "*Projet AM2*" in partnership with collaborators, with a primary emphasis on multi-material and multi-technology processes. This initiative involves integrating an aluminum roof into a body-in-white predominantly composed of steel. While the weight reduction potential of multi-material approaches is significant, challenges arise from temperature fluctuations during vehicle fabrication, leading to thermal buckling in thin structures like car roofs. This thesis addresses strategies to prevent and predict surface defects caused by thermal buckling while adhering to automotive industry standards. Despite the widespread use of aluminum alloys in the automotive industry, there is a lack of literature on the thermomechanical properties of aluminum alloys (EN AW 6016-T4 and EN AW 6056-T4) under slow heating conditions lasting 40-50 minutes up to 220°C, including natural aging effects. This study revealed a substantial non-linear increase in yield strength and a corresponding decrease in Young's modulus values with rising temperature. Furthermore, the plastic response varied notably depending on the heating cycle employed. The variations in diffusivity, specific heat, and conductivity were also studied with the increase in temperature. Regarding the instability phenomenon induced by differential expansion, comprehensive investigations were conducted using analytical, physical, and numerical analyses within a controlled laboratory environment. Two tests were devised to assess material behavior under different boundary conditions and geometries, revealing distinct stress states attributed to differing plastic regimes. A simulation method was developed to account for the evolving properties of aluminum alloys during temperature fluctuations, and the results were corroborated by the experimental tests. Additionally, thermal buckling onset was observed to occur within the material's elastic regime. Finally, numerical simulation models were developed to assess and predict the effects of differential expansions on the aluminum alloy roof at the scale of the body-in-white structure. Based on the analysis, a redesigned car roof was proposed, considering both industrial feasibility and brand-specific design criteria. Subsequently, an industrial-scale prototype featuring the proposed roof yielded promising outcomes, affirming the viability of the proposed design approach.

Table of Contents

General introduction……13

Chapter 1 - Industrial context and problem statement……..……15

Introduction – Chapter 1……..…….....15

1. Global industrial context: trends that will impact automotive designs from 2025 onwards……..……..……..……17

1.1 The concept of Industry 4.0…….……..……17

1.2 EU CO2 emission targets for vehicles and diversification of energies and variants…….…….....20

1.2.1 Brief historical context of EU targets for CO_2 emissions and Paris Agreement – 2015…….….20

1.2.2 Paris Agreement regulations for vehicles and diversification of energies and variants……...…….20

1.3 Evolution of standards and regional particularities.…….....23

1.4 Consequences of automotive trends…….....23

2. Stellantis industrial context: *Projet AM2*…….…24

2.1 Stellantis - Rennes: ATRP team..……..……..……24

2.2 Excelcar……. ……..……..……25

2.3 *Projet AM2*…….……..……..……26

3. Thesis problem statement, the production line and the body-in-white……..……29

3.1 Problem statement: *Projet V* – Groupe PSA (2010-2013).……..……...…29

3.2 The main stages of the production line……...……..……...…30

3.2.1 Stamping…….....30
3.2.2 Welding ……..31
3.2.3 Painting……...32
3.2.4 Assembly……32

3.3 Identification of thermal loads on the roof of the body-in-white during fabrication and throughout its life cycle……..…….....33

4. Conclusion - Chapter 1 / Methodology to solve the statement problem..…...……36

4.1 Conclusion…….……..……...…36

4.2 Methodology to solve the statement problem…….……...…37

Bibliography – Chapter 1……..……..…….....39

Chapter 2 – The challenges of using aluminum alloys in the automotive industry and characterization of EN AW 6016-T4 and EN AW 6056-T4 alloys……...……..…41

Introduction – Chapter 2…….…….……...…...41

1. Brief historical background of aluminum alloys…….....43

2. Alloy constitution - general explanation.……..…….…….……..44

3. General classification, nomenclature, and temper designation of aluminum alloys…….……44

3.1 General classification…….……..…….……44

3.2 Nomenclature system for wrought alloys..…….…...……45

3.3 T4 and T6 Temper designation for wrought alloys……46

3.4 Ageing...…….……..…….……47

4. Some applications of aluminum alloys in the automotive industry…….....……..48

5. Influence of natural ageing up to six months and slow heating condition on the thermo-mechanical properties of the aluminum alloys EN AW 6016-T4 and EN AW 6056-T4……..…….....51

5.1 Materials: EN AW 6016-T4 and EN AW 6056-T4……51

5.2 Tensile test…….52

5.2.1 Setting up the tensile sample……...52
5.2.2 Digital Image Correlation (DIC) method procedure for tensile test…….53
5.2.3 Setting up the tensile test…….55
5.2.4 Tensile test results and discussions…….56

5.3 Thermal expansion analysis……..64

5.3.1 Setting up the test……64
5.3.2 Results and discussions of the thermal expansion analysis……66

5.4 Laser Flash Analysis (LFA)……..67

5.4.1 Setting up the test……67
5.4.2 Results and discussions of the thermal diffusivity measurements……...69

5.5 Differential Scanning Calorimetry (DSC)……72

5.5.1 Setting up the test……72
5.5.2 Results and discussions……...73

6. Conclusion – Chapter 2…….…...…...…...……78

Bibliography – Chapter 2……..…….……..…….....79

Chapter 3 – Understanding the mechanisms of differential expansion of body-in-white sheets: theory and lab-scale testing……..……....……...……...……85

Introduction – Chapter 3…….…..……...…...85

1. Simplified example of the expansion problem and laboratory analysis methodology……..……..……..….87

2. Stability analysis and equilibrium conditions..……..……..…….……..90

3. Thermal buckling……...92

4. Thermal buckling behavior of a circular aluminum alloy plate using the digital image correlation technique and finite element analysis…….……93

4.1 Problem formulation: equations of thermal buckling for a clamped circular plate…….93

4.2 Numerical simulation: thermal buckling for a clamped circular plate…….100

4.3 Experimental analysis of the post-buckling of a clamped circular plate……..102

4.4 Numerical analysis of the post-buckling of a clamped circular plate……...105

4.5 Results and discussions……...107

4.6 Conclusion……...111

5. Investigation of thermal buckling behavior in the context of differential expansion …….…….112

5.1 Impact of boundary conditions on buckling: bar case…….…….113

5.2 Analysis of thermal expansion and thermal buckling: thermal buckling of a beam subjected to imposed displacement…….116

5.3 Coupling of two different materials under thermal loading……..120

5.3.1 Experimental set up: rectangular plates test……...120
5.3.2 Material analysis: steel DC01…….…..…..121
5.3.3 Buckle and post-buckle analysis: rectangular plates..……. …..123

5.4 Conclusion……...130

6. Conclusion – Chapter 3……...…….….132

Bibliography – Chapter 3……...…..133

Chapter 4 - Analysis and numerical study of body-in-white tests for evaluating roof appearance defects after thermal cycle in the painting phase……...…137

Introduction – Chapter 4…….……...……..137

1. Testing protocol for the structural car tests at the factory……...…….139

2. Aluminum alloy car roof with geometry equivalent to steel roof: thermal buckle and post-buckle analysis……..145

2.1 Thermal buckle simulation: aluminum alloy car roof with geometry equivalent to a steel roof……..146

2.2 Thermal post-buckle simulation: aluminum alloy car roof with geometry equivalent to a steel roof……..149

2.3 Conclusive insights from analyzing aluminum alloy car roof with steel roof geometry ……..160

3. Influence of the car roof's geometry parameters on the critical buckling temperature ……..……161

3.1 Influence of curvature of a fixed rectangular plate on the thermal buckling…….162

3.1.1 Flat rectangular plate (without curvature)……..162
3.1.2 Curved rectangular plate along the length or width……...164
3.1.3 Curved rectangular plate along the length and width……166

3.2 Influence of adding ribs on thermal buckling of a rectangular plate…….167

4. Simulations: proposal for a new roof geometry……..170

4.1 Ribs in the roof geometry…….170

4.2 Thermal buckle simulation: aluminum alloy car roof with proposed geometry…...……...174

4.3 Thermal post-buckle simulation: aluminum alloy car roof with proposed geometry…….....177

5. Conclusion – Chapter 4……181

Bibliography – Chapter 4……...…..183

General conclusion…….……..185

Appendices …….……..189

General introduction

The main final objective of this thesis is to provide Stellantis with a car structure that responds to the problem that will be presented. Thus, it is important that throughout this document the reader bears in mind that the three-year objective was to bring scientific and industrial answers for immediate application in a high-scale industrial structure. For this reason, a very clear understanding of the political, competitive, and regulatory context, associated with the problem statement, is as crucial as the scientific studies in this document and deserves an entire chapter for discussion. This thesis is then within the framework of research and development of the Aluminum Multi-Materials (AM2) project, more specifically in the classification of a CIFRE thesis carried out through the partnership between the company (Stellantis), the research laboratory IRDL (represented by ENSTA-Bretagne, UBO, UBS and ENIB) and the *Association Nationale de la Recherche et de la Technologie* (ANRT). With this context in mind, the following summary outlines the content of this work.

- **BRIEF CONTEXT**

Nowadays, the new requirements of the European Union in terms of CO2 emissions, the advance of technology with the idea of the Industry 4.0, the international regulatory changes and the new energy variants are stimulating the automotive industry to carry out research and development to incorporate lightweight materials in the future vehicles. Consequently, the vehicle of the future will consist of a patchwork of materials in order to avoid unnecessary excess weight in some areas of the cars. In other words, it is about putting the "right material in the right place" of the vehicle according to technical and economic criteria. However, this change must also respect the industrialization constraints of the automotive industry.

Knowing that it is important to propose innovative solutions that allow assembling multi-material structures, Stellantis has launched with some partners a new project called "*Projet AM2*". This project is structuring Stellantis around multi-materials and multi-technology processes with the introduction of an aluminum roof assembled in a body-in-white made mainly by steel. Therefore, it is in this field that this study is going to take place.

- **BRIEF PRESENTATION OF THE PROBLEM**

The use of multi-materials is a very interesting solution to achieve mass reduction in cars. However, it encounters some problems regarding one point: the heating of the body-in-white in the production line. For structures made of a single type of material, this heating condition causes no problem because the assembled parts expand homogeneously. On the other hand, for multi-material structures such as the body-in-white, each part expands regarding its own coefficient of expansion. These large temperature variations during the fabrication of vehicles result in a state of strain generated in the assembled structure, which it is necessary to predict. With regard to thin structures, such as the object of study in this thesis (roof of the car), there are debates at the moment among car manufacturers: Is it possible to urgently avoid and predict this problem respecting the industrial criteria? This questioning reveals a lack of scientific knowledge about the phenomena linked to an understanding of the problem of

differential thermal expansion generating appearance defects. This thesis work then focused on finding an answer to that.

- **DISSERTATION PLAN**

This dissertation is organized into five chapters.

- In Chapter 1, the trends that will impact vehicle design from 2025 onwards and the project that gave rise to this thesis are presented, along with the vehicle of study. Then the problem statement will be detailed, through the analysis of a case study carried out between 2010 and 2013. As the problem occurs in the production line, the main stages of this process will be shown, focusing on the process of greatest interest for the study. This chapter concludes with a didactic presentation of the methodology that will be employed throughout this dissertation to solve the stated problem.
- Once the context and the problem have been clearly understood, Chapter 2 will be addressed. In this chapter, scientific advancement will be made through the study of the aluminum alloys selected for the car roof design. While aluminum alloys are widely recognized, there is a paucity of literature references regarding the identification of thermomechanical properties of the chosen aluminum alloys under slow heating conditions and considering the natural aging of the material. In terms of the industrial aspect, the aim of this chapter is to establish a foundational understanding of the roof structure through material analysis.
- Following the characterization of the materials relevant to this thesis, Chapter 3 focuses on a comprehensive analysis of instability phenomena induced by differential expansion within a controlled laboratory setting. This chapter aims to explore the problem from analytical, physical, and numerical perspectives, proposing a simulation methodology that accounts for the evolving properties of aluminum alloys throughout thermal cycles. The primary objective is to establish a meaningful correlation between simulation outcomes and physical experimental data acquired in the laboratory. While Chapter 2 delved into the material characterization aspects, this chapter expands the scope to the mesoscale, enabling an examination of material behavior at a larger structural level.
- Following the understanding of materials and the development of numerical simulation models capable of identifying instability phenomena, chapter 4 is reached. To achieve the final objective of this thesis, numerical simulation models capable of predicting the impact of differential expansions on roofs made of aluminum alloy on a steel body-in-white were provided to Stellantis. Additionally, this chapter will elucidate the final roof design choices and discuss the results of the tested car bodies. From both scientific and industrial perspectives, the findings of this thesis will represent a significant advancement for the automobile industry, as this study stands as one of the pioneers in addressing this type of problem created by a very contemporary context.

This dissertation ends by reviewing results obtained in relation to the question initially asked and by an outline of the work to be continued in order to continue advancing in this field of study.

Chapter 1 - Industrial context and problem statement

Introduction – Chapter 1

The large-scale introduction of technologies in a world marked by globalization and the automation of data exchange associated with new stages and models of production constrain the automotive industry. Additionally, the growth of environmental awareness and the current economic context further pressure the industry to implement very contemporary concepts in its factories. Considering that this whole process is very recent and has a direct influence on the origin of the study, it is important and necessary to have a very clear notion of what are the trends and limitations that play a major role in the concept and production of vehicles nowadays. Thus, this chapter will begin by showing the three main contemporary global megatrends that will affect the automotive sector: the Industry 4.0, the EU CO_2 emission targets for vehicles and the new energy variants along with the changes in standards and regional particularities. This first part will end with a conclusion showing the impacts of these concepts on the design of a vehicle today.

From this broader perspective outlined, attention shifts to a more specific focus, centered around the context of Stellantis (the company where this thesis is conducted). This transition leads to a discussion on the "*Projet AM2*." This project was carried out to accelerate the implementation of multi-material solutions in the automotive industry and it has fostered the creation of several partnerships between companies and universities, among which led to the realization of this thesis. It is also in this part that the study vehicle will be presented.

The third part of this chapter will begin by presenting the problem through a case study previously carried out (*Projet V*). Then, analyzing from the manufacturing context, the production line will be presented, with the major stages of the manufacture of a vehicle at Stellantis - Rennes, from the arrival of the metallic materials to the end of the production line. Understanding this process will be important to know the reason why a focus will be made in the passage of the vehicle structure into the ovens after the cataphoresis phase. To establish a meticulous scientific framework regarding the temperature range encountered during the ovens from the painting phase, experiments were conducted to analyze temperature curves and determine the peak temperature reached by the car roof structure. This range serves as the cornerstone for ensuing scientific inquiries in subsequent chapters, laying the groundwork for forthcoming analyses and investigations.

Finally, once the context has been explained and the problem has been identified, the conclusion of this chapter will be highlighted with the methodology that has been chosen to solve the problem statement, indicating the field of study, the objectives, and the approach that will be taken in this thesis. By delineating the chosen methodology to address the problem statement, it becomes easier to provide clarity and direction, ensuring that the research efforts are focused, purposeful, and aligned with the overarching scientific goals of the study.

TABLE OF CONTENTS – CHAPTER 1

Chapter 1 - Industrial context and problem statement……...……15

Introduction – Chapter 1……...…….....15

1. Global industrial context: trends that will impact automotive designs from 2025 onwards……..……..……..……17

1.1 The concept of Industry 4.0…….……..……17

1.2 EU CO2 emission targets for vehicles and diversification of energies and variants…….…….....20

1.2.1 Brief historical context of EU targets for CO_2 emissions and Paris Agreement – 2015…….….20

1.2.2 Paris Agreement regulations for vehicles and diversification of energies and variants……...…….….20

1.3 Evolution of standards and regional particularities.…….....23

1.4 Consequences of automotive trends…….....23

2. Stellantis industrial context: *Projet AM2*……..…24

2.1 Stellantis - Rennes: ATRP team..…….……..……24

2.2 Excelcar……. …….……..……25

2.3 *Projet AM2*…….……..……26

3. Thesis problem statement, the production line and the body-in-white……..……29

3.1 Problem statement: *Projet V* – Groupe PSA (2010-2013).……..……...…29

3.2 The main stages of the production line……...…….……...…30

3.2.1 Stamping…….....30
3.2.2 Welding……..31
3.2.3 Painting……...32
3.2.4 Assembly……32

3.3 Identification of thermal loads on the roof of the body-in-white during fabrication and throughout its life cycle……...…….....33

4. Conclusion - Chapter 1 / Methodology to solve the statement problem..…...……36

4.1 Conclusion…….…….……...…36

4.2 Methodology to solve the statement problem…….……...…37

Bibliography – Chapter 1…….……..…….……..…39

1. Global industrial context: trends that will impact automotive designs from 2025 onwards

1.1 The concept of Industry 4.0

Since the XVIII century, society has been looking for a way to accelerate the production of goods and optimize the exploitation of natural resources under the influence of the consolidation of capitalism. This fact resulted in the creation of the First Industrial Revolution, and consequently the formation of large industries. This whole process caused major changes in the global economy, as well as in the way of life of humanity [1]. However, the First Industrial Revolution was only the pioneer of a long process of transformation. Several transformation processes took place in the industry and the main changes generated by Industries 1.0 to 3.0 are briefly shown below:

- Industry 1.0 (First Industrial Revolution) was marked by the use of steam energy and the mechanization of production. The use of machines in industries generated more dynamic productivity and this symbolized more work opportunities [2];

- Industry 2.0 (Second Industrial Revolution) was characterized by the discovery of electricity, population migration from rural areas to urban areas and use of combustion engines. In this period, the metallurgical, steel and automotive industries stood out. This phase was also known for its innovations capable of reducing the manufacturing time of products [3];

- Industry 3.0 (Third Industrial Revolution) began in the 1950s, after the Second World War. This phase of the Industrial Revolution is characterized, above all, by the insertion of technology in the scientific field, linking it to industry and the productive system. During this period, advancements and technological improvements never seen before were made. During the Third Industrial Revolution, high-technology industries stood out with considerable development mainly in the fields of genetics, robotics, information technology, telecommunications and electronics. This period was marked by the automation of production processes [4].

After these industrial revolutions, the narrative transitions to the present times. With globalization resulting in a very competitive market, factors such as cost, productivity and efficiency are crucial for the survival of brands. To face these challenges, amplified by the demands generated by the Covid-19 pandemic, an acceleration of the process of digital transformation and the development of bioenergy industry is underway. With current needs differing from the needs of past years, a new industrial revolution is therefore taking place. In this context, the concept of Industry 4.0 sparks a lot of interest among the industrial community.

According to [5] (Vaidyaa, Ambad, & Bhosle, 2018), in principle, Industry 4.0's proposal is to revolutionize the way products and services are generated. This is done by connecting and optimizing the entire value chain (information, people and equipment) with intensive use of digital technology. These strong interconnections between machines and

systems consequently generate strong profitability. That strong profitability is one of the main reasons for the interest of plant managers in this new industry. Studies and surveys indicate the potential of this way of doing for lower maintenance costs, energy consumption and increased efficiency. Figure 1 shows a schema of the Industry 4.0 for the manufacturing plants.

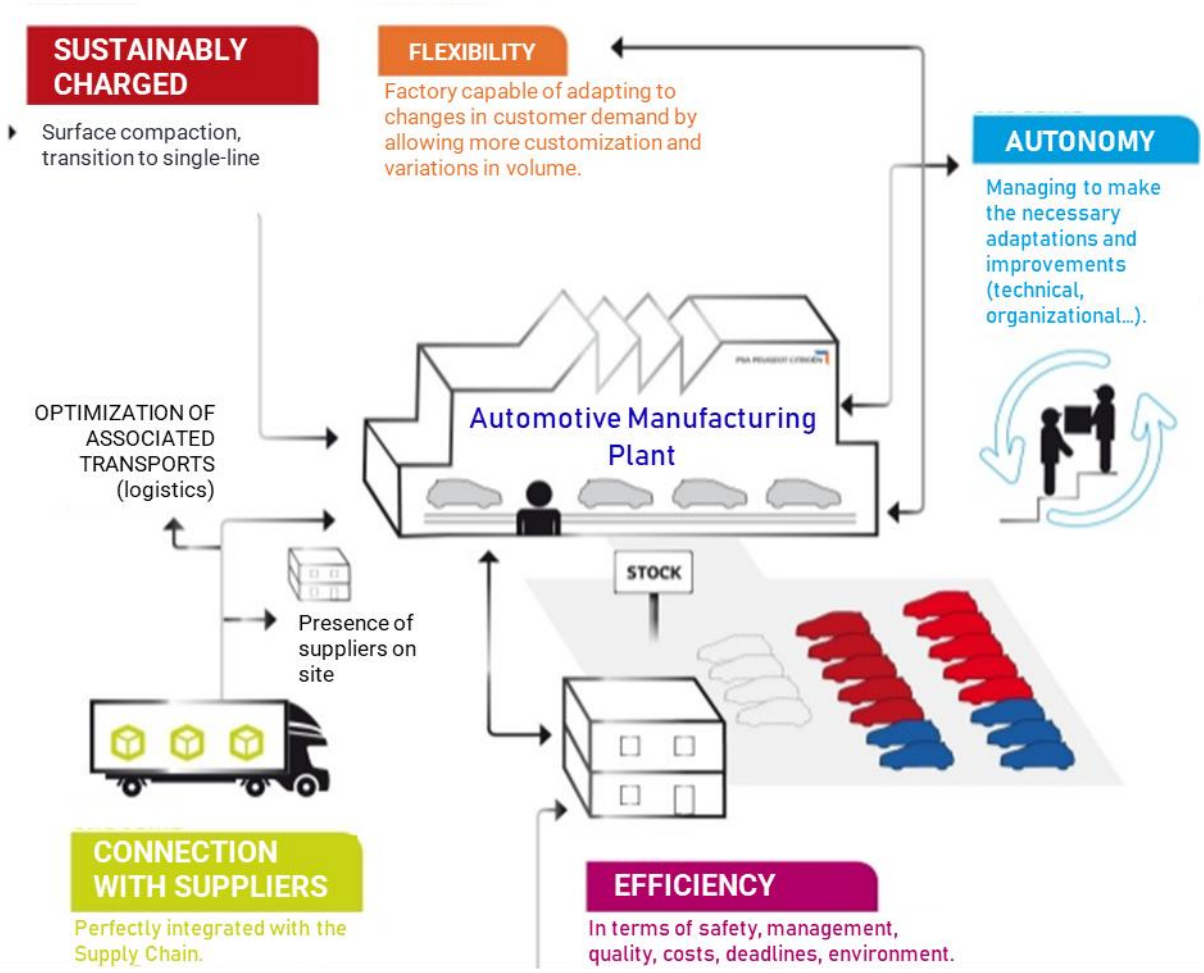

Figure 1 *Representative image of the concept of Industry 4.0. The image is from internal Stellantis documents with modifications made by the author.*

With regard to Stellantis, currently, the implementation of the Industry of the Future is something that is already taking its place. Projects are being developed to make some improvements in plants of the group. For example, the use of IoT (Internet of Things) to transport heavy materials on mobile supports is already used at Stellantis' Rennes plant, as it is possible to see in figure 2.

In addition to everything that has been explained, one of the greatest assets of these smart factories is the possibility of having better bonding between the production sites and the external environment (customers and partners). This better relationship is possible thanks to the flexibility of these smart factories, increasing the number of possible customizations in products for clients. With this flexibility and customization happening very quickly, for a large company to remain competitive it is necessary to move towards these changes proposed by Industry 4.0. Otherwise, companies will lose both in terms of customers and in terms of the cost of adapting the production line (if it is not flexible).

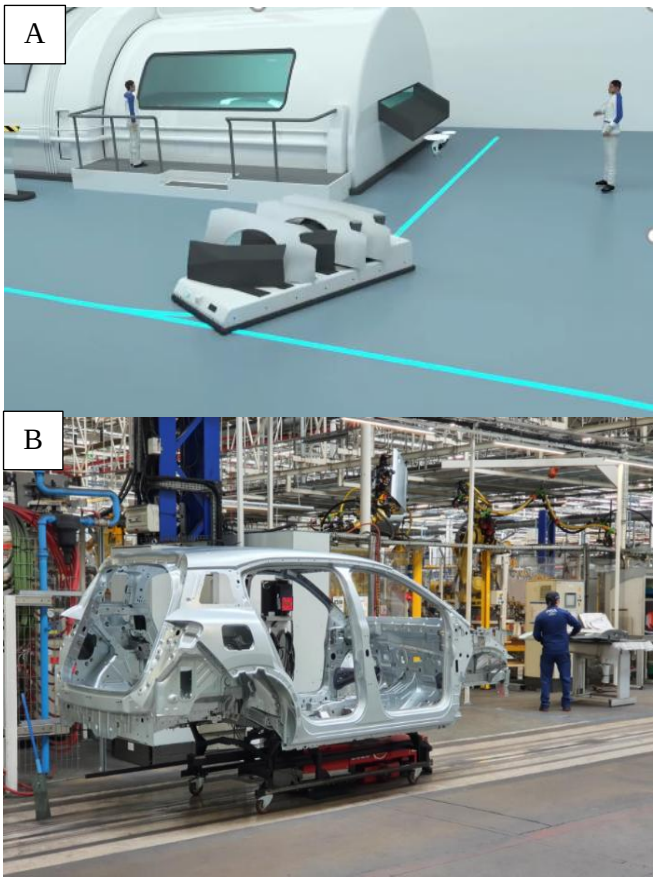

Figure 2 A) *Mobile support project that represents the introduction of IoTs into the Industry 4.0;* ***B)*** *Application of the project in the production lines.*

For example, in the automotive industry, being able to exchange car parts previously made of a specific material for parts of other materials without causing major changes in the production line generates a huge advantage in terms of production costs. Same thing if it is necessary to move from the production of a fuel-powered vehicle to an electric vehicle.

The result: the term "flexibility" is a major concept in these industries to satisfy the customization desired by the customer. Negligence in adopting this production method could be very costly in the future for automotive brand. Consequently, the plurality of materials in a single vehicle is a trend of Industry 4.0 that cannot be ignored. However, these transformations need to be carried out respecting industrial criteria such as cost, production rate and production line capacity.

In addition to the Fourth Industrial Revolution, other factors also contribute to the existence of some trends in the automotive industry. As mentioned before, one of the goals of Industry 4.0 is to know how to deal with the adaptability required in today's world. This adaptability is also linked to the new environmental requirements in connection to the Paris Agreement.

1.2 EU CO_2 emission targets for vehicles and diversification of energies and variants

1.2.1 Brief historical context of EU targets for CO_2 emissions and Paris Agreement – 2015

In the first years after the creation of the United Nations (UN - 1945), neither environmental issues nor climate change were a matter of concern. The only actions that were taken in these areas, at that time, were operational activities, carried out through the World Meteorological Organization (WMO). When attention was paid for the first time to natural resources and the environment, that attention was much more focused on the capacity of known natural resources to guarantee the economic development of many UN countries (mainly underdeveloped countries, as they were called) than on the responsibility ecological itself [6]. Only in 1968, 23 years after the creation of the UN, important organizations of the UN gave special attention to the environment.

After the Stockholm Conference (1972), Rio 92 (1992) and Kyoto Protocol (1997), countries all over the world had the feeling of the need to seek even more restrictive measures in favor of preservation and promotion of the human environment, as well as an action plan containing recommendations for international action in environmental matters against the climate changes. This culminated in the adoption of the **Paris Agreement**, in 2015, inaugurating a new phase of the multilateral regime, marked by greater ambition to face climate change on a global scale.

The adoption of the Paris Agreement was made through the 21st Conference of the Parties to the United Nations Framework Convention on Climate Change (Paris Conference - 2015). The Agreement represents a decisive and global response to the challenge of climate change, with the aim of keeping global warming well below 2ºC and redoubling efforts to limit the increase in temperature to 1,5ºC [7]. It offers a fair, ambitious, balanced and lasting global framework to support the efforts of all countries against climate change. The EU's main objective is to reduce greenhouse gas emissions by at least 40% by 2030, compared to 1990 levels [8]. The automotive industry is part of this percentage and the specific rules for this category are shown in the following section.

1.2.2 Paris Agreement regulations for vehicles and diversification of energies and variants

Passenger cars and vans ('light commercial vehicles') are responsible for around 12% and 2,5%, respectively, of total EU emissions of carbon dioxide (CO_2), the main greenhouse gas [9]. On the 17th of April 2019, the European Parliament and the Council adopted Regulation (EU) 2019/631, setting CO_2 emission performance standards for new passenger cars and for new vans in the EU. This Regulation started being applied on the 1st of January 2020.

In order to contribute to the objectives of the Paris Agreement, the transformation of the entire transport sector towards zero emissions needs to be accelerated, considering the Commission's communication of the 28th of November 2018 entitled 'A Clean Planet for all — a European strategic long-term vision for a prosperous, modern, competitive and climate neutral economy'. This communication outlines a vision of the economic and societal transformations required, engaging all sectors of the economy and society, to achieve the transition to net-zero greenhouse gas emissions by 2050. Emissions of air pollutants from transport need also to be drastically reduced without delay. Emissions from conventional combustion engine vehicles needed to be further reduced after 2020.

To meet environmental goals, zero- and low-emission vehicles must be widely adopted and capture a significant market share by 2030. Continued reductions in CO_2 emissions for both passenger cars and light commercial vehicles will be imperative post-2030. As per Regulation (EU) 2019/631, the newly established CO_2 emission targets for the entire fleet of newly registered EU light cars and vans stipulate a 15% reduction from 2025 and a 30% reduction from 2030, relative to 2021 levels, as illustrated in figure 3. Manufacturers (including Stellantis) are required to ensure correspondence between the CO_2 emissions recorded in the certificates of conformity of their vehicles and the CO_2 emissions of vehicles in-service measured according to the Worldwide Harmonized Light Vehicle Test Procedure (WLTP).

It is also important to highlight that vehicle emissions are not only related to its usage phase. They are also linked to the vehicle production stage. The transition to a circular economy in the automotive sector has become a major priority to reduce the environmental footprint of this industry. One of the most critical aspects of this transition is the integration of recycled materials into the vehicle manufacturing process. By incorporating recycled materials, such as recycled metals, automotive manufacturers can reduce their reliance on virgin resources, lower carbon emissions associated with the production of new materials.

The result: To achieve low carbon emissions during the usage phase, manufacturers must lighten their vehicles and offer hybrid/full electric options. However, these changes entail a significant cost, especially if existing materials and assemblies are retained. Therefore, to reduce emissions in the manufacturing phase as well, it is imperative to use different materials to decrease CO_2 emissions by reducing vehicle weight, highlighting the importance of introducing light recycled materials.

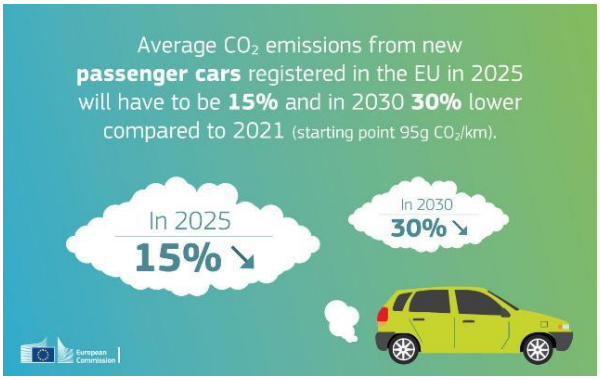

Figure 3 *The proposed 30% reduction target for passenger cars intending to make significant step forward in the fight against climate change [11].*

Despite conventional fuel-powered cars still dominating car sales in the EU with almost 60% of vehicles in 2021 (figure 4), between 2020 and 2021 the growth of battery electric vehicles (BEV), hybrid electric vehicles (HEV) and plug-in hybrid electric vehicles (PHEV) were expressive, as it is possible to see in figure 5. Government incentives for low- and zero-emission automobiles implemented in the wake of the COVID-19 pandemic played a significant role in this situation [12]. Moreover, this growth in sales of cars with alternative fuels further confirms the hegemony of Industry 4.0 in the very near future, because with the adaptability comes the diversification of types of energy.

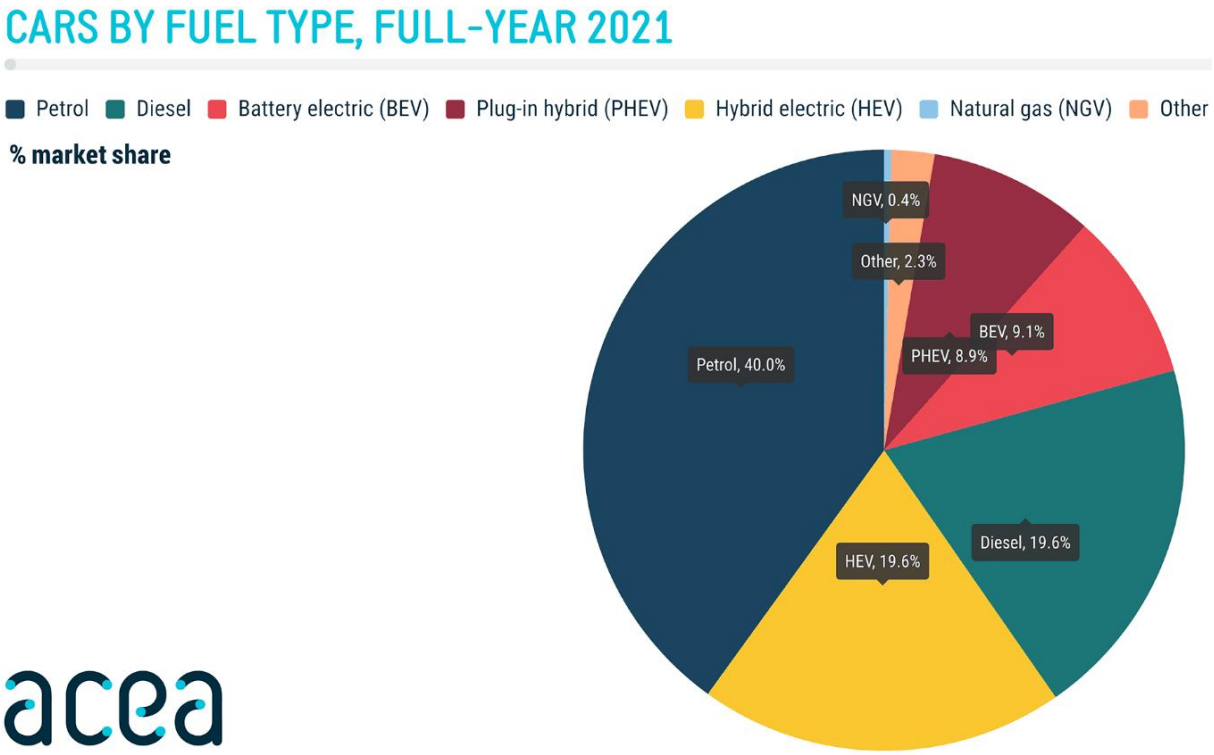

Figure 4 *Proportion of cars by type of fuel in 2021 [12].*

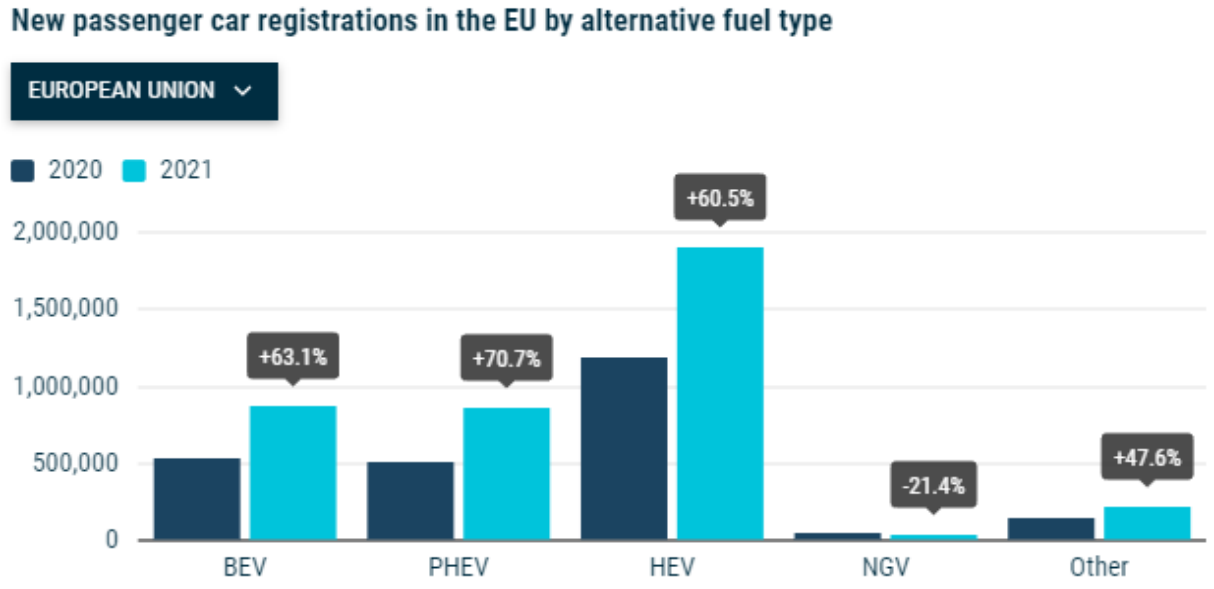

Figure 5 *Evolution between 2020 and 2021 of registrations of cars in the EU with alternative fuel type [13].*

1.3 Evolution of standards and regional particularities

Associated with this transition of fuel types, crash tests are more and more demanding, and certain geographic areas (US, China, etc.) impose constraints which require specific platforms. For example, regarding frontal impacts, in 2020 EuroNCAP replaced the traditional Offset-Deformable Barrier test (introduced in 1997), by the new Mobile Progressive Deformable Barrier. In the traditional Offset-Deformable Barrier test, the car used to be pushed at 64 km/h with a 40% overlap into a deformable barrier that mimics the oncoming vehicle [14]. Now, with the Mobile Progressive Deformable Barrier, the car at 50 km/h will be impacted with a 50% overlap by a deformable barrier on a 1400 kg trolley, coming towards the car also at 50 km/h [15]. Figure 6 shows the 5 stars result of the Jeep Grand Cherokee in this test.

It is important to achieve a good evaluation score in these types of tests, as these results directly influence consumers' choices when purchasing vehicles for their families and businesses. Moreover, these scores can help clients identify the safest choice for their needs. While there is a need to reduce the weight of vehicles, safety cannot be compromised and, in fact, needs to be improved to meet increasingly stringent safety tests.

The result: therefore, it is not only necessary to replace denser materials with lighter alternatives, but also to ensure that the correct material is placed in the appropriate location while adhering to international safety standards.



Figure 6 *Euro NCAP 2022 test of Jeep Grand Cherokee – Result: 5 stars. Figure from [16] (Euro NCAP) for print and online use only.*

1.4 Consequences of automotive trends

Analyzing the results of the trends created by Industry 4.0, the EU emission targets for vehicles, and the energy diversification associated with the evolution of safety regulations, it can be concluded that the car of the future will be made of a patchwork of materials that will need to be assembled by different processes, taking into account criteria such as:

- Environmental impact: respecting the current normative criteria for CO_2 emissions by automobiles, towards the reduction of the weight of vehicles, preferably with materials that can be recycled;
- Mechanical resistance: the vehicles need to be safe and have a great score on security tests;
- Product mix: up to six different vehicle silhouettes on the same production line (production of 60 vehicles per hour);
- Control of production costs and, therefore, of profitability: radically changing the structure of the production chain would cause huge financial damage to automobile companies and it would also require the empowerment of all staff to the new manufacturing process;
- Assembly capacity: maximize reuse of existing equipment (carry over factory) taking into account the high production rate of 60 vehicles per hour on a conventional factory.

In this way, the challenge of multi-material assembly emerges as a central focus of today's and tomorrow's industrial challenges in the automotive industry. It is within this challenge that this thesis is focused in. Knowing that the combination of different materials would bring about a considerable change in Stellantis' projects, the company, represented by the Advanced Technology & Regional Partnership team (ATRP), launched a long-term project called AM2, as part of the innovation process developed within the Stellantis - *Rennes la Janais* site. As the global context has already been explained, in the next section of this chapter, the focus will be on the industrial context of Stellantis. It will be at that moment that the company will be briefly presented along with the ATRP team, Excelcar and the AM2 project.

2. Stellantis industrial context: *Projet AM2*

2.1 Stellantis - Rennes: ATRP team

Stellantis has an industrial experience of more than 200 years. The field of activity of the group is the mastery of all trades of the automobile, from production to services and distribution. The origins of Stellantis starts with one of the first companies to produce and market gasoline cars at the end of the 19th century: Peugeot. Named PSA *(Peugeot Société Anonyme*), the company was founded in 1966. Ten years later, the merger of Citroën S.A. and Peugeot S.A. gave birth to Groupe PSA Peugeot Citroën [17]. In the 2000s, PSA Peugeot Citroën group boosted its international growth, particularly in high-growth countries such as China and Brazil. In 2016 PSA Peugeot Citroën became Groupe PSA and in 2017 Groupe PSA acquired Opel and Vauxhall brands [17].

Finally, in order to support the ambition of the brands in the global automotive market, Peugeot S.A. (« Groupe PSA ») and Fiat Chrysler Automobiles N.V. (« FCA ») have progressed in a 50:50 merger project, as defined in the combination agreement announced on December 18, 2019 [18]. The finalization of the merger project took place in the first quarter of 2021. The group now owns the brands Peugeot, Citroën, DS Automobiles, Opel, Vauxhall (from Groupe PSA) and Fiat, Alfa Romeo, Lancia, Maserati, Abarth, Jeep, Chrysler, Dodge, RAM (from the FCA Group). In total, a new group made of about 400.000 employees.

Concerning the Stellantis factory where this thesis is situated, the Rennes plant came into operation in 1961. Nowadays, this site produces two vehicles: Peugeot 5008 and Citroën C5 Aircross. The workforce registration in the site Stellantis Rennes shows that the numbers of workers are nearly 2000 employees [19]. Figure 7 shows the aerial view of the plant.

As the challenges of multi-material assembly call for innovative solutions, in Stellantis Rennes plant there is a group of employees called Advanced Technology & Regional Partnership team (ATRP). This team is responsible for developing innovative and collaborative projects with other partners to respond to the needs of Stellantis. Today, ATRP is composed of 28 workers, including working students, doctoral students, engineers and technicians, all of them working in innovations. As carrying out innovations also means carrying out projects and studies, it is important and necessary to have industrial partners. It is in this context that Excelcar plays an important role in the team.



Figure 7 *On the left, brands that compose Stellantis [20]. On the right, aerial view of the factory - PSA Rennes [19].*

2.2 Excelcar

Knowing all that has been mentioned before, it is very clear that there is a need to transform current industrial systems of production and design. Excelcar enters this part precisely to accelerate this development through a global product-process approach at a structural scale. Excelcar is then an industrial FabLab (manufacturing laboratory, figure 8) and open collaborative innovation platform, at the service of the ecosystem, manufacturers, Industry 4.0 and the vehicle and mobility sector [21]. Furthermore, it is possible to say that Excelcar is

an innovation platform to accelerate the market launch of product-process innovations in the industry.

As both organizations work with innovation, ATRP and Excelcar help each other to accelerate projects. This partnership brings up a lot of benefits for both parts. Talking in a perspective from Stellantis, the main benefits for the company are:

1. The solution to the problem of underinvestment in innovation at the preindustrial stage;
2. The development and qualification of innovation projects or the introduction of new technologies;
3. The reduction of the costs of technological and industrial tests;
4. The possibility of providing a layout of industrial and configurable environments at the scale of the structure without disrupting the production line;
5. The possibility of making links between academics and industrialists easily.

Among the innovation projects originating from the partnership between Stellantis and Excelcar, there is the project that culminated in this thesis: the ***Projet AM2*.**



Figure 8 *Openspace and test platform shared between Stellantis and Excelcar.*

2.3 *Projet AM2*

Now that the entire industrial context has been introduced, it will be easier to understand the motives of the AM2 project. Firstly, **AM2 stands for *Aluminum Multi-Matériaux* and it**

is a project that aims to structure Stellantis around multi-material and multi-process technologies with the massive introduction of aluminum on the steel body-in-white (BIW) [22].

Among the benefits that the AM2 will bring to the companies that surround the project, included are:

- The commercialization of 12 innovative products;
- The consortium benefits from the financial support of public entities - the *Banque Publique d'Investissement (BPI)*, the *Région Bretagne* and the *Rennes Métropole*;
- The creation of jobs distributed among the different partners;
- The increase in French automotive capability in technologies for shaping and assembling aluminum parts.

This project is nifty and important because it brings together industrial and academic partners (figure 9) to achieve the innovation goals in vehicle weight reduction in order to support the mobility of the future. The main concerns of AM2 are:

- Use of aluminum and composites in the structure of cars;
- Development of new hybrid assembly processes;
- Greater insertion of digital technology into physical chain of industrial processes;
- Industrial integration, respecting a high production rate.

This PhD thesis gives a special focus on the use of aluminum alloys as substitutes for some steel parts. Some reasons to justify this replacement are listed below:

1. The cost: the price of aluminum is relatively well known, thus investment is under control because it would largely take over the existing tools for steel;
2. Tools and design rules related to steel can also be applied to aluminum alloys;
3. The shaping processes for steels in the production line can also be used for aluminum alloys, in order to achieve shapes equivalent to the steel parts.



Figure 9 *Main participants of the AM2 consortium and objective of the project.*

However, there are currently technological constraints preventing the massive use of the aluminum alloys in some parts of the vehicle, and one of these problems is the statement problem of this dissertation. Even though the objective of AM2 is to allow the control and deployment of aluminum in the high-speed automotive industry, it is fundamental to ensure compatibility of this material with current (steels) and future (composites) materials. For that, assembly technologies linked to aluminum need to be developed in Stellantis context.

The vehicle of study for AM2 project is the Peugeot 5008 (figure 10 - B) and this thesis, in particular, is focused on the application of aluminum alloy on the car roof (figure 10 - A). **From then on, this dissertation will focus on the roof of the car and the consequences of the interaction between this structure and the body-in-white in the stages of the production line. To replace the steel on the roof of the car, two materials were chosen and will be the main study alloys: EN AW 6016-T4 and EN AW 6056-T4.** Chapter 2 will explain more about these materials.

Now that the entire context has been explained and the objectives of the AM2 project have been presented, the thesis will delve into the problem statement through a case study conducted in a past project called *Projet V*.

A



B



Figure 10 A) *Red arrow indicating the thesis study structure and highlighting the use of aluminum alloy instead of steel;* ***B)*** *Picture of vehicle of study in AM2 Project (Peugeot 5008) [23].*

3. Thesis problem statement, the production line and the body-in-white

3.1 Problem statement: *Projet V* – Groupe PSA (2010-2013)

Reducing the weight on the roof to lower the center of gravity and reducing pollutant emissions has always been a priority in automotive design. The use of aluminum alloys for car roof is well established in all-aluminum alloy bodies. However, the roof is usually an integral part of the structure. Therefore, **the integration of aluminum structural components in a steel structure requires an in-depth study of several aspects. The first problem is the realization of a reliable union between the different materials. The other problem is encountered in certain heating processes of the production line due to the differing thermal expansion coefficients of aluminum alloys and steel. It is precisely in this second aspect that this thesis will give a greater focus.**

This difference in the thermal expansion coefficient of the two materials means that the combination of the aluminum alloy roof attached to the steel body can create compressive stresses in the aluminum alloy roof when the body is subjected to high temperatures. During the development of *Projet V*, a roof of 1.2 mm thick made of EN AW 6016-T4 with side grooves was made to test how this structure would behave in a production line. This application would be used in the manufacture of the Citroen C8 and Peugeot 806 models. However, the result for the EN AW 6016-T4 roof can be seen in figure 11.

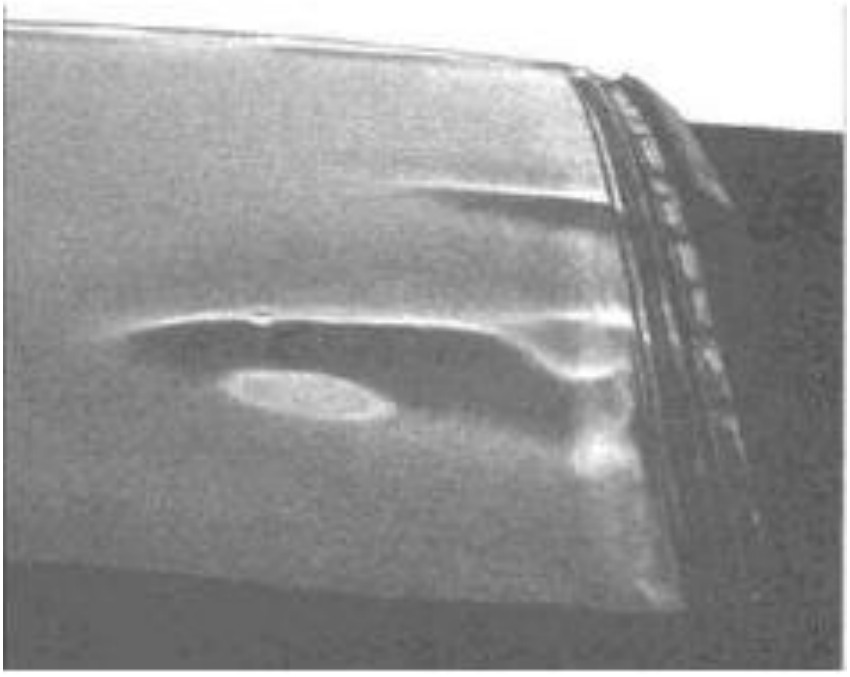

Figure 11 *Aluminum alloy roof on a steel body after bake paint cycle: EN AW-6016 [24].*

Visible defects on the car roof appeared, and they are not acceptable. Therefore, there is a necessity to find a solution that is to be validated before application in a vehicle through an industrial validation.

At this point, it is important to highlight two essential points:

1. The problem seen in figure 11 occurs at the scale of a car's structure. So, to solve the problem, a solution at the same level in terms of structure is needed. That is why the most important sample of the present thesis is the structure of the car and the solution must be applied directly to the vehicle, respecting the industrial limitations in terms of feasibility, brand design and boundary limit imposed by the production processes;

2. As it has been mentioned, the appearance defects that appear in the roof are related to the vehicle manufacturing process. To move forward with the studies, it is necessary to understand the main stages of the production line and know where the focus should be given in order to solve the problem.

Thus, the next section will briefly explain the steps that occur in the manufacturing process of a vehicle.

3.2 The main stages of the production line

3.2.1 Stamping

Each factory has its particularities and working methods. However, at the Rennes factory, the "just in time" concept is adopted, based on production according to demand and elimination of stocks. The first production process is called stamping. Metal plates arrive in coils, with labels that point to which models they are destined for. Once the metal plates are cut they are sent to the heavy stamping presses, where they will take shape. When the plates reach their shape they undergo a conformity check carried out by the personnel who work at this stage of manufacturing at the factory. Photos of the stamping process can be seen below in figure 12.

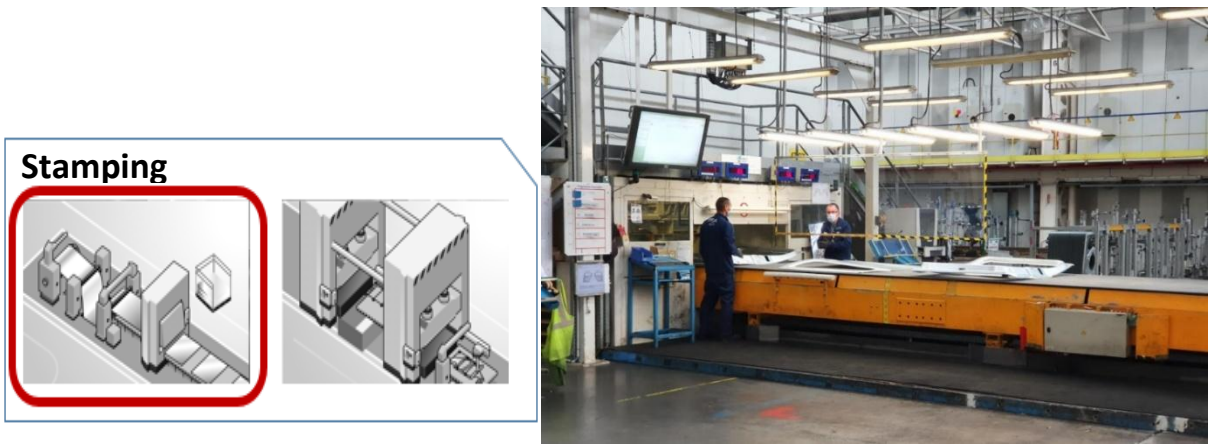

Figure 12 *Photo of the conformity area of the parts that come out of the stamping. Illustration of the stamping process is from internal Stellantis documents.*

3.2.2 Welding

The welding process involves the assembly of points through welding and brazing using various techniques. All different elements that arrived from the stamping are put together one in relation to the other. Most of these operations are done by robots, as shown in figure 13. Then, this final product made by joining parts will go through the painting process. It is after the end of this part that the body-in-white can be seen. From now on, the discussion will focus extensively on the body-in-white, so a brief definition of this structure will be provided.

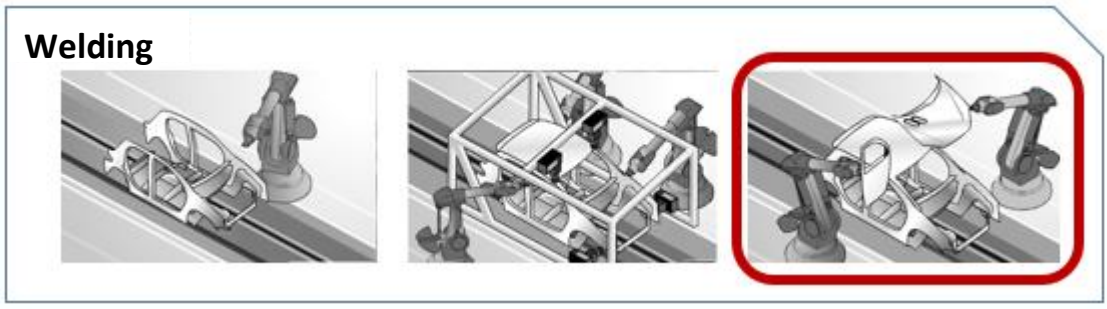

Figure 13 *Illustration of the welding and body assembly process. Image taken from internal Stellantis documents.*

According to [25] (Kutz, 2017), the body-in-white is the unpainted car body assembly, metal parts welded and rivets fastened, before painting and before the motor, chassis sub-assemblies, or trim (glass, seats, electronics, etc.) have been assembled in the frame structure (see figure 14). This structure is made up of a large number of materials, most of them steels of different grades. The body-in-white can be seen very well when leaving the body assembly process, just before entering the painting process.



Figure 14 *Body-in-white nearly complete and ready to move to the painting area.*

3.2.3 Painting

Painting begins with a pre-treatment that aims to remove impurities from the assembly process. Soon after, the car is immersed in an anti-corrosive liquid. The unit undergoes caulking, to prevent the infiltration of impurities, and a robotic application of primer, which leaves the body with a color very close to the final. It protects the paint from ultraviolet rays and prepares it for the ultimate color. Then, it is time to apply the base by spray, which gives the final color to the vehicle. To finish, the varnish is applied to protect and give the bodywork shine.

The painted body goes to the final assembly line without the doors. They follow their own path to receive the finishing with glass, doorknob, electrical wirings, rear view mirror and coating, as it is possible to see in figure 15.

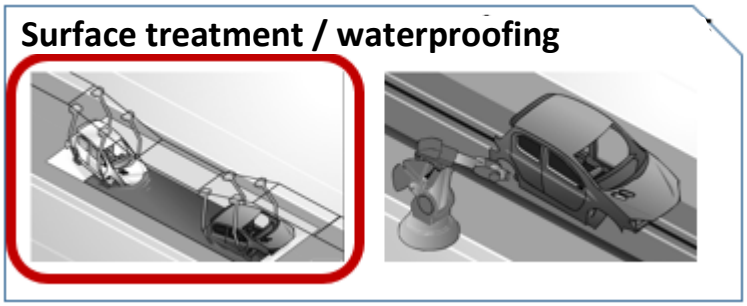

Figure 15 *Illustration of the surface treatment and waterproofing process. Image taken from internal Stellantis documents.*

3.2.4 Assembly

In this step, the doors are reinstalled again after the placement of items of greater volume in the car, such as seats, instrument panel, side and front windows and interior finishes. It is also in this process when engine and tires are added, as seen in figure 16. The fully assembled vehicle is subjected to a strict quality check in the final inspection process. If everything is within conformity, the vehicle is shipped as a finished automobile, as depicted in figure 17.



Figure 16 *Illustration of the assembly process. Image taken from internal Stellantis documents.*

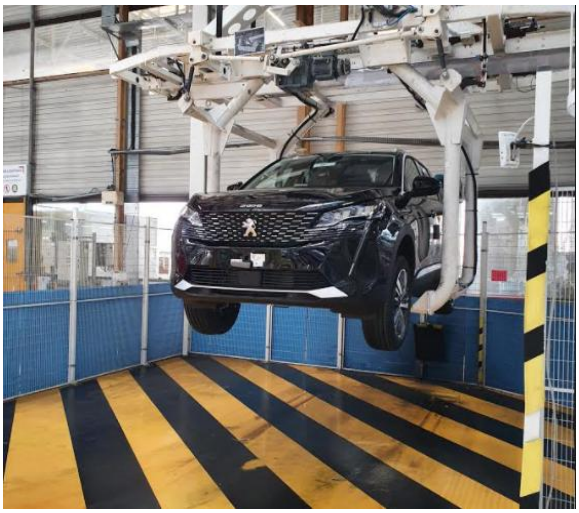

Figure 17 *Vehicle prepared for final compliance phase before the car leaves the factory.*

Among the operations mentioned above, special focus will be given to the phase of the painting ovens, which occurs between the end of the vehicle's immersion in the cataphoresis bath and the beginning of the assembly operation. This phase is of particular interest because it is at this time that the entire structure undergoes significant heating, and it is then that the appearance problems that were presented before are found.

3.3 Identification of thermal loads on the roof of the body-in-white during fabrication and throughout its life cycle

During the painting process, the body-in-white goes through a baking oven, as shown in figure 18, where the paint is cured at temperatures exceeding 180°C. The important point is the knowledge of these temperature changes over time and the difference that could exist between the oven setpoint and the temperatures at any point of the structure during the manufacturing phase. It will be important to identify the thermal loads to better identify the thermal boundary conditions of the problem.



Figure 18 *Body-in-white in the middle of the painting phase.*

Stellantis has two plants in France in which the Peugeot 5008 is manufactured: Sochaux Plant and Rennes Plant. Depending on the reference plant chosen, the heating kinetics vary. At the Rennes plant, the heating process takes place for 1 hour 30 minutes through the passage of the body-in-white in a tunnel which is approximately 200 meters long. The body-in-white crosses the tunnel at a speed of around 2.8 m/min and the tunnel remains heated at a temperature of 180°C thanks to hot blown air.

Aiming to detail the temperature evolution over time, a temperature measurement test was carried out at the Rennes Plant. A total of 15 temperature sensors were used on the ES G7/7 (0.75 mm) steel roof of a Peugeot 5008. The choice of location and number of sensors are described below:

- 7 sensors (sensors 3, 4, 6, 7, 8, 10 and 11, as shown in figure 19) positioned at different points on the car roof: as the car roof is the main object of study of the thesis, it is important to check the temperatures at different points on the roof;

- 7 sensors (sensors 1, 2, 5, 9, 12, 13 and 14) positioned on structures connected directly to the roof of the car: the objective is to use the temperature information of the structures connected to the roof of the car to feed a subsequent numerical simulation with these thermal data;

- 1 sensor (sensors 15) used to measure the air temperature in the baking oven: used to compare the temperature of the air in the oven with the temperature of the car parts, thus having a better idea of the time it takes for the heat air of the oven to be transmitted to the car parts by convection.

Figure 19 shows the position choices of the temperature sensors and figure 21 shows the test being done in reality.

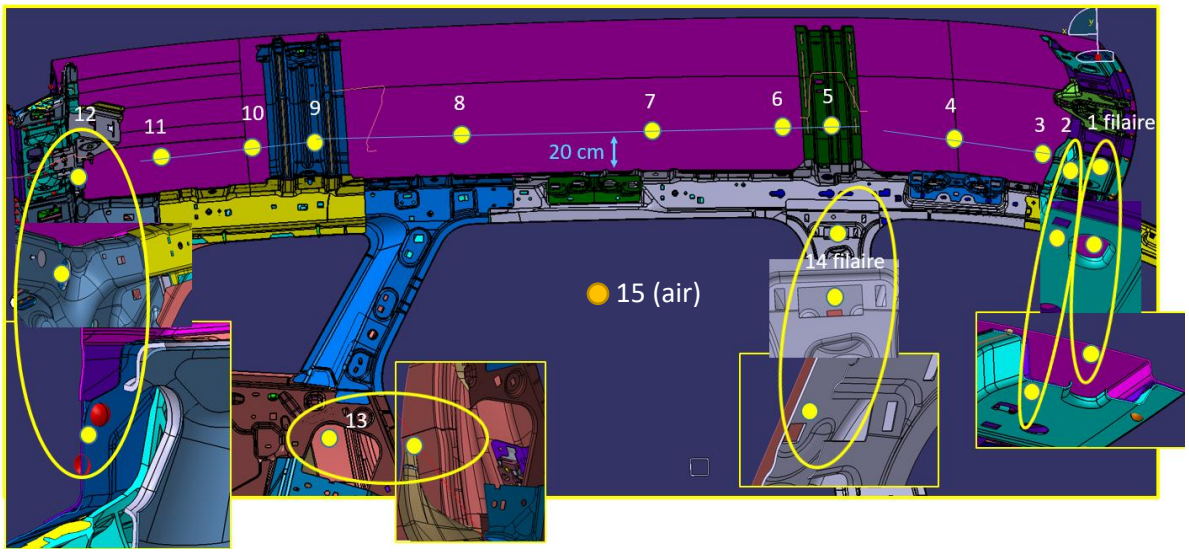

Figure 19 *Positions of temperature sensors on the upper part of body-in-white.*

It was chosen to place the sensors on only one side of the car because, by symmetry, these values can be extrapolated to the other half of the roof car. The chart below, figure 20, shows the temperatures recorded and some photos of the test.

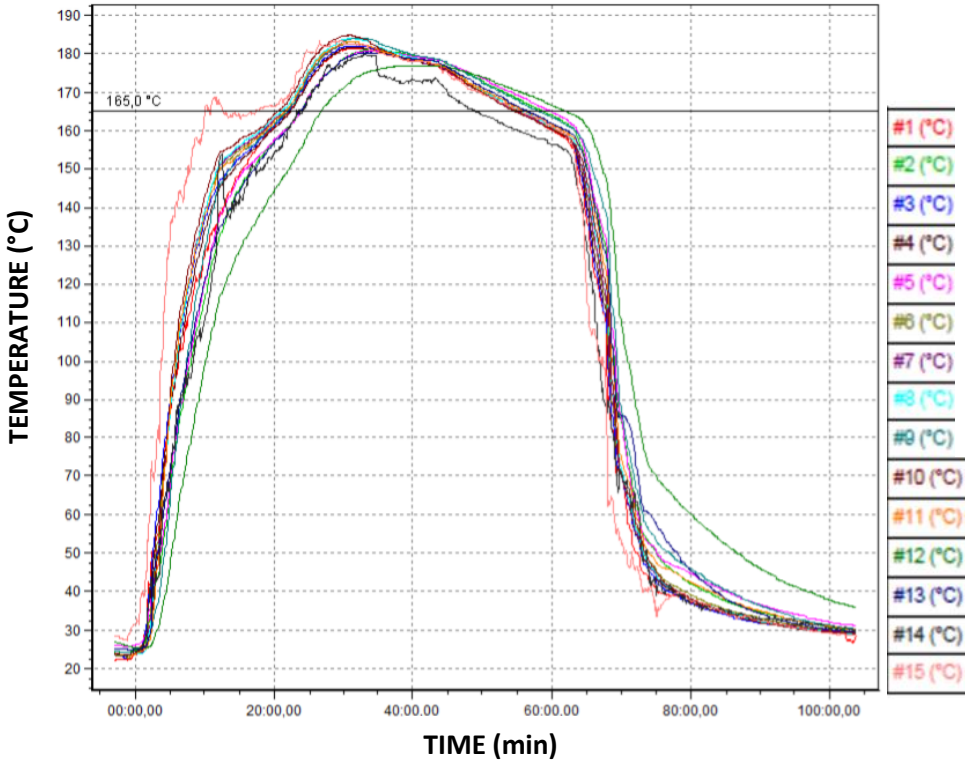

Figure 20 *Temperature evolution as a function of time obtained through the temperature sensors. Sensor 15 was set aside to measure the air temperature in the heating process.*



Figure 21 *Placement of temperature sensors on the body-in-white*

Once the answer about which thermal loading the car roof will suffer is obtained, the maximum temperature of the car roof in various usage scenarios is also sought. Based on internal references of Stellantis, an aging test was carried out in the United States to analyze what are the maximum temperatures in each part of the vehicle once it is used on the street. The roof of the car experienced a maximum temperature of 90°C in the upper area close to the rear face during use, as depicted in figure 22.



Figure 22 *Result of the maximum temperature obtained for aging tests done in the USA*

The purpose of this first test is to feed relevant information to the other tests that will be carried out in the laboratory and numerical simulations developed.

4. Conclusion - Chapter 1 / Methodology to solve the statement problem

4.1 Conclusion

This chapter aimed to make the reader understand in a very clear way the motivations for carrying out this thesis and the starting point of the study. Based on the information presented, it is evident that replacing a steel roof with one made of aluminum alloy (EN AW 6016 – T4 or EN AW 6056 – T4) is not a simple task within the introduced industrial context.

Thus, the contextual presentation of the *Projet AM2* reveals a significant issue concerning the thermal loads endured by the body-in-white, particularly during the post-cataphoresis heating phase, where temperatures reach up to 180°C. The emergence of visual defects, as illustrated in figure 11, poses a considerable challenge as it directly impacts the vehicle's conformity, production, and marketability. This underscores the critical and pressing necessity for the research conducted in this dissertation. The primary objective is to address and mitigate appearance defects resulting from differential thermal expansion, specifically focusing on an aluminum alloy roof integrated into a multi-material body-in-white. The information collected regarding temperature, particularly the peak temperature of 180°C, serves as a foundational basis for determining the temperature range of analysis in subsequent experimental tests. This data is pivotal in guiding the experimental investigations, ensuring they

are conducted within relevant temperature parameters and facilitating accurate assessment and control of appearance defects.

In addition to the conclusions drawn earlier, the analyses conducted in Chapter 1 highlight three key aspects that need to be considered in this thesis:

1. The solution to the problem must be directly applicable to the structure of the car. In this way, the main samples at the end of the thesis will be car bodies;

2. This solution must respect existing production processes, machines and tools. Consequently, the solution proposal needs to be made on the roof of the car and not on the production line with its ovens;

3. As a car brand has an identity, it is necessary to respect the style identity of the Peugeot line. Thus, the solution to be proposed needs to meet both engineering and design criteria.

4.2 Methodology to solve the statement problem

Once the study domain has been identified, the methodological steps will be presented. This will explain how to progress from the situation depicted in figures 23 – A and 23 – B to the final result shown in figure 23 – C. As the tests carried out on the structural scale are expensive, time-consuming and with several variables that make it difficult to reach conclusions, **it was chosen to divide this work into three scales of analysis: material scale, laboratory test scale and structure scale (as shown in figure 24).**

Visibly, it can be noted that the problem is due to a thermomechanical response of the structure to thermal loads. The thermal loading has already been shown in section 3.3 of this chapter and Stellantis already has a strong database of the different types of steels used in body-in-white. Therefore, what is necessary to understand is the behavior of the materials EN AW 6016 – T4 and EN AW 6056 – T4, chosen for the roof, in the temperature range of interest. Therefore, **Chapter 2 will focus on the material scale and it is then that the result of a series of analyzes of thermomechanical properties that influence the problem will be discussed.**

After characterizing the materials, it is necessary to move on to a study of the mechanisms that lead to the origin of the types of appearance defects observed in the presentation of the statement problem. Therefore, **Chapter 3 will focus on laboratory-scale tests. The tests in this type of controlled environment make it possible to carry out a predictive numerical model so that the mastery of the phenomenon will be possible and so that conclusions can be drawn.**

Once the behavior of the material is known and the phenomenon is predicted by numerical simulations, the next step involves the structural scale. **In chapter 4, based on what has already been discovered throughout this study, a numerical model made for the**

structure of the vehicle will be put into practice, which allows directing the decisions to be taken in the structure to avoid that the defects of aspects linked to the increase of temperature occur.

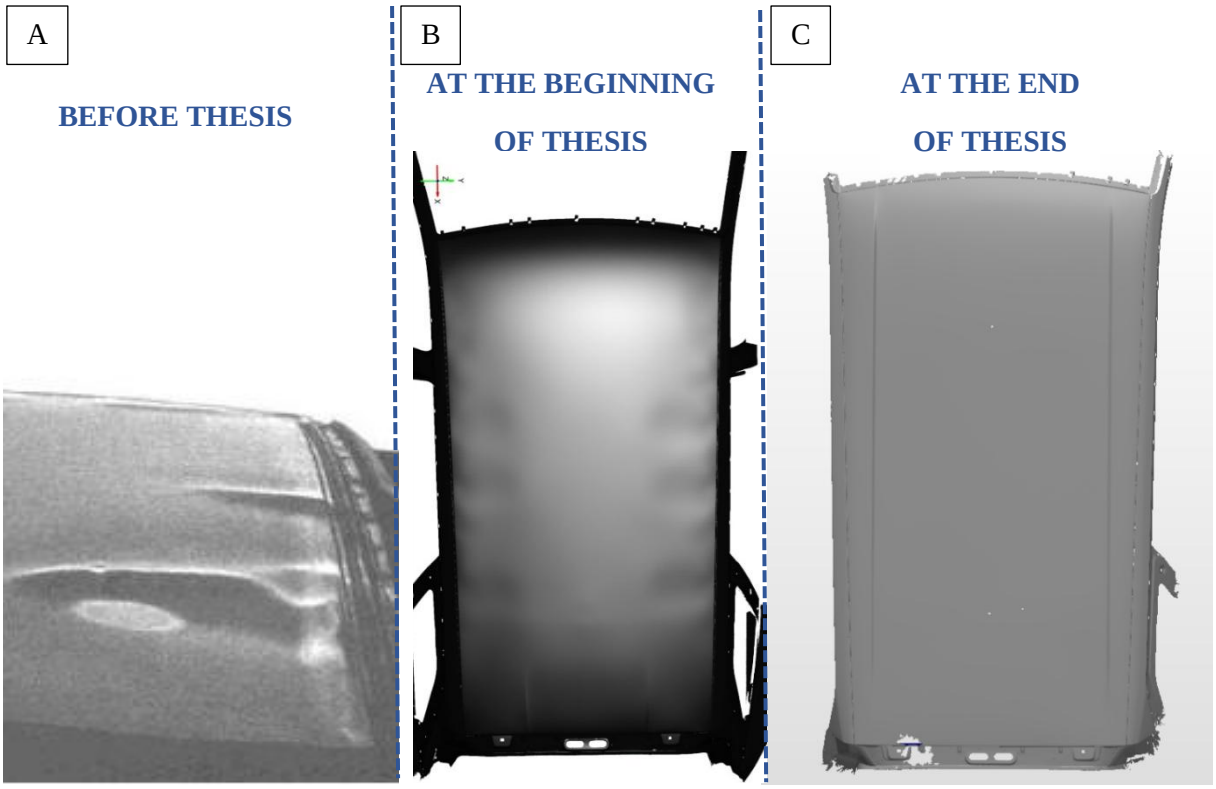

Figure 23 *Comparative state of evolution of problem statement solution* ***A)*** *Car roof after passing through the production line during Projet V period (2013) [24];* ***B)*** *Geometry of the car roof after passing through the production line at the beginning of thesis (2020);* ***C)*** *Geometry of the car roof after passing through the production line at the end of thesis and at the end of Project AM2 (2023).*

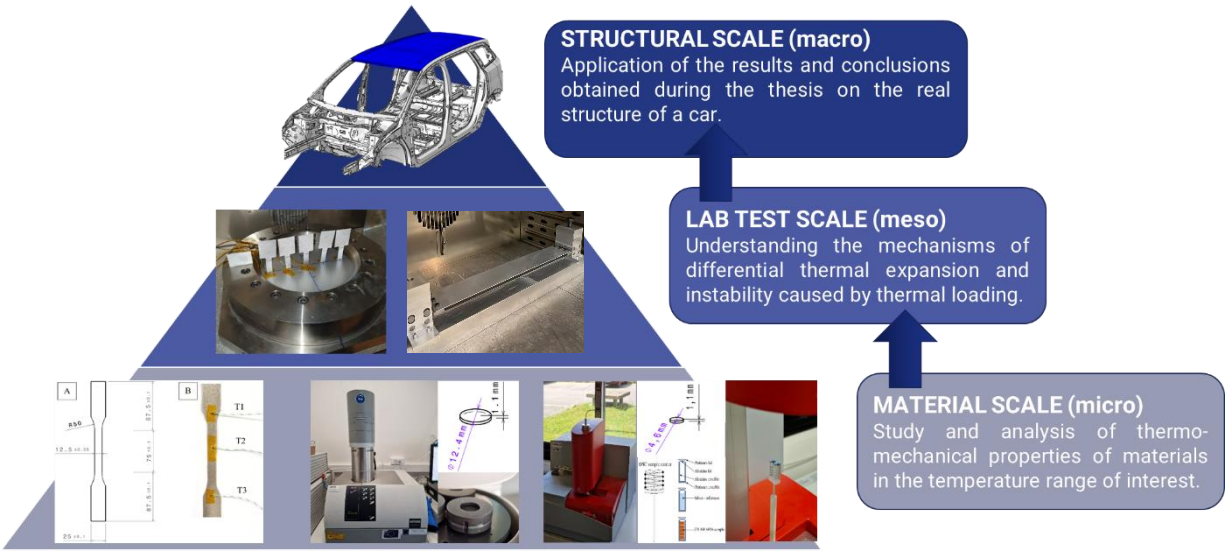

Figure 24 *Evidence pyramid used to show the methodology adopted to solve the statement problem.*

Bibliography – Chapter 1

[1] J.L. Hammond and Barbara Hammond. The Rise of Modern Industry (Economic History), 1st ed., Routledge, UK, 2013.

[2] P. Deane. The First Industrial Revolution, second edition, Cambridge University Press, Cambridge, 1965.

[3] J. Rutledge. Rust to Riches: The Coming of the Second Industrial Revolution, 1st ed., Harper & Row, New York, 1989.

[4] J. Rifkin. The Third Industrial Revolution: How Lateral Power Is Transforming Energy, the Economy, and the World, 1st ed., Palgrave Macmillan, New York, 2011.

[5] S. Vaidya, P. Ambad, and S. Bhosle. "Industry 4.0–a glimpse," Procedia Manuf., vol. 20, pp. 233–238, (2018), DOI: https://doi.org/10.1016/j.promfg.2018.02.034

[6] P. Jackson. From Stockholm to Kyoto: A Brief History of Climate Change. United Nations, 2007. Source: https://www.un.org/en/chronicle/article/stockholm-kyoto-brief-history-climate-change [accessed 14.03.2021].

[7] Acordo de Paris. Ministério da Ciência, Tecnologia, Inovações e Comunicações – MCTIC, 2021. Source: acordo_paris.pdf (www.gov.br) [accessed 14.03.2021].

[8] Acordo de Paris sobre alterações climáticas. European Council, 2022. Source: https://www.consilium.europa.eu/pt/policies/climate-change/paris-agreement/ [accessed 14.03.2021].

[9] CO_2 emission performance standards for cars and vans. European Commission. Source: https://ec.europa.eu/clima/policies/transport/vehicles/regulation_en [accessed 14.03.2021].

[10] The European Parliament and the Council of the European Union (2019). Regulation (EU) 2019/631 of the European Parliament and of the Council of 17 April 2019 setting CO2 emission performance standards for new passenger cars and for new light commercial vehicles. *Official Journal of the European Union*, L 111/13.

[11] Driving Clean Mobility: Questions & Answers on the initiatives that protect the planet, empower its consumers, and defend its industry and workers. European Commission, 2017. https://ec.europa.eu/commission/presscorner/detail/en/MEMO_17_4243 [accessed 08.01.2023].

[12] S. Fleming. These Countries Offer The Best Electric Car Incentives to Boost Sales. World Economic Forum, 2021. These Countries Offer The Best Electric Car Incentives to Boost Sales | World Economic Forum (weforum.org) [accessed 08.01.2023].

[13] Fuel types of new cars: battery electric 9.1%, hybrid 19.6% and petrol 40.0% market share full-year 2021. ACEA, 2022. Source : https://www.acea.auto/fuel-pc/fuel-types-of-new-cars-battery-electric-9-1-hybrid-19-6-and-petrol-40-0-market-share-full-year-2021/ [accessed 08.01.2023]

[14] Offset-Deformable Barrier – ODB. Euro NCAP. Source : https://www.euroncap.com/en/vehicle-safety/the-ratings-explained/adult-occupant-protection/previous-tests/offset-deformable-barrier/ [accessed 08.01.2023]

[15] Mobile Progressive Deformable Barrier. Euro NCAP. Source : https://www.euroncap.com/en/vehicle-safety/the-ratings-explained/adult-occupant-protection/frontal-impact/mobile-progressive-deformable-barrier/ [accessed 08.01.2023]

[16] Jeep Grand Cherokee - Euro NCAP 2022 Results - 5 stars. Euro NCAP, 2022. Source : https://euroncap.newsmarket.com/IMAGES-AND-VIDEOS/jeep-grand-cherokee---euro-ncap-2022-results---5-stars/s/8965bce0-b5e5-40ee-8927-844b36c6b4a0 [accessed 08.01.2023]

[17] Groupe PSA 200 ans d'histoire. Groupe PSA. Source: https://www.groupe-psa.com/fr/story/groupe-psa-200 ans-d-histoire/ [accessed 09.01.2021]

[18] Stellantis: le nom du nouveau groupe qui sera issu de la fusion de FCA et groupe PSA. Groupe PSA. Source: https://www.groupe-psa.com/fr/actualites/corporate/stellantis-le-nom-du-nouveau-groupe-qui-sera-issu-de-la-fusion-de-fca-et-groupe-psa/ [accessed 08.01.2021]

[19] A propos: Rennes, site de production de modèles SUV des marques Peugeot et Citroën. Groupe PSA. Source: https://site.groupe-psa.com/rennes/fr/a-propos/ [accessed 05.01.2021]

[20] Développer un nouveau modèle Retailer en Europe avec nos concessionnaires Stellantis pour améliorer l'expérience client. Stellantis, 2022. Source: Développer un nouveau modèle Retailer en Europe avec nos concessionnaires Stellantis pour améliorer l'expérience client | Corporate Communications | Stellantis [accessed 14.01.2023]

[21] Excelcar: qui sommes-nous?. Excelcar. Source: Qui sommes-nous ? - Excelcar [accessed 14.01.2023]

[22] Stellantis et ses partenaires du consortium AM2 co-innovent pour accélérer le déploiement de solutions multi-matériaux dans l'industrie automobile. Stellantis, 2021. Source: Stellantis et ses partenaires du consortium AM2 co-innovent pour accélérer le déploiement de solutions multi-matériaux dans l'industrie automobile | Corporate Communications | Stellantis [accessed 14.01.2023]

[23] Peugeot 5008. Stellantis. Source: https://www.peugeot.ch/fr/gamme/nos-vehicules/nouveau-peugeot-5008.html [accessed 06.01.2021]

[24] The aluminum automotive manual by aluminum Europe: roof-and-trim. European Aluminum Association, Brussels, Belgium, 2011. (european-aluminum.eu) [accessed 03.06.2021]

[25] Kutz, M. Applied Plastics Engineering Handbook. 2nd edition, Elsevier Inc., 2017

Chapter 2 - The challenges of using aluminum alloys in the automotive industry and characterization of EN AW 6016-T4 and EN AW 6056-T4 alloys

Introduction – Chapter 2

Nowadays, it is possible to see a significant increase in the use of aluminum alloys in the automotive, aeronautical and naval industries. As it was shown in Chapter 1, during industrial stages, these materials often undergo natural ageing and heating processes that can generate changes in their thermomechanical properties.

However, in the literature there is a lack of information on the characterization of some of these alloys in situations of slow heating, close to some industrial operations, such as the passage of the body-in-white in furnaces of the painting operation in the automotive industry (application of interest in this thesis). This often results in several simplification over numerical simulations of these industrial processes with regard to material property under high temperature conditions. This simplification, in turn, can make it extremely difficult to predict phenomena such as thermal buckling of some thin structures in the vehicle (problems which are going to be detailed in chapter 3 and 4).

In view of this need, the study made in the present chapter aims to show the results of the investigation of some thermo-mechanical properties of the EN AW 6016-T4 and the EN AW 6056-T4, taking into account criteria such as natural ageing (up to 6 months), slow heating situation (heating between around 40 minutes to 1 hour), temperature range from room temperature (around 20°C) to 250°C. At first, this chapter will serve as a basis for the reader to understand what an aluminum alloy is, the meaning of the alloy nomenclature and some applications of aluminum alloys in the automotive industry (first to fourth section). Then, the fifth section of this study is divided in two parts. The first one will show the results of the mechanical properties analyzed as a function of all these parameters. The second part of this study will show results related to some thermal properties obtained through analysis of dilatometry, Laser Flash Analysis (LFA) and Differential Scanning Calorimetry (DSC).

TABLE OF CONTENTS – CHAPTER 2

Chapter 2 – The challenges of using aluminum alloys in the automotive industry and characterization of EN AW 6016-T4 and EN AW 6056-T4 alloys……...……..…41

Introduction – Chapter 2…….…….……...…...41

1. Brief historical background of aluminum alloys…….....43

2. Alloy constitution: general explanation.……..…….…….……..44

3. General classification, nomenclature, and temper designation of aluminum alloys……..……44

3.1 General classification…….……..…….……44

3.2 Nomenclature system for wrought alloys..…….…...……45

3.3 T4 and T6 temper designation for wrought alloys……....…46

3.4 Ageing...…….……..…….……47

4. Some applications of aluminum alloys in the automotive industry…….....……..48

5. Influence of natural ageing up to six months and slow heating condition on the thermo-mechanical properties of the aluminum alloys EN AW 6016-T4 and EN AW 6056-T4……..…….....51

5.1 Materials: EN AW 6016-T4 and EN AW 6056-T4……51

5.2 Tensile test…….52

5.2.1 Setting up the tensile sample……...52
5.2.2 Digital Image Correlation (DIC) method procedure for tensile test…….53
5.2.3 Setting up the tensile test…….55
5.2.4 Tensile test results and discussions…….56

5.3 Thermal expansion analysis……..64

5.3.1 Setting up the test……64
5.3.2 Results and discussions of the thermal expansion analysis……66

5.4 Laser Flash Analysis (LFA)……..67

5.4.1 Setting up the test……67
5.4.2 Results and discussions of the thermal diffusivity measurements……...69

5.5 Differential Scanning Calorimetry (DSC)……72

5.5.1 Setting up the test……72
5.5.2 Results and discussions……...73

6. Conclusion – Chapter 2…….…...…...…...……78

Bibliography – Chapter 2……..…….……..…….....79

1. Brief historical background of aluminum alloys

As the problem statement revolves around an aluminum car roof, it is pertinent to explain the behavior of this metal. Due to its light weight, durability, recyclability, ductility, corrosion resistance and strength properties, aluminum is today the most produced non-ferrous metal in the world, being even more produced than all other non-ferrous metals combined [26 - 28]. Associated with its properties, the current environmental context of seeking to reduce CO_2 emissions leads to predictions that show that, by 2025, aluminum consumption will reach an increase of more than 2.5 times when compared to its consumption in 2006 [29]. Moreover, despite being the third most abundant element in the earth's crust, aluminum is the youngest metal used on industrial scale [30].

Discovered by Sir Humphrey Davy in 1809, aluminum was first isolated in 1825 by H. C. Oersted. However, it was only in 1886 that two scientists (figure 25) working independently, Charles Martin Hall, in the United States, and Paul Louis Héroult, in France, invented the same electrolytic procedure for reducing alumina in aluminum. This economical industrial reduction process was called the Hall-Héroult procedure, which is currently used in the industrial environment [31].

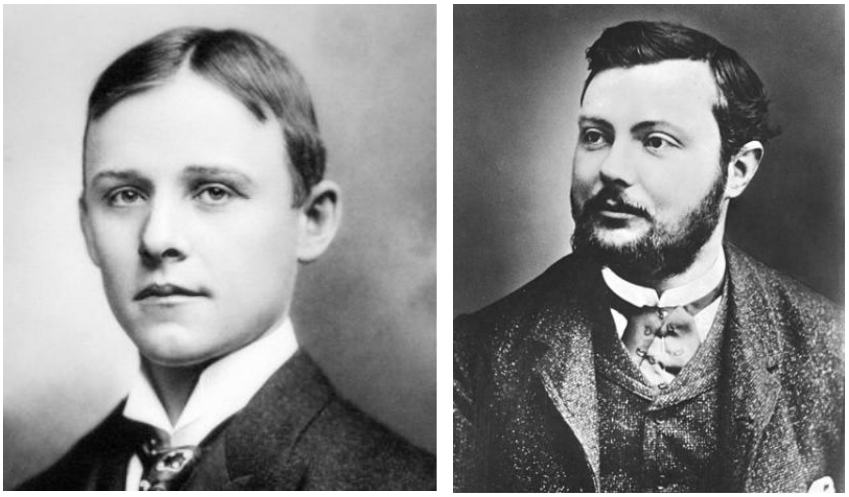

Figure 25 *On the left, photo of Charles Martin Hall (1863 – 1914). On the right, photo of Paul Louis Héroult (1863-1914) [32].*

According to [31] (*Associação Brasileira do Alumínio – ABAL*, 2007), with the increase in aluminum production at the end of the 19th century, the prices of this metal started to fall. Thus, this material was gradually used in kitchen utensils and some of first automobiles (center of interest of this thesis) began to have panels coated with commercially pure aluminum. However, the limited strength of this commercially pure metal restricted its applications, especially when there was some difficulty in the metallurgical industries in favor of more traditional materials. Consequently, the aluminum industries began to work on the production of aluminum alloys with higher mechanical properties than pure aluminum at the beginning of the 20th century.

Since it was something innovative, the first experiments were through trial and error. These experiments, coupled with insightful observations, led to further experiments based on

increasing knowledge of the fundamental metallurgical principles involved. Finally, the research activities carried out by the aluminum industry itself, by academic laboratories and by aluminum users have led to a rapid and notable growth in the importance of aluminum in the industry.

2. Alloy constitution: general explanation

Commercially pure aluminum (unalloyed) is defined as a material that contains a minimum of 99% of this “pure” metal in its composition [33]. However, it must be known that this material in its pure state does not have high tensile strength (around 90 MPa), it is ductile and soft [31]. With the advance of studies regarding this metal, it was discovered that with the addition of elements such as manganese, silicon, copper, magnesium and others, some properties of the aluminum could be improved and an aluminum alloy with properties tailored to specific applications could be produced [34].

Regarding the aluminum alloys, the first important point to highlight is that these alloying components mentioned in the previous paragraph can enter the crystalline structure of the material as a solid solution or they can build several constituent phases. These phases and, consequently, the behavior of the material depend on the kinetics of nucleation and growth processes, on the proportions of the alloying elements and on the temperature [34]. Thus, the conclusion that can be made is that the constitution of the elements present in the alloy is the determining factor in the final properties and in the behavior of this material during its applications.

Now that a general explanation of aluminum alloys has been introduced, a second key point to understand more about these materials is to know the basic groups in which aluminum alloys are classified.

3. General classification, nomenclature, and temper designation of aluminum alloys

3.1 General classification

The first classification of aluminum alloys refers to its production process, being categorized as: casting alloys or wrought alloys. Starting with casting alloys first and then explaining wrought alloys.

- **Casting alloys**

According to (Kaufman, 2000) [33], the designation "casting alloys" is used for alloys that are generally used in castings for the final or near-final shape and for the ingot from which such castings are made. Since these types of alloys are used to obtain the almost finished shape, processes such as forging, extrusion, rolling and others shaping processes are generally not used with casting alloys.

The main characteristics of casting alloys are strength, mold-filling capability, and quality finish. However, it is worth noting that few alloy series have these three characteristics simultaneously. For example, in terms of strength, the series 2xx.x alloys are very good, but this series is also known for the lack of good surface characteristics and for being one of the most difficult to cast. On the other hand, in terms of casting, especially for large and complex foundries, the 3xx.x series are the most used because their high silicone content provides excellent mold-filling capacity and fluidity. To conclude with the applications of casting alloys, the 5xx.x and 7xx.x series are the most used in terms of finishing, even with the 7xx.x series being recurrently used for the manufacture of bearings [33].

- **Wrought alloys**

In general, this classification designates alloys produced in billets or ingots that are then worked to produce semi-finished products [33]. Among these works, it can be mentioned: extrusion, forging, rolling, drawing, among other processes from which the final products are subsequently made.

Wrought aluminum alloys have vast striking characteristics [33], among which the main ones include:

- Resistance to corrosion (emphasis on series 1xxx, 3xxx, 5xxx, and 6xxx), being widely used for applications where the material has direct contact with water (including sea water);

- High thermal and electrical conductivity;

- Good ratio between weight and mechanical resistance. It is worth mentioning that this characteristic, together with the great capability of recycling and resistance to corrosion, is one crucial parameter that has made the automobile industry look at aluminum in a more focused way;

- Better ductility and mechanical resistance at low temperatures;

- Possibility of producing a wide range of shapes that can be used to support the applied loads more efficiently.

Now that a summary of the first general classification of aluminum alloys has been made, the study will be narrowed further. As it was explained in Chapter 1, by the nomenclature, the aluminum alloys that will be used for application on the roof of the car are wrought alloys (EN AW 6016–T4 and EN AW 605 –T4 alloys). For that reason, from now on this report will focus more on wrought alloys and their respective nomenclature and temper designations.

3.2 Nomenclature system for wrought alloys

First, it is important to highlight that there are three main organizations responsible for international designation systems for aluminum alloys: American National Standard Institute

(ANSI), International Organization for Standardization (ISO) and *Comité Européen de Normalisation* (CEN). As this thesis has an application for Stellantis' factories in Europe, the nomenclature system that will be used and detailed in this report will be the one described by the CEN.

The first rule for the nomenclature of aluminum alloys according to European standards is that the number of the series must be preceded by the prefix EN AW (i.e. **A**luminum **W**rought) in the case of wrought alloys [35].

Then, the first digit of the alloy series is used to indicate the major alloying element [33]. The called "major alloying elements" are the components introduced in the alloy to directly confer some significantly change in specific properties for the alloy [34]. Figure 26 shows more clearly the association between the first digit of the alloy series and the major alloying components.

Alloy	Main alloying element
1*xxx*	Mostly pure aluminum; no major alloying additions
2*xxx*	Copper
3*xxx*	Manganese
4*xxx*	Silicon
5*xxx*	Magnesium
6*xxx*	Magnesium and silicon
7*xxx*	Zinc
8*xxx*	Other elements (e.g., iron or tin)
9*xxx*	Unassigned

Figure 26 *Major alloying elements in the wrought alloy designation system [28].*

The second number defines variations in the original basic alloy, being this variation defined by differences in one or more alloy elements from 0.15 to 0.50% or more (depending on the quantity of the added element). That digit is always zero (0) for the original composition, one (1) for the first variation, two (2) for the second variation, and so forth. To conclude, the third and fourth digits designate the specific league within the series [33].

3.3 T4 and T6 temper designation for wrought alloys

After indicating the prefix and serial number of the alloy, a hyphen is placed followed by the designation of the temper. The first characteristic indicated for the temper is its general class, which is represented by a capital letter that can be F, O, H, W or T. The general class of the aluminum alloys studied in this thesis is of type T, which means that the material was "thermally treated to produce stable tempers other than F, O or H" [35].

In addition to the basic designation of the alloy, it is necessary to indicate its subdivision. The two aluminum alloys studied for the car roof application are aluminum alloys with T4 type tempering. This T4 subdivision is used to indicate that the alloy was heat treated and naturally

aged to a substantially stable condition [33]. However, a temper of type T4 can become artificially aged and become a T6 type temper, which means that the material has been treated, then artificially aged to obtain greater strength [35].

Heat treatment in tempers of type T is understood as heating the wrought alloy to a desired temperature, keeping the material at that temperature for a desired time to allow the constituents of the alloy to enter the solid structure. Then, the process is finished with a fast cooling to take advantage of subsequent precipitation and the associated strengthening (i.e. precipitation hardening) [33].

3.4 Ageing

(European Aluminium Association (a), 2002) [34] mentions the aging process as the most important mechanism to increase the strength of wrought aluminum alloys. This bibliography also mentions that a massive majority of the car parts made of aluminum alloys are made from the age-hardening process of the 6xxx and 7xxx series.

After quenching in the heat treatment process, described in the previous section, the aluminum alloy comes out of the process in a W temper state, which means in a very soft state. Then, after approximately 1 hour at room temperature, the material starts to get harder, and this process continues for a week or more. This is what is called "natural aging," and the final temper obtained is a T4. Figure 27 illustrates this process with a graph.

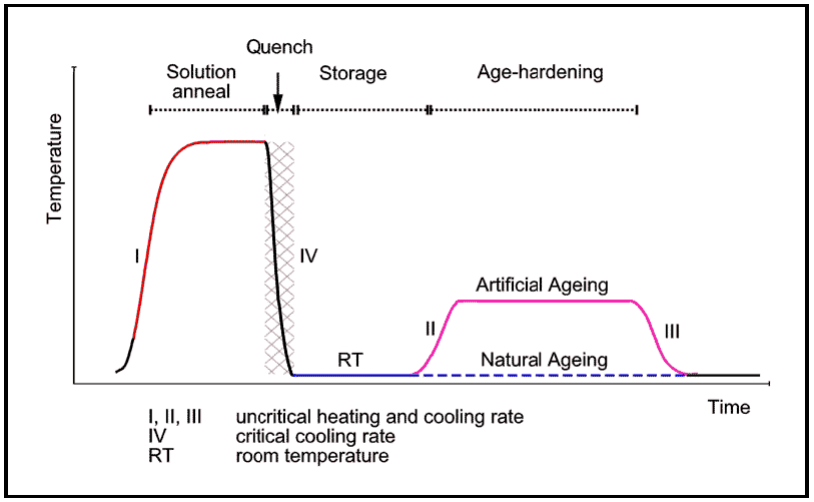

Figure 27 *Process cycle of solution anneal + quench + RT storage + artificial aging of wrought aluminum alloys [34].*

(Huppert-Schemme, 1997) [36] adds that the reason for this hardening effect is that T4 strength is mainly caused by clusters, which slows down and reduces growth and nucleation to obtain a T6 phase. However, there are special T4 tempers called "stabilized", which are represented by T4* which are not standardized but they have improved response to aging in order to reach a T6 better strength over heating processes or subsequent ageing [34].

After explaining wrought alloys, the nomenclature system, temper designation, and aging, the meaning of **EN AW 6016-T4** and **EN AW 6056-T4** aluminum alloys, which will be

applied to the project of this thesis, is clear. From now on, all this information presented above will serve as basis for understanding the next topics on the aluminum alloys used in this thesis. Among the industries that make the use of these alloys increase, it is possible to mention the transport industry, as this material and its alloys have been used as a substitute for several components made of steel [26] [28]. Thus, in the next section, some applications of aluminum alloys in the automotive industry will be presented.

4. Some applications of aluminum alloys in the automotive industry

According to [37] (European Aluminium Association (c), 2011), in the early 1980s, with the discovery of economically viable aluminum manufacturing processes, several aluminum cars were produced, usually with some aluminum alloy parts to replace some steel parts in existing car models. However, in 1981, a sporty Porsche 928 with an all-aluminum body was shown at the Frankfurt IAA. The aluminum body was developed in conjunction with the company Alusuisse and was made of Anticorodal®-120 alloy sheets (EN AW-6016). The weight of the aluminum body was 161 kg, 106 kg less than the steel body. Soon after, Audi began to focus on aluminum. Later, an aluminum body based on the Audi 100 was developed (figure 28).



Figure 28 *« Aluminum sheet concept car based on the Audi 100 (1985) » [37].*

Despite Audi's effort, the first commercially produced car with an all-aluminum monocoque body was the Honda Acura NSX (figure 29), introduced in 1989 [37]. The Honda Acura NSX, a high-performance two-seater sports car, used to be assembled by hand, and because of that it was produced in a very small number. It had an all-aluminum monocoque body weighing approximately 163 kg that contained some extruded aluminum profiles in the frame and suspension. The use of aluminum in the body saved almost 200 kg of weight compared to the steel equivalent model, while the aluminum suspension saved also more 20 kg. The exterior had a special painting process that included an airplane-like chrome finish. This coating was used to chemically protect the aluminum body. The body structure used high-strength aluminum alloys and special construction techniques. A combination of spot welding and MIG was used to join the structure. In addition, the NSX-T offered a removable aluminum roof panel. This panel was light and strong. It had its own storage compartment under the rear window.



Figure 29 *Honda Acura NSX with an all-aluminum monocoque body [37].*

In 2006, Jaguar introduced the new XK (figure 30), a luxury and high-performance car for long journeys. The second generation of the XK had a monocoque aluminum body. However, XK needed a properly adapted solution, as the package restrictions were stricter, and it was also desired to create a roofless version. The new XK went a step further with the extensive use of lightweight aluminum parts and profiles, as the vast majority of connections in the new XK structure were made by a combination of riveting and bonding. The use of epoxy bonding and riveting techniques created a very rigid, but also lightweight, chassis. With its lower weight and greater rigidity, the light body concept provided the basis for better performance, safety, economy, less pollutant gas emissions and better driving dynamics. In the convertible version, the body-in-white weight was only 287 kg (equivalent to a weight reduction of 19% compared to the previous XK convertible in steel).



Figure 30 *Jaguar XK [37].*

In 2020, the case of the new Land Rover Defender (figure 31) is a good example of a large aluminum alloy car headliner. The brand already knew that paint ovens could create problems for this aluminum structure. Thus, they chose to achieve a very flat car roof, with a design favoring an increase in the rigidity of the structure (by grooves), several cross members connecting the roof to the body-in-white. All of this was done in order to minimize any problems that could be caused in the roof due to thermal expansion [38].



Figure 31 *Land Rover Defender 2020 [38].*

These cases presented above are just a few examples that show the efficiency and benefits of introducing aluminum alloy parts in the body-in-white of cars. As observed, the massive introduction of aluminum alloys is very recent when compared to the history of the automobile industry. Therefore, there are still many works to be carried out in this field of study.

In the same way that the industrial applicability of EN AW 6016-T4 and EN AW 6056-T4 is notorious, it is important to keep in mind that many times the industrial restrictions result in the need for the material to be stored between industrial stages for an important period. Associated with this, at some point during the production line, the material can also be taken through processes that involve increase in temperature (as shown in Chapter 1). As some pieces of the body-in-white have a small thickness and large area (e.g.: car roof), all these processes need to be correctly known in order to avoid, in the final product, any appearance defects caused by temperature variation in the production line. Thus, it is often necessary to predict through numerical simulations what will happen to the structure during these manufacturing processes and, for that, having a well-defined database of thermomechanical properties is paramount.

Moreover, due to the chemical composition of EN AW 6016-T4 and EN AW 6056-T4, the materials are susceptible to hardening processes due to changes in its microstructure as a function of the natural ageing time and the thermal cycle to which the materials are subjected [39 - 40][44 - 46]. Consequently, this fact leads the alloy to a variation of its thermomechanical properties that must be known.

Some studies have already been carried out to analyze the variations of these properties in a situation of rapid heating, in order to provide information about what happens to these materials in welding situations [39][41 - 43][46]. However, **there is currently a lack of information in the literature concerning the alterations in the thermo-mechanical properties of these alloys during gradual heating, considering the natural aging process. Such information is valuable for various industrial applications, including heating processes during the painting phase of automotive vehicles in the automotive sector.**

The EN AW 6016-T4 and EN AW 6056-T4 are two alloys that are sensitively susceptible to artificial ageing. In this way, they present results of its thermo-mechanical properties very different in the situation of slow heating when compared to fast heating. Thus, the main focus of the next topic is to show and discuss the results of the investigation of some thermomechanical properties of EN AW 6016-T4 and EN AW 6056-T4 in slow heating situations (40 minutes to 1 hour) also taking into account a natural ageing of the material of up to 6 months.

5. Influence of natural ageing up to six months and slow heating condition on the thermo-mechanical properties of the aluminum alloys EN AW 6016-T4 and EN AW 6056-T4

This section can be divided into two major parts. The first part concerns the analysis of mechanical properties, such as Young's modulus, elastic limit, and stress-strain curves depicting the elastic-plastic behavior of the studied materials. This analysis was conducted through tensile tests performed from room temperature to 220°C, following the ISO 6892-1:2019 and ISO 6892-2:2018 standards. The Digital Image Correlation (DIC) method was employed for this analysis.

The second part of the study will focus on the analysis of the variations of the thermal properties of EN AW 6016-T4 and EN AW 6056-T4 up to 250°C. First, the analyzes referring to the thermal expansion of the materials under natural ageing conditions of three months and six months will be shown and discussed. Then, the thermal diffusivity results obtained by the LFA method will be discussed. Finally, DSC tests were carried out, in order to show sensitively the variation in the specific heat capacity of the materials, taking into account their precipitation as a function of the heating temperature. To facilitate understanding, figure 32 shows the organization of this section.

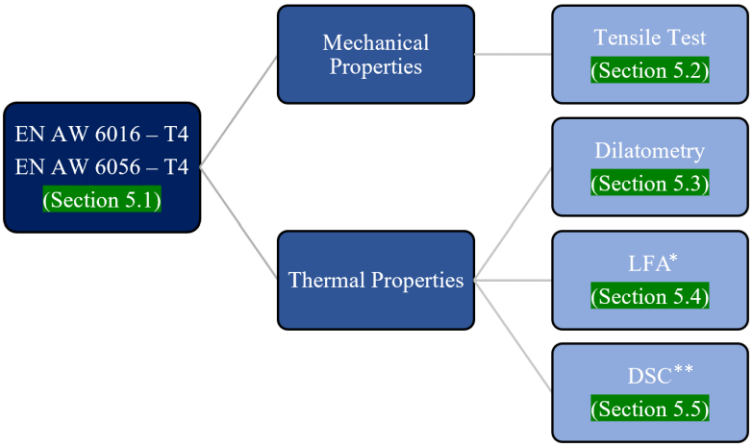

Figure 32 *Organization of section 5. Influence of natural ageing up to six months and slow heating condition on the thermo-mechanical properties of the aluminum alloys EN AW 6016-T4 and EN AW 6056-T4. *LFA = Laser Flash Analysis / **DSC = Differential Scanning Calorimetry.*

5.1 Materials: EN AW 6016-T4 and EN AW 6056-T4

Both EN AW 6016-T4 and EN AW 6056-T4 were supplied by the company Constellium*** and their chemical compositions are given in Table 1 and 2. The nomenclature of these alloys follows the *Comité Européen de Normalisation* (CEN) standards. As explained before, this means that the prefix EN AW is used in the case of a wrought aluminum alloy [35] and it also means that the material underwent a heat treatment before reaching the laboratory

*** https://www.constellium.com/about-us

for testing: the T4 heat treatment. This information is important because, since some mechanical and thermal properties of these two alloys vary over time and in function of temperature, the T4 heat treatment indicates the initial state of the alloys. To better control the natural ageing process in the laboratory, the materials were stored in freezers at -18°C upon arrival from the supplier.

Table 1 *Chemical composition of EN AW 6016-T4 studied (wt.%)*

Si	Fe	Cu	Mn	Mg	Cr	Zn	Ti	Al
0.92	0.19	0.09	0.07	0.41	0.01	0.00	0.031	Balance

Table 2 *Chemical composition of EN AW 6056-T4 studied (wt.%)*

Si	Fe	Cu	Mn	Mg	Cr	Zn	Ti	Al
0.88	0.24	0.94	0.45	0.74	0	0.15	0.026	Balance

5.2 Tensile test

For the performance of the tensile tests for both alloys, the standards ISO 6892-1:2019 [71] and ISO 6892-2:2018 [72] were used to define the guidelines of the tests at room temperature and at high temperature conditions, respectively. The process commenced with the preparation of the tensile samples.

5.2.1 Setting up the tensile sample

The thickness of the specimens was 1.10 mm (± 0.02 mm) and their geometry (figure 33 - A) was chosen in a way that respects the dimensions defined by the two standards for a thickness condition between 0.1 mm and 3 mm. The specimens were manufactured using water jet cutting, in order to prevent material transformation due to high cutting temperatures in other methods (laser cutting, for example), thus avoiding high heterogeneity of the material in the same specimen.

Two type K thermocouples were positioned at the ends of the calibrated length and a thermocouple of the same type was positioned in the center of the specimen, totaling three type K thermocouples with uncertainty of +/- 0.5°C positioned along the specimen (figure 33 - B). These thermocouples were fixed to the specimen with the help of adhesive and high-temperature adhesive tape. This was done in order to comply with the ISO 6892-2:2018 standard in terms of maximum variation of admissible temperature of 3°C along the specimen.

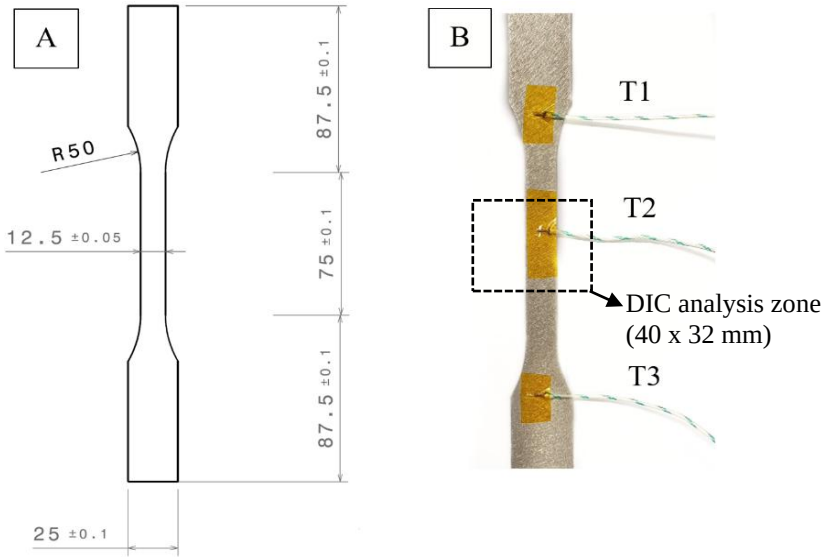

Figure 33 A) *Geometry of the specimens for tensile tests (units in millimeter);* ***B)*** *A specimen ready to be tested with three thermocouples (T1, T2 and T3) distributed along its length.*

5.2.2 Digital Image Correlation (DIC) method procedure for tensile test

Traditionally, tensile tests use mechanical strain gauges attached to the sample to obtain strain data. However, using these devices at temperatures above the operating temperature provided by the manufacturer can severely damage them. Thus, it was necessary to find another alternative to obtain data related to strain for the case of the tensile tests in this study. Research works show that the results of the tensile tests performed using DIC present a good result for temperatures below 650°C using in the measurements optical glass and white light source for different strain rate situations up to $10s^{-1}$ [47-51]. Thus, as in this work the mechanical properties of the EN AW 6016-T4 and the EN AW 6056-T4 were studied up to 220°C, DIC is a reliable method for analyzing tensile test results.

The DIC method has been known since the 1970s and it is capable of measuring displacements and deformations, using one (2D measurements) or two digital cameras (3D measurements), based on the recognition of the change in an image sequence [48]. For this work, only the 2D deformation was necessary and the software chosen for analysis and post treatment of data was GOM Correlate Pro [73]. Figure 34 – A shows the system used for DIC.

To carry out the tensile tests, an image served as a reference image is taken just before each test, then images of the specimen are taken during the deformation process until rupture. Seeking better deformation accuracy, the technique of random speckle patterns on the object was used. So, a black–white pattern was sprayed onto the study surface of the samples (figure 34 – B). Also, in order to obtain a successful correlation between the images taken, the resolution of the images was improved by zooming only in the area of interest to be analyzed (area of reduced section of the specimens). Once the measurement system assembly is completed, the system configuration must be calibrated. It is this phase that will make the conversion of the number of pixels into a measure of length (in this case, millimeters). As the size of the calibration target should be similar to the size of the sample to be investigated, the calibration target of size 23 x 18 mm was chosen. As the software chosen for image analysis

was GOM Correlate Pro, some images of the calibration target at the sample position with different inclination angles and directions were needed to generate the calibration file. For accurate results, the calibration process is done with the calibration target inside the traction machine (with its door closed and with the camera observing the calibration target through the optical glass).

Knowing that the accuracy and precision in DIC measurements depends also on the quality of the pattern [52 - 53], tests were only taken into account if the speckle patterns were of a considerably good quality according to GOM Correlate software (high contrast in pattern, 50 / 50 black and white distribution, speckle size between 3 – 5 pixels and speckles well distributed within facet) [74]. In addition, for the manufacture of the painting on the specimen, inks suitable for high temperature (up to 700°C) were used. This prevents the paint quality from being degraded at high temperature and also prevents the paint from peeling or cracking. The analysis of the quality of the speckle pattern can be seen in figure 34 - C. In figure 34 - D it is possible to see that the displacement on the X axis presents a distribution that shows that the specimen was correctly subjected to a pure tensile load, which is obtained thanks to a good alignment of the machine parts.

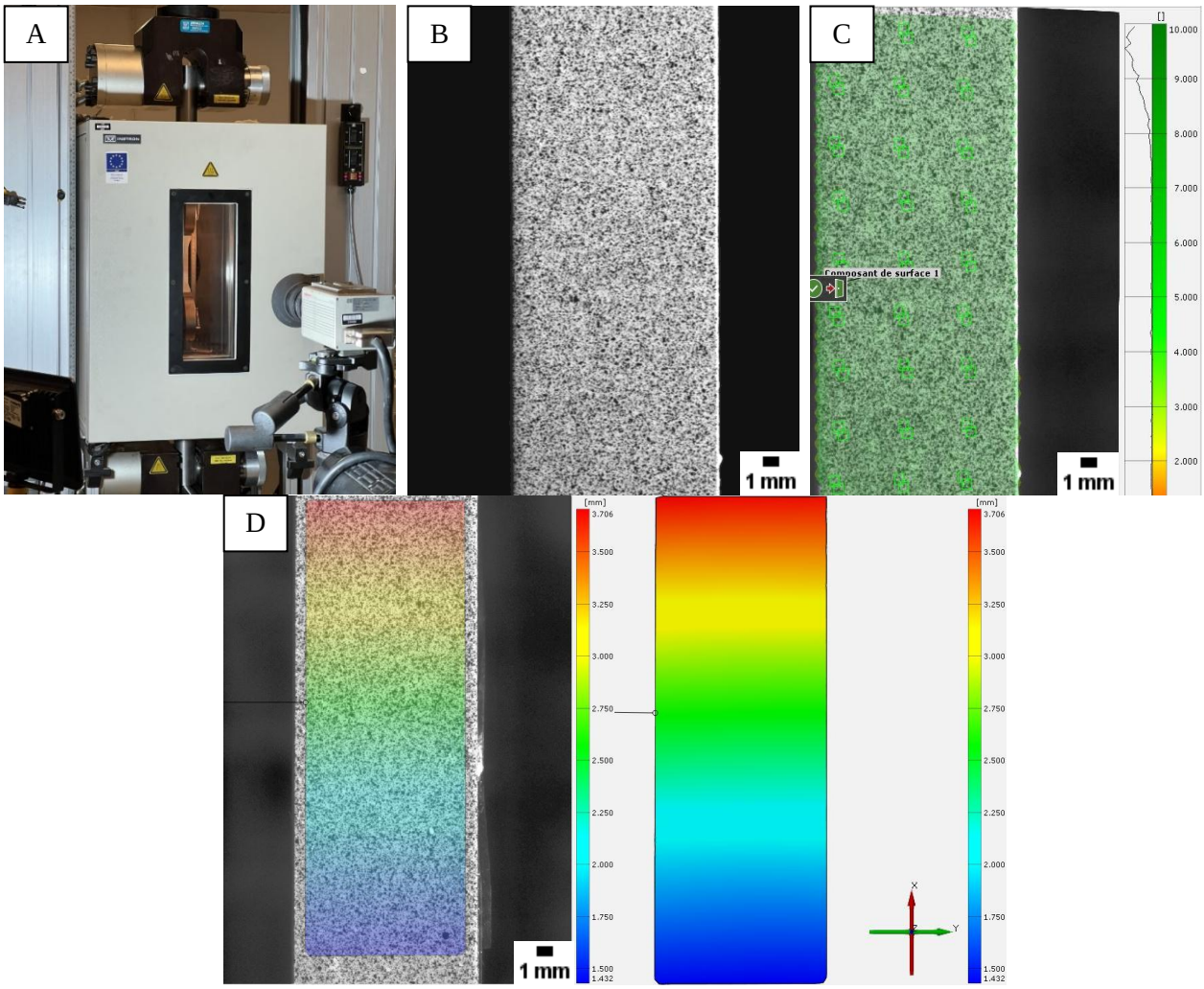

Figure 34 A) *Photo of the assembly for the tensile test;* ***B)*** *Pattern for a tensile test at 220°C;* ***C)*** *Pattern quality on a scale from zero to ten according to the GOM Correlate Pro software;* ***D)*** *Average displacement in the X direction.*

5.2.3 Setting up the tensile test

Tensile tests were performed using a universal testing machine INSTRON 5585 with a load cell with a maximum load capacity of 200 kN and an environmental chamber INSTRON 3119-407. The loading rate of the upper crosshead was set as 1.13 mm/min, following the limits of the crosshead separation speed range of the ISO 6892-1:2019 and ISO 6892-2:2018 standards, to indirectly reach the deformation speed required by the standards (0.00025 s^{-1}). The stress-strain curve data were obtained each 2 seconds by associating the stress data obtained by the tensile testing machine and the strain data obtained through the DIC method using the software GOM Correlate Pro.

Regarding the analysis of the stress and strain results, it is known that in the plastic part these materials present a reasonably large strain. The width and thickness shrink as the length of the test sample increases, which makes the properties calculated using the initial cross-sectional area of study ($A_{initial}$) not the most suitable. Therefore, in this study, the graphs will not be drawn from the engineering stress (σ_{eng}) and engineering strain (ε_{eng}), but from the instant cross-sectional area ($A_{instant}$), consequently obtaining the true stress (σ_{true}) and the true strain (ε_{true}).

σ_{eng} is obtained through the following equations:

$$(1)\ \sigma_{eng} = \frac{F}{A_{initial}}$$

$$(2)\ A_{initial} = t_{initial} \cdot w_{initial}$$

Where F is the load (kN) applied by the tensile machine to the specimen. The geometric parameters $t_{initial}$ and $w_{initial}$ are, respectively, the initial thickness of the specimen and the initial width of the cross section in the study zone of the specimen. These last two mentioned parameters are measured directly on the specimen with the help of a caliper with an uncertainty of ± 0.02 mm.

Considering the constant volume assumption (the Incompressibility Assumption), one can obtain a mathematical relation between the multiplication of the initial area by the initial length ($L_{initial}$) and of the instantaneous area by the instantaneous length ($L_{instant}$). In this way, the following equations are obtained:

$$(3)\ A_{instant} \cdot L_{instant} = A_{initial} \cdot L_{initial}$$

$$(4)\ A_{instant} = \frac{A_{initial} \cdot L_{initial}}{L_{instant}}$$

The definition of engineering strain (ε_{eng}) is that it is the variation of length (ΔL) divided by the original length ($L_{initial}$).

$$(5)\quad \varepsilon_{eng} = \frac{\Delta L}{L_{initial}}$$

$$(6)\quad \Delta L = L_{instant} - L_{initial}$$

Applying equation (6) to equation (5):

$$(7) \quad \varepsilon_{eng} = \frac{L_{instant}}{L_{initial}} - 1$$

In the same way as it was done for equation (1), the value of the true stress (σ_{true}) will be mathematically expressed as a function of the load and the instantaneous cross section area ($A_{instant}$):

$$(8) \quad \sigma_{true} = \frac{F}{A_{instant}}$$

By developing equation (8) with equations (4) and (7) it is possible to obtain an expression for the true stress as a function of engineering stress and engineering strain:

$$(9) \quad \sigma_{true} = \sigma_{eng} \,.\, (1 + \varepsilon_{eng})$$

As for the true deformation (ε_{true}), it can be calculated by:

$$(10) \ \varepsilon_{true} = \ln(\frac{L_{instant}}{L_{initial}})$$

Through equation (7), equation (10) can be rewritten in such a way that the true deformation is a function of the engineering deformation:

$$(11) \quad \varepsilon_{true} = \ln(1 + \varepsilon_{eng}\ )$$

Observing equations (9) and (11), it can be noticed that the engineering stress can be obtained directly from the result provided by the tensile testing machine and the engineering strain can be obtained through the post-treatment of the results of the DIC system. Thus, the true stress and true strain data obtained from tensile tests were used to analyze the mechanical properties of the material in function of temperature and natural ageing.

5.2.4 Tensile test results and discussions

The results and conclusions were divided into four different parts of interest regarding the analysis of the mechanical properties obtained through the tensile tests with the EN AW 6016-T4 and the EN AW 6056-T4:

I. Mechanical properties

In order to obtain information about properties such as the Young's modulus ($\boldsymbol{E}$), elastic limit ($\boldsymbol{Rp_{0.2}}$) and the way the materials react in their plastic regimes, it is important to analyze the stress x strain curves. This information is generally used as input to simulate the mechanical response of the material to a heating process in industry or in the laboratory. However, with increasing temperature there is a strain softening behavior that evolves. This fact is due to the phenomena of formation of Mg- and Si- clusters, formation of Guinier-Preston zones (GP-zones) and formation of β"-precipitates. According to the literature [39][54 - 60], the sequence and approximate temperatures at which these phenomena occur for the 6xxx series Al–Mg–Si alloys is listed below:

- Around 80°C – formation of Mg- and Si-clusters;

- Around 150°C – GP-zones;

- Around 230°C – formation of β''-precipitates.

In figure 35 – A, obtained from [61], it is possible to observe the cross sections of the edge-on precipitates. The cross sections of D1 and D2 show a clear crystal pattern and they are approximately rectangular with the long edge straight and aligned in the [0 0 1] direction. In this direction, there is a high coherence between the precipitate and the aluminum matrix. D1 and D2 present, respectively, cross sections measuring 8.3 nm × 2 nm and 7.8 nm × 3 nm.

In figure 35 – B, also taken from [61], it is possible to observe precipitates (D3, D4, D5) with cross sections with much more irregular shapes and no clear crystallographic pattern. According to [61], the occurrence of this type of precipitate is only around 5%, which means that its contribution in volume can be neglected.

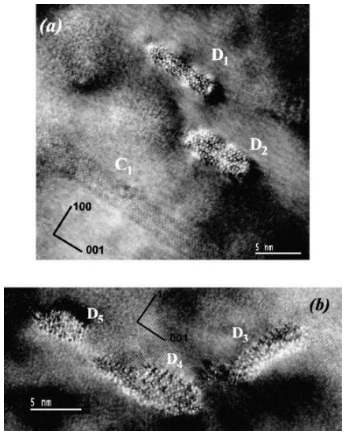

***Figure 35 (a)** and **(b)** HRTEM images of the precipitation microstructure of 6056-T6 alloy [61].*

The formation of precipitates is generally a phenomenon that interferes in a notorious way in the response of the material to a mechanical load. Moreover, the dislocation creep occurs in aluminum alloys at about 250°C [62]. All these facts explain the reason why the curves of stress vs strain at 220°C start to have a tendency to show slight negative slopes in the plastic deformation zone.

Figure 36 illustrates the true stress vs. true strain curves of the materials. With regard to the analysis of the **elastic limit**, its values were determined at 0.2% offset (Rp0.2). As shown in figure 37 – A, with increasing temperature there is a significant increase in yield strength in a non-linear way. Examining the average elongation of the material in figure 36, a tendency towards reduced ductility at elevated temperatures can be observed. The reason for this phenomenon is that, as previously mentioned, these materials are susceptible to age-hardening. Thus, the formation of β"-precipitates around 230°C works as a barrier that prevents dislocation phenomena. Consequently, on the one hand the yield strength is increased, on the other hand the ductility is reduced.

The average values obtained for the **Young's modulus (*E*)** were calculated from the slope of the elastic part of the curves shown in figure 36. As can be seen in figure 37 - B,

contrary to what occurs with the elastic limit, the values of ***E*** decrease in a non-linear way with the increase of the temperature. This softening can be explained because with the increase in temperature, the materials begin to approach one-third of their melting temperature (approximately 600°C), allowing them to distribute stresses more easily.

EN AW 6016–T4

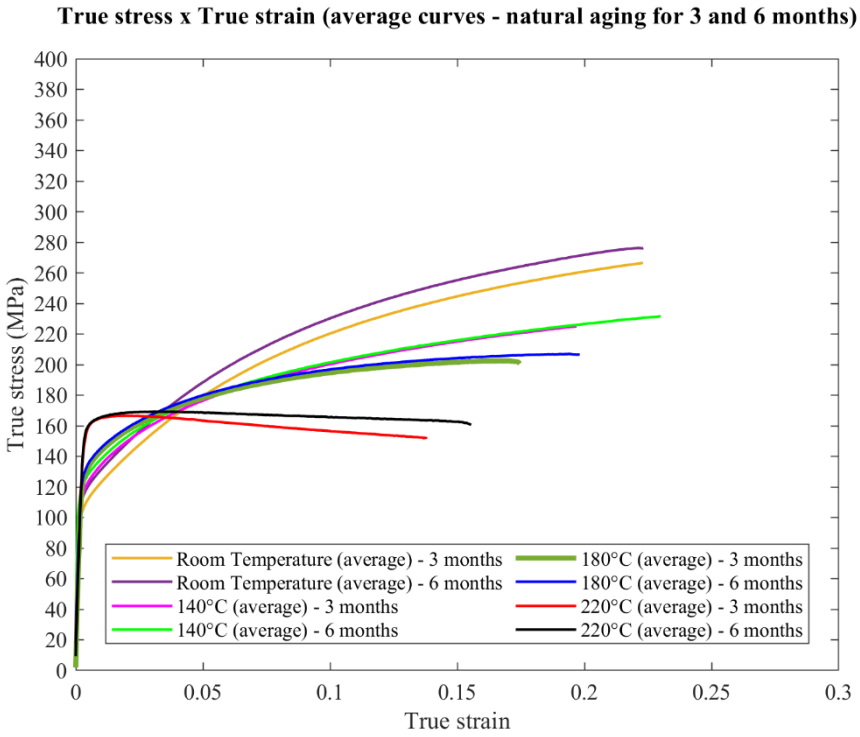

EN AW 6056-T4

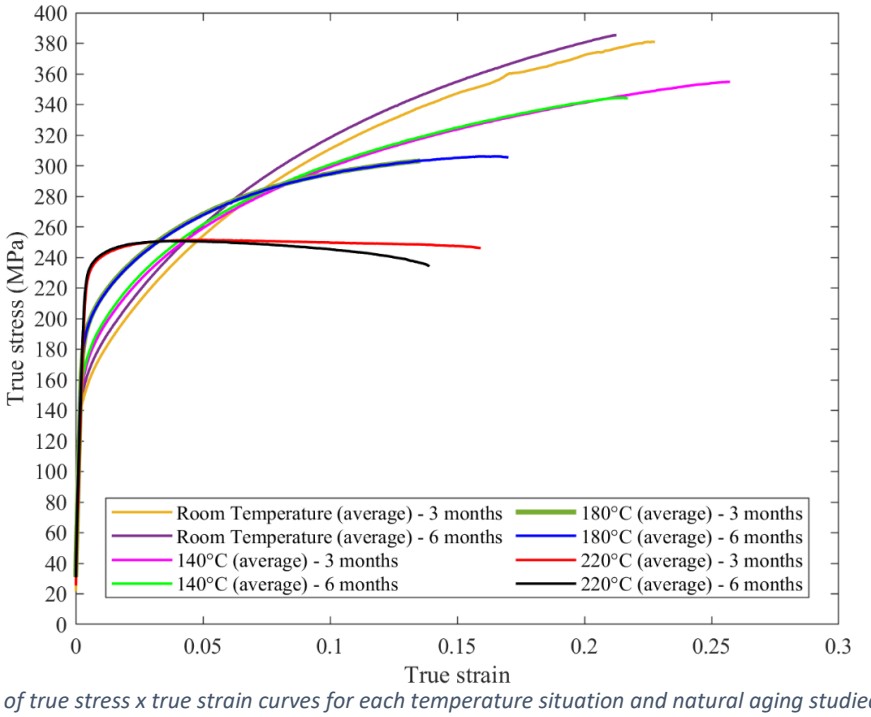

Figure 36 *Average of true stress x true strain curves for each temperature situation and natural aging studied.*

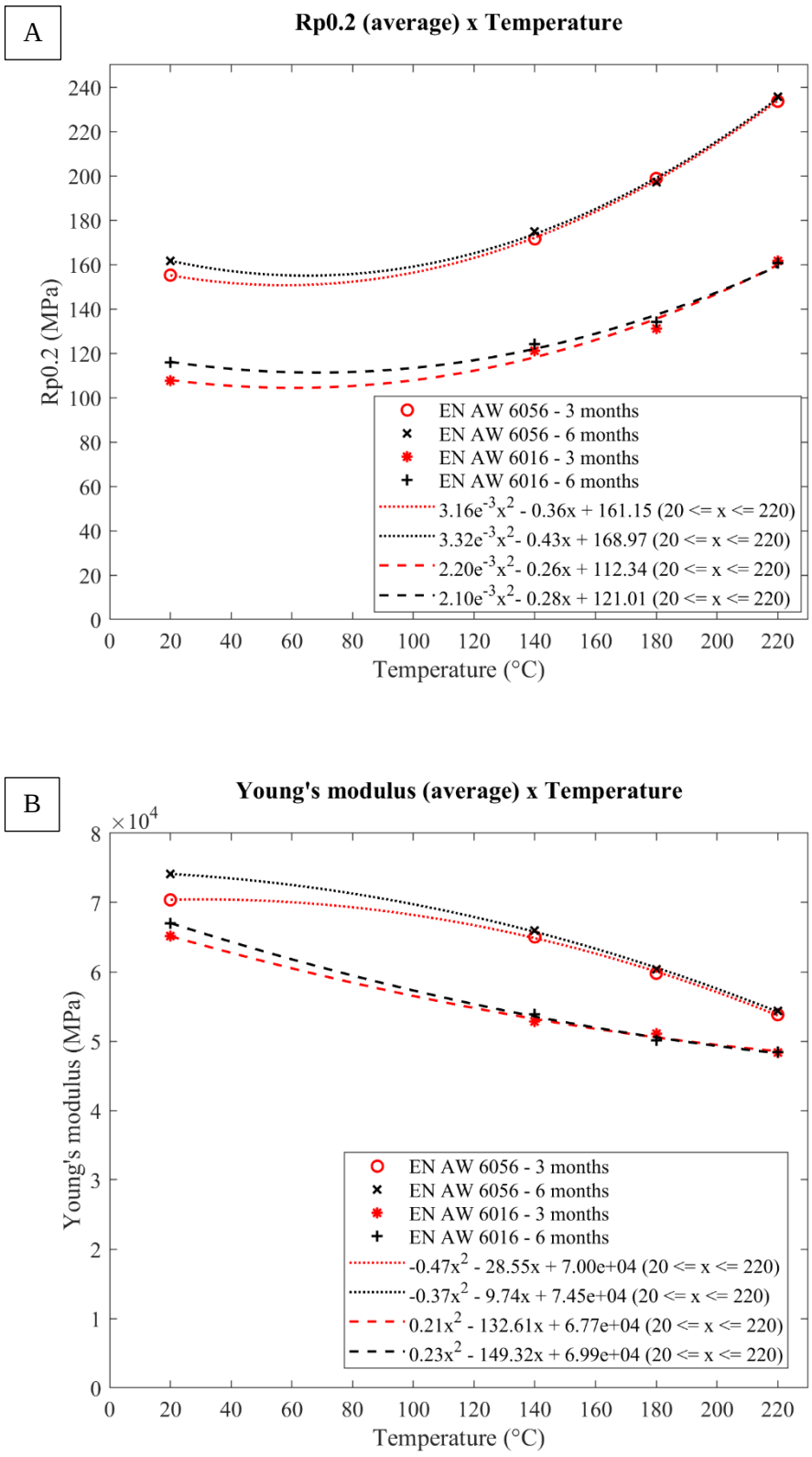

Figure 37 A) *Average evolution of the elastic limit at 0.2% of the elastic zone in relation to the temperature evolution;* ***B)*** *Average evolution of Young's modulus in relation to temperature evolution.*

Table 3 *Result of the analysis of the mechanical properties.* $\overline{Rp_{0.2}}$ *is the average of the elastic limits obtained with an offset of 0.2% from the elastic zone;* $\sigma(\overline{Rp_{0.2}})$ *is the standard deviation of the elastic limits;* $\overline{E}$ *is the average of the Young's moduli;* $\sigma(\overline{E})$ *is the standard deviation of Young's moduli;* $\overline{Rp_{0.2}}^{0^\circ}$ *and* $\overline{Rp_{0.2}}^{90^\circ}$ *are, respectively, the averages of the elastic limits obtained from the specimens cut at 0 °C from the rolling direction and at 90°C; Similarly,* $\overline{E}^{0^\circ}$ *and* $\overline{E}^{90^\circ}$ *are the averages of the Young's moduli obtained from specimens cut at 0°C from the rolling direction and at 90°C.*

EN AW 6016-T4

	Temperature (°C)	$\overline{Rp_{0.2}}$ (MPa)	$\sigma(\overline{Rp_{0.2}})$ (MPa)	$\overline{E}$ (GPa)	$\sigma(\overline{E})$ (GPa)	$\frac{\overline{Rp_{0.2}}^{0^\circ}}{\overline{Rp_{0.2}}^{90^\circ}}$	$\frac{\overline{E}^{0^\circ}}{\overline{E}^{90^\circ}}$
3 months	Room Temp.	107.67	4.34	65.19	0.46	1.07	1.02
	140	121.10	5.05	52.83	0.70	1.02	1.00
	180	131.21	1.69	51.11	1.60	1.02	1.06
	220	161.59	8.93	48.33	1.18	0.93	0.97
6 months	Room Temp.	115.93	2.74	67.01	1.35	1.04	1.01
	140	124.17	3.82	53.86	2.92	1.04	1.07
	180	134.08	2.12	50.10	3.09	1.02	1.07
	220	160.60	0.21	48.45	0.28	1.00	1.01

EN AW 6056-T4

	Temperature (°C)	$\overline{Rp_{0.2}}$ (MPa)	$\sigma(\overline{Rp_{0.2}})$ (MPa)	$\overline{E}$ (GPa)	$\sigma(\overline{E})$ (GPa)	$\frac{\overline{Rp_{0.2}}^{0^\circ}}{\overline{Rp_{0.2}}^{90^\circ}}$	$\frac{\overline{E}^{0^\circ}}{\overline{E}^{90^\circ}}$
3 months	Room Temp.	155.20	1.39	70.38	0.90	1.00	0.99
	140	171.56	2.66	65.03	1.58	0.97	1.02
	180	198.79	1.13	59.78	0.85	1.01	1.00
	220	233.58	1.21	53.82	1.30	1.00	0.99
6 months	Room Temp.	161.55	1.52	74.10	1.02	1.01	0.98
	140	175.00	1.99	65.96	0.79	1.02	1.00
	180	197.12	1.30	60.32	1.38	0.99	1.03
	220	235.67	3.39	54.34	1.30	0.99	1.01

Observing the data in table 3, it is possible to see that the EN AW 6016-T4 presents lower values of elastic limit and Young's modulus than the EN AW 6056-T4. This occurs because the elements that provide increased strength for aluminum alloys are copper, magnesium, manganese, silicon, and zinc [63], and the solubility of these elements in aluminum increases with increasing temperature. Analyzing the chemical composition of the materials studied, the alloy EN AW 6056-T4 has a higher proportion of copper, magnesium, manganese, and zinc than the EN AW 6016-T4, which explains the reason of that behavior.

II. Natural ageing of the material

The mechanical properties show right before were analyzed in a period of 3 months and 6 months after the exit of the alloys from its manufacturing process. As it was shown in figure 36, both alloys naturally aged for 6 months present slightly higher mechanical properties than the material aged for 3 months. For example, in table 3 it can be seen that for the EN AW 6016-T4, the $Rp_{0.2}$ of the material aged for 3 months is 107.67 MPa at room temperature, against 115.93 MPa for the material aged for 6 months. The same occurs with the $Rp_{0.2}$ of EN AW 6056-T4 at room temperature (155.20 MPa for 3 months aging condition against 161.55 MPa for 6 months aging condition). This fact was already expected because the precipitation kinetics during the natural ageing process is slow. Thus, natural ageing over a period of up to 6 months generates slight changes in the materials but does not significantly interfere with their mechanical properties in a temperature range from room temperature to 220°C.

III. Artificial ageing of the material

Tensile tests were carried out not only at room temperature, but also at 140°C, 180°C and 220°C, thus allowing the analysis of mechanical properties at temperatures generally used in the production lines of the automotive industry (as it was presented in Chapter 1). For each of these temperatures, at least 3 tests were performed. This study allowed for the acquisition of information about the two alloys, as they no longer remain in a T4 state once heating begins. This heating phase is also a heat treatment that takes the material to an intermediate state between T4 and T6.

As previously informed, each specimen tested had its temperature measured at three points along its length. The average temperature of each thermocouple at the beginning of the tensile tests is shown in figure 38 - A. It is also possible to observe in figure 38 - B the average thermal cycle of each temperature mentioned (140°C, 180°C and 220°C) obtained by the central thermocouple (T2). In figure 38 - B it is possible to see that there is a drop in temperature at a given time. This temperature drop is due to the experimental procedure. Once the specimen reaches the desired temperature for the first time, the door of the oven coupled to the tensile testing machine is opened for a few seconds to tighten the upper self-locking jaw. Then, the door is closed again and the specimen is expected to reach the desired temperature for the test. Once the specimen reaches again the desired temperature according to ISO 6892-2:2018 (maximum variation of admissible temperature of 3°C along the specimen), the load is tared, and the tensile test is then started. This procedure is done for two reasons: tare the load at the desired temperature and prevent the specimen from buckling during the moment of temperature increase. Table 4 shows the average measurements obtained by the thermocouples for the temperature and their respective standard deviations at the beginning of the tests.

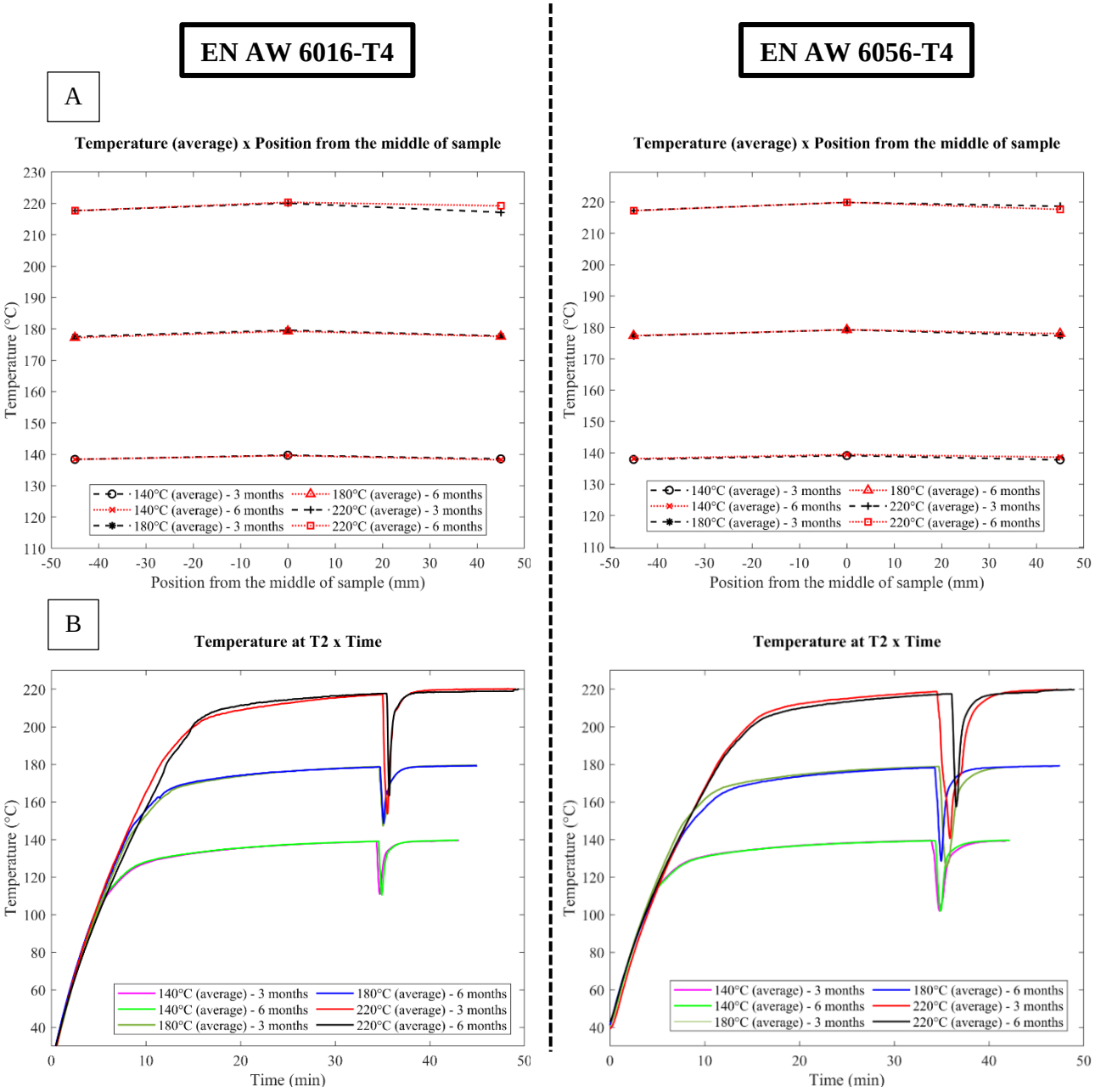

Figure 38 A) *Average temperature of each thermocouple at the beginning of the tensile tests;* ***B)*** *Average temperature evolution measured by the thermocouple located at T2 (figure 33 - B) for the tests carried out at 140°C, 180°C and 220°C.*

Table 4 *Results of the average temperatures obtained by thermocouples at the beginning of the tests and their respective standard deviations.* $\overline{T1}$, $\overline{T2}$ *and* $\overline{T3}$ *are respectively the average temperatures at T1, T2 and T3.* $\sigma(\overline{T1})$, $\sigma(\overline{T2})$ *and* $\sigma(\overline{T3})$ *are respectively the standard deviation of* $\overline{T1}$, $\overline{T2}$ *and* $\overline{T3}$ *results.*

EN AW 6016-T4

	Desired temperature (°C)	$\overline{T1}$ (°C)	$\sigma(\overline{T1})$ (°C)	$\overline{T2}$ (°C)	$\sigma(\overline{T2})$ (°C)	$\overline{T3}$ (°C)	$\sigma(\overline{T3})$ (°C)
3 months	140	138.39	0.19	139.72	0.06	138.55	0.12
	180	177.54	0.68	179.58	0.69	177.74	0.26
	220	217.70	0.89	220.07	2.10	217.16	0.22
6 months	140	138.38	0.03	139.61	0.15	138.25	0.16
	180	177.21	0.20	179.26	0.57	177.59	0.56
	220	217.68	0.19	220.36	1.33	219.25	1.85

EN AW 6056-T4

	Desired temperature (°C)	$\overline{T1}$ (°C)	$\sigma(\overline{T1})$ (°C)	$\overline{T2}$ (°C)	$\sigma(\overline{T2})$ (°C)	$\overline{T3}$ (°C)	$\sigma(\overline{T3})$ (°C)
3 months	140	137.77	0.40	139.12	0.30	137.89	0.25
	180	177.33	0.65	179.23	0.91	177.27	1.12
	220	218.63	3.64	219.84	1.11	217.27	0.18
6 months	140	138.60	0.11	139.47	0.05	138.12	0.12
	180	178.02	0.57	179.25	0.21	177.36	0.51
	220	217.62	0.53	219.88	1.57	217.21	0.90

IV. Material isotropy or anisotropy

To find out if the materials studied have isotropic or anisotropic behavior, the specimens were made and tested in two directions: in the rolling direction (0°C) and at 90° from the rolling direction. Observing the results of the proportion between the elastic limit at 0.2% ($\boldsymbol{Rp_{0.2}}$) for the samples cut in the rolling direction and at 90° (table 3 – page 60), it can be concluded that the result is very close to 1 for all cases of temperature and for the natural ageing condition of 3 and 6 months. Also, according to the results of table 3, the same statement can be made for the Young's Modulus analyzes.

Thus, the test results show that both materials behave as isotropic materials, with little variation in the mechanical properties analyzed in relation to 0° and 90° from the rolling direction. The results obtained from this study align with the conclusions drawn in the work of (O. Engler, 2022) [70]. In that study, an analysis of the EN AW 6016 -T4 alloy was conducted

for three distinct in-plane orientations to the rolling direction: 0°, 45°, and 90°. The findings from this examination echo the observation that the sheet material displays minimal in-plane anisotropy. Notably, a slight discrepancy of only 2 MPa exists between the maximum and minimum yield strengths, evident at orientations 0° and 90°.

Similar congruence is evident in the investigations undertaken by (V. Simões et al, 2015) [43]. In their study, uniaxial tensile tests were performed across a range of temperatures, spanning from ambient conditions to 300°C. These experiments employed the Gleeble machine, generating rapid heating within seconds, and encompassed deformation rates from $2x10\text{-}4s^{-1}$ to $2x10\text{-}2s^{-1}$. The outcomes underscore a parallel observation: uniaxial tensile tests conducted at distinct orientations (0°, 45°, and 90°) relative to the rolling direction consistently reveal the material's negligible anisotropic behavior in terms of yield stresses, regardless of temperature variations.

5.3 Thermal expansion analysis

In order to complement the study carried out in relation to the mechanical properties of the two studied alloys, this part of the research aims to verify whether the natural ageing of up to 6 months and whether the transformation of the material, initially in a T4 state, would have any impact on the coefficient expansion of the materials with the evolution of temperature.

5.3.1 Setting up the test

Thermal expansion measurements were carried out from room temperature to 250°C, using a LINSEIS dilatometer composed of an oven capable of reaching 1100°C, a linear variable differential transformer (LVDT) and an acquisition chain (figure 39 - D). The thermal strain due to thermal expansion of the sample was measured by a LVDT made of quartz.

The geometry of the specimens is shown in figure 39 - C. To measure the temperature, a small hole of 0.7 mm in diameter was made and during the test the sample temperature was measured using a thermocouple adjacent to the sample positioned inside this drilled hole (figure 39 - B). The tests were carried out in such a way that the identical position of the furnace over the sample was always maintained, so that the heating condition was the same in each test.

In all tests, a heating rate of 5°C/min was used, resulting in the average temperature curve shown in figure 40. This choice was made to match the heating rate of the industrial oven at Stellantis Rennes. Both the LVDT data and the temperature sensor data were requested every five seconds. At least three specimens were tested under the same conditions to verify that the data obtained were coherent according to the repeatability of the tests.

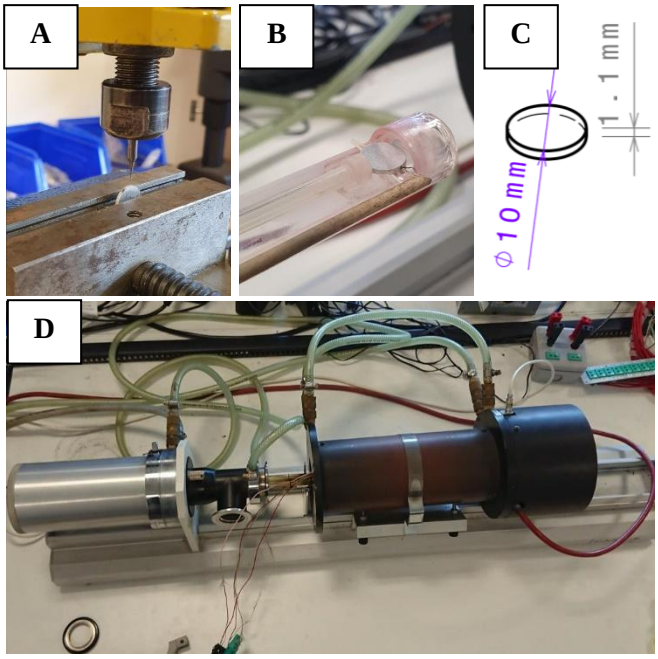

Figure 39 A) *Procedure to create a small hole where the thermocouple will be placed in the specimen;* ***B)*** *Sample ready to be positioned inside the oven and tested;* ***C)*** *Geometry of the sample for the thermal expansion tests;* ***D)*** *Equipment used to carry out the thermal expansion test.*

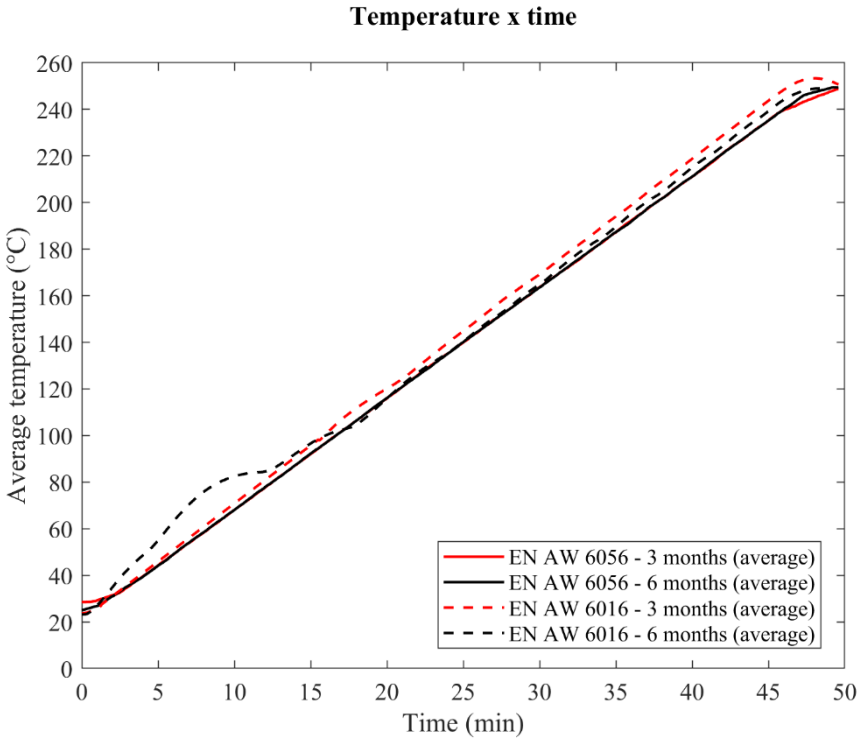

Figure 40 *Average temperature curves for specimens naturally aged for 3 and 6 months. As it can be seen, the thermal cycle is similar for both materials.*

5.3.2 Results and discussions of the thermal expansion analysis

Using the conditions described previously, it is possible to calculate the expansion in the sample diameter (dL) using equation 12, where M is the measuring range of dL in mV, V is the magnification adjusted at the amplifier (mV / mm), S is the writing width of the used recorder in mm.

$$(12) \quad dL = \frac{\Delta L \cdot M}{V \cdot S} \cdot 0{,}25$$

The thermal deformation (ε_{th}), zero at room temperature, evolves with increasing temperature. As can be seen from figure 41, this evolution does not show sudden changes in the slope of the curve of thermal strain evolution for the temperature range studied (from room temperature to 250°C). Furthermore, the calculation of R^2 (coefficient of determination for the regression line) showing values very close to one confirms that the evolution of thermal strain as a function of temperature can be represented by a straight line, for each of the analyzed cases.

Thus, ε_{th} can be represented by equation (13), where L_0 is the initial measured diameter of the specimen, α_{th} is the linear expansion coefficient of the material and dT is the differential temperature.

$$(13) \quad \varepsilon_{th} = \frac{dL}{L_0} = \alpha_{th}.dT$$

In the same way as it was concluded for the results of the analysis of the mechanical properties, the results summarized in table 5 show that natural ageing in up to 6 months does not seem to significantly influence the way in which the materials thermically expand. Both EN AW 6016-T4 and EN AW 6056-T4 have similar coefficient of expansion.

Table 5 *Results of the average linear coefficient of expansion ($\overline{\alpha_{th}}$) and their respective standard deviations($\sigma(\overline{\alpha_{th}})$).*

	EN AW 6016-T4		
	Number of samples	$\overline{\alpha_{th}}$ **(°C^{-1})**	$\sigma(\overline{\alpha_{th}})$ **(°C^{-1})**
3 months	3	$2.24 \cdot 10^{-5}$	$0.13 \cdot 10^{-5}$
6 months	3	$2.11 \cdot 10^{-5}$	$0.19 \cdot 10^{-5}$
	EN AW 6056-T4		
	Number of samples	$\overline{\alpha_{th}}$ **(°C^{-1})**	$\sigma(\overline{\alpha_{th}})$ **(°C^{-1})**
3 months	3	$2.23 \cdot 10^{-5}$	$0.12 \cdot 10^{-5}$
6 months	3	$2.11 \cdot 10^{-5}$	$0.14 \cdot 10^{-5}$

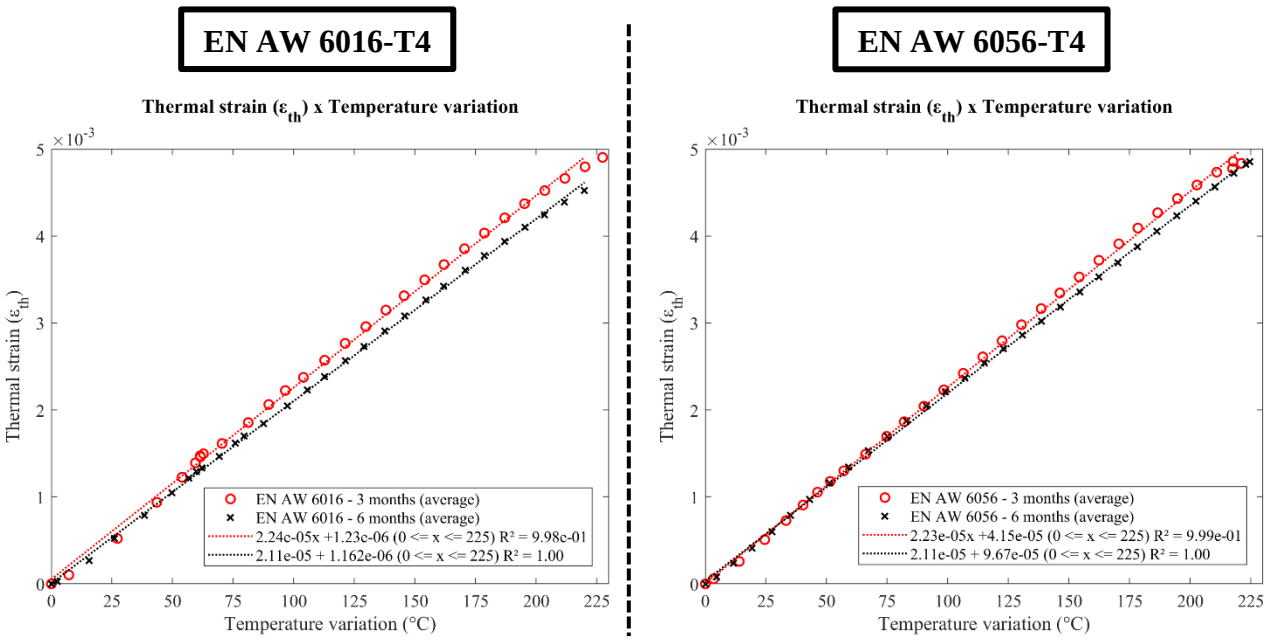

Figure 41 *Evolution of average thermal strain as a function of temperature.*

5.4 Laser Flash Analysis (LFA)

Thermal diffusivity (α - $mm^2.s^{-1}$) is a material property that describes unsteady heat conduction. It is characterized by the speed at which heat propagates, by conduction, within a body. The lower its value, the longer it will take the hot heat source to pass through the thickness of the material. This property depends on the precipitation state in Al alloys, which in turn depends on the thermal cycle applied to the material [68]. In that way, in order to predict the behavior of the material on heating processes similar to industrial automotive operations, the evolution of the thermal diffusivity must be known in the desired temperature range.

5.4.1 Setting up the test

The measurement of thermal diffusivity can be obtained through Laser Flash Analysis (LFA), introduced by Parker et al. [64]. To perform a measurement, the lower surface of a sample with parallel planes (figure 42 - A) is heated by a short pulse of energy. The resulting temperature change on the upper surface is then measured with an infrared detector. The temperature equilibrium is determined from both the sample temperature signal and the stability of the detector signal. The typical evolution of the temperature is shown in figure 42 - B. The greater the thermal diffusivity of the sample, the faster the signal increases. According to the method from [65], using the time half ($t_{1/2}$, time value at half signal height) and the thickness of the sample, the thermal diffusivity and thermal conductivity can be calculated using the following equation:

$$(14) \qquad \alpha = 0.1388 \frac{e^2}{t_{1/2}}$$

With :

- α the thermal diffusivity ($mm^2.s^{-1}$)
- e the thickness (mm)
- $t_{1/2}$ (s) the time during which the back side of the sample reaches half its maximum temperature.

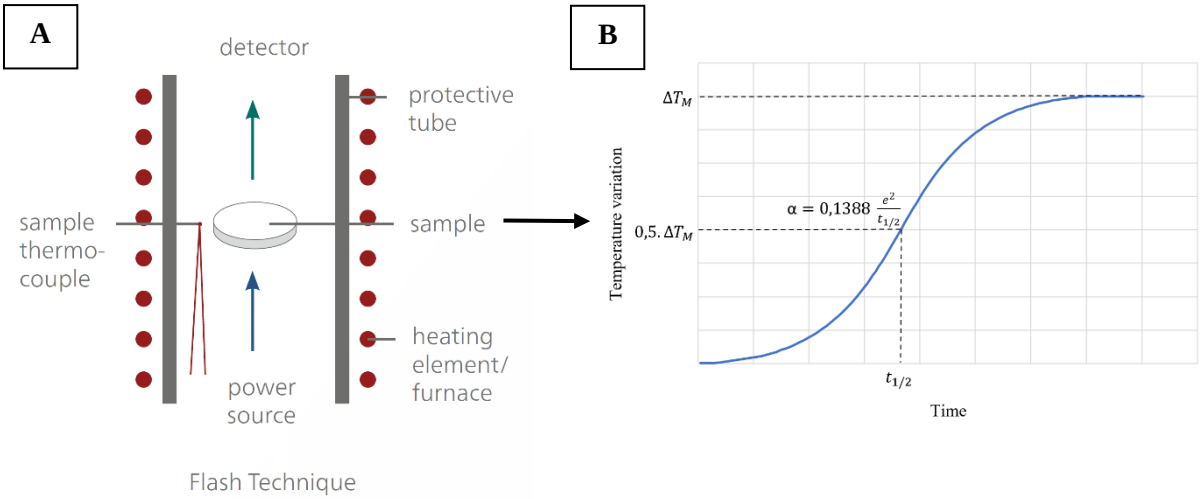

Figure 42 A) *Explanatory image of the LFA method procedure [66];* ***B)*** *Typical evolution of the temperature in the sample during LFA.*

In this work, the machine used to measure the thermal diffusivity was the LFA 457 MicroFlash®, from the company Netzsch (figure 43 - A). This machine has a Neodymium Glass Laser, and an InSb nitrogen cooled sensor. In figure 43 - B, it is possible to see the geometry of the specimens manufactured. The specimens were cleaned with ethyl alcohol, air-dried and then covered with a thin layer of graphite to allow good flashlight absorption and to optimize temperature rise. This procedure made, the specimens were placed on a base plate for 3 samples. The sample holder is made of SiC, for samples of a diameter up to 12.7 mm.

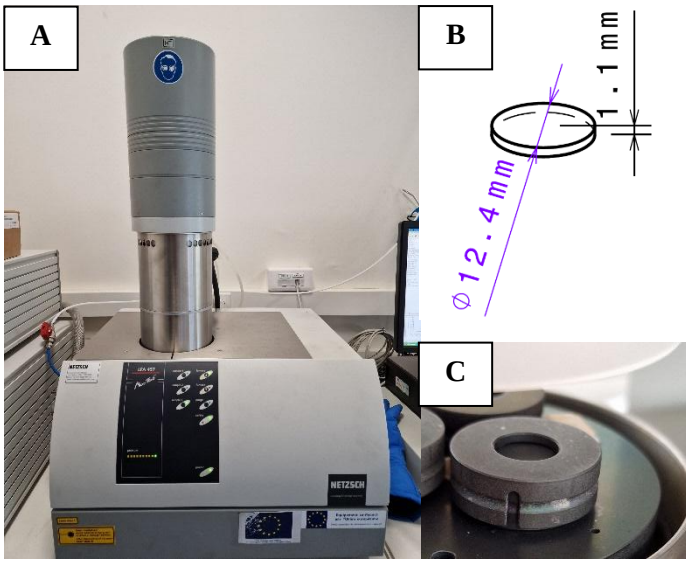

Figure 43 A) *LFA 457 MicroFlash® machine (Netzsch) used for the LFA tests;* ***B)*** *Geometry of the specimens used;* ***C)*** *Specimen inside the used sample holder.*

The recommendation for tests made with the LFA is that the measurement environment must be filled with an inert atmosphere, vacuum or oxidizing. So, before starting the experiment, a vacuum situation was performed and then this atmosphere was filled with argon gas. During the test, an argon flow was maintained to prevent the environment from being polluted with air. Also, to avoid polluting the test atmosphere, the test chamber is made of non-porous materials.

In the LFA, the heating rate used was 5 K/min and measurements are made in isothermal points. Regarding the parameters and method used in the tests, the capacitor voltage was 1538 V and the flash pulse width was 0.5 ms. The model used to approximate the signal curve as a function of time was Cape-Lehmann with pulse correction. This model takes into account heat losses due to radiation from both the facial and radial parts of the specimen.

5.4.2 Results and discussions of the thermal diffusivity measurements

Results were obtained from at least 3 samples in the same conditions, with three single-shot measurements at 30°C, 100°C, 180°C, 220°C, 250°C. Figure 44 - A shows the pulse voltage, figure 44 – B, the responding IR detector voltage during a flash and their respective approximation curves (red curves) with the Cape-Lehmann model [75] with pulse correction in one of the tests with the EN AW 6056-T4 under isothermal conditions at 250°C.

Figure 45 and table 6 show the results for tests carried out using the LFA method between 30°C and 250°C. Although the results for the materials aged naturally for 6 months are slightly higher than the results for the material aged naturally for 3 months, they are very similar. Even some of the standard deviation zones are touching each other. Thus, the difference in natural ageing between 3 months and 6 months did not show significant variations. In contrast, the effect of temperature on test results is considerable.

During the heating phase, it is noted that the thermal diffusivity increases with the increase in temperature, and these evolutions can be represented through second-order polynomial equations. The variation in the diffusivity results is a consequence of the influence by which precipitation phenomena occur [67], and the formation of precipitates in solid solution is responsible for the increase in thermal diffusivity [68]. Thus, studies with the DSC technique were then carried out to better explain what happens to the material in terms of precipitation and the influence of β"-precipitates on the thermal properties of the material in comparison with the formation of Mg- and Si -clusters and GP zones.

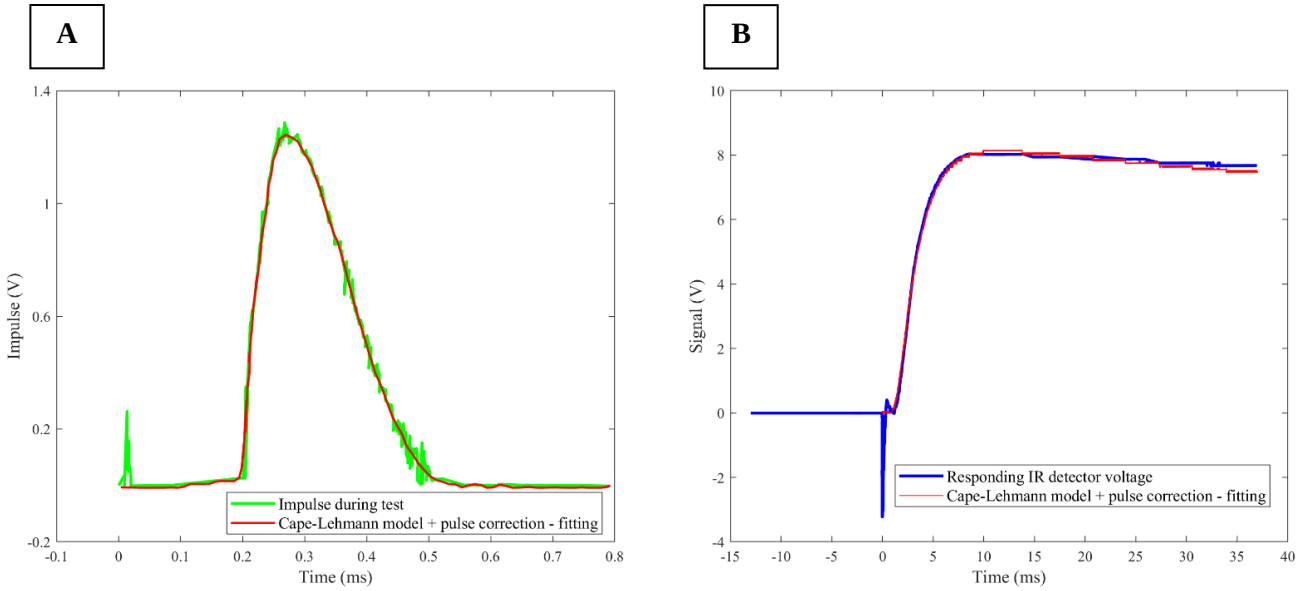

Figure 44 *Results for test under isotherm at 250°C:* ***A)*** *Pulse voltage and Cape-Lehmann + pulse correction fitting curve.* ***B)*** *Responding IR detector voltage during a flash and curve of Cape-Lehmann model with pulse correction.*

Table 6 *Results of the average thermal diffusivity ($\overline{\alpha}$) and their respective standard deviations ($\sigma(\overline{\alpha})$) at average temperatures ($\overline{T}$ (°C)). $\sigma(\overline{T})$ is the standard deviation of the temperatures.*

EN AW 6016-T4

	Desired temperature (°C)	$\overline{T}$ (°C)	$\sigma(\overline{T})$ (°C)	$\overline{\alpha}$(mm²/s)	$\sigma(\overline{\alpha})$ (mm²/s)
3 months	30	29.75	0.4	63.82	8.16
	100	98.50	0.4	64.12	1.16
	180	180.40	0.1	65.18	0.48
	220	221.80	0.4	65.90	0.27
	250	251.55	0.4	66.62	0.38
6 months	30	26.27	0.37	66.48	5.16
	100	100.43	1.12	67.61	1.42
	180	180.43	0.14	70.03	0.80
	220	221.30	1.51	70.80	0.79
	250	250.47	0.20	71.41	0.46

	EN AW 6056-T4				
	Desired temperature (°C)	$\bar{T}$ **(°C)**	$\sigma(\bar{T})$ **(°C)**	$\bar{\alpha}$**(mm²/s)**	$\sigma(\bar{\alpha})$ **(mm²/s)**
3 months	30	33.77	1.46	61.46	4.31
	100	100.47	1.02	62.20	0.85
	180	180.47	0.14	63.95	0.82
	220	221.40	1.42	64.94	0.65
	250	250.40	0.37	65.89	0.42
6 months	30	32.20	1.96	62.69	4.66
	100	100.45	1.04	63.53	2.32
	180	180.53	0.17	64.99	0.87
	220	221.25	1.58	66.25	0.39
	250	250.48	0.49	66.99	0.46

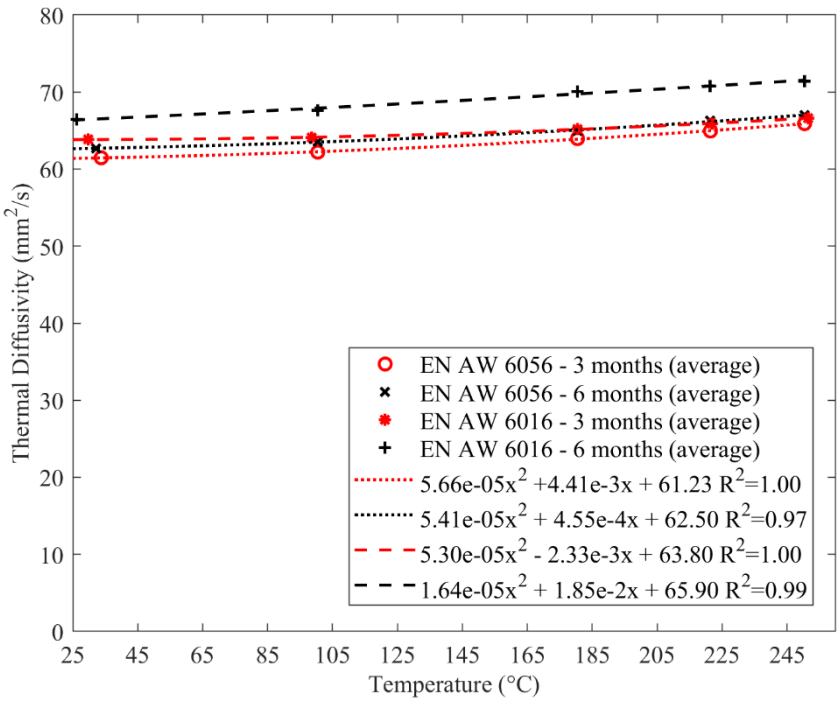

Figure 45 *Evolution of thermal diffusivity as a function of temperature for natural ageing for 3 and 6 months.*

5.5 Differential Scanning Calorimetry (DSC)

The Differential Scanning Calorimetry (DSC) is a technique that is very sensitive to physical-chemical changes (changes in state, phase or structure) of a material. It is for this reason that it is a good technique to analyze the influence of the natural ageing and the temperature on the variation of the specific heat capacity, denoted Cp, of the aluminum alloy under study.

5.5.1 Setting up the test

The DSC machine used to make the measurements was the LABSYSTM EVO (figure 46) from the company SETARAM, with a 3D Cp sensor with eleven thermocouples mounted in series which completely surround the sample of 11 mm high and 4.8 mm in diameter. The knowledge of this maximum dimension is important for the fabrication of the test piece, since the analysis of the precipitation kinetics at low temperature rate in aluminum alloys requires a relatively large mass of material [69]. As the mass of the specimen must be considerable large, the mass of the reference must also be proportional, respecting the relationship below:

$$(15)\quad m_{sample} \,.\, Cp_{sample} \approx m_{ref} \,.\, Cp_{ref}$$

Where m_{sample} and m_{ref} are, respectively, the mass of the test specimen in EN AW 6016 or EN AW 6056-T4 and the mass of the used reference, and cp_{sample} and cp_{ref} are, respectively, the specific heat capacity of the tested materials (desired variable) and the specific heat capacity of the reference (known value). Thus, 863.31 mg of silver (Ag) with a degree of purity of 99.9% were used as the chosen reference material. Using the ratio showed in (15), the amount of alloy used was on average 227.53 mg. The test specimens were made by waterjet cutting a 1.1 mm thick plate of the studied aluminum alloy, thus resulting in the geometry shown in the figure 46 - B. To reach the test mass, it was necessary to place five stacked cylinders in the pan, as shown in figure 46 – B.

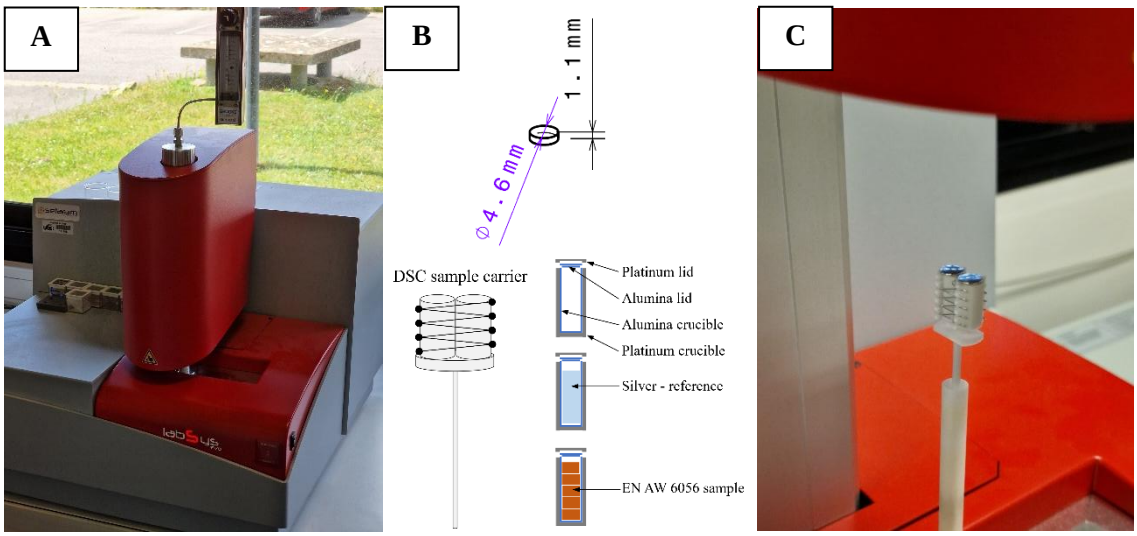

Figure 46 A) *LABSYSTM EVO machine used to carry out the DSC tests;* ***B)*** *At the top, geometry of the test specimens tested. At the bottom, a graphic diagram showing the configuration of the sample carrier and the materials used in the crucibles;* ***C)*** *Specimens ready to be tested.*

In the same way as it is recommended for the LFA, in the DSC the tests were carried out in an atmosphere filled with argon gas (inert gas). Regarding the chosen thermal cycle, the tests started at 30°C, with a ten-minute isotherm, followed by heating up to a temperature of 250°C, with a temperature increase rate of 5 °C/min and ending the heating cycle with another ten-minute isotherm at 250°C. The material was then cooled to 30°C again (figure 47).

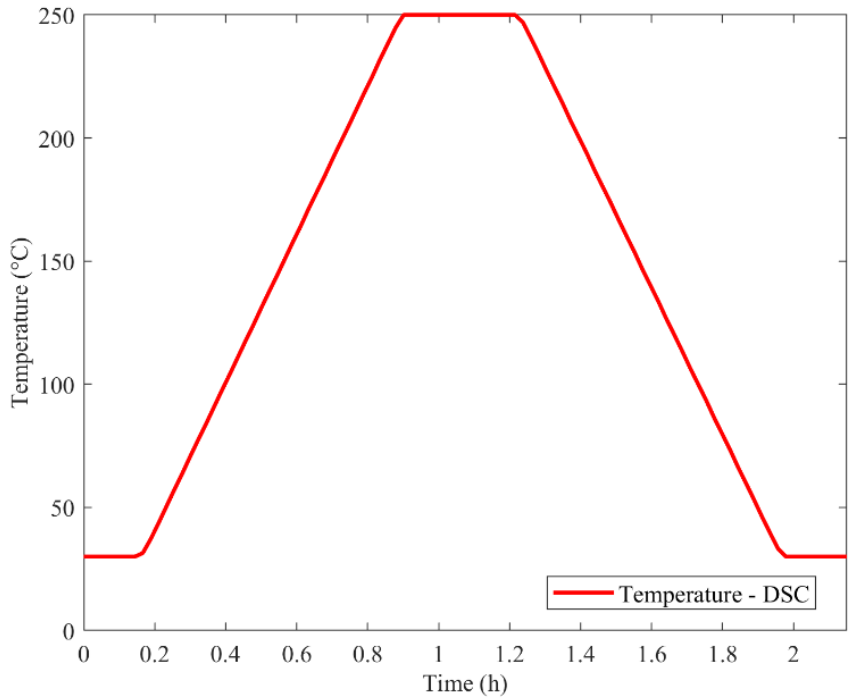

Figure 47 *Defined thermal cycle for DSC tests.*

5.5.2 Results and discussions

Figure 48 shows the heat flow curves obtained as a function of temperature using the DSC in the continuous measurement method. As expected, the curve of the tested materials lies between the curves of the reference pan and the reference made by silver. The calculation of the specific heat capacity is conducted in the processing part using the machine software according to the following equation:

$$(16) \quad Cp_{sample} = Cp_{ref}.\frac{m_{ref}\,(A_{sample}-A_b)}{m_{sample}\,(A_{ref}-A_b)}$$

In this equation, A_b, A_{sample} and A_{ref} are the amplitudes measured in µV respectively of the reference pan, the sample measurement and the reference made by silver. To ensure that the measured amplitude signal is sufficiently stabilized, the first specific heat measurements were got from 100°C. Figure 49 shows the results for specific heat values obtained as a function of temperature.

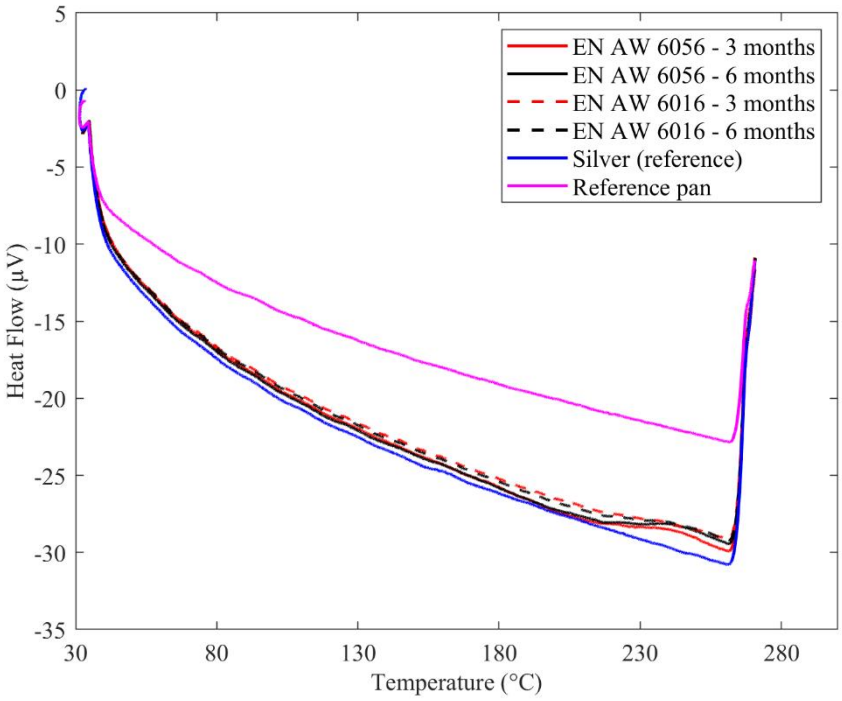

Figure 48 *Curve obtained in the DSC tests showing the result of the heat flow amplitude as a function of temperature.*

Observing the results obtained in figure 49, it is noted that the specific heat values of the more naturally aged EN AW 6016-T4 and EN AW 6056-T4 (6 months) are slightly higher than the values of the less aged materials (3 months). However, as the temperature increases, the results converge to the same values. It can also be noted that, for both cases of materials aged for 3 months and 6 months, from 160°C onwards, the specific heat value varies in relation to the trend that the graph would have. This can be explained due to changes in the microstructure of the material.

According to the literature, these alloys goes through three steps in the temperature range of this study (between room temperature and 250°C), as described in section 5.2.4. Around 80°C, temperature corresponding to the formation of Mg- and Si-clusters, there are no expressive peaks in the thermograms for the studied materials. Even the curve of specific heat over temperature is practically linear, confirming that the change on that property only depends on the temperature. This can be explained by the fact that the materials have undergone a heat treatment, and at the beginning of the test they are already in a T4 state. This artificial ageing done by the material supplier tends to suppress the formation of Mg- and Si-clusters [59].

On the other hand, the first small trend changes are seen from 160°C, which is justified by the presence of GP-zones, and a significant trend change is seen above 200°C, corresponding to the formation of β" -precipitates [59]. As the calculation of the specific heat depends on the amplitudes measured in the DSC test, the most influential transformations that occur in the microstructure of the materials are also translated to a consequent variation in the specific heat coefficient. Cp values for some temperatures are given in table 7.

Table 7 *Mass of specimens used in the DSC and Cp result for some temperatures.*

EN AW 6016-T4

	Sample mass (mg)	Temperature (°C)	(Cp) (J.g^{-1}.K^{-1})
3 months	225.67	100	0.87
		140	0.91
		180	0.96
		220	0.97
		250	0.92
6 months	233.35	100	0.91
		140	0.97
		180	0.98
		220	0.96
		250	0.91

EN AW 6056-T4

	Sample mass (mg)	Temperature (°C)	(Cp) (J.g^{-1}.K^{-1})
3 months	225.70	100	0.87
		140	0.91
		180	0.96
		220	0.97
		250	0.89
6 months	227.66	100	0.90
		140	0.95
		180	1.00
		220	0.99
		250	0.89

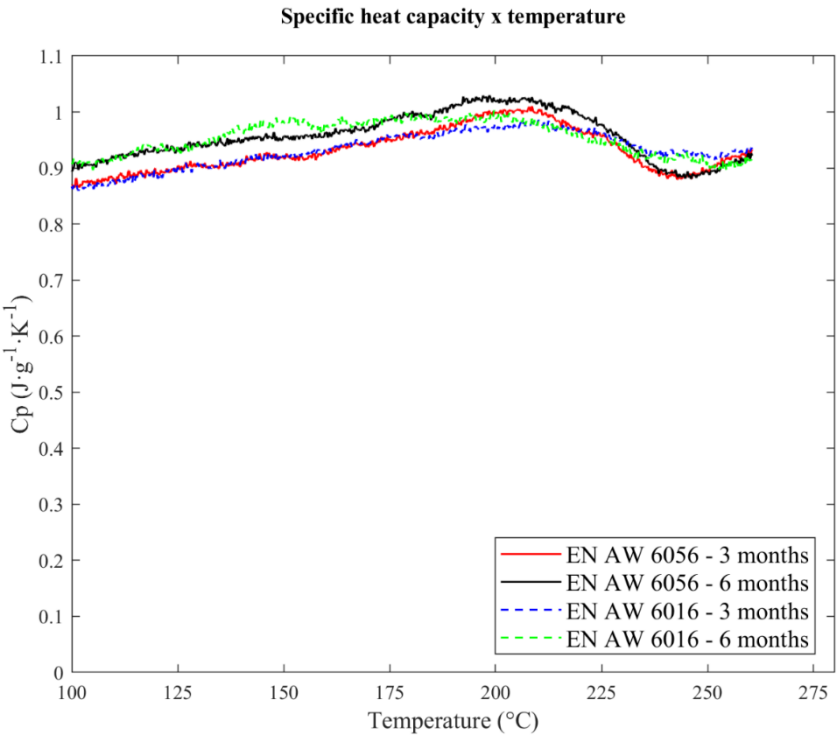

Figure 49 *Cp variation curve as a function of temperature.*

Knowing the coefficient of expansion, the value of the thermal diffusivity, the value of the specific heat and the density of the materials, the thermal conductivity can be indirectly calculated. Equation (17) shows the relationship between each of these variables:

$$\lambda(T) = \alpha(T).Cp(T).\rho(T) \quad (17)$$

Where λ is the thermal conductivity ($W.m^{-1}.K^{-1}$), and ρ the density ($kg.m^{-3}$) which can be calculated from the following equation:

$$\rho(T) = mass / V(T) \quad (18)$$

Where $V(T)$ is the volume as a function of temperature.

Table 8 shows the calculated values for the thermal conductivity of EN AW 6016-T4 and EN AW 6056-T4. From figure 50, it is possible to see that the thermal conductivity values for EN AW 6016-T4 are slightly higher than the values for EN AW 6056-T4. For example, the biggest difference is 13.7 $W.m^{-1}.K^{-1}$ between the values, comparing the case of 250°C with the materials aged for 6 months. This difference is mainly explained by the reason that the thermal diffusivity values of the EN AW 6016-T4 are greater than the values of the EN AW 6056-T4.

Table 8 Calculated values of thermal conductivity

EN AW 6016-T4			
	Temperature (°C)	**λ (W.m^{-1}.K^{-1})**	**$\sigma(\lambda)$ (W.m^{-1}.K^{-1})**
3 months	100	144.35	8.16
	180	161.05	4.80
	220	164.09	2.70
	250	157.02	3.80
6 months	100	160.04	4.16
	180	177.62	5.00
	220	175.47	3.90
	250	167.45	3.60
EN AW 6056-T4			
	Temperature (°C)	**λ (W.m^{-1}.K^{-1})**	**$\sigma(\bar{\alpha})$ (W.m^{-1}.K^{-1})**
3 months	100	140.75	8.31
	180	158.84	4.20
	220	162.54	6.50
	250	151.02	4.20
6 months	100	148.80	8.70
	180	168.29	4.66
	220	169.41	3.90
	250	153.71	4.60

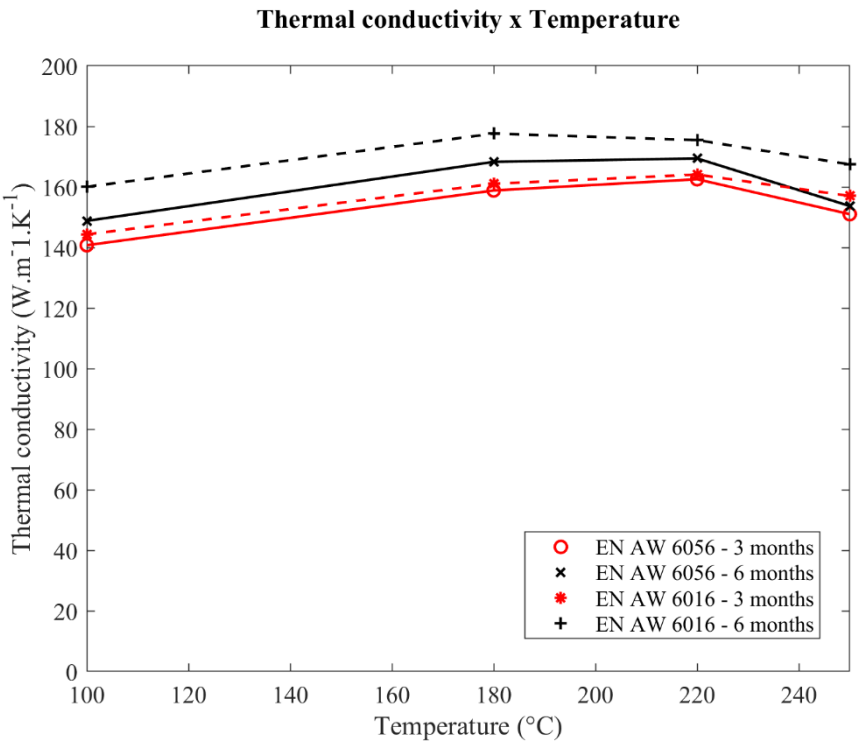

Figure 50 Thermal conductivity as a function of temperature.

6. Conclusion – Chapter 2

The EN AW 6016-T4 and the EN AW 6056-T4 have been widely used in the transport industries. Knowing the influence of natural ageing up to six months and slow heating condition on the thermomechanical properties of these materials is of vital importance to simulate the behavior of these aluminum alloys during heating processes in the painting part of production lines in the automotive industry. Consequently, the present study aimed to respond to the problem of the lack of information in the literature on the variation of the thermomechanical properties of the studied alloys in situations of slow heating up to 250°C and natural ageing of up to 6 months. The results can be summarized in the following statements:

1) In terms of mechanical properties, the materials exhibit isotropic behavior, both at room temperature and at the elevated temperatures studied (140°C, 180°C, and 220°C). Natural aging over a period of up to 6 months does not significantly impact the Young's modulus or the elastic limit of the materials across the temperature range from room temperature up to 220°C. The greatest discrepancies in the elastic limit were observed at room temperature, with a 7 MPa difference in the elastic limit of EN AW 6016-T4 between 3 months and 6 months of aging, which is not considered substantial. Similarly, the greatest discrepancy in Young's modulus was observed at room temperature, with a 4 GPa difference in the Young's modulus of EN AW 6056-T4, also not considered significant compared to the value of this property for these materials.

2) As the temperature rises, there is a trend towards slight negative slopes in the plastic deformation zone, attributed to dislocation creep in aluminum alloys at around 250°C. The increase in temperature leads to a significant non-linear increase in yield strength, which can be attributed to the formation of β"-precipitates. This effect is most pronounced in EN AW 6056-T4 aged for 3 months, where the yield strength increases by 78 MPa between room temperature and 220°C. In contrast to the behavior of the elastic limit, Young's modulus values decrease non-linearly with increasing temperature. The most notable decrease in Young's modulus was observed in EN AW 6056-T4 aged for 6 months, with a decrease of 20 GPa between room temperature and 220°C.

3) Thermal expansion analysis indicates that natural aging over a period of up to 6 months exerts minimal influence on the thermal expansion behavior of the materials. The largest disparity observed in this property amounted to 0.13×10^{-5} °C^{-1}, notably observed in the comparison between EN AW 6016-T4 aged for 3 months and 6 months. This marginal difference underscores the robustness of the material's thermal expansion characteristics over the aging period considered;

4) The LFA showed that the thermal diffusivity increases with the increase in temperature and that for a more detailed analysis of what occurs in the changes in the microstructure of the materials it would be necessary to carry out DSC tests;

5) The DSC tests concluded that up to around 160°C, the specific heat of the materials vary linearly as the artificial ageing to arrive at the T4 state tends to suppress the formation of Mg- and Si-clusters. From 160°C the specific heat varies non-linearly due to the appearance of GP-zones and the formation of β"-precipitates. This is also reflected in the results of thermal conductivity, where between 100°C and 220°C it is possible to see an increase in values and from 220°C values start to drop.

6) When comparing EN AW 6016-T4 with EN AW 6056-T4, a notable trend emerges wherein the former generally displays lower elastic limits and Young's moduli compared to the latter. For example, a substantial difference of 75 MPa in elastic limit is discernible between EN AW 6016-T4 and EN AW 6056-T4 at 220°C when aged for 6 months. This observed variance can be attributed to disparities in their chemical compositions, with EN AW 6056-T4 boasting higher proportions of copper, magnesium, manganese, and zinc than EN AW 6016-T4. Such compositional discrepancies significantly influence the mechanical properties of these materials, resulting in distinct elastic behaviors under similar thermal conditions. In terms of thermal analysis, both materials demonstrate similar coefficients of thermal expansion, ranging from 2.23 to 2.24 x 10^{-5} $°C^{-1}$ when aged for 3 months and 2.11 x 10^{-5} $°C^{-1}$ when aged for 6 months. However, EN AW 6016-T4 exhibits slightly higher values of specific heat capacity (Cp) and diffusivity compared to EN AW 6056-T4. As a result, the thermal conductivity of EN AW 6016-T4 is higher than that of EN AW 6056-T4.

Bibliography – Chapter 2

[26] D. Brough, H. Jouhara, The aluminum industry: A review on state-of-the-art technologies, environmental impacts and possibilities for waste heat recovery, Int. J. of Thermofluids 1–2 (2020) 100007.

[27] H. Kvande, Occurrence and production of aluminum. Encycl. Inorg. Bioinorg. Chem. (2015) 1-10. https://doi.org/10.1002/9781119951438.eibc2350

[28] Zhao R, Nowicki C, Gosselin L, Duchesne C. Energy and exergy inventory in aluminum smelter from a thermal integration point-of-view. Int J Energy Res Aug. (2016);40(10): 1321–38. https://doi.org/10.1002/er.3508

[29] Menzie, W.D., Barry, JJ, Bleiwas, D.I., Bray, E.L., Goonan, T.G., and Matos, Grecia, 2010, The global flow of aluminum from 2006 through 2025: U.S. Geological Survey Open-File Report 2010–1256, 73 p., available at http://pubs.usgs.gov/of/2010/1256/

[30] História do Alumínio. Associação Brasileira do Alumínio - ABAL. Source: https://abal.org.br/aluminio/historia-do-aluminio/#:~:text=O%20alum%C3%ADnio%2C%20apesar%20de%20ser,jovem%20usado%20em%20escala%20industrial [accessed 30.01. 2021].

[31] Associação Brasileira do Alumínio - ABAL. Fundamentos e Aplicações do Alumínio. Associação Brasileira do Alumínio – ABAL, São Paulo, Brasil, 2007.

[32] Science History Institute. (30th Jan 2021). Science History Institute. Source: Science History Institute: https://www.sciencehistory.org/historical-profile/paul-heroult-and-charles-m-hal

[33] J.G. Kaufman. Introduction to Aluminum Alloys and Tempers (pp. 3-6). ASM International, Ohio, USA, 2000.

[34] European Aluminum Association (a). The Aluminum Automotive Manual: Materials - alloy constitution. European Aluminum, Brussels, Belgium, 2002.

[35] European Aluminum Association (b). Materials – Designation system. European Aluminum, Brussels, Belgium, 2002.

[36] Huppert-Schemme, G. (1997). AlMgSi-Bleche für den Fahrzeugbau - Metallkunde und Fertigungstechnik. Düsseldorf: Alu Media.

[37] European Aluminum Association (c). (2011). The aluminum automotive manual by aluminum europe. Brussels, Belgium: European Aluminum Association.

[38] Land Rover. (2020). New Land Rover Defender. EuroCarBody 2020.

[39] M. Zain-ul-abedin, D. Nélias, J.-F. Jullien, A.I. Wagan, Thermo-mechanical characterisation of AA 6056-T4 and estimation of its material properties using Genetic Algorithm, Mater. Des. 31 (9) (2010) 4302–4311. https://doi.org/10.1016/j.matdes.2010.03.056

[40] C. Blanc, G. Mankowski, Susceptibility to pitting corrosion of 6056 aluminum alloy. Corros. Sci., 39 (5) (1997), pp. 949-959. https://doi.org/10.1016/S0010-938X(97)81160-2

[41] M. Pakdil, G. Cam, M. Kocak, S. Erim, Microstructural and mechanical characterization of laser beam welded AA6056 Al-alloy, Mat. Sci. Eng. A-Struct., 528 (2011), pp. 7350–7356. https://doi.org/10.1016/j.msea.2011.06.010

[42] D. Yan, A. Wu, J. Silvanus, Q. Shi, Predicting residual distortion of aluminum alloy stiffened sheet after friction stir welding by numerical simulation, Mater. Des., 32 (2011), pp. 2284–2291. https://doi.org/10.1016/j.matdes.2010.11.032Get rights and content

[43] V. M. N. Simões - Influence of aging in the warm forming of 6xxx series aluminum alloys. Coimbra, 2017. Doctoral thesis. http://hdl.handle.net/10316/79762

[44] Ghosha, M., Mirouxa, A., Werkhoven, R., Bolt, P., & Kestens, L.. Warm deep-drawing and post drawing analysis of two Al–Mg–Si alloys. *Journal of Materials Processing Technology*, pp. 756–766, 2004.

[45] F. Delmas, M. Vivas, P. Lours, M.J. Casanove, A. Couret, A. Coujou, Straining mechanisms in aluminum alloy 6056. In-situ investigation by transmission electron microscopy, Mater. Sci. Eng., 340 (2003), pp. 286-291. https://doi.org/10.1016/j.msea.2022.143152

[46] J. Cheng et al., Improving heat-affected zone softening of aluminum alloys by in-situ cooling and post-weld rolling, Journal of Materials Processing Technology, 306 (2022). https://doi.org/10.1016/j.jmatprotec.2022.117639

[47] M. Quanjin, M. Rejab, Q. Halim, M. Merzuki, M. Darus, Experimental investigation of the tensile test using digital image correlation (DIC) method, Mater. Today.: Proc., 27 (2020), pp. 757-763. https://doi.org/10.1016/j.matpr.2019.12.072

[48] M. Rund, R. Procházka, P. Konopík, J. Džugan, H. Folgar, Investigation of sample-size influence on tensile test results at different strain rates, Procedia. Eng., 114 (2015), pp. 410-415. https://doi.org/10.1016/j.proeng.2015.08.086

[49] Y.H. Wang, et al., Whole field sheet-metal tensile test using digital image correlation, Experimental Techniques, 34 (2) (2010), pp. 54-59. DOI:10.1111/j.1747-1567.2009.00483.x

[50] Lyons, J.S., Liu, J. & Sutton, M.A. High-temperature deformation measurements using digital-image correlation. Experimental Mechanics 36, 64–70 (1996). https://doi.org/10.1007/BF02328699

[51] Yu, L., Pan, B. Overview of High-temperature Deformation Measurement Using Digital Image Correlation. Exp Mech 61 (2021), pp. 1121–1142. https://doi.org/10.1007/s11340-021-00723-8

[52] B. Pan, Z. Lu, H. Xie, Mean intensity gradient: an effective global parameter for quality assessment of the speckle patterns used in digital image correlation, Opt. Laser. Eng., 48 (2010), pp. 469-477. https://doi.org/10.1016/j.optlaseng.2009.08.010

[53] Dong, Y., Pan, B., A Review of Speckle Pattern Fabrication and Assessment for Digital Image Correlation, Exp Mech 57 (2017), pp. 1161–1181. https://doi.org/10.1007/s11340-017-0283-1

[54] Chakrabarti D.J., Laughlin D.E., Phase relations and precipitation in Al-Mg-Si alloys with Cu additions, Prog. Mater. Sci., 49 (3–4) (2004), pp. 389-410. https://doi.org/10.1016/j.commatsci.2022.111871

[55] Miao, W.F., Laughlin, D.E. Effects of Cu content and preaging on precipitation characteristics in aluminum alloy 6022. Metall Mater Trans A 31 (2000), pp. 361–371. https://doi.org/10.1007/s11661-000-0272-2

[56] Saga, M.; Sasaki, Y.; Kikuchi, M.; Yan, Z.; Matsuo, M. Effect of Pre-Aging Temperature on the Behavior in the Early Stage of Aging at High Temperature for Al-Mg-Si Alloy. Mater. Sci. Forum (1996), 217–222, pp. 821–826. http://doi.org/10.4028/www.scientific.net/MSF.217-222.821

[57] Gallais, C.; Denquin, A.; Bréchet, Y.; Lapasset, G., Precipitation microstructures in an AA6056 aluminum alloy after friction stir welding: Characterisation and modelling, Mater. Sci. Eng. A (2008), 496, pp. 77–89. http://doi.org/10.1016/j.msea.2008.06.033

[58] Edwards, G.A.; Stiller, K.; Dunlop, G.L.; Couper,M.J. The precipitation sequence in Al–Mg–Si alloys. ActaMater. (1998), 46, 3893–3904. http://doi.org/10.1016/S1359-6454(98)00059-7

[59] Winter, Lisa & Hockauf, Kristin & Scholze, Mario & Hellmig, R.J. & Lampke, Thomas, Influence of Pre-Aging on the Artificial Aging Behavior of a 6056 Aluminum Alloy after Conventional Extrusion, Metals - Open Access Metallurgy Journal 11(3):385 (2021). https://doi.org/10.3390/met11030385

[60] M. Murayama , K. Hono , Pre-precipitate clusters and precipitation processes in Al-Mg-Si alloys, Acta Materialia (1999), 47, pp. 1537–1548. https://doi.org/10.1016/S1359-6454(99)00033-6

[61] F. Delmas, M. J. Casanove, P. Lours, A. Couret, A. Coujou. Quantitative TEM study of the precipitation microstructure in aluminum alloy Al (MgSiCu) 6056 T6, Mater. Sci. Eng.: A (2004), 373, pp. 80-89. https://doi.org/10.1016/j.msea.2003.12.068

[62] Wang, G.S.; Liu, K.; Wang, S.L., Evolution of elevated-temperature strength and creep resistance during multi-step heat treatments in Al-Mn-Mg alloy, Materials, 11, 1158 (2018). https://doi.org/10.3390/ma11071158

[63] J.R. Davis. Alloying: Understanding the Basics, ASM International® (2001), pp. 367. DOI: 10.1361/autb2001p351

[64] W.J. Parker, R.J. Jenkins, C.P. Butler, G.L. Abbott, Flash method of determining thermal diffusivity, heat capacity, and thermal conductivity, J. Appl. Phys., 32 (1961), pp. 1679-1684. https://doi.org/10.1063/1.1728417

[65] R.L. Rudkil, R.J. Jenkins, W.J. Parker, Thermal diffusivity measurements on metals at high temperature, Rev. Sci. Inst., 33 (1962), pp. 21-24. https://doi.org/10.1063/1.1717653

[66] Netzsch. LFA 457 MicroFlash®. Brochure <https://analyzing-testing.netzsch.com/fr/produits-solutions/diffusivite-thermique-et-conductivite-thermique-lfa-ghp-hfm/lfa-457-micro-flash>; [accessed 03.12.2022].

[67] Kemsies, R.H., Milkereit, B., Lindemann, A. et al. In situ investigation of precipitation in aluminum alloys via thermal diffusivity from laser flash analysis. J. Therm. Anal. Calorim. 140 (2020), pp. 725–733. https://doi.org/10.1007/s10973-019-08880-8

[68] S.W. Choi, Y.M. Kim, and Y.C. Kim, Influence of Precipitation on Thermal Diffusivity of Al-6Si-0.4 Mg-0.9Cu-(Ti) Alloys, J. Alloys Compd., 775 (2019), pp. 132–137. https://doi.org/10.1016/j.jallcom.2018.10.068

[69] Milkereit, B.; Kessler, O.; Schick, C. Recording of continuous cooling precipitation diagrams of aluminum alloys. Thermochim. Acta, 492 (2009), pp. 73–78. https://doi.org/10.1016/j.tca.2009.01.027

[70] O. Engler, Effect of precipitation state on plastic anisotropy in sheets of the age-hardenable 515 aluminium alloys AA 6016 and AA 7021, Mater. Sci. Eng. A. 830 (2022) 142324. 516 https://doi.org/10.1016/j.msea.2021.142324

[71] ISO 6892-1:2019 Metallic materials - Tensile testing - Part 1: Method of test at room temperature. Technical Committee : ISO/TC 164/SC 1. ICS : 77.040.10 (2019) https://www.iso.org/standard/78322.html

[72] ISO 6892-2:2018 Metallic materials - Tensile testing - Part 2: Method of test at elevated temperature. Technical Committee : ISO/TC 164/SC 1. ICS : 77.040.10 (2018) https://www.iso.org/standard/72571.html

[73] ZEISS INSPECT Correlate (2023) https://www.gom.com/en/products/metrology-software/gom-correlate-pro

[74] ZEISS Industrial Metrology. Import Existing 2D Images with ZEISS INSPECT Correlate (2/6). YouTube. (2023). https://www.youtube.com/watch?v=_RSe50EPjug&list=PLMjGCcUyqpJww7V2sXuQ1I-zl2IIOcC79&index=2

[75] Cape, J. and Lehman, G. Temperature and Finite Pulse-Time Effects in the Flash Method for Measuring Thermal Diffusivity. Journal of Applied Physics, 34, 1909-1913 (1963). http://dx.doi.org/10.1063/1.1729711

Chapter 3 - Understanding the mechanisms of differential expansion of body-in-white sheets: theory and lab-scale testing

Introduction – Chapter 3

In this chapter, the knowledge gained about the aluminum alloys EN AW 6016-T4 and EN AW 6056-T4 will be utilized to study their behavior under thermal expansion conditions. The ultimate goal of this thesis is to develop a simulation approach that can provide preventive insights and propose changes to avoid appearance defects on the car's roof. However, transitioning from material analyses to the complex geometry of the body-in-white can be a challenging task, given the numerous variables that hinder a comprehensive understanding of the real-world scenario. Additionally, it is crucial to propose, test, and validate a numerical simulation methodology through simpler theoretical and practical scenarios. Therefore, it is essential to have a numerical simulation that can effectively correlate theoretical predictions with practical observations in a controlled laboratory environment.

Thus, three types of analyses are necessary to understand the phenomenon occurring in the car's roof: analytical, numerical, and experimental. This chapter investigates the cause of the conformity issues, describes the phenomenon, and examines the factors that may influence it. The initial focus lies in investigating the behavior of a circular plate composed of the aluminum alloys previously studied, possessing the same thickness as the car's roof, when subjected to heating. The edges of the plate are fixed to a steel support to simulate real-world conditions accurately. This test is used to propose a numerical model and validate it against both reality and analytical calculations. Subsequently, the concept of differential expansion is highlighted through a test conducted with two plates of the same thickness and aluminum alloys as those used in the car's roof. Finally, with a comprehensive understanding of material behavior, analysis of the phenomenon, and correlations with practical cases, the study advances to Chapter 4 (where the validated findings and insights are applied to the study of the body-in-white).

TABLE OF CONTENTS – CHAPTER 3

Chapter 3 – Understanding the mechanisms of differential expansion of body-in-white sheets: theory and lab-scale testing……..……....……..……..……85

Introduction – Chapter 3…….……...…...85

1. Simplified example of the expansion problem and laboratory analysis methodology.……...……..…….....87

2. Stability analysis and equilibrium conditions..……...……..…….…….……..90

3. Thermal buckling……...92

4. Thermal buckling behavior of a circular aluminum alloy plate using the digital image correlation technique and finite element analysis…….……93

4.1 Problem formulation: equations of thermal buckling for a clamped circular plate…….93

4.2 Numerical simulation: thermal buckling for a clamped circular plate…….100

4.3 Experimental analysis of the post-buckling of a clamped circular plate……..102

4.4 Numerical analysis of the post-buckling of a clamped circular plate……...105

4.5 Results and discussions……...107

4.6 Conclusion……...111

5. Investigation of thermal buckling behavior in the context of differential expansion…….……112

5.1 Impact of boundary conditions on buckling: bar case…….…….113

5.2 Analysis of thermal expansion and thermal buckling: thermal buckling of a beam subjected to imposed displacement…….116

5.3 Coupling of two different materials under thermal loading……..120

5.3.1 Experimental set up: rectangular plates test……...120
5.3.2 Material analysis: steel DC01…….…..…..121
5.3.3 Buckle and post-buckle analysis: rectangular plates..……. …..123

5.4 Conclusion……...130

6. Conclusion – Chapter 3……...……..…132

Bibliography – Chapter 3……...…..133

1. Simplified example of the expansion problem and laboratory analysis methodology

The study has reached a stage where the material data is well-established, enabling progression towards higher Technology Readiness Levels. Prior to analyzing the car roof in conjunction with the overall vehicle structure, it is essential to conduct laboratory tests for several important reasons. Firstly, it is crucial to gain a qualitative and quantitative understanding of the scientific processes taking place within the vehicle structure. Moreover, given the recurring observations of roof deformations, certain questions need to be addressed: What is the cause of this phenomenon? How can it be described? What factors might influence it? However, structural-level analyzes are time-consuming, labor-intensive, and highly expensive.

Additionally, results obtained from tests at an industrial scale often stem from numerous interactions between various influencing factors, making it challenging to draw precise conclusions. Therefore, the analysis phase involves tests conducted on smaller scales within a controlled laboratory environment. This allows for the evaluation of the studied system's behavior and the verification of practical conditions necessary for the occurrence and reproducibility of the phenomenon. As experiments are performed, evidence is gathered, and hypotheses are formulated. These hypotheses serve the purpose of explaining observations and guiding experimental planning to gain further insights into the observed phenomena. The obtained results will be validated through the comparison of experimental, analytical, and numerical simulation analyzes utilizing the Finite Element Method (FEM). The data collected, along with the corresponding interpretations, will support the validation of hypotheses and provide explanations for the observed phenomena.

To provide a clear and illustrative representation of the study structure, figure 51 displays the metallic components of the vehicle in three distinct configurations. In figure 51-A, the body-in-white structure, primarily composed of steel elements, is depicted without the car roof. In the second scenario, figure 51-B showcases the vehicle roof in its current market configuration. Lastly, figure 51-C displays the integration of the vehicle roof (highlighted in blue) with the body structure. This last configuration will undergo a heating process during the painting process, as mentioned in Chapter 1.

As widely recognized in the field of engineering, a rise in temperature induces vibration and separation between the constituent atoms of a solid body. Consequently, the body experiences an expansion in its dimensions, referred to as thermal expansion. The classification of solid expansion into linear, superficial, or volumetric is contingent upon the predominant expansion observed in a particular dimension (length, width, or depth). Within the automotive industry, the body-in-white is predominantly constructed using lightweight and thin components, leading to a scenario where the thermal expansion in thickness is significantly smaller compared to expansions occurring in other dimensions.

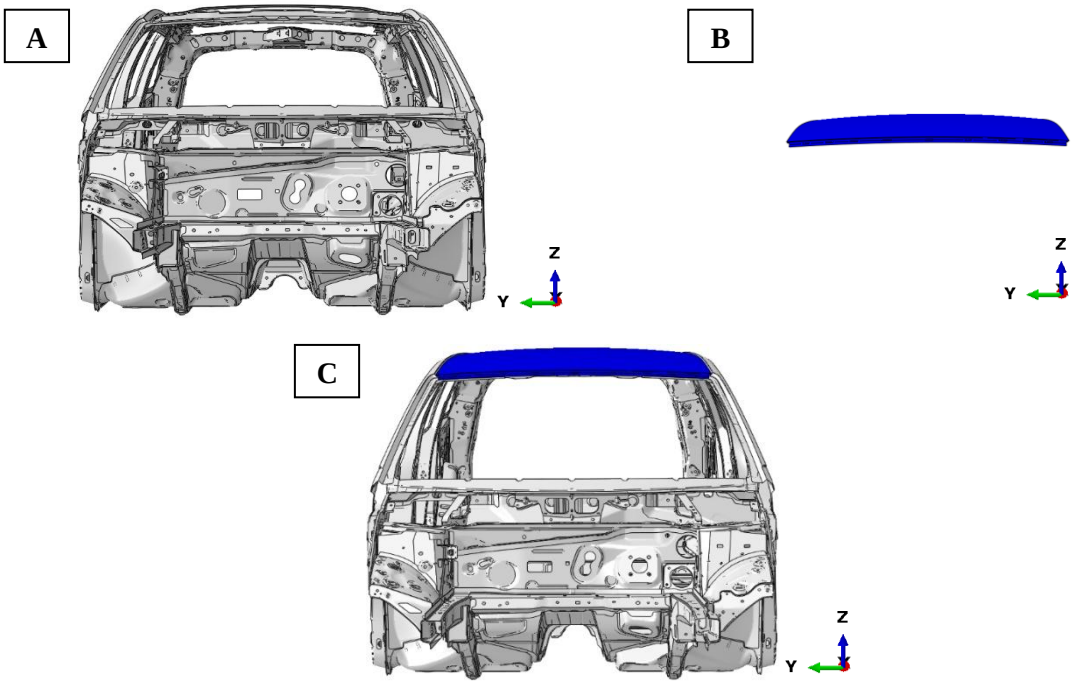

Figure 51 A) *Metallic structure of the body-in-white of the study vehicle without the roof;* ***B)*** *Vehicle roof in its current market configuration;* ***C)*** *Structure resulting from the integration of the vehicle roof with the body structure.*

The behavior of the car's structure during the production line's heating and cooling cycles is primarily influenced by the effects of thermal expansion. For analysis, an example will be considered where the car's structure depicted in figures 51-A and B is isolated within a hypothetical space. The focus will be specifically on examining the thermal expansion that takes place in the Y-direction. Under the assumption of a heating process, the temperature is increased, represented by the value ΔT. By drawing a very simplified analogy, the thermal expansion effect exhibited by both structures can be likened to the behavior observed in the two bars illustrated in figure 52. This analogy enables understanding and interpretation of the thermal expansion phenomenon in a simple manner, similar to the demonstrated case.

In figure 52-A and B, in the case of a temperature increase of value ΔT, the initial length $\boldsymbol{L_0}$ of both bars would experience a dimensional increase of values $\Delta \boldsymbol{y_1}$ and $\Delta \boldsymbol{y_2}$ for the steel and aluminum bars, respectively.

$$\Delta \boldsymbol{y_1} = \boldsymbol{L_0} \cdot \boldsymbol{\alpha_{th-steel}} \cdot \Delta T \quad (19)$$

$$\Delta \boldsymbol{y_2} = \boldsymbol{L_0} \cdot \boldsymbol{\alpha_{th-aluminum}} \cdot \Delta T \quad (20)$$

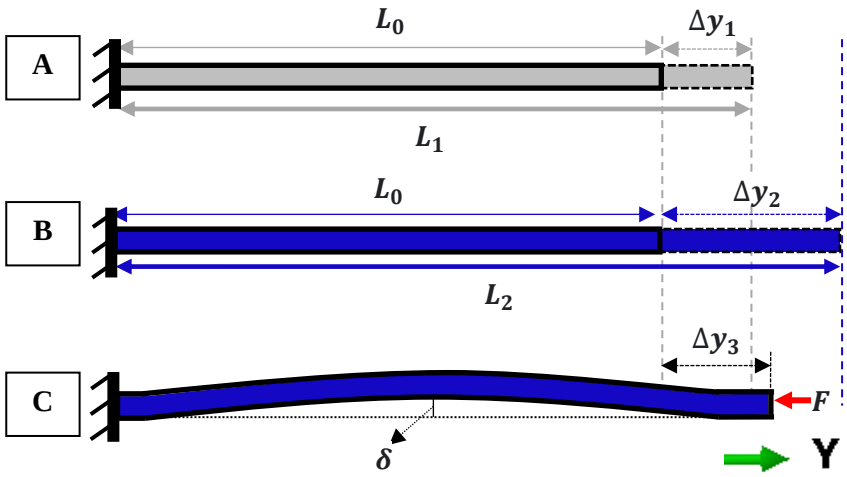

Figure 52 *Linear thermal expansion caused by an increase in temperature ΔT in bars of initial length L_o.* ***A)*** *A steel bar exhibiting a linear coefficient of thermal expansion $\alpha_{th-steel}$. The variation in length (Δy_1) represents the change in length resulting from thermal expansion;* ***B)*** *An aluminum bar demonstrating a linear coefficient of thermal expansion $\alpha_{th-aluminum}$ and length variation (Δy_2);* ***C)*** *This scenario showcases the application of a compressive force of intensity F, which restricts the aluminum bar from expanding as it should, generating a variation in length (Δy_3). Consequently, if F is important enough, a deflection (δ) can be observed.*

According to equations (19) and (20), these dimensional increases would be proportional to the temperature variation ($\boldsymbol{\Delta T}$), the initial length of the bars ($\boldsymbol{L_0}$), and the coefficient of thermal expansion of the material used, represented by $\boldsymbol{\alpha_{th-steel}}$ and $\boldsymbol{\alpha_{th-aluminum}}$.

Figure 52-C serves as a highly simplified representation of the behavior observed when examining the study structure presented in figure 51-C. The two structures are composed of different materials, thus transforming the problem from a mere isolated thermal expansion issue to a problem of differential expansion. In this scenario, the thermal expansion of one structure directly influences the other, and vice versa. Assuming that the steel structure (body-in-white) possesses significantly greater stiffness and mass compared to the thin aluminum structure (roof), the displacement of the aluminum structure will be constrained by the expansion of the steel structure under heating conditions. This causes the final length variation of the aluminum structure to be smaller than naturally expected (length variation in this case: $\boldsymbol{\Delta y_3}$, where $\boldsymbol{\Delta y_2} > \boldsymbol{\Delta y_3} > \boldsymbol{\Delta y_1}$).

Nonetheless, the constraint on displacement caused by differential expansion in certain thin-walled structures can give rise to concerns regarding their stability and instability. Consequently, after analyzing the problem from a simplified perspective and employing linear equations to describe thermal expansion, the study will now delve into progressively more intricate concepts.

2. Stability analysis and equilibrium conditions

It is possible to say that a structure is approaching an unstable condition when it appears unable to withstand the induced stresses and ceases to be in its original stable equilibrium condition, to the point that even a small change in the external loads - thermal or mechanical - produces a significant deformation and causes divergence from the equilibrium condition [76 - 77].

The concept of stability, pertaining to diverse forms of equilibrium, is frequently elucidated by employing the equilibrium analysis of a rigid-body ball in various positions [78] as exemplified in figure 53. The graphical representation shown in figure 53 provides a simplified illustration of two distinct scenarios: one demonstrating a stable state, and the other depicting an unstable state. The equilibrium conditions for the two balls in their respective positions differ.

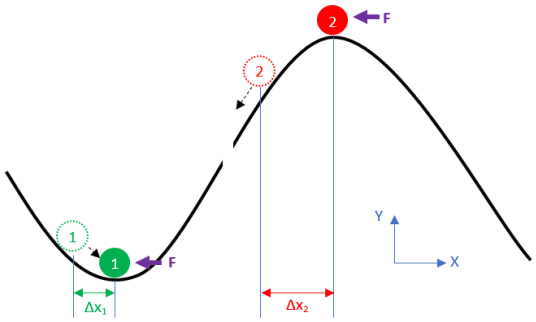

Figure 53 *Representation of two different stability situations. Each ball are subjected to a force vector $\vec{F}$. Analyzing the displacements along the x-axis for ball 1 (Δx_1) and for ball 2 (Δx_2) after the application of the force, it can be observed that ball 1 is positioned in a manner where minor disturbances result in its return to the original position, indicating a state of stable equilibrium. On the other hand, ball 2 is placed in a location where any disturbance will cause it to deviate from the original position, signifying an unstable equilibrium.*

Assuming that both ball 1 and ball 2 are disturbed by a force vector $\vec{F}$ with a magnitude of F, the behavior of both balls will be examined over a period of time t (identical for both scenarios). Ball 1 is situated in such a way that small disturbances lead to its return to the original position, indicating a state of **stable equilibrium**. On the other hand, ball 2 is positioned at a location where a disturbance (in this example, the same as that experienced by ball 1) will cause it to deviate from the original position, signifying an **unstable equilibrium**.

In addition to the two situations presented in figure 53, there is a third one called **neutral equilibrium**. This situation occurs when there is no change in energy during a displacement in the conservative force system. It is commonly assumed that a state of equilibrium exists at the transition from a stable to an unstable condition. From this fact, it can be inferred that the load at which stability no longer applies is equivalent to a condition at which neutral equilibrium is possible. This load is usually referred to as the **critical load**.

To provide a more mathematical and physical definition of equilibrium conditions, the study will systematically adopt the global energy approach using the Stability Theorem of

Lagrange-Dirichlet. According to the Lagrange-Dirichlet Theorem, assuming the continuity of the total potential energy, the equilibrium of a system containing only conservative and dissipative forces is stable if the total potential energy of the system has a strict minimum or, in other words, is positive-definite. This theorem is a global energy criterion for stability, and it will be used systematically to derive all the equations of stability loss required for any arbitrary elastic structure [79].

The transition of a system from a stable to an unstable state occurs at the critical load P_{cr}, at which point a neutral equilibrium is reached when $\Pi''(u;\ P) = 0$, where P represents the load and u represents the kinematics of the system. The stability condition for the total potential energy $\Pi(u)$ is positive-definiteness, which means that the second derivative Π'' with respect to the kinematic variables of the system has to be positive at these equilibrium points. As a result, instability of an equilibrium corresponds to $\Pi'' < 0$. In summary:

- $\Pi'' > 0$ denotes stability;
- $\Pi'' = 0$ denotes neutral equilibrium;
- $\Pi'' < 0$ denotes instability.

Using the example shown previously in figure 53, the equations that show the equilibrium condition of the situation will be developed. Since the ball is considered perfectly rigid, the system's total potential energy now consists only of gravitational potential energy, $\Pi = \Pi_0 + m.g.y(x)$, where $\Pi_0 = \Pi(x_0 = 0)$ is a constant at the initial equilibrium position x_0, m is the mass of the ball and g is the acceleration of gravity. Locally, the shape of the surface is described by the graph of $y(x) = a.x^2$, which is the first term in the Taylor series for the surface around the initial equilibrium point. The scalar $a > 0$ for convex, $a < 0$ for concave, and $a = 0$ for neutral equilibrium cases, respectively.
Therefore,

$$\Pi = \Pi_0 + m.g.a.x^2 \quad (21)$$

Imagine that the initial equilibrium configuration at $x_0 = 0$ is disturbed by a small amount δx. As a result, the total potential energy of the system is:

$$\Pi(x_0 + \delta x) = \Pi(x_0) + \left.\frac{d\Pi(x)}{dx}\right|_{x_0} \delta x + \frac{1}{2}.\left.\frac{d^2\Pi(x)}{dx^2}\right|_{x_0} (\delta x)^2 + \frac{1}{3!}.\left.\frac{d^3\Pi(x)}{dx^3}\right|_{x_0} (\delta x)^3 + \cdots \equiv \Pi(x_0) + \delta\Pi|_{x_0} + \frac{1}{2}.\delta^2\Pi|_{x_0} + \frac{1}{3!}.\delta^3\Pi|_{x_0} + \cdots \quad (22)$$

Since x_0 is an equilibrium point, then $\delta\Pi|_{x_0} = 0$. Rewriting the above equation in a condensed form yields the equation providing the sign of the increment of the total potential energy between the perturbed and the initial equilibrium state:

$$(23) \qquad \Delta\Pi = \Pi(x_0 + \delta x) - \Pi(x_0) = \frac{1}{2}.\delta^2\Pi|_{x_0} + \frac{1}{3!}.\delta^3\Pi|_{x_0} + \cdots$$

Keeping only up-to the second order term:

$$(24) \qquad \Delta\Pi = \frac{1}{2}.\frac{d^2\Pi(x)}{dx^2}\bigg|_{x_0} (\delta x)^2 = m.g.a\,(\delta x)^2 + o(\delta x)^3$$

It should be noted that in this straightforward discrete scenario, which involves a very small number of discrete kinematic parameters (specifically, just one: x), the sign of the potential energy can be obtained through direct application of the Lagrange-Dirichlet stability theorem.

$$(25) \qquad \Pi'' = 2.m.g.a$$

As a result, when $a > 0$ (which corresponds to a locally convex surface), the initial equilibrium x_0 is stable, whereas it is unstable for $a < 0$ (which corresponds to a locally concave surface), and indifferent when $a = 0$. For more details about the equations, please refer to [80].

Now, with a better understanding of the concept of instability, it is important to note that it can arise in various ways depending on the characteristics of the physical system in question. Instability can be dynamic, which occurs in systems subject to vibrations or oscillations. Other types of instability include instability due to phase changes in a material. However, some of the most common examples of instability include buckling, which is a form of instability that occurs in systems subject to compression, just like in the problem addressed in this thesis. Therefore, the focus will now shift to the type of buckling that affects the vehicle structure as it goes through the paint curing ovens: thermal buckling.

3. Thermal buckling

In 1757, Euler published a work on buckling in columns, marking a significant advancement in the understanding of this phenomenon. Over the years, subsequent research has continued to enrich the comprehension of buckling. According to (Beer; Johnston & DeWolf, 2015) [81], buckling occurs when a quasi-static external mechanical or thermal load is applied to an elastic structure, causing the structure to deform proportionally until the load reaches a limiting amount, at which point it acts non-proportionally. As previously mentioned in this report, the buckling of the structure occurs in the heating ovens during the painting phase. Thus, the origin of the problem's load is a result of the thermal loading gradient that causes materials to expand differently. This frames the issue related to the industrial application of this thesis in the type of buckling called thermal buckling. As a result, many theoretical analyzes and experimental investigations have been conducted on thermal buckling to adapt to the fast

development and changes in technologies. For example, thermal buckling analysis of functionally graded plates has been frequently studied [82-85], as well as thermal buckling in structures made of composite materials [86-87], among other researches. Regarding the industrial context, the buckling of thin plates due to thermal loads has attracted significant attention in the design and analysis of engineering structures in diverse fields such as the pipeline industry [88 -89], aerospace engineering [90-91], oil refineries [92–93], and nuclear engineering [94]. However, in the automotive industry, these studies on thermal buckling are still relatively rare, and when they are present, they are usually to analyze structural components, such as brake discs and rotors [95 - 96].

For design purposes, a detailed analysis of the stability behavior of structures can be conducted using numerical methods, specifically a Geometrical and Material Nonlinear Analysis (GNMA), which leverages the capabilities of Finite Element technology. This analysis involves considering the geometric and material nonlinearities in a real structure, accounting for imperfections. By performing this analysis, it is possible to obtain load-displacement curves that can help identify bifurcations and limit points. However, it is crucial to ensure that the analysis of the load-displacement curves is conducted reliably. Additionally, a simulation methodology must be tested before performing a numerical analysis of the entire metal structure of the vehicle under consideration. This ensures that the numerical analysis is reliable enough to be used at the scale of the vehicle structure. Furthermore, in addition to the simulation's predictive capabilities, it is important to understand how thermal buckling functions within the context of thermal loads. Analytical calculations for simpler structures and tests conducted in a controlled environment, such as a laboratory, can provide valuable insights into the key parameters influencing thermal buckling.

To address these considerations, two laboratory tests have been developed. The first test, which will be discussed in section 4 of this chapter, involves a circular plate with its edges clamped to a steel support. The second case, presented in section 5, involves two plates fixed at one end to a support, while their other ends are connected to each other. This setup helps highlight the phenomenon of thermal buckling due to differential thermal expansion.

4. Thermal buckling behavior of a circular aluminum alloy plate using the digital image correlation technique and finite element analysis

4.1 Problem formulation: equations of thermal buckling for a clamped circular plate

Considering a circular plate with radius R and thickness t (figure 54). The parameter z is denoted as the coordinate axis that passes through the plate's thickness. Additionally, it is assumed that the Poisson's ratio (ν) is constant throughout the plate's thickness. For a plate with material uniformly distributed through its thickness, the equation for the relationship between the Young's modulus (E) and the z-axis is:

$$E(z) = E \quad (26)$$

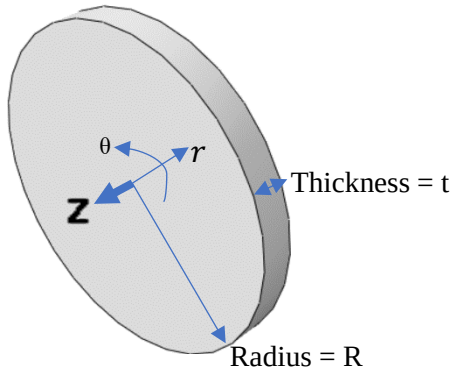

E - Young's modulus
ν - Poisson's ratio
ε - deformation
σ - stress
G - shear modulus
z - axial coordinate
r - radial coordinate
θ - circumferential coordinate
σ_{ij} - stress tensor components, where i and j can take values of r, θ, and z.
ε_{ij} - deformation tensor components, where i and j can take values of r, θ, and z.

Figure 54 *Geometry of the circular plate.*

Taking into account the plane-stress condition, the relationships between stress and deformation can then be given by the following equations:

$$\varepsilon_{rr} = \frac{1}{E} . (\sigma_{rr} - \nu . \sigma_{\theta\theta}) \quad (27)$$

$$\varepsilon_{\theta\theta} = \frac{1}{E} . (\sigma_{\theta\theta} - \nu . \sigma_{rr}) \quad (28)$$

$$\varepsilon_{r\theta} = \frac{1}{G} . (\sigma_{r\theta}) \quad (29)$$

Where r is the radial coordinate, θ is the circumferential coordinate, G is the shear modulus of the material, ε is the deformation, and σ is the stress. By using Love-Kirchhoff assumptions (where it is assumed that normals to the median surface stay straight and normal throughout deformation) and Sanders assumption, equations (27), (28), and (29) can be rewritten as:

Love-Kirchhoff assumptions:

$$\varepsilon_{rr} = \bar{\varepsilon}_{rr} + z . k_{rr} \quad (30)$$

$$\varepsilon_{\theta\theta} = \bar{\varepsilon}_{\theta\theta} + z . k_{\theta\theta} \quad (31)$$

$$\varepsilon_{r\theta} = \bar{\varepsilon}_{r\theta} + 2 . z . k_{r\theta} \quad (32)$$

Sanders assumptions:

$$(33) \quad \varepsilon_{rr} = \frac{\partial u}{\partial r} + \frac{1}{2}.\left(\frac{\partial w}{\partial r}\right)^2 - z.\left(\frac{\partial^2 w}{\partial r^2}\right)$$

$$(34) \quad \varepsilon_{\theta\theta} = \frac{1}{r}.\frac{\partial v}{\partial \theta} + \frac{u}{r} + \frac{1}{2}.\left(\frac{1}{r}.\frac{\partial w}{\partial \theta}\right)^2 - z.\left(\frac{1}{r}.\frac{\partial w}{\partial r} + \frac{1}{r^2}.\frac{\partial^2 w}{\partial \theta^2}\right)$$

$$(35) \quad \varepsilon_{r\theta} = \frac{1}{r}.\frac{\partial u}{\partial \theta} + \frac{\partial v}{\partial r} - \frac{v}{r} + \left(\frac{1}{r}.\frac{\partial w}{\partial r}\right).\frac{\partial w}{\partial \theta} + 2.z.\left(-\frac{1}{r}.\left(\frac{\partial^2 w}{\partial r \partial \theta}\right) + \frac{1}{r^2}.\frac{\partial w}{\partial \theta}\right)$$

Where u, v and w are the corresponding components of displacement of a point on the middle plate surface, $\bar{\varepsilon}$ is a strain component in the median surface, and k are the curvatures which can be expressed in terms of the displacement components. By calculating the total potential energy (V) of the studied case:

$$(36) \quad V = U + L$$

$$(37) \quad U = \frac{1}{2}\int_0^r \int_0^{2\pi} \int_{-\frac{t}{2}}^{\frac{t}{2}} (\varepsilon_{rr}.\sigma_{rr} + \varepsilon_{\theta\theta}.\sigma_{\theta\theta} + \varepsilon_{r\theta}.\sigma_{r\theta}) r \, dr \, d\theta \, dz$$

$$(38) \quad L = -\int_0^r \int_0^{2\pi} \int_{-\frac{t}{2}}^{\frac{t}{2}} (l_r.u) r \, dr \, d\theta$$

Where U and L are, respectively, the strain energy for a circular plate and the potential energy of applied loads. The load distributed over the surface of the plate in the r component is l_r. Based on the equations that have been shown and the assumptions used, it is possible to arrive at the potential energy equation. The derivation of the stability equations involved in the analysis is extensive and, therefore, not included in this report to maintain brevity. However, for a detailed understanding of the equations and their derivation, please refer to the source [97].

To obtain the stability equations for thin circular plates subjected to a uniform compression load, the energy method can be employed. By considering the potential energy functional and applying the Euler equations, it is possible to derive these equations. Let the total potential energy of the plate be denoted as V. Expanding V around the equilibrium state using a Taylor series, the expression can be written as follows:

$$(39) \quad \Delta V = \delta V + \frac{1}{2}\delta^2 V + \frac{1}{6}\delta^3 V + \cdots$$

The stability of the plate in the neighborhood of equilibrium condition can be determined by examining the sign of the second variation. The condition $\delta^2 V = 0$ is used to derive the stability equations for buckling problems [98]. Examining the scenario of axisymmetric buckling of a circular plate, the analysis focuses on a plate not affected by thermal loading but subjected to uniform compressive loading ($-p$) along its edge. In such conditions, it is possible to obtain the first and third stability equations:

(40) $$\frac{\int_{-\frac{t}{2}}^{\frac{t}{2}} E(z)dz}{1-v^2}\left(\frac{d^2u_1}{dr^2}+\frac{1}{r}\frac{du_1}{dr}-\frac{u_1}{r^2}\right)+\frac{\int_{-\frac{t}{2}}^{\frac{t}{2}} E(z).z\,dz}{1-v^2}\left(-\frac{d^3w_1}{dr^3}-\frac{1}{r}\frac{d^2w_1}{dr^2}+\frac{1}{r^2}\frac{dw_1}{dr}\right)=0$$

(41) $$\frac{\int_{-\frac{t}{2}}^{\frac{t}{2}} E(z).z^2\,dz}{1-v^2}\nabla^4 w_1-N_{r_0}\frac{\partial^2 w_1}{\partial r}-\frac{1}{r}N_{\theta_0}\left(\frac{dw_1}{dr}\right)+\frac{\int_{-\frac{t}{2}}^{\frac{t}{2}} E(z).z\,dz}{1-v^2}\left(\frac{1}{r^2}\frac{du_1}{dr}-\frac{u_1}{r^3}-\frac{2}{r}\frac{d^2u_1}{dr^2}-\frac{d^3u_1}{dr^3}\right)=0$$

Equation (41) involves the terms N_{r_0} and N_{θ_0}, which are the prebuckling forces that can be calculated through an equilibrium analysis of the plate. u_1, v_1 and w_1 are arbitrary small increments of displacements. Ignoring the pre-buckling rotations, the following expression can be obtained:

(42) $$N_{r_0}=N_{\theta_0}=-p$$

Substituting equation (42) into the equation (41) the following result is obtained:

(43) $$\frac{\int_{-\frac{t}{2}}^{\frac{t}{2}} E(z).z^2\,dz}{1-v^2}\nabla^4 w_1-\frac{1}{r}\frac{d}{dr}\left(r.N_{r_0}\frac{dw_1}{dr}\right)+\frac{\int_{-\frac{t}{2}}^{\frac{t}{2}} E(z).z\,dz}{1-v^2}\left(\frac{1}{r^2}\frac{du_1}{dr}-\frac{u_1}{r^3}-\frac{2}{r}\frac{d^2u_1}{dr^2}-\frac{d^3u_1}{dr^3}\right)=0$$

To solve the stability equation, consideration of the following set of interdependent stability equations is necessary:

(44) $$A\left(\frac{d^2u_1}{dr^2}+\frac{1}{r}\frac{du_1}{d_r}-\frac{u_1}{r^2}\right)+C\left(-\frac{d^3w_1}{dr^3}-\frac{1}{r}\frac{d^2w_1}{dr^2}+\frac{1}{r^2}\frac{dw_1}{dr}\right)=0$$

(45) $$B\,\nabla^4 w_1-\frac{1}{r}\frac{d}{dr}\left(r.N_{r_0}\frac{dw_1}{dr}\right)+C\left(\frac{1}{r^2}\frac{du_1}{dr}-\frac{u_1}{r^3}-\frac{2}{r}\frac{d^2u_1}{dr^2}-\frac{d^3u_1}{dr^3}\right)=0$$

Where:

$$A=\frac{\int_{-\frac{t}{2}}^{\frac{t}{2}} E(z)\,dz}{1-v^2}\qquad B=\frac{\int_{-\frac{t}{2}}^{\frac{t}{2}} E(z).z^2\,dz}{1-v^2}\qquad C=\frac{\int_{-\frac{t}{2}}^{\frac{t}{2}} E(z).z\,dz}{1-v^2}$$

$$\frac{dw_1}{dr}=Y\qquad \frac{d^2w_1}{dr^2}=\frac{dY}{dr}=Y'\qquad \frac{d^3w_1}{dr^3}=\frac{d^2Y}{dr^2}=Y''$$

And substituting these equations into equation (44) the following result is found:

(46) $$r^2.q''+r.q'-q=0$$

Where: (47) $q=A.u_1-C.Y$

The solution to equation (46) can be determined as follows:

$$(48) \quad q = o_1.r + o_2.\left(\frac{1}{r}\right)$$

The clamped edge condition is equal to the following boundary conditions:

$$(49) \quad u_1 = \frac{dw_1}{dr} = finite \text{ at } r = 0$$

$$(50) \quad u_1 = \frac{dw_1}{dr} = 0 \text{ at } r = R$$

Implementing the boundary conditions to equations (48), the following is obtained:

$$(51) \quad o_1 = 0 \quad o_2 = 0$$

Substituting the constants of integration from equation (51) into equation (48), gives $q = 0$. This value is then set in equation (47) and solved for u_1 to give:

$$(52) \quad u_1 = \frac{\int_{-\frac{h}{2}}^{\frac{h}{2}} E(z).z\, dz}{\int_{-\frac{h}{2}}^{\frac{h}{2}} E(z)\, dz} \frac{dw_1}{dr}$$

The solution for u_1 from Eq. (52) is set in the second stability equations (45) to give:

$$(53) \quad \left(B - \frac{C^2}{A}\right)\nabla^4 w_1 = \frac{d}{dr}\left(N_{r_0}\frac{dw_1}{dr}\right)$$

Substituting the value of N_{r_0}in equation (42) into Eq. (53) and integrating with respect to r gives:

$$r^2\beta'' + r\beta' - \beta(\lambda^2 r^2 - 1) = 0 \qquad (54)$$

Where:

$$\beta = -\frac{dw_1}{dr} \qquad \lambda^2 = \frac{p}{D_1} \qquad (55)$$

The solution of Eq. (54) is :

$$\beta = c_3 J_1(\lambda r) + c_4 Y_1(\lambda r) \qquad (56)$$

Where J_1 and Y_1 are Bessel functions of first order and second kind respectively, and c_3 and c_4 are integration constants. Since:

$$\beta = 0 \text{ at } r = 0 \text{ and } Y_1(0) \rightarrow \infty,\ c_4 = 0 \text{ and } \beta = c_3 J_1(\lambda r) \qquad (57)$$

For the clamped edge $\beta = 0$ at $r = R$, where R is the plate radius, and hence:

$$J_1(x) = 0 \qquad x = \lambda_1 R \qquad (58)$$

The critical thermal load is expressed in terms of $x_1 = \lambda_1 R$, where x_1 is the first zero of the Bessel function of first order and kind namely

$$\lambda_1 R = 3.831 \quad (59)$$

Using the value of $\lambda_1 a$ and substituting in equation (55) gives:

$$P_{cr} = 14.68.\frac{D_1}{R^2} \qquad (60)$$

For clamped boundary conditions (as in the studied case), k has a value of 14.68.

$$(61)\ P_{cr} = 14.68\,.\frac{1}{R^2}\,.\frac{E.t^3}{12.(1-\nu^2)}$$

If the stress of the aluminum plate only resulted from the thermal expansion, it can be assumed that the mechanical strain (ε_{mec}) is identical to the thermal strain (ε_{th}). The critical buckling temperature (ΔT_{cr}) is obtained using:

$$(62) \quad \varepsilon_{mec} = \varepsilon_{th}$$

The stress (σ) and mechanical deformation (strain - ε) are related by Hooke's law:

$$(63) \quad \sigma = E.\varepsilon$$

Knowing that the lateral strain in a linear elastic material subjected to uniaxial stress is related to the axial strain by Poisson's ratio, ν:

$$(64) \quad \sigma.(1-\nu) = E.\varepsilon_{axial}$$

$$(65) \quad \frac{P_{cr}}{t}.(1-\nu) = \varepsilon_{\mathrm{mec}}\,.\mathrm{E}$$

$$(66) \quad \frac{P_{cr}}{t}.(1-\nu) = \varepsilon_{\mathrm{th}}\,.\mathrm{E}$$

$$(67) \quad \frac{P_{cr}}{t}.(1-\nu) = \alpha_{al}\,.\Delta T\,.\mathrm{E}$$

$$(68) \quad \Delta T = \frac{P_{cr}}{t.\alpha_{al}.\mathrm{E}}.(1-\nu)$$

$$(69) \quad \Delta T = \frac{\sigma_{cr}}{\alpha_{al}.\mathrm{E}}.(1-\nu)$$

$$(70) \quad \Delta T = 14.68\,.\frac{1}{R^2}\,.\frac{t^2}{12.(1-\nu^2)}.\frac{1}{\alpha_{al}}.(1-\nu)$$

According to equation (70), it is evident that the critical buckling temperature variation is dependent on two structural parameters (radius and thickness) and two material parameters (thermal expansion coefficient and Poisson's ratio). To demonstrate the influence of each parameter in equation (70), two 3D graphs were created.

The first graph, figure 55-A, highlights the influence of the structural parameters on the variation of the critical buckling temperature to reach the first natural mode. It can be observed that the most favorable condition for avoiding thermal buckling is achieved with a small radius and a large thickness, which is not surprising. However, it is important to note that in some

situations, a small increase in thickness can significantly increase the critical buckling temperature to reach the first mode. For instance, in the hypothetical scenario of a circular plate with a radius of 100 mm, when the thickness is close to zero, the critical buckling temperature also approaches 0.00°C. However, with a mere 2.00 mm increase in thickness, the critical temperature can rise to around 14.82°C.

The second graph, figure 55-B, emphasizes the influence of material parameters. As the Poisson's ratio for most metallic materials is typically close to 0.30, it becomes challenging to vary this parameter in practice. However, the coefficient of thermal expansion plays a dominant role in the variation of the critical buckling temperature. Considering that both aluminum alloys analyzed in this dissertation, EN AW 6016-T4 and EN AW 6056-T4, have very similar material parameters and were tested with the same geometry, it is expected that circular plates made from these materials will exhibit similar variations in buckling temperature. Assuming a Poisson's ratio of 0.33 for both aluminum alloys and using the thermal expansion coefficients obtained in Chapter 2 ($\overline{\boldsymbol{\alpha}_{\boldsymbol{th}_{6016}}} = 2.24 \,.\, 10^{-5}\ °C^{-1}$ and $\overline{\boldsymbol{\alpha}_{\boldsymbol{th}_{6056}}} = 2.23 \,.\, 10^{-5}\ °C^{-1}$), it is possible to calculate the critical temperature for a circular plate with a thickness of 1.10 mm and a radius of 100 mm, resulting in $\Delta T_{crit_{6016}} = 4.97\ °C$ and $\Delta T_{crit_{6056}} = 4.99\ °C$.

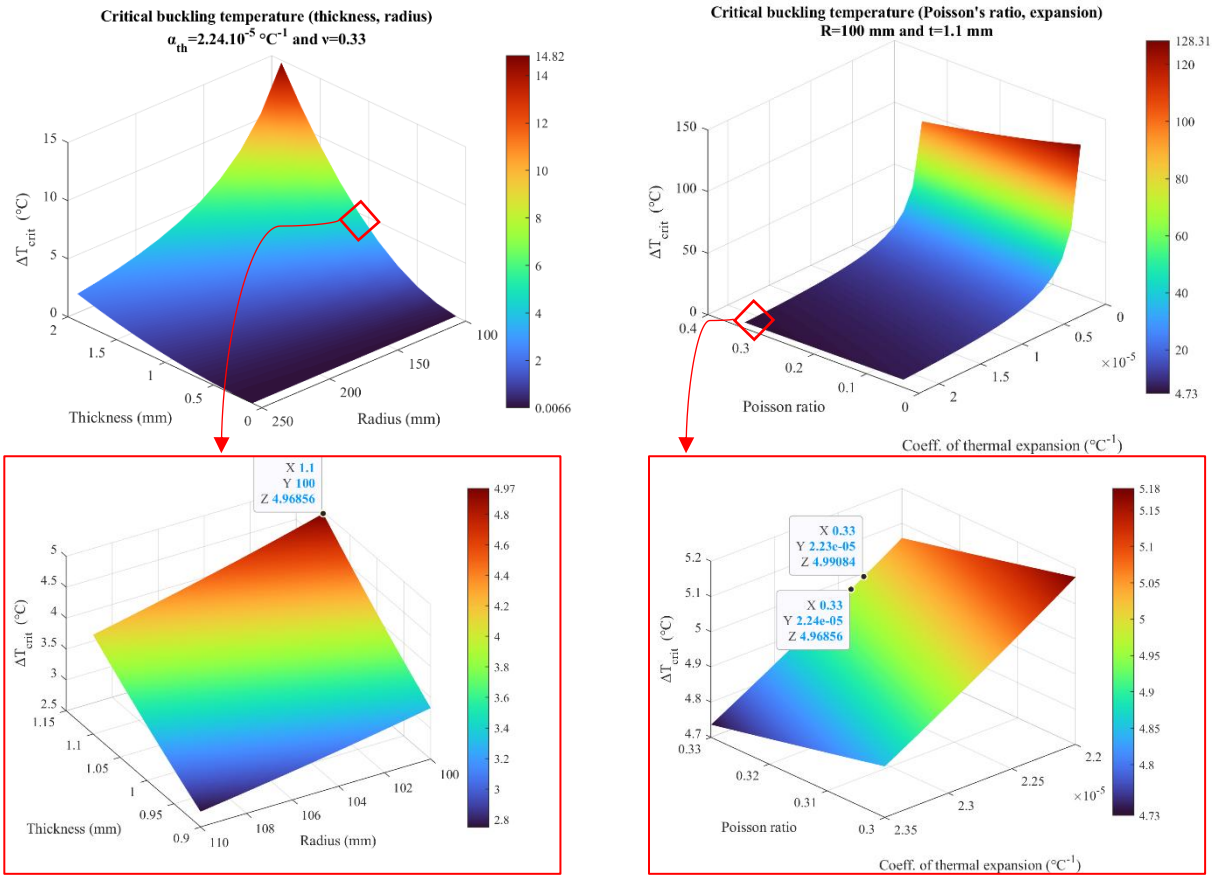

Figure 55 *3D graphs illustrating:* ***A)*** *the influence of material parameters (thickness and radius) on the critical buckling temperature, and* ***B)*** *the influence of material parameters (Poisson's ratio and coefficient of thermal expansion). The highlighted points correspond to the specific material and geometric parameters employed in the experiment.*

4.2 Numerical simulation: thermal buckling for a clamped circular plate

The numerical simulations were conducted using ABAQUS software [99]. The initial simulations focused on the analysis of buckling and had two objectives: the first one was to compare the critical temperature results of the simulation for the first natural mode with the analytically obtained results; the second objective was to predict the shapes of the buckling modes that the clamped circular aluminum plate possesses. This analysis will also be important for post-buckling analyzes, as analytically, it is expected that the critical temperature variations will be very small compared to the temperature range to which the plate will be exposed (from ambient temperature to 180°C). To obtain the eigen modes, it was opted for the Subspace method on ABAQUS, as it may be faster than the Lanczos method when fewer than 20 Eigen modes are required [99]. The number of Eigenvalues needed depends on the structure's complexity and desired level of accuracy, but in the studied case, focus is given on the first four Eigen modes of the plate. For a clamped circular plate with a radius of 100 mm and thickness of 1.1 mm, this quantity of eigenvalues suffices to capture the dominant post-buckling response. Given that axisymmetric structures subjected to compressive loading can fail in non-axisymmetric modes, it was critical to perform the analysis with the complete geometry [99]. Furthermore, dealing with a clamped circular plate that has a small thickness compared to the other dimensions, a deformable planar shell model was chosen.

The mechanical and thermal properties of EN AW 6016-T4 and EN AW 6056-T4 used in this study were consistent with those outlined in Chapter 2, for the 3-month aging condition (when both aluminum alloys exhibit lower values of Young's Modulus and elastic limit, hence the more critical case). The Poisson's ratio value was set at 0.33, and the material density was 2.7×10^{-9} ton/mm^3, and these values were applied to both materials. Once these properties were set to the model, the clamped boundary conditions were subsequently applied. It is important to note that the problem involves analyzing proper buckling modes, meaning that the model has a stiffness matrix, and the focus is on finding disturbance values (loads) that cause this matrix to become singular. From a mathematical perspective, utilizing the notation outlined in the ABAQUS User Guide, the software aims to determine the outcomes of the subsequent equation:

$$K^{MN} v^M = 0 \quad (71)$$

Where K^{MN} is the tangent stiffness matrix when the loads are applied, and the v^M are nontrivial displacement solutions.

Developing equation (71) leads to:

$$({K_0}^{NM} + \lambda_i {K_\Delta}^{NM})\, {v_i}^M = 0 \quad (72)$$

Where ${K_0}^{NM}$ is the stiffness matrix corresponding to the base state, which includes the effects of the preloads, λ_i are the load multipliers, also called eigenvalues (for this reason the

magnitude of the load is not important, as it will be multiplied by this factor until reaching the solutions of the equation), $K_\Delta{}^{NM}$ is the differential initial stress and load stiffness matrix due to the incremental loading pattern, $v_i{}^M$ are the buckling mode shapes (eigenvectors), $N\ and\ M$ refer to degrees of freedom M and N of the whole model and i refers to the ith buckling mode. If the preloads are denoted as P^N and the incremental loading pattern Q^N, the critical buckling loads are then $P^N + \lambda_i Q^N$. This justifies the fact that for eigen mode analysis there needs to be a disturbance load in the model [99].

In the case of the studied model, it is important to understand that the disturbance load will be the temperature variation that will cause a thermal expansion or contraction of the material. To facilitate the calculations, an initial temperature of 0°C is chosen for the model, and a temperature range of +1°C is applied. Thus, the results of the eigenvalues given by the simulation will be the buckling temperatures of each mode.

In order to determine the necessary mesh resolution for obtaining a precise and reliable solution, a mesh convergence study was performed, with results shown in table 9 and figure 56 - A. It was observed that a mesh with 1501 elements (figure 56 – B) yields a solution that converges to the numerically obtained critical temperature value. Therefore, all results for the analyzed circular plate will be obtained using this element quantity. Figure 57 presents the simulation results of some eigen modes for the full-geometry model, employing a S4 mesh, which means 4-node stress-displacement shell elements endowed with large-strain formulation.

Table 9 *Mesh convergence study for buckle simulation.*

EN AW 6016-T4		**EN AW 6056-T4**	
Number of elements	**Critical temperature – 1st mode (°C)**	**Number of elements**	**Critical temperature – 1st mode (°C)**
156	5.15	**156**	5.17
356	5.12	**356**	5.14
1501	5.09	**1501**	5.11
3884	5.09	**3884**	5.11

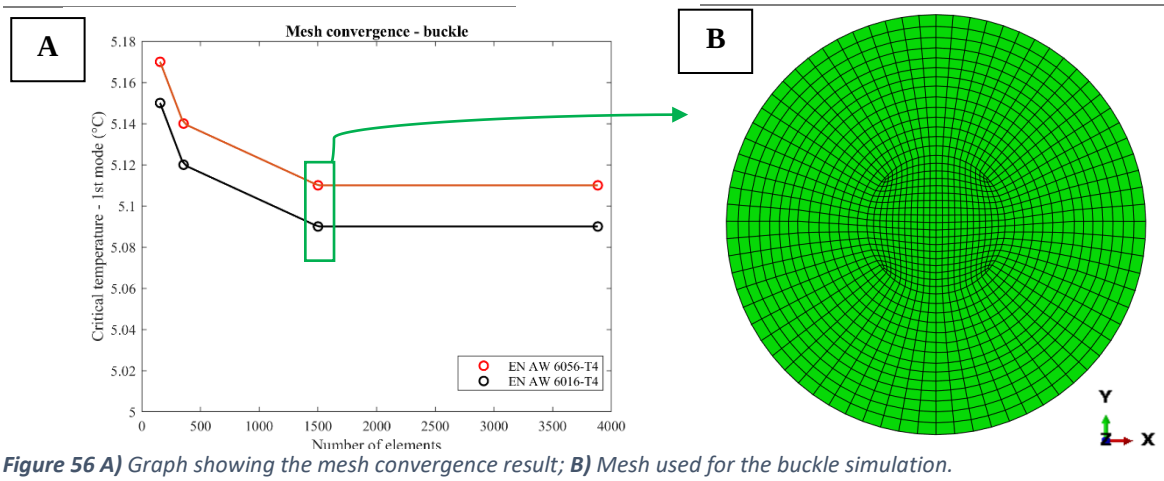

Figure 56 A) *Graph showing the mesh convergence result;* ***B)*** *Mesh used for the buckle simulation.*

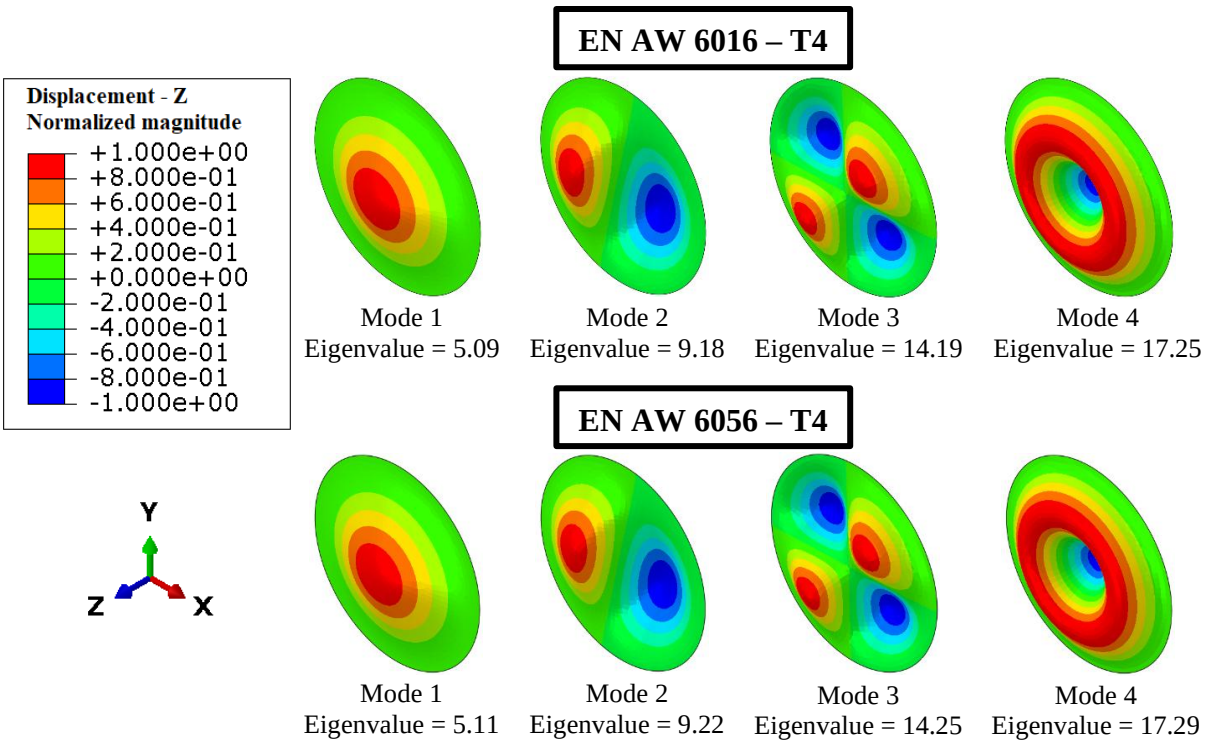

Figure 57 *Buckling mode shapes represented through normalized vectors, so that the maximum displacement component has a magnitude of 1.0.*

4.3 Experimental analysis of the post-buckling of a clamped circular plate

As mentioned in Chapter 1, under industrial conditions in the automotive industry, structures are subjected to temperatures much higher (180°C) than the analytically and numerically determined critical temperatures for reaching the first mode of buckling. Consequently, a post-buckling analysis becomes necessary. However, performing these calculations is challenging due to the involvement of complex equations and interdependencies of variables, which require significant time and assumptions to simplify and solve the equations. Furthermore, the thermomechanical properties of the materials analyzed change with temperature, resulting in different material properties at each temperature. These complexities make numerical methods, such as finite element simulation, the most suitable approach for post-buckling analysis.

Therefore, it is essential to validate the developed numerical model through experimental analyzes. This assessment helps in evaluating the reliability of the numerical simulation compared to real-world observations. To accomplish this, a round support device made of steel (figure 58) was designed. This device enables the study of post-buckling behavior in circular structures composed of EN AW 6016-T4 and EN AW 6056-T4 aluminum alloys.

By conducting experimental tests using this support device, insights into the accuracy and effectiveness of the numerical simulation method can be gained.

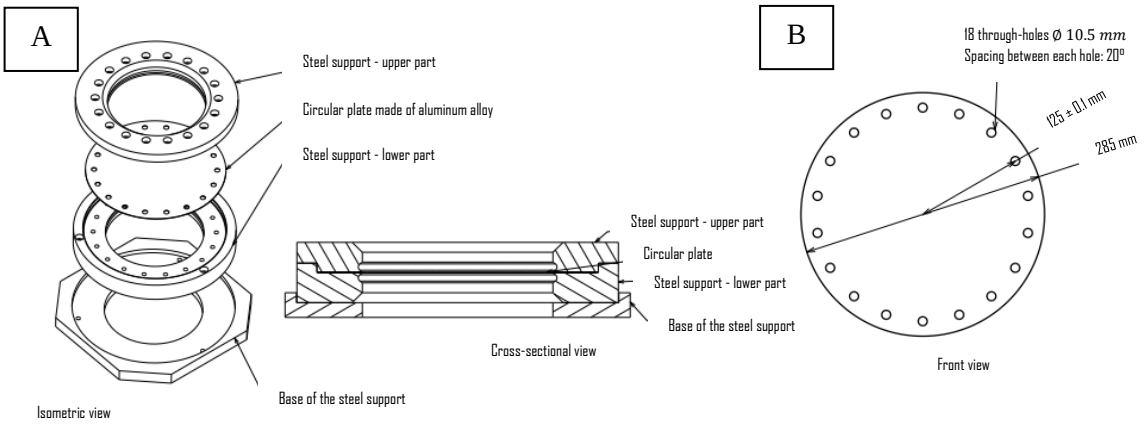

Figure 58 A) *Support;* ***B)*** *Geometry of the tested aluminum alloy plates.*

As the aluminum alloy plates had a diameter of 285 mm (figure 58 - B), it was necessary to conduct the tests in an oven that could accommodate the dimensions of the plate and the support. However, since the oven is enclosed and has an optical glass with dimensions smaller than the plate diameter, a line passing through the center of the plate was drawn, and thin markers were placed at five points along this line along with three type K temperature sensors, as shown in figures 59 – A and B. As depicted in figure 59 – B, the study zone measures 200 mm in diameter. This area extends from the steel support's fixed end to the aluminum plate. It is the region of interest for the analysis and the geometry that will be utilized later for numerical simulation purposes. Temperature measurements were taken simultaneously every two seconds. The temperature results obtained by the temperature sensors for the tests conducted with EN AW 6016-T4 and EN AW 6056-T4 are shown in figures 60 - A and B, respectively.

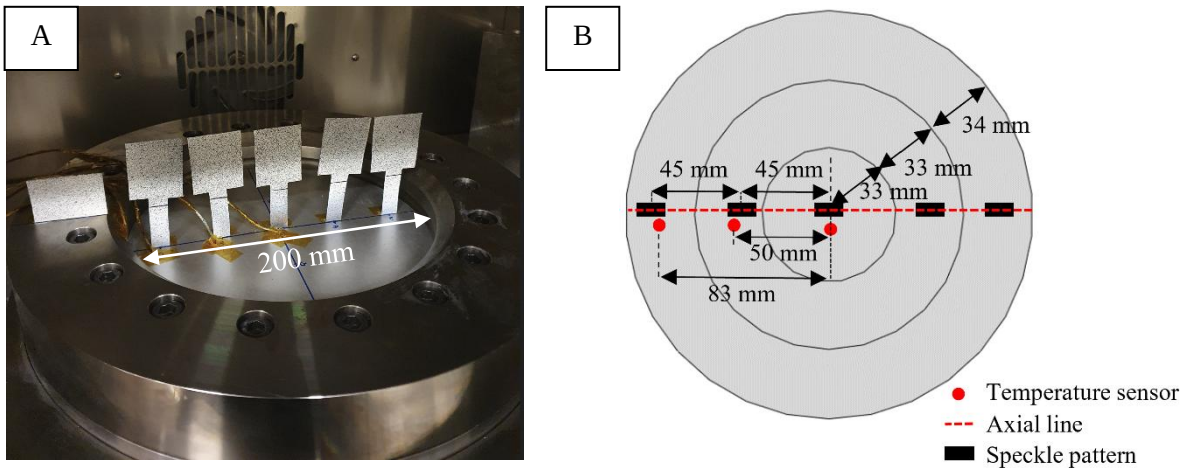

Figure 59 A) *Assembly with markers on tested plate;* ***B)*** *Arrangement of markers and temperature sensors distributed on the tested plate.*

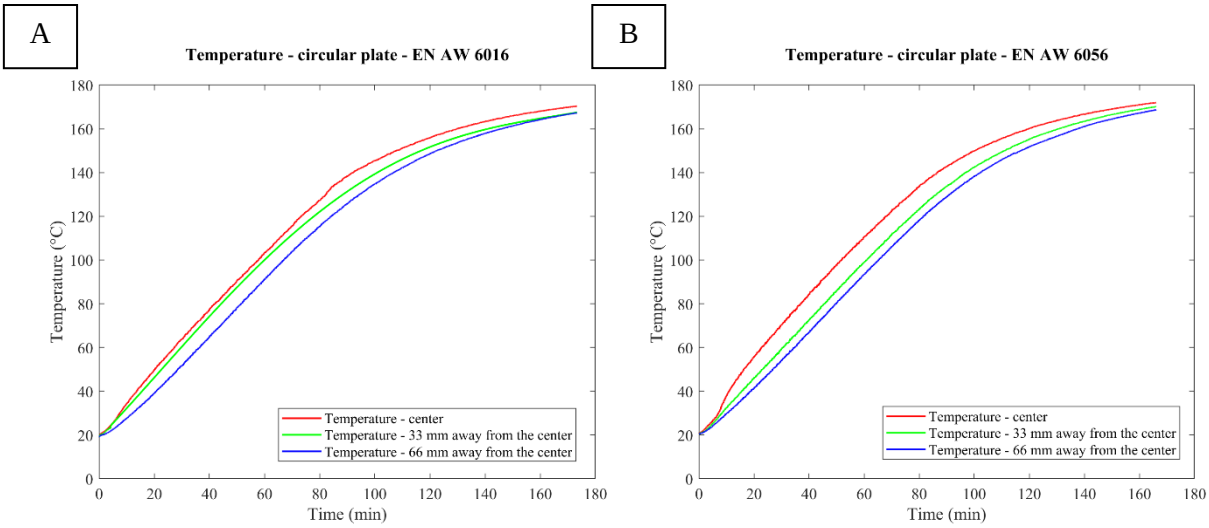

Figure 60 *Temperatures obtained by the sensors for the test with the circular plate made of materials* ***A)*** *EN AW 6016-T4 and* ***B)*** *EN AW 6056-T4.*

Then, the assembly is subjected to heating in an oven, and the vertical displacement of the speckle patterns, and consequently, the displacements of the tested plate, are measured using Digital Image Correlation (DIC) with the GOM Correlate Pro software. Images for analysis were captured every ten seconds. Due to the significant thermal inertia of the support compared to the tested plate, measuring the temperature of the support becomes challenging.

Therefore, to eliminate the thermal expansion effects of the markers and the support, a marker was fixed on the steel support (pattern number 6 in figures 61 - A and B). This allows access to the horizontal displacement of the support, which will be used as a boundary condition in the post-buckling simulation in the next section. The results of the vertical displacement values for each pattern are shown in figure 62 - A (for the circular plate made of EN AW 6016-T4) and figure 62 - B (for the circular plate made of EN AW 6056-T4).

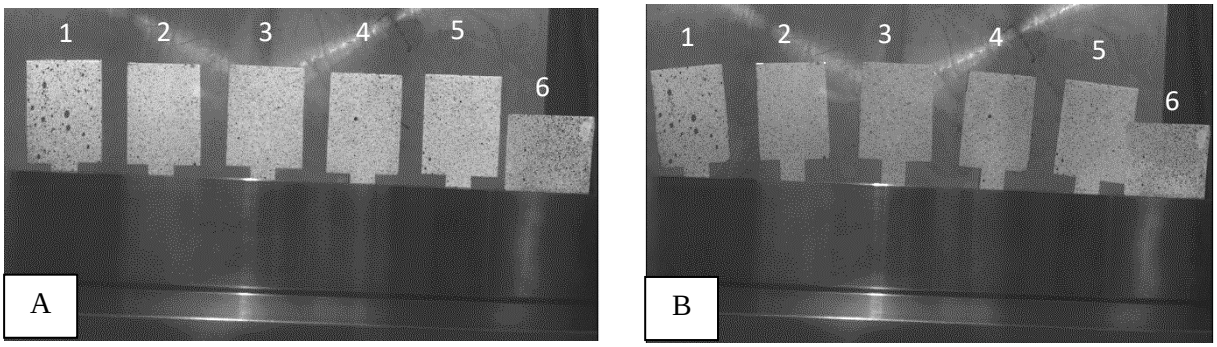

Figure 61 *Photos and nomenclature of the markers on the circular plate. Photo* ***A)*** *was taken before the start of the heating test and photo* ***B)*** *was taken when the oven temperature reached 180 ° C*

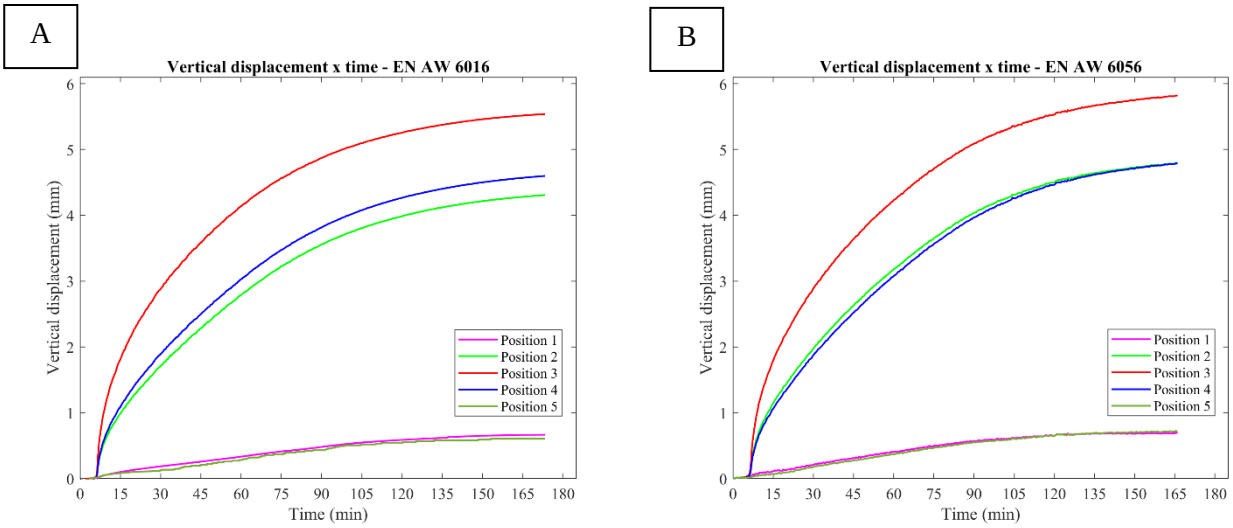

Figure 62 *Vertical displacement x time curve obtained after correction for thermal expansion of the system for circular plates made of* ***A)*** *EN AW 6016-T4 and* ***B)*** *EN AW 6056-T4.*

With these results available, progression towards conducting numerical simulations of thermal post-buckling can now be pursued. This advancement allows for comparison of the outcomes obtained from physical testing with those generated by the numerical simulation.

4.4 Numerical analysis of the post-buckling of a clamped circular plate

As previously mentioned and evident from the eigenvalue results in section 4.2, the maximum temperature to which the plate will be exposed (approximately 180°C) is significantly higher than the temperature at which the first buckling mode occurs (EN AW 6016-T4: 5.09°C / EN AW 6056-T4: 5.11°C). Consequently, a post-buckling analysis is crucial to assess the structural behavior beyond the initiation stage of buckling.

On ABAQUS, post-buckling analyzes are conducted using complementary information obtained from the buckling simulation. Since the thermal loads depicted in figure 60 – A and B are gradually applied to the structure over time without significant acceleration effects, an implicit analysis is suitable for the problem. Furthermore, as deformations during post-buckling are not proportional to the applied loads, geometric nonlinearity was incorporated in the simulation. Hence, the importance of material property analyzes conducted with respect to temperature in Chapter 2.

There are several numerical methods available for simulating the post-buckling behavior of structures. Two commonly used approaches involve applying a load to trigger the activation of buckling modes [100] or imposing displacements at specific locations on the structure [101]. In this dissertation, a different strategy has been adopted where the shapes of

the buckling modes are utilized as geometric imperfections within the model. The reason for this choice is that in real-world scenarios, engineering structural elements inherently possess initial geometric imperfections. Therefore, in the buckling simulation conducted using the complete geometry, interest lies in utilizing the shapes of the buckling modes as data for the subsequent post-buckling analysis.

On ABAQUS, the imperfection takes the form of:

$$\Delta x_i = \sum_{i=1}^{M} w_i . \phi_i \qquad (73)$$

Where ϕ_i represents the ith mode shape and w_i is the associated scale factor, M is the number of selected buckling modes to be considered in the post-buckling analysis, and Δx_i denotes the resulting imperfection value [102]. However, it is crucial to emphasize that the choice of the magnitude of imperfections has a direct impact on the structural response [103-105]. Figure 63 - B illustrates a comparison of the results obtained for the vertical displacement of the central point of the circular plate made of EN AW 6056-T4, considering various degrees of imperfection. It can be observed that, for the studied structure, an imperfection factor of up to 0.10 yields similar results to those obtained with smaller factors of imperfection. However, a significant difference in the structural response during the post-buckling condition can be observed for higher orders of imperfection factors, specifically for the case with an imperfection factor of 1 compared to the others.

To determine the appropriate imperfection factor for the circular plate, an analysis of the plate's imperfection was conducted using a dial gauge (figure 63 - A), resulting in imperfections on the order of 0.01 mm. With the identified imperfection factor, it is possible to numerically plot displacement curves over time, as shown in figures 64 - A and 64 - B.

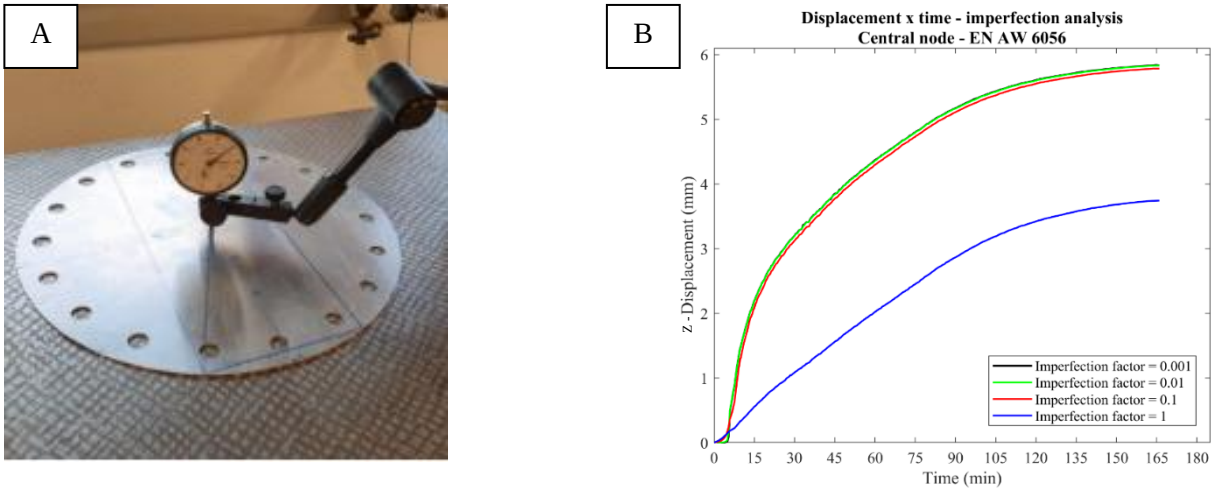

Figure 63 A) *Measurement of the structure using a dial gauge was conducted to verify the order of magnitude of imperfections, resulting in imperfections on the order of 0.01 mm;* ***B)*** *Vertical displacement-time curve obtained through post-buckling numerical analysis of the central point of the circular plate made of EN AW 6056-T4 with different imperfection factors.*

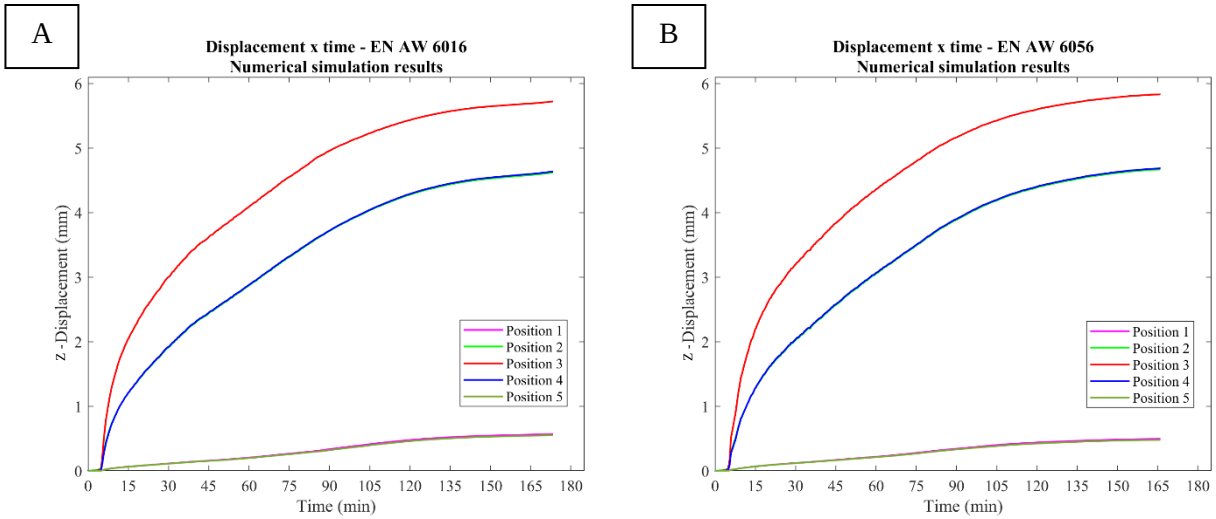

Figure 64 *Vertical displacement-time curves obtained through post-buckling analysis for the circular plate made of* ***A)*** *EN AW 6016-T4 and* ***B)*** *EN AW 6056-T4*

4.5 Results and discussions

Following the acquisition of the displacement-time curves, it is viable to establish a correlation between this data and the temperature information over time, thereby generating displacement-temperature graphs. These graphs facilitate the identification of critical buckling temperatures, both in experimentally studied cases and numerical analyses.

The determination of the critical buckling temperature typically involves identifying an abrupt change in the curvature of the displacement response curve concerning the applied load. However, the precise definition of this point is subjective in some cases due to the influence of geometric nonlinearity and the introduced imperfections within the model. To address this problem, the method proposed by M. Shariyat [106] was employed, which utilizes the bisector of the pre- and post-slopes within the region of significant slope change to locate the buckling point. Given that the displacement is most prominent at the central point of the plate, the analysis was focused on this specific location for the buckling temperature evaluation.

Applying this method resulted in buckling temperatures of 26.8°C for the EN AW 6016-T4 test and 25.2°C for the numerical simulation of this material, as depicted in figures 65 – A and B and table 10. For EN AW 6056-T4, the experimental test resulted in a buckling temperature of 27.5°C, while the numerical simulation yielded a value of 26.4°C.

Notably, the experimentally derived buckling temperatures slightly exceeded those obtained numerically and analytically. This disparity can be attributed to slight inherent imperfections resulting from the manufacturing process of both the circular plate and the

support. These imperfections lead to minor initial gaps, inducing slight variations in boundary conditions compared to the idealized conditions assumed in the numerical model.

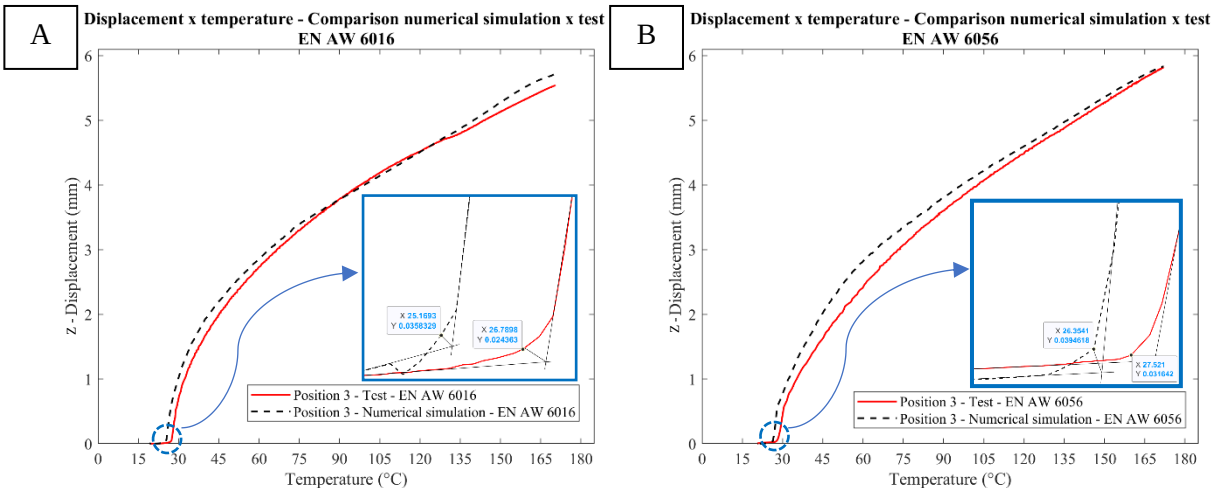

Figure 65 *Comparison between the vertical displacement-time curves obtained through tests and post-buckling numerical analysis of the central point of the circular plate made of* ***A)*** *EN AW 6016-T4 and* ***B)*** *EN AW 6056-T4.*

Table 10 *The results of the critical buckling temperatures obtained through tests ($T_{crit_{test}}$), analytical calculations ($T_{crit_{theory}}$), and numerical simulations ($T_{crit_{sim}}$) are presented. The errors between the cases are represented by T_{error}.*

Material	$T_{crit_{test}}$ (°C)	$T_{crit_{theory}}$ (°C)	$T_{error_{test-theory}}$	$T_{crit_{sim}}$ (°C)	$T_{error_{test-sim}}$
EN AW 6016-T4	26.8	24.3	10.3%	25.2	6.3%
EN AW 6056-T4	27.5	25.6	7.4%	26.4	4.2%

Comparing the critical temperatures obtained from the tests and numerical results with those derived analytically, lower theoretical critical temperatures were observed (24.3°C for EN AW 6016-T4 and 25.6°C for EN AW 6056-T4). This small discrepancy primarily arises from the non-homogeneous temperature distribution within the tested aluminum plate and the thermal expansion of the steel support, factors not accounted for in the analytical calculations, but taken into account in the numerical simulations. Given the satisfactory correlation between the results from the tests and numerical analyses concerning displacement, reliance will now be placed on the numerical model to analyze the structural behavior. Figures 66 and 67 present the results of the numerical analyses for transverse displacements, plastic deformation, and compressive stresses in the plates. The displacement in the Z-direction follows the pattern of the first buckling mode, indicating that the other modes do not significantly influence the displacement of the plate after it has buckled in the first mode.

By analyzing the maximum principal plastic deformation, it is evident that both circular plates buckle within the elastic range and do not reach the plastic deformation stage. However, towards the end of the heating cycle, at the maximum temperatures, plastic deformation becomes noticeable. The circular plate made of EN AW 6016-T4 exhibits a maximum plastic deformation of 3.0E-3, while the circular plate made of EN AW 6056-T4 has a plastic deformation nearly half that value, measuring 1.6E-3. This difference can be primarily

attributed to the higher yield strength of EN AW 6056-T4 compared to EN AW 6016-T4 (198.79 MPa versus 131.21 MPa at a temperature of 180°C, as presented in Chapter 2). This indicates that, during a potential cooling phase, the circular plate made of EN AW 6056-T4 has a greater chance of returning closer to its original shape.

The higher yield strength of EN AW 6056-T4 allows it to withstand higher levels of stress and deformations before permanent plastic deformation occurs. Consequently, it exhibits a more resilient behavior, potentially recovering more effectively upon cooling. Understanding the differential plastic deformation behavior between the two materials provides valuable insights into their respective performance under thermal loading. This knowledge can inform material selection, and potential mitigation strategies to ensure structural integrity and resilience in practical applications.

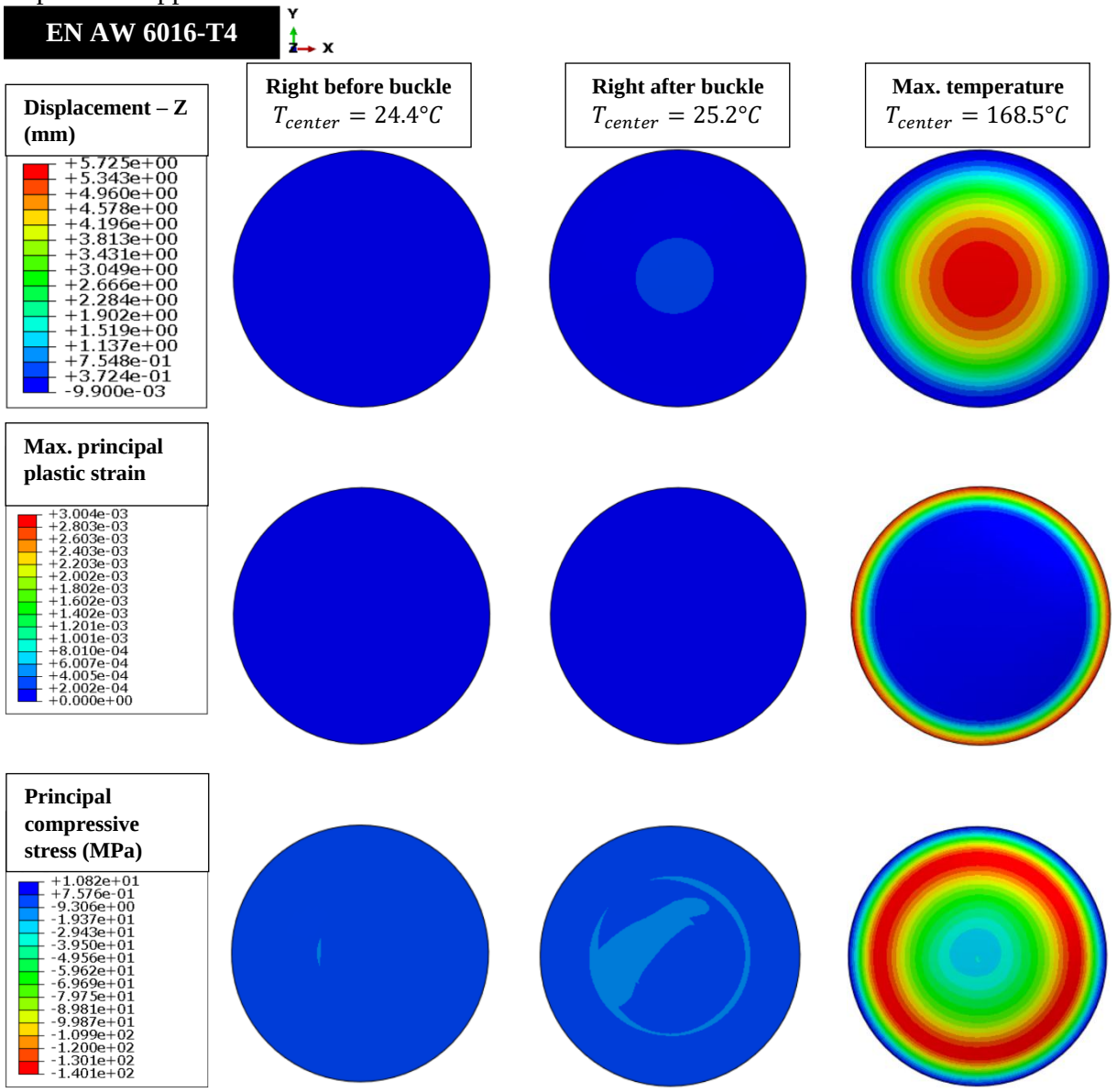

Figure 66 *Results of the post-buckling numerical analysis for the circular plate made of EN AW 6016-T4.*

The analysis of compressive stresses in the principal direction reveals that the circular plate made of EN AW 6056-T4 experiences higher compressive stresses (with a maximum value of -173.2 MPa) compared to the compressive stresses generated in the EN AW 6016-T4 plate (with a maximum value of -140.1 MPa). This difference can be attributed to the disparity in Young's modulus between the two materials at high temperatures, which directly affects the stress values (51.11 GPa for EN AW 6016-T4 and 59.78 GPa for EN AW 6056-T4 at 180°C).

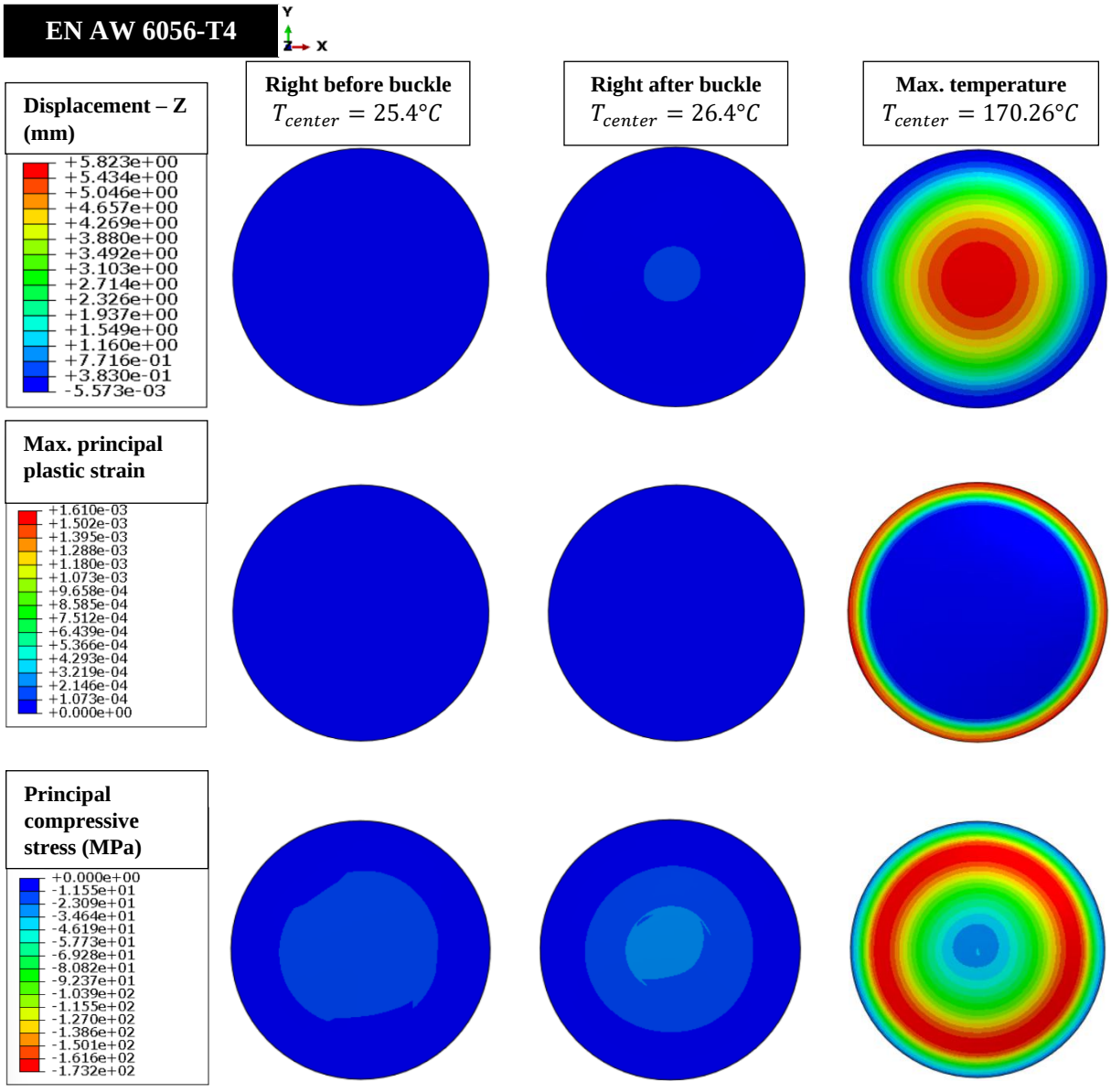

Figure 67 *The results of the post-buckling numerical analysis for the circular plate made of EN AW 6056-T4.*

4.6 Conclusion

This study investigated a case of thermal buckling in a circular plate made from two aluminum alloys, EN AW 6016-T4 and EN AW 6056-T4, clamped within a steel support. The research comprehensively explored the influence of material and geometric parameters on the critical buckling temperature. Through this investigation, the study highlighted the importance of considering thermal buckling phenomena in practical applications. The decision to initially focus on the circular plate was based on its simple and symmetrical geometry, which facilitated both theoretical and numerical analyses of the phenomenon. Moreover, the scenario of the clamped circular plate provided a robust framework for juxtaposing theoretical and numerical outcomes against well-established analytical solutions, thereby enabling the validation of numerically employed analytical methods.

In the analysis of the critical temperature for thermal buckling, several factors are considered, including material properties and geometric parameters. Material properties such as the thermal expansion coefficient, Poisson's ratio, and Young's modulus are crucial, as they directly influence how a material responds to thermal loads. Additionally, geometric parameters such as radius, thickness, and imperfections play a significant role. It is evident that the radius and thickness of the material are particularly influential parameters in determining the critical temperature. This is because they have a power of two in the equation governing thermal buckling, indicating a nonlinear relationship with the critical temperature. Therefore, small changes in radius or thickness can lead to significant variations in the critical temperature. Furthermore, since imperfections are related to the initial geometry of the structure, depending on their magnitude, they can either accelerate or delay the onset of thermal buckling. For the analysis of the circular plates, the measured imperfection was 0.01 mm.

As a result of this preliminary approach, it was observed that for an effective circular zone with a 200 mm diameter, the required temperature variations to reach critical buckling temperatures were relatively modest, approximately 5-6°C above room temperature. Moreover, consistent with previous findings, the difference in critical temperature between two materials with identical geometric configurations was at most 1.3°C in theoretical calculations. This disparity arose from comparing analytically obtained critical temperatures, revealing that the circular plate composed of EN AW 6016-T4 experienced buckling before its EN AW 6056-T4 counterpart. This slight variation can be attributed to the marginally higher thermal expansion coefficient of EN AW 6016-T4 in comparison to EN AW 6056-T4. Furthermore, the difference was even smaller (0.7°C) when comparing critical temperatures obtained from tests, with EN AW 6016-T4 buckling at 26.8°C compared to 27.5°C for EN AW 6056-T4 (due to non-homogenous temperature distribution in the device).

However, despite the similar buckling temperatures of the two materials, the analysis of plastic deformation revealed distinct characteristics between the EN AW 6016-T4 and EN AW

6056-T4 alloys. The circular plate made of EN AW 6016-T4 exhibited a maximum plastic deformation of 3.0E-3, nearly twice that of the EN AW 6056-T4 plate (1.6E-3). This discrepancy indicated the superior resilience of the EN AW 6056-T4 alloy, suggesting its potential for more effective recovery under cooling conditions. Furthermore, the analysis of the plate displacements highlighted that the displacement in the Z-direction predominantly followed the pattern of the first buckling mode , characterized by the formation of an axially symmetric bump at the center of the plate. The absence of significant influence from other modes emphasized the dominance of the first mode in determining the post-buckling displacement behavior.

The analysis of compressive stresses in the principal direction revealed significantly higher stress levels in the circular plate made of EN AW 6056-T4, with a recorded value of -173.2 MPa, compared to -140.1 MPa experienced by the plate made of EN AW 6016-T4. This increase in compressive stresses can be attributed to the higher Young's modulus of the EN AW 6056-T4 alloy. This suggests that the EN AW 6056-T4 alloy may offer superior structural rigidity and load-bearing capacity compared to EN AW 6016-T4.

Overall, the numerical analysis, incorporating thermal implicit analysis, geometric nonlinearity, 4-node stress-displacement shell elements endowed with large-strain formulation, and temperature-dependent material properties, proved to be a valuable tool for studying thermal buckling behavior. The strong correlation between the numerical model and physical tests was evidenced by low errors of 6.3% for the critical temperature of the EN AW 6016-T4 circular plate and 4.2% for the EN AW 6016-T4 circular plate. These findings provide essential insights for design considerations, material selection, and structural optimization to ensure the stability, and reliable performance of circular plates subjected to thermal loading conditions.

5. Investigation of thermal buckling behavior in the context of differential expansion

The observations and findings derived from the study of the circular plate case have played a crucial role in obtaining relevant conclusions regarding the phenomenon of thermal buckling. Additionally, they have contributed to the selection of an appropriate numerical approach to the problem, based on analytical calculations and experimental test results. These conclusions have demonstrated that the use of implicit numerical simulations, taking into consideration the geometric nonlinearity of the structure, yield satisfactory results in predicting this phenomenon in slow heating situations, particularly in cases involving thin geometries.

Given the considerably greater complexity and dimensions of the vehicle structure under investigation compared to the laboratory-analyzed case, an additional analysis has been deemed necessary. This comprehensive analysis entails a thorough modification of the geometry and boundary conditions to shed light on the critical importance of boundary conditions in the structural response to thermal buckling phenomena. Furthermore, it aims to empirically demonstrate the effects of differential expansion, which is an inherently crucial component of the problem. The importance of this analysis stems from the fact that, in the case of the circular plate fixed at the extremities, the steel support exhibited significantly higher thermal inertia and rigidity than the thin aluminum plate under study. This discrepancy made it challenging to fully comprehend the intricate nature of the differential expansion phenomenon. Thus, the supplementary analysis seeks to address this limitation by providing a more comprehensive understanding of the complex interaction between the materials and their response to differential expansion.

Moreover, the primary objective is to evaluate the ongoing reliability of the simulation in the face of a geometry alteration that closely resembles the actual configuration of the vehicle's roof. Simultaneously, this assessment considers boundary conditions that better represent the seamless integration of the roof into the body structure. By doing so, the analysis aims to provide a more realistic and reliable representation of the structural behavior under thermal buckling conditions, enhancing the overall understanding and predictive capabilities of the numerical simulation in real-world scenarios.

5.1 Impact of boundary conditions on buckling: bar case

To commence the investigation, the study delves into a compelling yet straightforward case study that aims to accentuate the profound influence of boundary conditions on the buckling phenomenon. Specifically, the behavior of a bar subjected to three distinct boundary conditions is explored. In each scenario, a force of intensity P will be applied at one end of the bar, serving as the primary loading condition.

The first case involves the bar being fixed at one end while the other end remains free to move. The second case entails the bar being hinged at both ends, allowing for rotational freedom. Lastly, the third case examines a bar that is firmly fixed at both ends, effectively eliminating any translational or rotational motion. Detailed representations of these three cases are provided in figure 68 - A, B, and C, respectively.

It is worth noting that these cases have already been extensively studied by Euler [107] and Timoshenko [108]. Consequently, the focus will primarily be on a succinct deduction of the critical buckling load equations within the elastic domain.

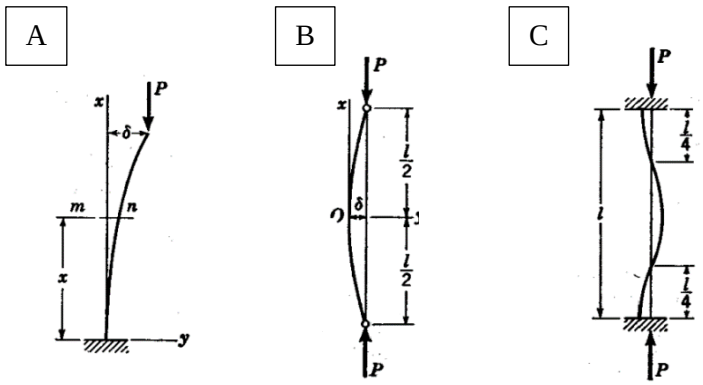

Figure 68 *Force of intensity P applied to create a buckling situation in three different cases:* ***A)*** *A bar fixed at one end while the other end remains free;* ***B)*** *A bar being hinged at both ends;* ***C)*** *A bar fixed at both ends. [102]*

Considering the behavior of an ideal column, assumed initially to be perfectly straight and compressed by a centrally applied load, the critical load for a compressed bar is of interest. Consider the first case shown in figure 68 - A. Assuming the column is perfectly elastic and subjected to stresses below its proportional limit, if the applied load P is below a critical value, the bar remains straight and experiences only axial compression. This straight form of elastic equilibrium is stable, meaning that any small deflection caused by a lateral force will disappear when the force is removed, and the bar returns to its original straight shape. As P is gradually increased, a point is reached where the straight equilibrium becomes unstable, making the system deviate from its current state in response to small perturbations, potentially leading to a new state or behavior. This critical load, also known as the Euler load, is the axial force required to maintain the bar in a slightly bent state. The critical load can be determined by solving the differential equation of the deflection curve. In figure 68 - A, assuming the coordinate axes as indicated and the column in a slightly deflected position, the bending moment M at any cross-section "mn" is:

$$M = -P.(\delta - y) \quad (74)$$

And with the differential equation for the curvature of the axis of the bar being $E.I\frac{d^2y}{dx^2} = -M$, it is possible to arrive at

$$E.I\frac{d^2y}{dx^2} = P.(\delta - y) \quad (75)$$

Where:

$E.I$ = Flexural rigidity

I = Moment of inertia of a plane area in respect to z axis

E = Modulus of elasticity

δ = deflection

Given that the upper end of the column is free, it becomes evident that buckling of the bar will transpire in the plane that possesses the minimum flexural rigidity. In the analysis, the plane is assumed to be a plane of symmetry. Then, the following considerations are made:

$$(76) \quad k^2 = \frac{P}{E.I}$$

Thus, it is observed that the equation (75) takes the following form:

$$(77) \quad \frac{d^2y}{dx^2} + k^2 y = k^2.\delta$$

Which possesses a general solution of the form:

$$(78) \quad y = A.\cos kx + B.\sin kx + \delta$$

Through the general solution of the equation and the known boundary conditions of the case illustrated in figure 68 - A, it can be concluded that:

For a clamped end condition: $y = \frac{dy}{dx} = 0$ at the position $x = 0$.

For a free end condition: $y = \delta$ at the position $x = l$, where l is the total length of the bar.

With the aforementioned conditions applied to the general solution equation (77) and utilizing the formulation of k^2 as shown in (76), the conclusion can be drawn that:

$$(79) \quad k.l = (2.n - 1).\frac{\pi}{2}$$

Where n is a positive integer. Thus, considering the expression (79), it can be observed that the smallest value of $k.l$ occurs when $n = 1$. By substituting the value of k, obtained from expression (76), into expression (79), the value of the smallest critical load for the case illustrated in figure 68 - A can be deduced as:

$$(80) \quad P_{crit} = \frac{\pi^2.E.I}{4.l^2}$$

In the situation where the bar is bi-pivoted (figure 68 - B), it is evident that each half of the bar behaves similarly to the case that was just analyzed. Therefore, resulting in $\frac{l}{2}$ instead of l in equation (80). Thus, the expression becomes:

$$(81) \quad P_{crit} = \frac{\pi^2.E.I}{l^2}$$

In the case where the bar has both ends fixed (figure 68 - C), reactive moments arise to prevent rotation of the column ends during buckling. These end moments, along with the axial compressive forces, can be considered equivalent to an eccentrically applied force P. The deflection curve intersects the line of action of P at the inflection points, where the bending moments are zero. These inflection points, along with the midpoint, divide the bar into four equal regions, each of which behaves similarly to the bar in figure 68 - A. Consequently, the

critical load for a column with fixed ends can be determined by substituting $\frac{l}{4}$ for l in equation (80), which gives:

$$(82)\quad P_{crit} = \frac{4.\pi^2.E.I}{l^2}$$

Just by analyzing these three simple cases, an important conclusion can be drawn: a particular characteristic of the buckling phenomenon is that it is highly dependent on the boundary conditions. As seen, a beam fixed at both ends will adopt a significantly different buckling geometry compared to a beam fixed at one end and free at the other. With just this difference in boundary conditions, the critical buckling load of a double-fixed beam will be eight times higher, through the use of an effective length four times shorter.

In the study of thermal buckling in elasticity, specifically in the unidirectional case, it is indeed possible to relate the critical load to the critical temperature variation, ΔT_{crit} , under the assumptions that the bar is constrained from expanding axially, which means that the thermal strain induces mechanical stresses within the bar. Thus, the mechanical deformation of the bar is solely due to thermal expansion. In this scenario, it can be assumed that the mechanical strain ε_{mec} is identical to the thermal strain ε_{th} in the critical buckling condition.

$$(83)\quad \varepsilon_{mec} = \varepsilon_{th}$$

$$(84)\quad \Delta T_{crit} = \frac{P_{crit}}{E.S.\alpha_{th}} = \frac{\pi^2.I}{l_{eff}^2.S.\alpha_{th}}$$

Where:

l_{eff} = Effective length

S = Cross-sectional area

α_{th} = linear thermal expansion coefficient

5.2 Analysis of thermal expansion and thermal buckling: thermal buckling of a beam subjected to imposed displacement

Now that a clear relationship between the critical temperature variation and the different boundary conditions for a bar has been established, it is time to delve further into the concept of thermal buckling associated with an imposed displacement within the context of beam analysis previously studied. As stated before in this dissertation, the research focus lies on a scenario where the roof panel undergoes expansion but is constrained by the thermal expansion of the predominantly steel body-in-white, a material with a lower coefficient of expansion compared to aluminum alloys. This results in compression of the aluminum roof panel by the steel body-in-white. However, the phenomenon of differential thermal buckling holds greater significance for the problem than simple buckling. Specifically, if the body-in-white expands in the same direction as the roof, it reduces the stress exerted on the latter. Thus, the objective

is to determine the extent to which it is possible to leverage this differential expansion phenomenon to mitigate buckling in the structure that is more prone to such instability.

In this section, the analysis of the clamped bar problem is extended by introducing mechanical loading in addition to the thermal load. A beam subjected to both thermal loading, which generates compressive forces dependent on the boundary conditions, and an imposed displacement ($U_{imposed}$) in tension is considered. This imposed displacement represents the displacement that the vehicle's body imposes on the roof.

When no displacement is imposed, the critical buckling temperature is equal to the critical Euler load, which can be calculated using equation (84). To analyze this problem, the beam is modeled in a 2D plane, neglecting the effects related to plasticity:

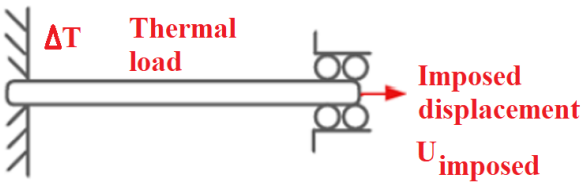

Material	*Aluminum*
Young's modulus (E)	*69.10³ MPa*
Cross-sectional area (S)	*Square :* 100 mm^2
Initial length (L_0)	*500 mm*
Moment of inertia (I_z)	833 mm^4
Expansion coefficient ($\alpha_{aluminum}$)	2.3.10^{-5} °C^{-1}

Figure 69 *Boundary conditions and characteristics of the beam studied for the model with imposed displacement.*

The selection of material and geometric parameters shown in figure 69 is purely illustrative, aimed at simplifying calculations for ease of comprehension. Analytically analyzing the problem, the critical buckling temperature obtained when no displacement is imposed equals the critical load calculated by Equation (84). However, it is possible to impose a displacement that fully compensates for buckling ($U_{imposed,crit}$). This displacement is equal to what the beam would experience if it were free at its end:

$$U_{imposed,crit} = \alpha_{alu}.L_0.\Delta T_{imposed} \quad (85)$$

Where $\Delta T_{imposed}$ represents the imposed temperature variation in the bar.

In practice, numerical analysis with ABAQUS is utilized to model the beam as a 2D "beam" element, where each finite element has two translation degrees of freedom and one rotation degree of freedom. 100 B22 elements, representing 3-node quadratic beams in a plane, are assigned. Similar to the study of the circular plate, a buckle analysis step is conducted, applying clamping at one end of the beam and imposing a displacement U at the other end, with the desired value. Additionally, a thermal loading of $\Delta T_{imposed}$ = 1°C is applied. Upon completing the calculation, a buckled appearance of the beam is observed (figure 70 - B). This

procedure is repeated for different displacement values, which are presented in table 11 and graphically represented in figure 70 - A.

Table 11 *Values of critical temperature as a function of imposed displacement*

$U_{imposed}$ (mm)	ΔT_{crit} (°C) – ABAQUS simulation	$U_{imposed}$ (mm)	ΔT_{crit} (°C) – ABAQUS simulation
0	56.99	0.007	145.63
0.0005	59.58	0.0085	218.45
0.001	62.41	0.009	262.13
0.0015	65.53	0.0095	327.67
0.002	68.98	0.01	436.89
0.0025	72.82	0.0105	655.34
0.0035	81.92	0.011	1310.70
0.0045	93.62	0.0115	$(\rightarrow +\infty)$

A

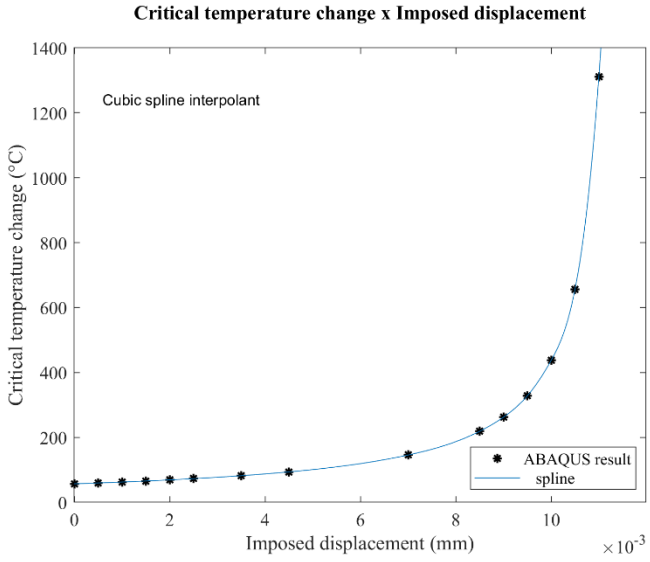

B

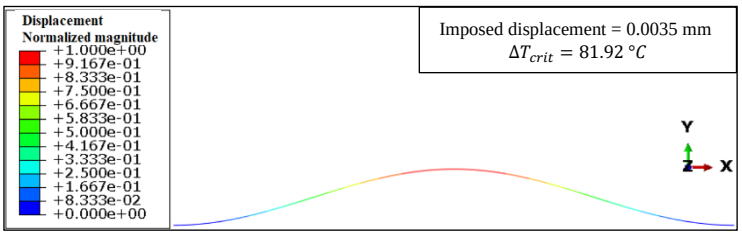

Figure 70 A) *Critical Temperature-Imposed Displacement curve for the values in Table 11;* ***B)*** *Buckled appearance of the beam with an imposed displacement of 0.0035 mm.*

Considering the trend of the obtained curve being hyperbolic, the inverse of the temperature is plotted as a function of displacement (figure 71). It is evident that the inverse of the critical buckling temperature is linearly related to the imposed displacement.

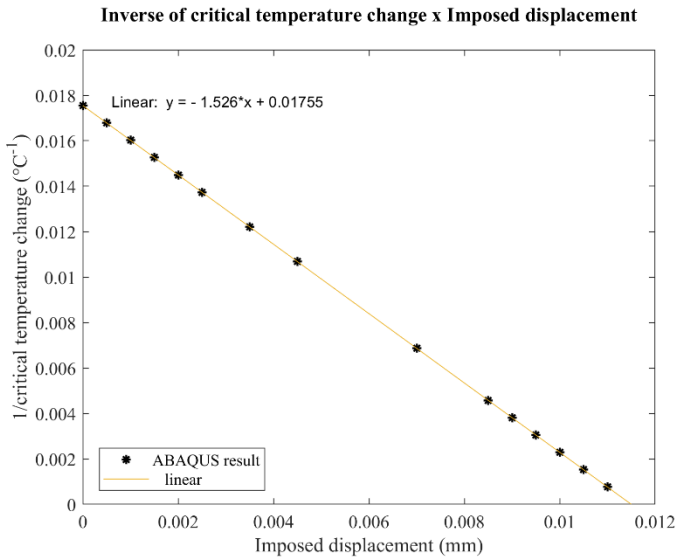

Figure 71 *Graph of the inverse of the critical temperature change as a function of the imposed displacement. The relationship between the inverse of the critical temperature and the imposed displacement is found to be linear, suggesting a proportional relationship between these two variables.*

Therefore, the parameters A and B are sought such that:

$$\Delta T_{critique} = \frac{1}{A.U_{imposed}+B}. \quad (86)$$

On one hand,

$$\frac{1}{\Delta T critique}(U_{imposed} = 0) = B = \frac{l_{eff}^2.S.\alpha_{th}}{\pi^2.I} \quad (87)$$

On the other hand:

$$\frac{1}{\Delta T critique}(U_{imposed} = U_{imposed,crit} = \alpha_{th}.L_0.\Delta T_{imposed}) = 0 \quad (88)$$

From this, it is possible to deduce:

$$A = -\frac{l_{eff}^2.S}{\pi^2.I.L_0.\Delta T_{imposed}} \quad (89)$$

Therefore, the final equation becomes:

$$\Delta T_{critique} = \frac{\pi^2.I.L_0.\Delta T_{imposed}}{l_{eff}^2.S}.\frac{1}{\alpha_{alu}.L_0.\Delta T_{imposed} - U_{imposed}} \quad (90)$$

$$\Delta T_{critique} = \frac{\pi^2.I.L_0.\Delta T_{imposed}}{l_{eff}^2.S}.\frac{1}{U_{imposed,crit} - U_{imposed}} \quad (91)$$

When the imposed temperature variation ($\Delta T_{imposed}$) is 1°C, equation (91) takes the following simplified form:

$$\Delta T_{critique} = \frac{\pi^2.I.L_0}{l_{eff}^2.S}.\frac{1}{\alpha_{alu}.L_0 - U_{imposed}} \quad (92)$$

In conclusion, the analysis of the derived equation reveals that the critical temperature change exhibits an inverse relationship with the difference between the imposed critical displacement, where buckling is fully compensated, and the imposed displacement. This relationship indicates that a greater difference between these displacements results in a smaller change in the critical temperature required to initiate the first buckling mode. Furthermore, it is notable that when the imposed displacement is zero, the equation for the critical temperature change aligns with equation (84), demonstrating consistency in the theoretical framework.

5.3 Coupling of two different materials under thermal loading

Based on the derivation of the equation enabling the calculation of the critical buckling temperature concerning an imposed displacement, attention is now directed towards the analytical and numerical correlation in a specific real-life case. The focus lies on the thermal buckling of a component made of aluminum alloy under thermal loading, where the displacement in the component is induced by the interaction between the thermal expansion of a steel DC01 structure and the thermal expansion of the aluminum alloy structure.

5.3.1 Experimental set up: rectangular plates test

For the purpose of this study, a laboratory test setup was designed and illustrated in figure 72 - A, consisting of two plates with dimensions as depicted in figure 72 - C. These plates are fixed within an aluminum device, with one end clamped and connected to the support through the use of an aluminum bracket positioned between the two plates under evaluation, while the other end remains free to move along the longitudinal direction, facilitated by ample lubrication and a clearance provided between the aluminum bracket located between the plates and the test support.

The entire structure, as illustrated in figure 72 - A, is subjected to a controlled heating process in an oven, where it is gradually heated from room temperature to 180°C. Specifically, the EN AW 6016-T4 and EN AW 6056-T4 alloys are selected as the materials for the tested aluminum plate. Similar to the previous analysis of the circular plate in this chapter, the material properties for these alloys, with three months of natural aging, as discussed in Chapter 2, are used for this test.

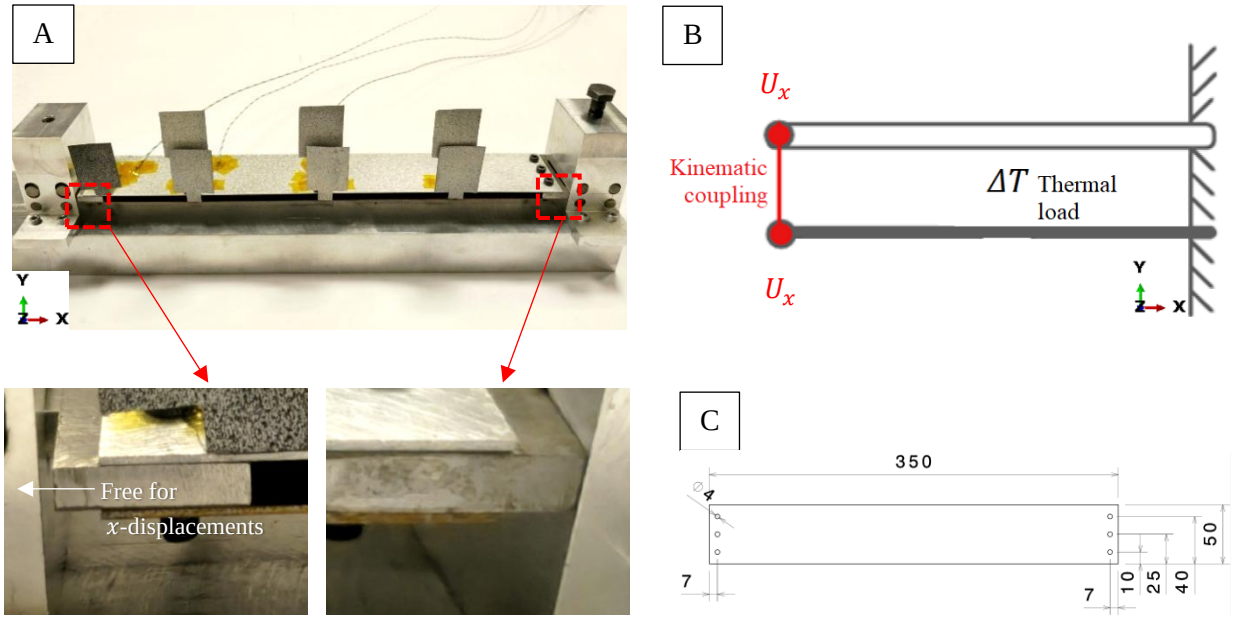

Figure 72 A) *Laboratory test setup for investigating the thermal interaction between two metal plates, where the thermal expansion of one plate influences the boundary condition of the other;* ***B)*** *Illustration of the boundary conditions of the test. One side has fixed edges, and the edges on the other side move only in the direction of the x-axis;* ***C)*** *Dimensions of the test specimen.*

5.3.2 Material analysis: steel DC01

As evident, the preceding chapter extensively delved into the intricacies of aluminum alloy properties, enabling the leverage of the acquired results as foundational input. However, this paradigm doesn't extend to the steel under examination. Specifically, DC01 steel (a variant characterized by its low carbon content and cold-rolled production method) was employed for the targeted analysis.

Consequently, tensile tests were executed adhering to the identical protocols outlined in Chapter 2, encompassing assessments at both ambient and elevated temperatures. Once more, a minimum of three valid trials were conducted to extract the material's mechanical attributes, supplemented by Digital Image Correlation (DIC) techniques to capture strain data.

In contrast to the approach with aluminum alloys, where more cases were studied in terms of temperature, the investigation of this steel only focused on two distinct thermal conditions: room temperature and 180°C. This decision was influenced by the characteristic melting range of low-carbon steels, including DC01, which typically falls between 1370°C and 1540°C. This means that at 180°C, the material behaves stably enough to not undergo significant changes in properties such as yield strength and Young's modulus, unlike what occurred with the aluminum alloys EN AW 6016-T4 and EN AW 6056-T4. The stress-strain curve for DC01 is graphically depicted in figure 73, while the quantified values for yield strength and Young's modulus are presented in table 12.

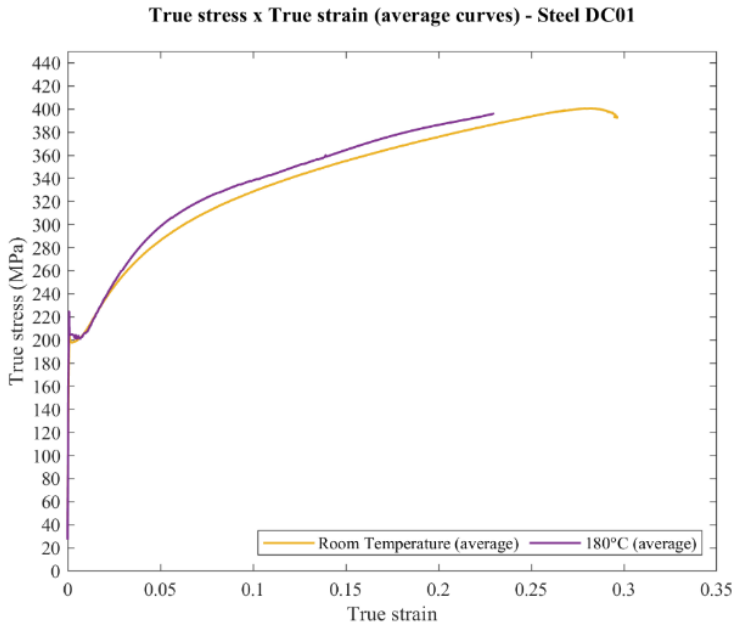

Figure 73 *Average of true stress x true strain curves of steel DC01 for two temperature situation: room temperature and at 180°C.*

Table 12 *Result of the analysis of the mechanical properties for the steel DC01.* $\overline{Rp_{0.2}}$ *is the average of the elastic limits obtained to cause 0.2% of plastic deformation;* $\sigma(\overline{Rp_{0.2}})$ *is the standard deviation of the elastic limits;* $\overline{E}$ *is the average of the Young's moduli;* $\sigma(\overline{E})$ *is the standard deviation of Young's moduli.*

Temperature (°C)	$\overline{Rp_{0.2}}$ (MPa)	$\sigma(\overline{Rp_{0.2}})$ (MPa)	$\overline{E}$ (GPa)	$\sigma(\overline{E})$ (GPa)
Room temperature	198.02	5.81	212.13	5.66
180	206.43	6.95	217.24	1.61

The acquired results reveal that the transition from room temperature to 180°C in the case studies yielded a negligible alteration in the yield strength of DC01, with a modest increment from 198 MPa to 206 MPa, denoting an increase of merely 8 MPa. A comparable trend is observed in the context of Young's modulus, with the material demonstrating 212 GPa and 217 GPa at room temperature and 180°C, respectively, manifesting a deviation of merely 5 GPa. In aggregate, the mean stress-strain profiles for the experimental scenarios at room temperature and 180°C, as depicted in figure 73, evince a striking similarity. This underscores the material's steadfastness within this temperature spectrum of assessment.

Given that the focal material of scrutiny in this dissertation is not the DC01 steel, and recognizing the established stability of material properties in steels at 180°C, alongside the extensive thermal property data repository held by Stellantis, the thermal characteristics sourced from the company's material database were deployed [109]. Hence, the following parameters were adopted: a coefficient of thermal expansion for steel ($\alpha_{th_{steel}}$) of $1.10 \cdot 10^{-5}\ °C^{-1}$, a specific heat ($Cp_{steel}$) of 0.45 $J.g^{-1}.K^{-1}$, and a thermal conductivity (λ_{steel}) of 23 $W.m^{-1}.K^{-1}$.

Subsequent to acquiring the pertinent material data for the experimental endeavor, the buckle and post-buckle analyses were executed through numerical simulations and subjected to a comparative evaluation with the empirical test outcomes.

5.3.3 Buckle and post-buckle analysis: rectangular plates

In conducting the numerical analysis for the rectangular plate test, the ABAQUS software will again be utilized, employing the identical methodologies as those applied in the simulation of the circular plate. These methods have demonstrated a commendable alignment between physical and numerical outcomes. This entails initiating the analysis with a buckle simulation, utilizing the Subspace method. In this phase, an initial perturbation load, solely thermal in nature, will be introduced, with a 1°C differential applied to the model for Eigenvalue determination. Additionally, attention will be directed towards the examination of the first four Eigen modes specific to the rectangular plates.

For the simulation, it was employed an effective length of 330 mm out of the total length of 350 mm, taking into account the edge fixations of the plate. It's worth emphasizing that given the sevenfold disparity between the width and length of the plate, the structure can be simplified akin to the previously discussed scenario of compression bars. Figure 74 provides a comprehensive view of the plate geometries, along with the positioning of temperature sensors and black-white speckle patterns.

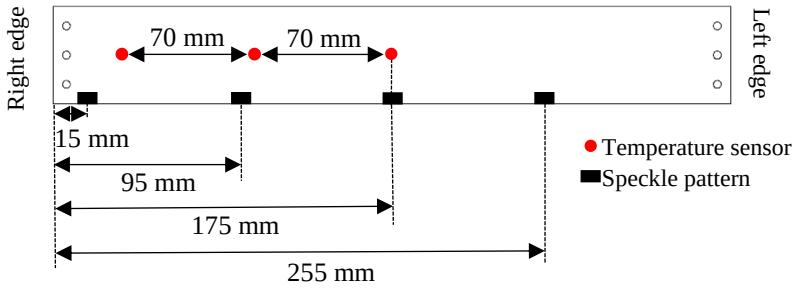

Figure 74 *Location of temperature sensors and speckle patterns along the specimen.*

However, due to the use of thermal loading, it is necessary to have elements that can establish the relationship between thermal effects and displacement. This capability is not present in bar-type elements in Abaqus, as they lack the degrees of freedom required for this coupling. Therefore, S4 elements (4-node doubly curved general-purpose shell, finite membrane strains) were selected for the temperature-displacement simulation, with only one element across the width of the plate. The boundary conditions applied in the numerical model are depicted in figure 75.

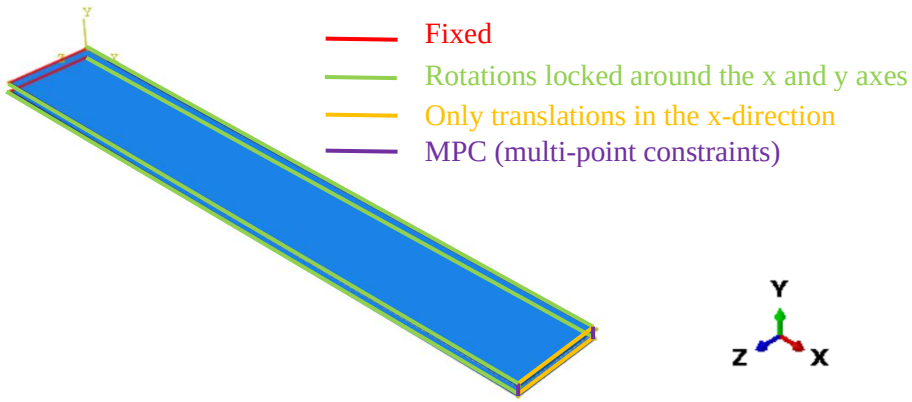

Figure 75 *Boundary conditions applied in the simulation of the test with the two plates.*

After conducting the mesh convergence study, similar to what was demonstrated for the circular plate case, it was concluded that a total of 80 elements along the length of the plate were sufficient, as depicted in figure 76 and table 13. Figure 77 presents the simulation results of the first four eigenmodes for the full-geometry model.

Table 13 *Mesh convergence study for buckle simulation.*

EN AW 6016-T4	
Number of elements	**Critical temperature (°C) – 1st mode**
10	5.07
20	4.87
40	4.84
80	4.83
160	4.83

EN AW 6056-T4	
Number of elements	**Critical temperature (°C) – 1st mode**
10	5.23
20	5.02
40	4.99
80	4.98
160	4.98

A

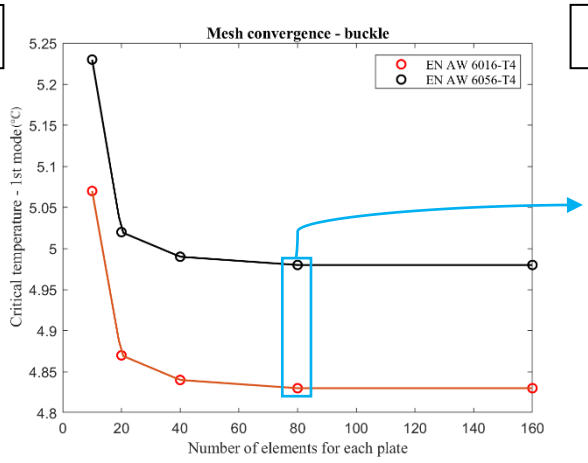

B

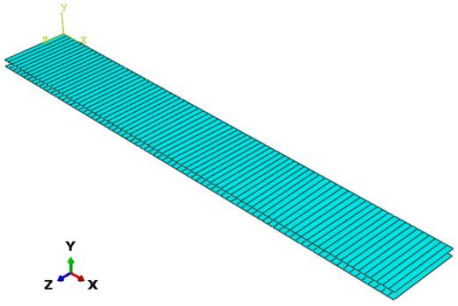

Figure 76 A) *Graph showing the mesh convergence result for the rectangular plate test;* ***B)*** *Mesh used for the buckle simulation.*

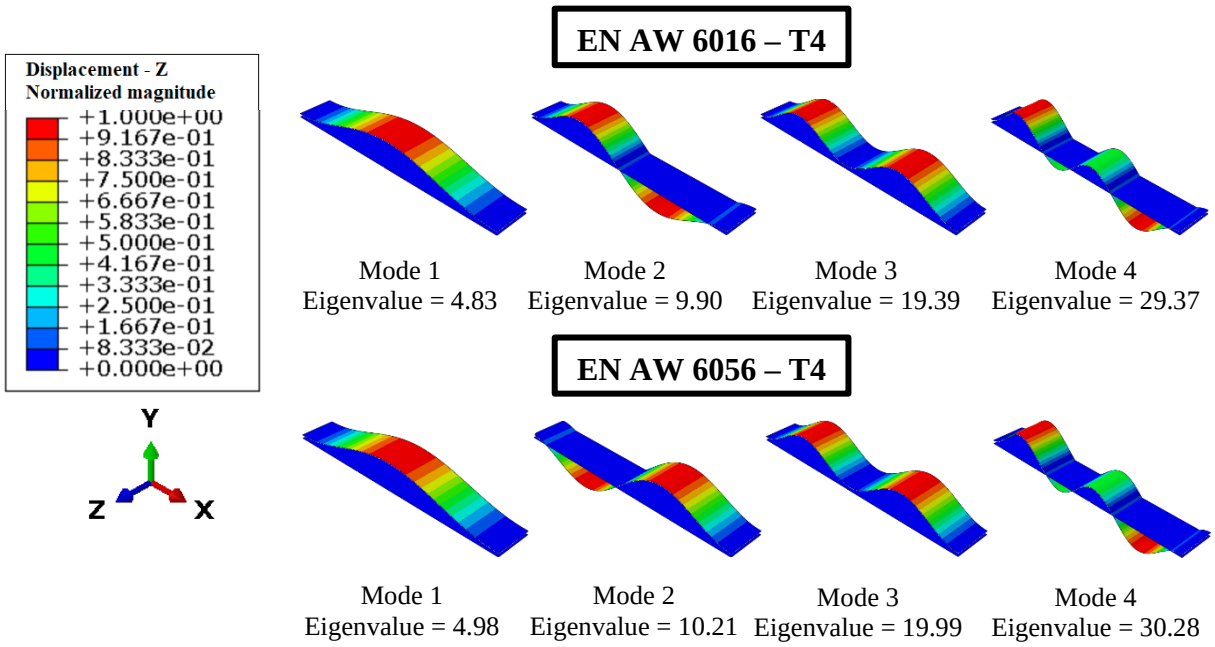

Figure 77 *Buckling shapes of the first four modes for the rectangular plates. Buckling mode shapes are normalized vectors, so that the maximum displacement component has a magnitude of 1.0.*

Based on the isolated buckling simulation, it is evident that the aluminum alloy structure buckles at remarkably low temperatures (4.83°C for a structure made of EN AW 6016 – T4 and 4.98°C when made of EN AW 6056 – T4). However, to achieve a more representative buckling temperature that accounts for temperature heterogeneities and to comprehend the behavior post-buckling, a post-buckling simulation was conducted employing the same methodology as previously outlined for the circular plate case in Section 4 of this chapter.

For the post-buckling simulation of the rectangular plates, the temperatures obtained from the practical laboratory test were used as input. Temperature measurements were acquired using three type K thermocouples in direct contact with the aluminum plate. Temperatures were captured at two-second intervals. The temperature data collected from the sensors for the tests conducted with EN AW 6016-T4 and EN AW 6056-T4 are concurrently presented in figures 78 - A and B.

Similarly to what was done with the circular plate, as can be observed in figures 78 A and B, the tests with the rectangular plates were carried out up to a maximum temperature of 180°C. The reason for this choice is based on the fact that in the Stellantis Rennes plant, the vehicle will be subjected to this heating temperature. Additionally, it is worth noting that the analyses of the thermo-mechanical properties of the aluminum alloys under study were also conducted within this temperature range.

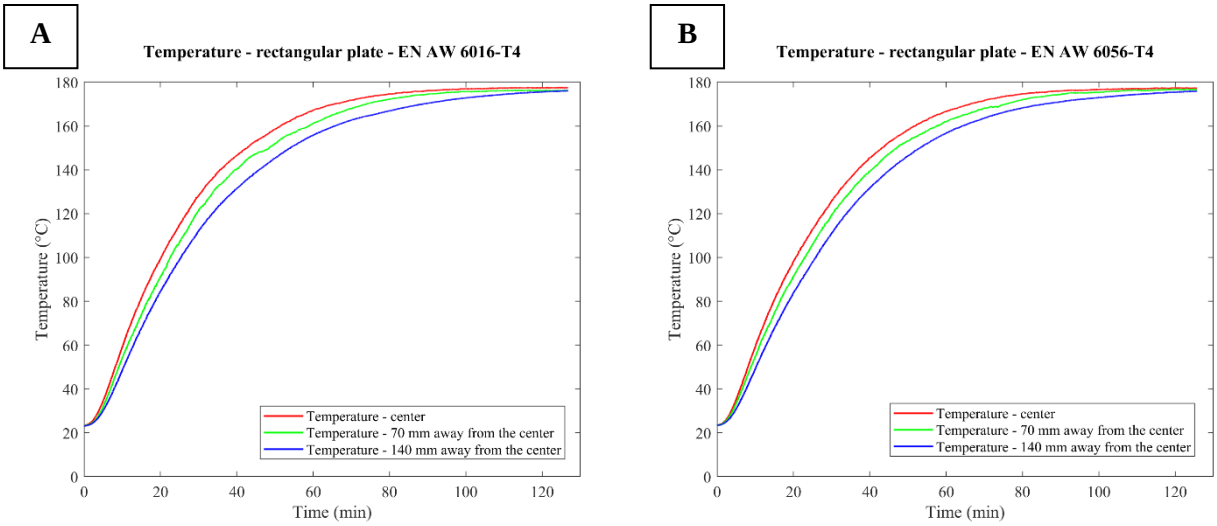

Figure 78 *Temperatures obtained by the sensors for the test with the rectangular plate made of:* ***A)*** *EN AW 6016-T4 and* ***B)*** *EN AW 6056-T4.*

As can be observed from the temperature graphs, the central temperature of the plate experiences a faster rate of change compared to the temperatures recorded by sensors closer to the edges. This is attributed to a thermal inertia effect of the more substantial mass of the support, which surpasses that of the tested plates. Given that the plates have similar geometries and very thin thicknesses (1.1 mm for the aluminum plate and 0.9 mm for the steel plate), the assumption was made that both plates are at the same temperature during the test.

Subsequently, the vertical displacement of the patterns (with the same shape as those used for the circular plate test), and consequently, the displacements of the tested plates, are assessed using Digital Image Correlation (DIC) through the GOM Correlate Pro software. Images for analysis were captured at ten-second intervals. This enables the determination of the vertical displacement of the plates in areas where the patterns are affixed.

The previously obtained temperature data, will serve as input, along with the vertical displacement data acquired from the DC01 steel plate (figures 79 – A and B), for the post-buckling simulation. Given that EN AW 6056-T4 is a stiffer material compared to EN AW 6016-T4, it is clear that the steel plate will experience a larger displacement when connected to the first material rather than the second, owing to the end connections between the steel and the aluminum alloy plate. Subsequently, the displacement computed for the aluminum plate in the simulation will be compared with the results derived from the experimental test. The recorded vertical displacement values for each pattern are presented in figure 79 - C (for the plate made of EN AW 6016-T4) and figure 79 - D (for the plate made of EN AW 6056-T4).

However, in this particular test, there is an aspect regarding the imperfection factor that needs to be applied in the post-buckling simulation. Measuring the imperfection factor before the plates are affixed to the support is challenging due to the plates being considerably long and thin (recalling the dimensions: 350 mm in length x 1.1 mm in thickness). Consequently, when

the plates are fixed to the support, an inherent imperfection arises in the fastening process, causing the plates to exhibit a slight curvature relative to their length.

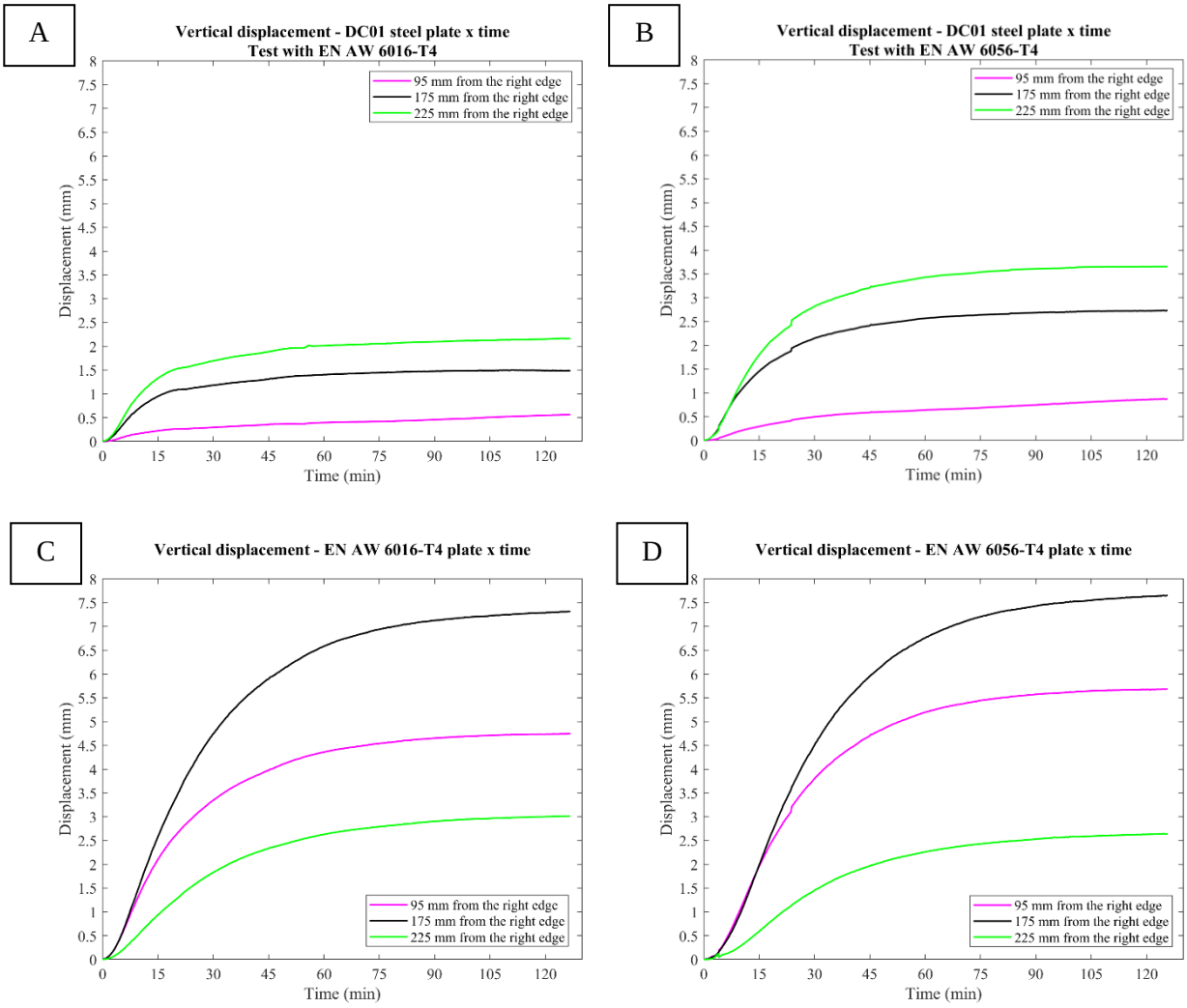

Figure 79 *Vertical displacements obtained through DIC from the practical tests.* ***A)*** *Vertical displacement result obtained in the DC01 steel plate tested with the EN AW 6016-T4 aluminum alloy;* ***B)*** *Vertical displacement result obtained in the DC01 steel plate tested with the EN AW 6056-T4 aluminum alloy;* ***C)*** *Vertical displacement result obtained in the EN AW 6016-T4 aluminum alloy plate;* ***D)*** *Vertical displacement result obtained in the EN AW 6056-T4 aluminum alloy plate;*

For this reason, graphs of vertical displacement at the center of the EN AW 6016-T4 and EN AW 6056-T4 aluminum alloy plates, obtained in the laboratory test, were plotted alongside graphs of vertical displacement derived from post-buckling simulations using different imperfection factors, as shown in figures 80 – A and B, respectively. The central point was chosen for analysis because it represents the location where displacements occur with the greatest amplitude, facilitating the identification of the appropriate imperfection factor for simulation. Upon analysis of the results in figure 80, and considering the comparison between the final amplitudes of the test and the simulation, as well as evaluating the displacement trajectories obtained, it is evident that imperfection factors of 4.00 and 5.00 demonstrate a more

favorable correlation between the test and numerical calculation for the respective materials EN AW 6016-T4 and EN AW 6056-T4, compared to the other imperfection factors tested (0.01, 1.00, 3.00, and 6.00). Figure 81 - A illustrates the results of vertical displacement obtained in the numerical simulation for the case where EN AW 6016-T4 is tested, and figure 81 - B for the case of EN AW 6056-T4.

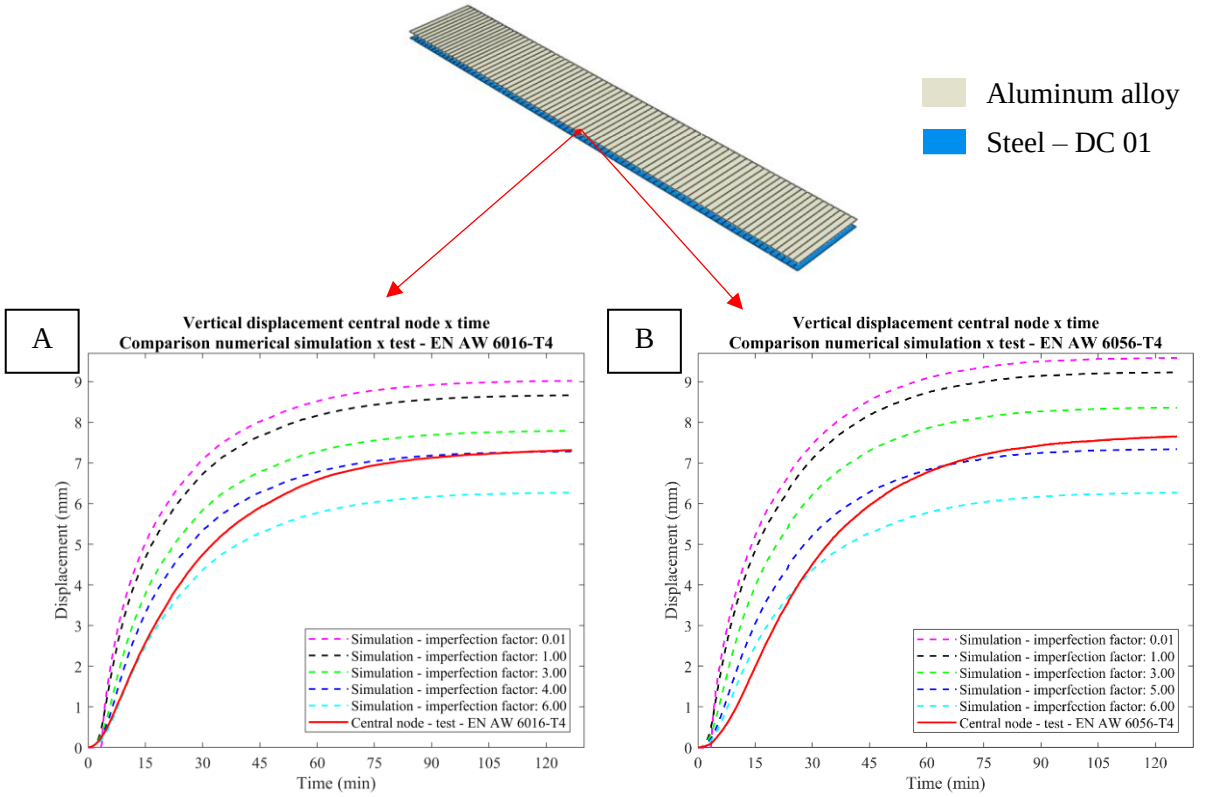

Figure 80 *Graphs of vertical displacement derived from post-buckling simulations using different imperfection factors.* ***A)*** *EN AW 6016-T4 situation with imperfection factor of 4.00 demonstrate a more favorable correlation with test result;* ***B)*** *EN AW 6056-T4 situation with imperfection factor of 5.00 demonstrate a more favorable correlation with test result.*

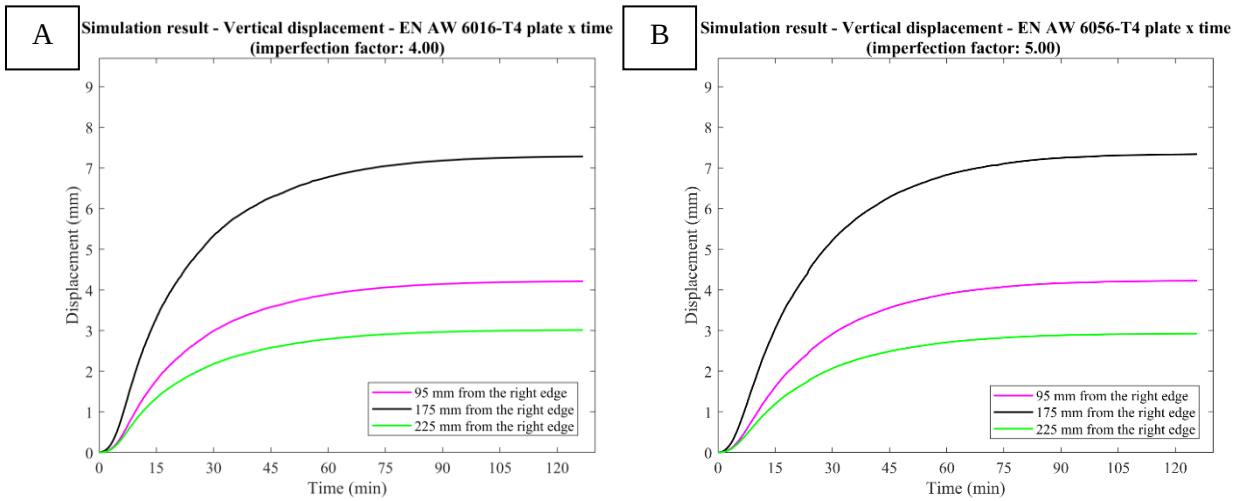

Figure 81 A) *Vertical displacement result obtained in the numerical simulation for the case where EN AW 6016-T4 is tested;* ***B)*** *Vertical displacement result obtained in the numerical simulation for the case where EN AW 6056-T4 is tested.*

Subsequently, to ascertain the critical buckling temperature, a displacement-versus-time graph was delineated in figure 82. This graph illustrates the temperature point at which buckling initiates, encompassing scenarios involving physical tests, post-buckling simulations employing an imperfection factor of 0.01, and post-buckling simulations utilizing the previously identified more fitting imperfection factors (4.00 for the EN AW 6016-T4 and 5.00 for the EN AW 6056-T4).

Upon scrutinizing the curves, it can be deduced that results acquired with an imperfection factor of 0.01 ($T_{crit_{sim}0.01-6016}$ = 28.4°C and $T_{crit_{sim}0.01-6056}$ = 28.6°C) exhibit commendable concordance when juxtaposed with analytically derived outcomes based on plate buckling theory ($T_{crit_{theory-6016}}$ = 27.7°C e $T_{crit_{theory-6056}}$ = 28.0°C), as tabulated in table 14. These theoretical outcomes were computed employing equation (92) $\Delta T_{critique} = \frac{\pi^2.I.L_0}{l_{eff}^2.S} \cdot \frac{1}{\alpha_{alu}.L_0 - U_{imposed}}$, elucidated earlier, with $U_{imposed_{6016}} = 0.004668$ mm and $U_{imposed_{6056}} = 0.004717$ mm, values obtained from the numerical simulation. This proximity between the theoretical and the imperfection factor of 0.01 case occurs because the imperfection factor of 0.01 is small in comparison to the actual imperfection factor of the plate. As a result, it gets closer to the theoretical case, where the imperfection has a less significant influence on the displacement before the buckling moment.

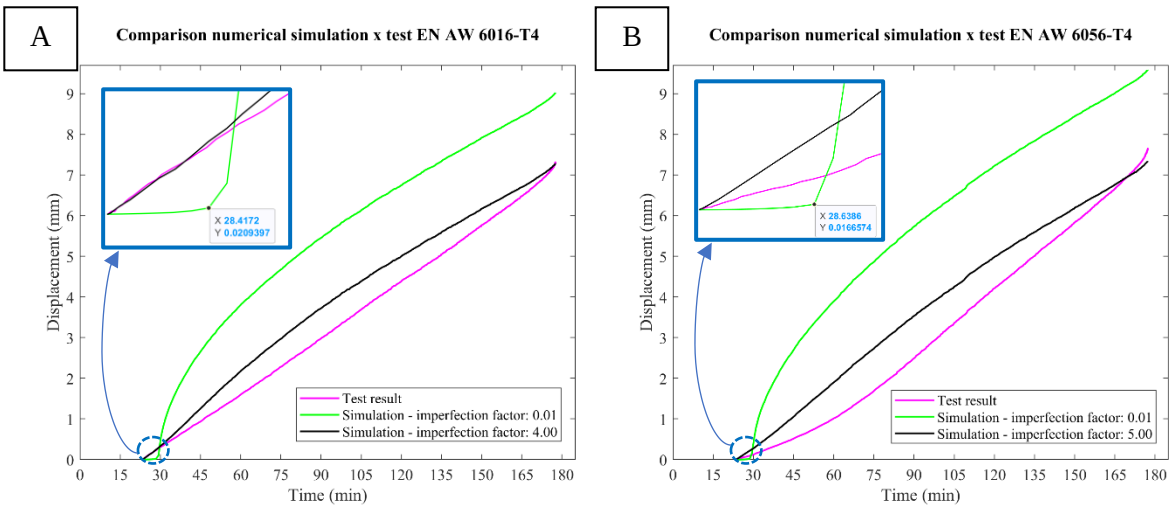

Figure 82 *Comparison between the vertical displacement-time curves obtained through tests and post-buckling numerical analysis of the central point of the rectangular plate made of* ***A)*** *EN AW 6016-T4 and* ***B)*** *EN AW 6056-T4.*

Table 14 *Values of critical temperature as a function of imposed displacement*

Material	$T_{crit_{theory}}$ (°C)	$T_{crit_{sim}0.01}$ (°C)	$T_{error_{theory-sim}}$
EN AW 6016-T4	23.3 + 4.4 = 27.7	28.4	2.5%
EN AW 6056-T4	23.4 + 4.6 = 28.0	28.6	2.1%

In the process of enhancing the conclusive analyses derived from figure 82, it is imperative to take into account that the buckling temperature experiences a decrement as the imperfection factor escalates. When the geometric imperfection factor is augmented, imperfections wield a more substantial impact on the distribution of stresses and deformations within the structure. This augmented influence can precipitate points of stress and strain concentration, rendering the structure more predisposed to buckling. Consequently, the critical buckling temperature undergoes a reduction. In instances of accelerated buckling, the timeframe available for accumulating significant deformations is curtailed. This signifies that the structure lacks the same window of opportunity to deform prior to the onset of buckling. Consequently, when buckling ultimately transpires, there will be a diminished reservoir of accumulated energy in the form of deformation. This diminished reservoir of energy amassed during buckling translates to reduced displacements during the post-buckling phase. This phenomenon arises from the fact that, with fewer accumulated deformations, the structure is inclined to exhibit a less conspicuous response during the post-buckling phase characterized by instability. Hence, as discernible in figure 82, the precise determination of the buckling temperature in scenarios featuring an imperfection factor of 4.00 or 5.00 becomes a challenging task due to the rapid instability of the structure at very low temperatures. Despite this, when comparing the amplitudes of vertical displacement at the analyzed central point, it is evident that the numerical model still manages to exhibit a satisfactory correlation with the results obtained in the practical test, especially concerning the final point. In this regard, a notable proximity is observed, particularly when the plates reach a more homogeneous condition at 180°C. This is highlighted in the simulation for the EN AW 6016-T4 alloy with an imperfection factor of 4.00, where the displacement is 7.3 mm, aligning closely with the experimental test result of 7.3 mm. Similarly, in the simulation for the EN AW 6056-T4 alloy with an imperfection factor of 5.00, the displacement is 7.3 mm, closely matching the observed value in the experimental test of 7.6 mm.

5.4 Conclusion

The exploration of thermal buckling behavior in the context of differential expansion enabled additional observations and the derivation of important conclusions not present in the circular plate study, thus providing continuity to the investigation of differential expansion. Starting with the different boundary conditions of the problem, which closely resemble roof and body-in-white conditions, the significance of precisely defining these boundary conditions was emphasized. A notable characteristic of the buckling phenomenon is its strong dependence on boundary conditions, as seen in the distinct buckling geometries of beams fixed at both ends versus those fixed at one end and free at the other. With just this variation in boundary conditions, the critical buckling load of a double-fixed beam can be eight times higher, utilizing an effective length four times shorter.

Subsequently, the analysis of differential expansion and thermal buckling through the case of a beam subjected to imposed displacement led to the conclusion that when no displacement is imposed, the critical buckling temperature equals the critical Euler load. When a displacement is imposed, it becomes possible to fully compensate for buckling by imposing an external displacement (referred to as $U_{imposed,crit}$), representing the displacement the beam would experience if it were free at its end.

Following the derivation of the equation for calculating the critical buckling temperature with respect to an imposed displacement, the focus shifted to analytical and numerical correlation in a real-life scenario. The focus was on the thermal buckling of a component made of aluminum alloy under thermal loading, where the displacement results from the interaction between the thermal expansion of a steel DC01 structure and the thermal expansion of the aluminum alloy structure. It was observed that the critical temperature change for the aluminum alloy structure exhibits an inverse relationship with the difference between the imposed critical displacement (fully compensating for buckling) and the imposed displacement. This relationship suggests that a greater difference between these displacements results in a smaller change in the critical temperature required to initiate the first buckling mode.

The numerical simulations using S4 elements revealed that the aluminum alloy structure buckles at remarkably low temperature differentials (4.83°C for EN AW 6016 – T4 and 4.98°C for EN AW 6056 – T4), consistent with the findings from the circular plate test, where buckling temperatures were similarly low. This outcome not only emerged from theoretical and numerical analyses but also from physical tests, where imperfections were more pronounced, resulting in extremely low and challenging-to-determine buckling temperatures. This underscores the importance of imperfections in both numerical and experimental outcomes. An example of how changes in the imperfection factor can alter the mechanical response of the structure was demonstrated through numerical analysis of the rectangular plate test. With an imperfection factor of 0.01, the vertical displacement of the central node of the rectangular plate composed of EN AW 6016-T4 was 9.0 mm, whereas with an imperfection factor of 6, this value decreased to 6.3 mm. Similarly, for the rectangular plate made of EN AW 6056-T4, a 0.01 imperfection factor yielded a vertical displacement of the central node of 9.6 mm, which decreased to 6.3 mm with an imperfection factor of 6.00.

Finally, despite these challenges, the comparison of amplitudes of vertical displacement at the analyzed central point revealed that the numerical model still exhibited a satisfactory correlation with the practical test results, especially regarding the final point, when the plates reached a more homogeneous condition at 180°C. This was evident in the simulation for EN AW 6016-T4 alloy with an imperfection factor of 4.00, resulting in a vertical displacement of 7.3 mm, closely mirroring the practical test result of 7.3 mm. Similarly, in the simulation for EN AW 6056-T4 alloy with an imperfection factor of 5.00, the vertical displacement was 7.3 mm, closely matching the observed value in the practical test of 7.6 mm.

6. Conclusion – Chapter 3

In Chapter 3, thermal buckling phenomena were investigated in both circular plates and the coupling of different materials under thermal loading. The investigation thoroughly explored the influence of material and geometric parameters on critical buckling temperature, considering essential material properties like thermal expansion coefficient, Poisson's ratio, and Young's modulus, alongside geometric parameters such as radius, length, thickness, and imperfections.

The primary focus was on circular plates made of two aluminum alloys, EN AW 6016-T4 and EN AW 6056-T4, clamped within a steel support. The findings underscored the importance of accounting for thermal buckling phenomena in practical applications, revealing modest temperature variations of approximately 5-6°C to reach critical buckling temperatures. The analysis of plate displacements emphasized the dominance of the first buckling mode in determining post-buckling behavior, with Z-directional displacements following this pattern. Despite the comparable buckling temperatures of both materials, an analysis of plastic deformation unveiled discernible differences between the EN AW 6016-T4 and EN AW 6056-T4 alloys. Specifically, the circular plate crafted from EN AW 6016-T4 displayed a maximum plastic deformation of 3.0E-3, nearly twice that observed in the EN AW 6056-T4 plate (1.6E-3). The analysis of compressive stresses in the principal direction at maximum test temperature unveiled markedly higher stress levels in the circular plate composed of EN AW 6056-T4, with a recorded value of -173.2 MPa, in contrast to the -140.1 MPa experienced by the plate crafted from EN AW 6016-T4. The numerical analysis, integrating thermal implicit analysis, geometric nonlinearity, and temperature-dependent material properties, proved immensely valuable for investigating thermal buckling behavior and yielded indispensable insights for design, material selection, and structural optimization.

The exploration into the coupling of different materials under thermal loading extended the understanding. The investigation emphasized the critical role of boundary conditions in buckling phenomena, with distinct geometries observed under varying conditions. Differential expansion analysis elucidated the compensation for buckling through imposed displacement, presenting critical implications for beam behavior. The examination of thermal buckling in aluminum alloy components, influenced by the interaction with a steel structure, uncovered an inverse relationship between critical temperature change and differences in imposed displacements. Numerical simulations demonstrated remarkably low temperatures (less than 5°C of temperature difference) for aluminum alloy buckling, corroborating findings in physical tests and highlighting the crucial role of imperfections in results. Despite challenges, the comparison of vertical displacements between numerical simulations and practical tests revealed satisfactory correlations. The model demonstrated close agreement with practical results, particularly at the final stage when plates reached a more uniform temperature condition

at 180°C. This was evident in the simulation for the EN AW 6016-T4 alloy with an imperfection factor of 4.00, yielding a vertical displacement of 7.3 mm, closely aligning with the practical test result of 7.3 mm. Similarly, in the simulation for the EN AW 6056-T4 alloy with an imperfection factor of 5.00, the vertical displacement was 7.3 mm, mirroring the observed value in the practical test of 7.6 mm. This emphasized the robustness of the numerical model and its practical relevance in simulating thermal buckling behavior.

Based on these findings, the close alignment between numerical predictions and practical test results underscores the reliability and applicability of the developed numerical model in capturing thermal buckling effects on structures. This robust correlation instills confidence in leveraging numerical simulations for subsequent investigations and optimizations, particularly focusing on the primary structure of this thesis: the car roof integrated into the body-in-white.

Bibliography – Chapter 3

[76] Hibbeler, R.C.. Mechanics of Materials, chap. 13, 11th ed., Pearson, US, 2022.

[77] Galambos, Theodore V. & Surovek, Andrea E.. Structural Stability of Steel: Concepts and Applications for Structural Engineers, 1st ed., John Wiley & Sons, New Jersey, 2008.

[78] Timoshenko, S. P. & Gere, J. M. (1961). Theory of Elastic Stability, 2nd ed., McGraw-Hill, New York, 1985.

[79] Bažant, Z. P. & Cedolin, Luigi. Stability of Structures: Elastic, Inelastic, Fracture, and Damage Theories, World Scientific, Singapore, 2010.

[80] D. Baroudi. Stability Lectures. Source: https://mycourses.aalto.fi/pluginfile.php/1260824/course/section/173429/Main_book_Structural_Mechanics_2020_STAB_version_2_Optimized.pdf [accessed 13.12.2022].

[81] Beer, F.P., Johnston Jr., E.R. & DeWolf, J.T. Mechanics of Materials, 7th ed., McGraw-Hill Education, 2015.

[82] S.A.M. Ghannadpour, H.R. Ovesy, M. Nassirnia. Buckling analysis of functionally graded plates under thermal loadings using the finite strip method, Comput. Struct., 108–109 (2012), pp. 93-99. https://doi.org/10.1016/j.compstruc.2012.02.011

[83] X. Zhao, Y.Y. Lee, K.M. Liew. Mechanical and thermal buckling analysis of functionally graded plates, Compos Struct, 90 (2) (2009), pp. 161-171. https://doi.org/10.1016/j.compstruct.2009.03.005

[84] H. Wu, S. Kitipornchai, J. Yang, Thermal buckling and post-buckling of functionally graded graphene nanocomposite plates, Mater. Des., 132 (2017), pp. 430-441. https://doi.org/10.1016/j.matdes.2017.07.025

[85] T. Van Do, D.H. Doan, N.D. Duc, T.Q. Bui. Phase-field thermal buckling analysis for cracked functionally graded composite plates considering neutral surface, Compos. Struct., 182 (2017), pp. 542-548. https://doi.org/10.1016/j.compstruct.2017.09.059

[86] D. Wang, J. Hui, W. Cao, Y. Yang, Y. Wan, H. Zuo, B. Zhang. The influence of geometric imperfections on post-buckling behavior and free vibrations of a fiber-reinforced composite laminated plate under thermal loading, Compos. Struct., 306 (2023). https://doi.org/10.1016/j.compstruct.2022.116568

[87] G. Manickam, et al. Thermal buckling behavior of variable stiffness laminated composite plates, Mater Today Commun, 16 (2018), pp. 142-151. https://doi.org/10.1016/j.compstruct.2023.117138

[88] Wang Z.K., Soares C.G.. Theoretical investigation on the upheaval thermal buckling of a lined subsea pipeline, Ocean Eng., 261 (2022), article 111843. https://doi.org/10.1016/j.oceaneng.2022.111843

[89] Z. Wang, C. Guedes Soares. Upheaval thermal buckling of functionally graded subsea pipelines, Appl Ocean Res, 116 (2021), article 102881. https://doi.org/10.1016/j.apor.2021.102881

[90] Matthew J. Santer. Composite Tube Flexures at Nanosatellite Scale, AIAA 2017-0622. Session: Small Satellite Deployable Structures (2017). https://doi.org/10.2514/6.2017-0622

[91] William L. Ko. Thermal Buckling Analysis of Rectangular Panels Subjected to Humped Temperature Profile Heating, NASA Dryden Flight Research Center, Edwards, California (2004). H-2539.Ko.fm (nasa.gov)

[92] Y. Li, J. Jiang, Y. Yu, Z. Wang, Z. Xing, Q. Zhang, Thermal buckling of oil-filled fixed-roof tanks subjected to heat radiation by a burning tank. Eng. Fail. Anal. 138 (2022), article 106393. https://doi.org/10.1016/j.engfailanal.2022.106393

[93] R.C. Jaca, L.A. Godoy, H.D. Calabró, S.N. Espinosa. Thermal post-buckling behavior of oil storage tanks under a nearby fire, Int. J. Pres. Ves. Pip., 189 (2021), article 104289. https://doi.org/10.1016/j.ijpvp.2020.104289

[94] A. Ghorbanpour Arani, M. Ahmadi, A. Ahmadi, A. Rastgoo, H.A. Sepyani. Buckling analysis of a cylindrical shell, under neutron radiation environment, Nucl. Eng. Des., 242 (2012). https://doi.org/10.1016/j.nucengdes.2011.08.022

[95] Huizhou Yang. Finite Element Analysis of Thermal Buckling in Automotive Clutch and Brake Discs (2015). Electronic Theses and Dissertations, University of Denver, 1056. https://digitalcommons.du.edu/etd/1056

[96] M.H. Pranta, M.S. Rabbi, S.C. Banik, M.G. Hafez, Y.M. Chu. A computational study on structural and thermal behavior of modified disk brake rotors, Alexandria Eng. J., 61 (3) (2022), pp. 1882-1890. https://doi.org/10.1016/j.aej.2021.07.013

[97] M.M. Najafizadeh, M.R. Eslami. Buckling analysis of circular plates of functionally graded materials under uniform radial compression, Int J Mech Sci, 44 (12) (2002), pp. 2479-2493. https://doi.org/10.1016/S0020-7403(02)00186-8

[98] D. O. Brush & B. O. Almroth. Buckling of Bars, Plates, and Shells. McGraw-Hill, New York, 1975.

[99] Abaqus Analysis User's Guide (a). 6.2.3 Eigenvalue buckling prediction. SIMULIA. Source: http://130.149.89.49:2080/v6.14/books/usb/default.htm?startat=pt03ch06s02at02.html [accessed 24.02.2021].

[100] Humer, A., Pechstein, A.S. Exact solutions for the buckling and post-buckling of a shear-deformable cantilever subjected to a follower force. Acta Mech 230, 3889–3907 (2019). https://doi.org/10.1007/s00707-019-02472-1

[101] S.G.P. Castro, E.L. Jansen, Displacement-based formulation of Koiter's method: application to multi-modal post-buckling finite element analysis of plates, Thin-Walled Struct. 159 (2021) 107217. https://doi.org/10.1016/j.tws.2020.107217

[102] Abaqus Analysis User's Guide (b). 11.3.1 Introducing a geometric imperfection into a model. SIMULIA. Source: https://classes.engineering.wustl.edu/2009/spring/mase5513/abaqus/docs/v6.6/books/usb/default.htm?startat=pt04ch11s03aus55.html [accessed 24.02. 2022].

[103] I. Sheinman, M. Adan. Imperfection sensitivity of a beam on a nonlinear elastic foundation, Int. J. Mech. Sci. 33 (1991), pp. 753–760. https://doi.org/10.1016/0020-7403(91)90070-J

[104] S.A. Emam. A static and dynamic analysis of the postbuckling of geometrically imperfect composite beams, Compos. Struct. 90 (2009), pp. 247–253. https://doi.org/10.1016/j.compstruct.2009.03.020

[105] Yaghoobi H., Torabi M.. Post-buckling and nonlinear free vibration analysis of geometrically imperfect functionally graded beams resting on nonlinear elastic

foundation, Appl Math Model, 37 (2013), pp. 8324-8340. https://doi.org/10.1016/j.apm.2013.03.037

[106] M. Shariyat. Thermal buckling analysis of rectangular composite plates with temperature-dependent properties based on a layerwise theory. Thin-Walled Structures 45 (2007), pp. 439-452. https://doi.org/10.1016/j.tws.2007.03.004

[107] Leonhard Euler. Methodus inveniendi lineas curvas maximi minimive proprietate gaudentes. Lausanne and Geneva, 1744.

[108] Stephen P. Timoshenko, J. M. Gere. Theory of elastic stability, 2nd ed., Mc Graw Hill, London, 1961.

[109] ANSA pre-processor – Stellantis material library. Stellantis France, 2020.

Chapter 4 - Analysis and numerical study of body-in-white tests for evaluating roof appearance defects after thermal cycle in the painting phase

Introduction – Chapter 4

In the culmination of this comprehensive research endeavor, the intricate terrain of material behavior has been traversed, the depths of the observed phenomenon have been delved into, and correlations with practical cases have been forged. With this enriched understanding firmly established, a seamless transition is made to Chapter 4, where the insights validated and gleaned from the previous chapters will now be skillfully applied to the real case of the body-in-white.

Chapter 4 will commence with a presentation of the testing protocol for vehicle-scale structures. Subsequently, the same numerical calculation methodology applied in Chapter 3 will be employed, but this time on a much larger structure with a considerably greater number of materials and elements. The initial thermal buckle and post-buckle analyses will be conducted on the aluminum alloy car roof, which has a geometry equivalent to the steel roof. The goal is to draw conclusions about the occurring buckling and to guide the material choice for further study.

Following that, in an effort to better understand what could be done to solve the problem, a study was conducted on the influence of the car roof's geometry parameters on the critical buckling temperature. With the conclusions obtained, improvements to the car roof design were proposed to stiffen the areas showing the initial signs of buckling. The aim was to find a solution that could meet the desired industrial criteria while being more efficient in terms of time and costs.

This new car roof geometry was first tested numerically, and after showing satisfactory results in reducing appearance defects according to simulations, tests were carried out with a physical car structure, thus concluding the findings of the entire research conducted during this thesis.

TABLE OF CONTENTS – CHAPTER 4

Chapter 4 - Analysis and numerical study of body-in-white tests for evaluating roof appearance defects after thermal cycle in the painting phase……...…137

Introduction – Chapter 4……..137

2. Testing protocol for the structural car tests at the factory……...…….139

2. Aluminum alloy car roof with geometry equivalent to steel roof: thermal buckle and post-buckle analysis……..145

2.1 Thermal buckle simulation: aluminum alloy car roof with geometry equivalent to a steel roof……..146

2.2 Thermal post-buckle simulation: aluminum alloy car roof with geometry equivalent to a steel roof……..149

2.3 Conclusive insights from analyzing aluminum alloy car roof with steel roof geometry……..160

3. Influence of the car roof's geometry parameters on the critical buckling temperature……..……161

3.1 Influence of curvature of a fixed rectangular plate on the thermal buckling…….162

3.1.1 Flat rectangular plate (without curvature)……..162
3.1.2 Curved rectangular plate along the length or width……...164
3.1.3 Curved rectangular plate along the length and width……166

3.2 Influence of adding ribs on thermal buckling of a rectangular plate…….167

4. Simulations: proposal for a new roof geometry……..170

4.1 Ribs in the roof geometry…….170

4.2 Thermal buckle simulation: aluminum alloy car roof with proposed geometry…...……...174

4.3 Thermal post-buckle simulation: aluminum alloy car roof with proposed geometry…….....177

6. Conclusion – Chapter 4……181

Bibliography – Chapter 4……...…..183

1. Testing protocol for the structural car tests at the factory

Making a brief recapitulation, the ultimate goal of this thesis is to provide a viable solution to a company in the automotive industry for predicting and preventing appearance defects in the aluminum alloy roof structure assembled in a body-in-white mostly made of steel. In this way, two points can be highlighted: firstly, the main test subject of this thesis involves a full-scale car body, highlighting the real-world applicability of the proposed solution; secondly, the complexity of achieving a structure of this magnitude necessitates a thoughtful and strategic approach, considering the intricate interactions between the various components.

Hence, leveraging the image depicted in Chapter 1 (figure 83) that illustrates the methodology employed in this thesis to attain the specified objectives, the research methodology adheres to a systematic progression. The investigation commences with analyses at the material scale, utilizing Technology Readiness Levels (TRL) ranging from 1 to 3. Subsequently, it progresses to laboratory-scale prototype testing, encompassing TRL levels 4 to 6. Finally, the study culminates in the present chapter, which involves full-scale body-in-white, specifically vehicle structure tests, at TRL levels 7 to 9.

Throughout the preceding Chapters 1, 2, and 3, an array of crucial studies were undertaken, significantly contributing to the comprehensive understanding of various aspects. This includes gaining insights into the contextual background, comprehending the problem, understanding material behavior within the targeted temperature range, and identifying instability phenomena associated with boundary conditions. This collective knowledge base sets the foundation for the conclusive chapter of this dissertation.

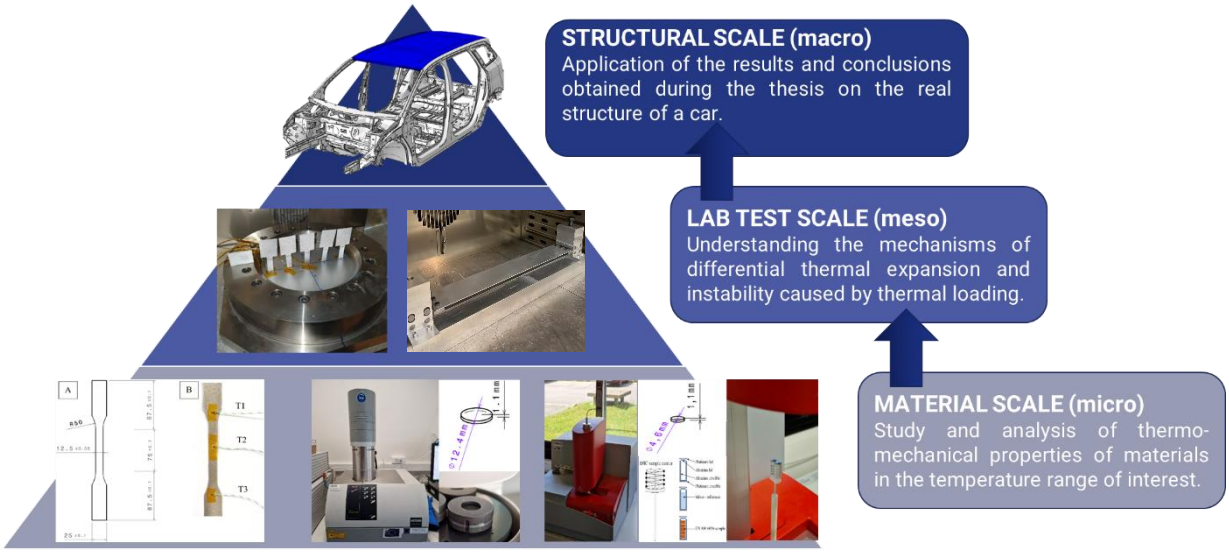

Figure 83 *Evidence pyramid used to show the methodology adopted to solve the statement problem.*

In this chapter, the focus shifts to the structural scale (macro). Consequently, the preparation for tests conducted on the vehicle is not as straightforward as the preparation for smaller scale tests carried out in the laboratory. Therefore, the first step towards advancing in the direction of structural analysis at the vehicle scale is to understand the manufacturing, fixation, and post-analysis processes related to the study of the car roof's behavior.

The primary objective behind the presentation of the vehicle testing process at the plant is to enhance comprehension of the industrial procedure involved in the assembly of the car roof within the body-in-white. By gaining a more detailed and comprehensive understanding of the manufacturing of the components and the interworking of equipment to produce the final product, potential industrial opportunities for optimizing the structure in relation to the specific studied issue can be identified.

The industrial process used for manufacturing the body-in-white remains consistent with the production line until the painting stage. As previously demonstrated in Chapter 1, the production stages for the structure involve stamping, followed by welding/assembly. Since the body-in-white is intended to be assembled with a new car roof that is not yet produced on the regular production line, the car body structure is retrieved from the production line before undergoing the painting process. After adhering to the standard manufacturing procedures and being removed from the production line, the roofless structure (depicted in figure 84) is subsequently transported to the specialized FabLab for the analyses conducted for *Projet AM2*.

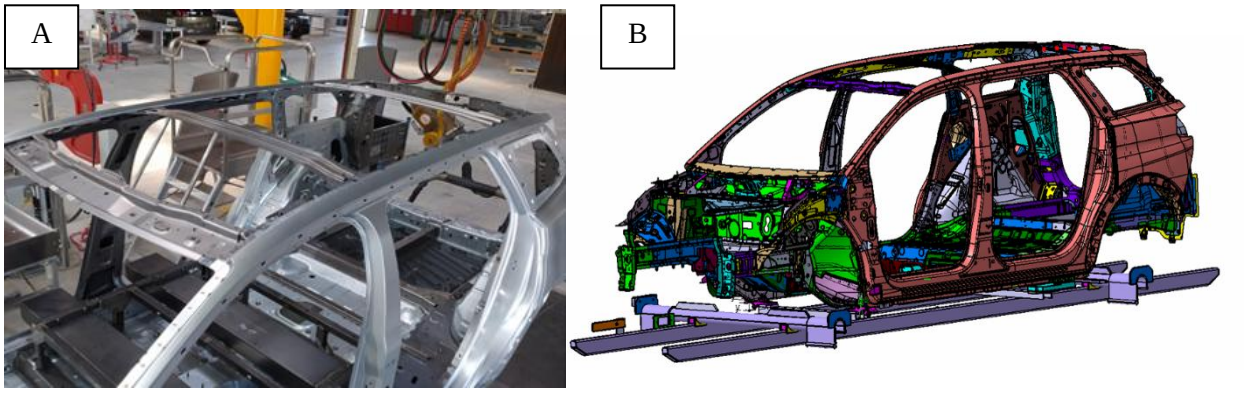

Figure 84 A) *Structure of the Body-in-White after the welding phase, still without the roof;* ***B)*** *Numerical design of the structure, where each color represents a different material.*

The incorporation of an aluminum alloy roof in the investigated vehicle model represents a novel approach in its manufacturing process. Specifically, the implementation of the aluminum alloys EN AW 6016-T4 and EN AW 6056-T4 marked their first utilization within the company for car roof fabrication. However, due to significant disparities in mechanical properties between these alloys and the materials conventionally used in vehicle roofs, their incorporation into the regular production line presses was not yet feasible.

The attempt to use the same parameters utilized for stamping standard steel roofs resulted in significant conformity issues, and in some instances, structural cracks emerged in the aluminum alloy roof. Consequently, to address these challenges, the development of a specialized modular stamping die for the aluminum alloy roof (figure 85) was imperative. This dedicated tool allowed the attainment of a structural configuration aligning with the shape of the standard steel car roof through cold-forming techniques. The cost incurred for the creation of this tool amounted to approximately 300 k€.

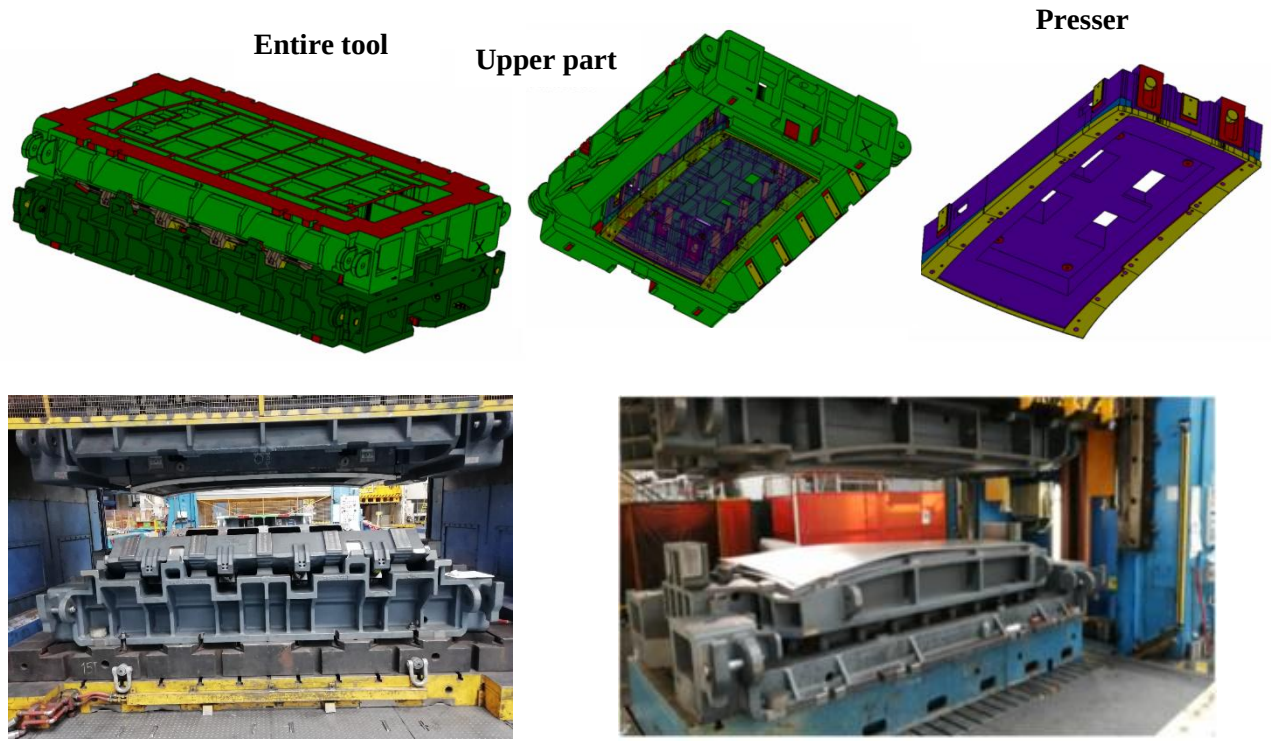

Figure 85 *Modular stamping die developed for the aluminum alloy roof.*

After being stamped into its final shape, the aluminum alloy roof undergoes a conformity assessment process. In this process, a comparison is made between the obtained geometry and a geometry of reference (figure 86). Upon verifying that the geometric variances adhere to the conformity criteria, the aluminum alloy roof undergoes a positioning process onto the body-in-white structure.



Figure 86 *Tool designed to serve as a geometric reference for car roofs manufactured through stamping.*

Following the aforementioned conformity stage, the manufacturing process progresses to the execution of welding points on both the front and rear sections of the aluminum alloy roof. Figure 87 provides a visual representation of the locations where these welding points are applied in the rear part of the vehicle. These welding points not only join the roof to the body-in-white structure but also play a significant role in distributing the load and stresses evenly throughout the vehicle's framework. In addition to joining the roof with the body-in-white structure, they (and the brazing lines) play a crucial role as boundary conditions in the numerical model developed for the completed structure.

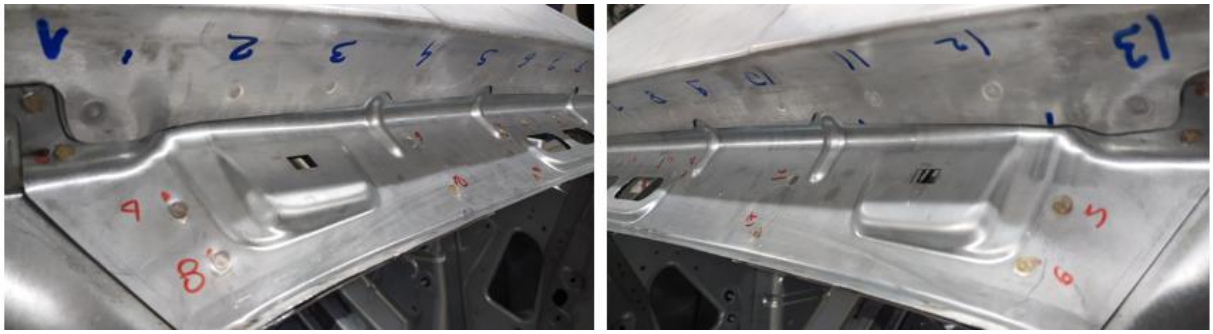

Figure 87 *Distribution of welding points to connect the roof and the rear part of the vehicle.*

Then, the entire structure is taken to a welding cabin. During this stage, the car's roof is laterally integrated with the body-in-white structure through a continuous welding procedure. The process is fully automated, utilizing robotic systems, while monitoring occurs via an internal camera (figure 88). Detailed accounts of the continuous welding and spot welding procedures are omitted in this study, as they pertain to separate research projects beyond the scope of this dissertation. The relevant information is to understand the types of connections made between the structures, which will later be translated into boundary conditions in the numerical simulation.

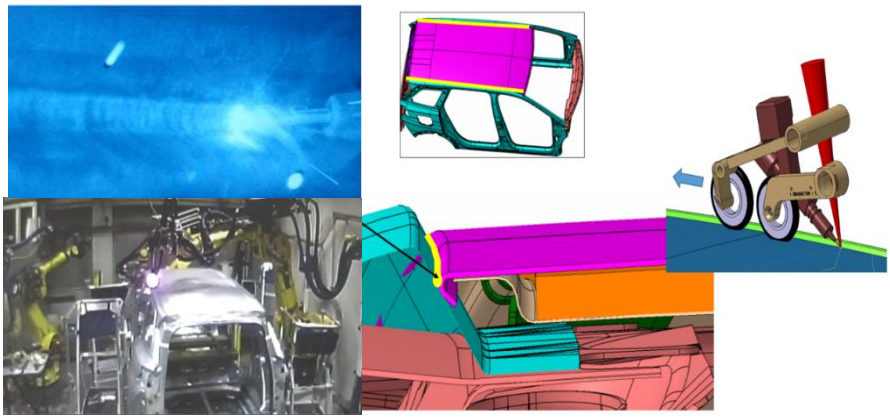

Figure 88 *Operation of brazing between the side parts of the car roof and the side parts of the body-in-white.*

Once the entire structure is prepared, it is sent back to the production line for the final phase of painting, which includes the heating process as presented in Chapter 1 - Section 3.3.

After the painting process is completed, the structure is taken to a scanning cabin for further evaluation. In the scanning cabin, a scan is performed, generating a series of data points that allow for the virtual reconstruction of the structure. Through this virtual analysis, it becomes possible to assess the final state of the car's roof and, consequently, identify any shape defects that may have occurred.

Unfortunately, the current displacement and deformation measurement systems available in the market do not provide access to information regarding the geometry of the car's roof within the heating tunnel of the production line. Existing image-based stereocorrelation systems, although advanced technologically, are not designed to operate in environments with temperatures exceeding 50°C. Moreover, their size tends to be substantial. While other high-temperature sensors are available, they only offer single-point measurements, lacking the capability to provide data for a wider measurement area.

In the context of optical systems specifically designed to operate at high temperatures, a significant challenge lies in the integration of their cooling systems into a body-in-white structure. The size and complexity of these cooling systems make it impractical to seamlessly incorporate them into the vehicle's structural framework. Therefore, alternative approaches need to be explored to address this limitation. Furthermore, the autonomy of such a system must be carefully optimized, incorporating a lightweight battery to avoid interfering with the vaporization process. In summary, the limitations faced by different measurement systems nowadays are as follows:

1. Electronic components often cannot withstand temperatures above 50°C;
2. Cooling systems are bulky and energy-intensive;
3. Some systems cannot quantify displacement fields;
4. Some systems rely on the electrical grid or have limited autonomy;
5. Certain systems are excessively large and heavy;
6. There is a complete lack of illumination in the heating tunnel.

Given all these difficulties in relation to our application and current measurement systems, a patent was developed during this thesis (figure 89). For more comprehensive information and technical details, the annex section provides a thorough explanation of the patent's intricacies.

The idea was to use an optical measurement system capable of measuring displacement fields associated with structural expansion phenomena in an environment subjected to high temperatures, around 200°C, when protected by an insulating thermal enclosure (keeping the interior temperature below 45°C for 90 minutes to integrate the appropriate electronics). This system would be attached to the body-in-white and operate autonomously.

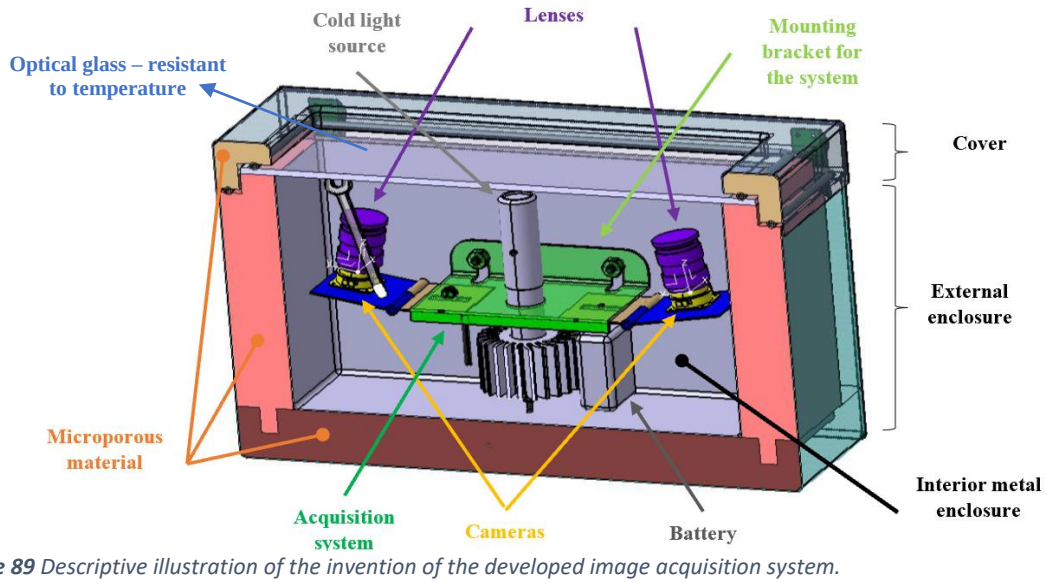

Figure 89 *Descriptive illustration of the invention of the developed image acquisition system.*

Despite the innovation and potential usefulness of this system, due to time constraints and administrative processes related to the invention, it was not utilized for measurements in this thesis. Therefore, the measurements presented in this report will be conducted by scanning the car roof after the heating phase.

The conducted research encompassed over fifteen full-scale body-in-white structures subjected to a rigorous manufacturing process and painting phase from 2020 to 2023. In pursuit of analysis and synthesis, this dissertation will present the outcomes of three distinct variations, each possessing different specifications:

1. The first two cases entail an in-depth examination of car roofs constructed with EN AW 6016-T4 and EN AW 6056-T4 aluminum alloys, featuring the identical geometry found in currently marketed steel roofs;

2. Subsequently, the last case scrutinizes the car roof constructed from the aluminum alloy displaying superior results for buckling and post-buckling characteristics, chosen from the two aforementioned aluminum alloys. This examination, however, incorporates a distinct geometry proposed specifically to address the problem central to this thesis. The aim is to thoroughly analyze the implications of this optimized combination to enhance the car roof's structural conformity.

Thus, the next sections 2 and 4 of this chapter will respectively present the numerical simulations conducted with the car roof having geometry equivalent to a steel roof and the numerical simulations carried out with the newly proposed geometry. By subjecting this optimized car roof to the same thermal load conditions, the aim is to evaluate its structural performance and assess the effectiveness of the proposed enhancements. The comparative analysis of these simulations against the stated problem will shed light on the efficacy of the

proposed optimizations. The goal is to identify how well the optimized car roof performs compared to the traditional steel roof geometry and whether the proposed improvements result in a more structurally conforming car roof.

2. Aluminum alloy car roof with geometry equivalent to steel roof: thermal buckle and post-buckle analysis

In this stage of the study, the primary objective of the analysis is to evaluate whether the unmodified roof configuration poses a potential risk of buckling during the heating process in the painting phase. The outcomes of the buckle and post-buckle analyses will serve as a basis for choosing the material that best meets the required performance criteria. The material that demonstrates superior behavior, both in terms of structural performance and visual appearance, will be selected for further continuation of the study.

The simulation of the entire vehicle structure was conducted using two software tools: ANSA for model preparation (figure 90) and Abaqus as the solver. The numerical model of the metallic part of the vehicle is remarkably intricate, comprising:

- 18 different kinds of different steels: TD1080, MS1500, 22MnB5, CP1000, DP1180, DP450, DP590, DP780, DP980, E275D, E335D, E390D, FB45, FB60, HC340LA, HC380LA, HD300LA, P260. Material properties for these steels were sourced from the Stellantis material library [120];
- 821 components;
- 3,797 connections between various parts;
- Mesh with a total of 1 559 783 elements.

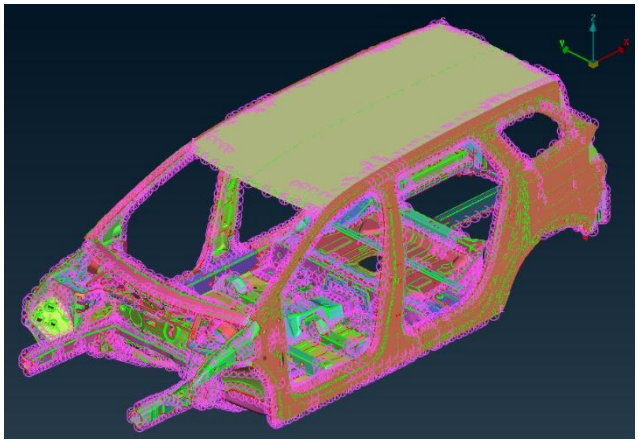

Figure 90 *Simulated structure displayed in the ANSA software interface. Each color represents a different material, and each purple circle represents a type of connection between the parts composing the model's structure.*

In other words, due to the sheer complexity of this large-scale structure, conducting numerous analytical analyses or structural tests becomes impractical in terms of cost, time, and understanding the underlying physical phenomena. However, through the results of correlated numerical-physical tests obtained in Chapter 3 for the laboratory experiments, it has been established that the simulation methodology is reliable for the problem of thermal buckling with slow heating situations.

Leveraging the proven reliability of the developed simulation method, the same numerical procedure will be used, this time for the entire car roof structure assembled onto the body-in-white:

1. Firstly, the structural performance of the studied SUV roof (with dimensions depicted in figure 91) assembled in a body-in-white will be initially evaluated concerning thermal buckling. This analysis will be conducted through a linear buckling analysis utilizing the ABAQUS software. Recognizing that structures subjected to compressive loading can buckle in non-axisymmetric modes, the buckling analysis will be performed with the complete geometry;

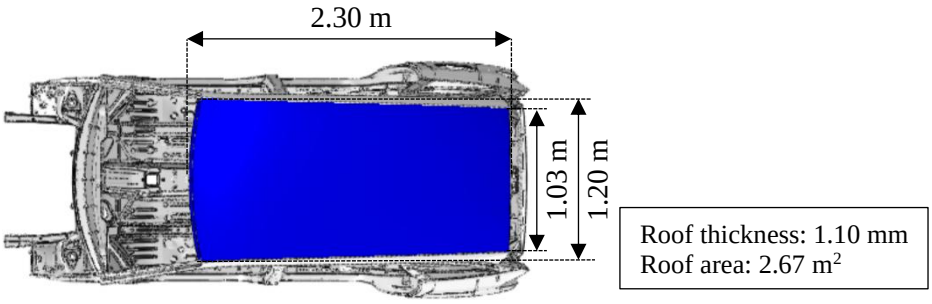

Figure 91 *Structural dimensions of the assembled roof in the body-in-white.*

2. Subsequently, the results obtained from the previous simulation will be used as input to perform a post-buckling simulation of the temperature-displacement implicit type, considering geometric non-linearities.

2.1 Thermal buckle simulation: aluminum alloy car roof with geometry equivalent to a steel roof

As emphasized in Chapter 3, establishing accurate boundary conditions is of paramount importance to achieve a precise representation of the buckling phenomenon. Therefore, it is crucial to numerically simulate these conditions in a manner that closely mimics real-world practices. In this context, the car roof is interconnected with the body-in-white through spot welding and brazing, as illustrated in figure 92. To capture the essence of these connections in

numerical simulations, MPCs (multi-point constraints) are employed. These constraints act as rigid beams between two nodes, constraining the displacement and rotation at the first node to match those at the second node. This simulates the presence of a rigid beam between the two nodes, ensuring that the translational and rotational behaviors of the interconnected points remain consistent. This prevents any relative rotation or translation between the car roof and the body-in-white at these specific points.

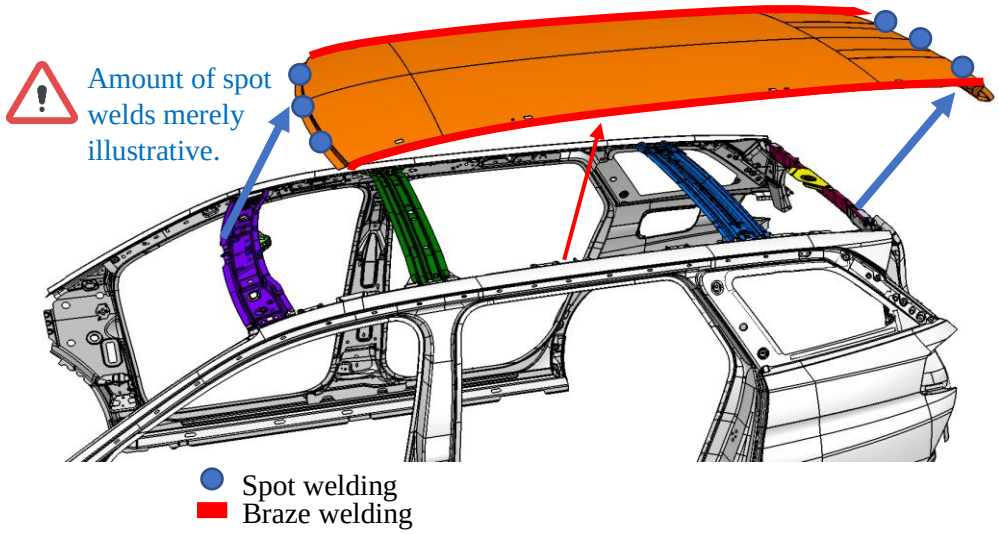

Figure 92 *Boundary conditions of the vehicle roof in relation to the body-in-white structure.*

Beyond the assembly approach, another crucial aspect to consider is the numerical model's meshing. Employing the Stellantis method and meshing criteria, all vehicle structures underwent meticulous meshing. Notably, the car roof received predominantly quadrangular meshes of type S4 (4-node doubly curved general-purpose shell, finite membrane strains) with an approximate global size of 5 mm per side. This resulted in an extensive mesh, comprising a total of 111 540 elements solely dedicated to modeling the car roof. Figure 93 visually depicts the final mesh representation for the car roof.

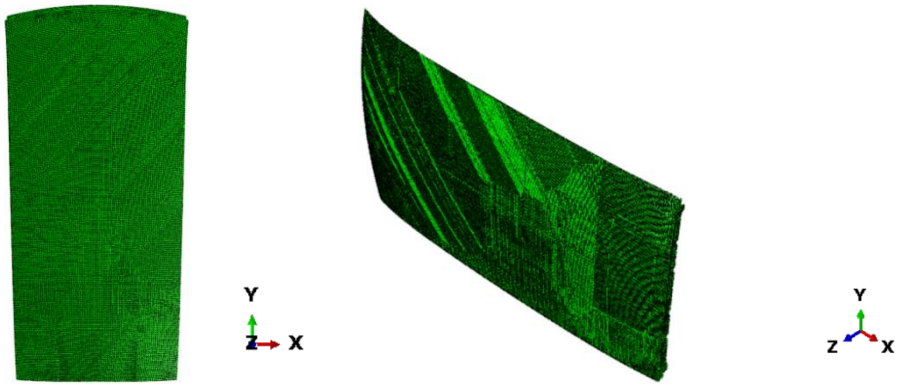

Figure 93 *Numerical mesh used in the car roof section. A total of 111,540 elements, predominantly of type S4, were employed to obtain the numerical solution for this part of the vehicle. The other type of elements, representing less than 0.1% of the roof mesh are elements of type S3R - 3-node triangular shell element with reduced integration. These last elements are used to handle geometry complexity parts.*

Just as it was carried out in the buckling analyses conducted for laboratory tests, the studied model employed a perturbing load in the form of temperature variation, inducing thermal expansion of the materials. To streamline the calculations, an initial temperature of 0°C was set for the model, and a temperature range of +1°C was applied as the perturbation load. As a result of the simulation, eigenvalues were obtained, which represent the buckling temperatures for each mode. Figure 94 illustrates the simulation results of the first eigenvalues for each side of the full-geometry model.

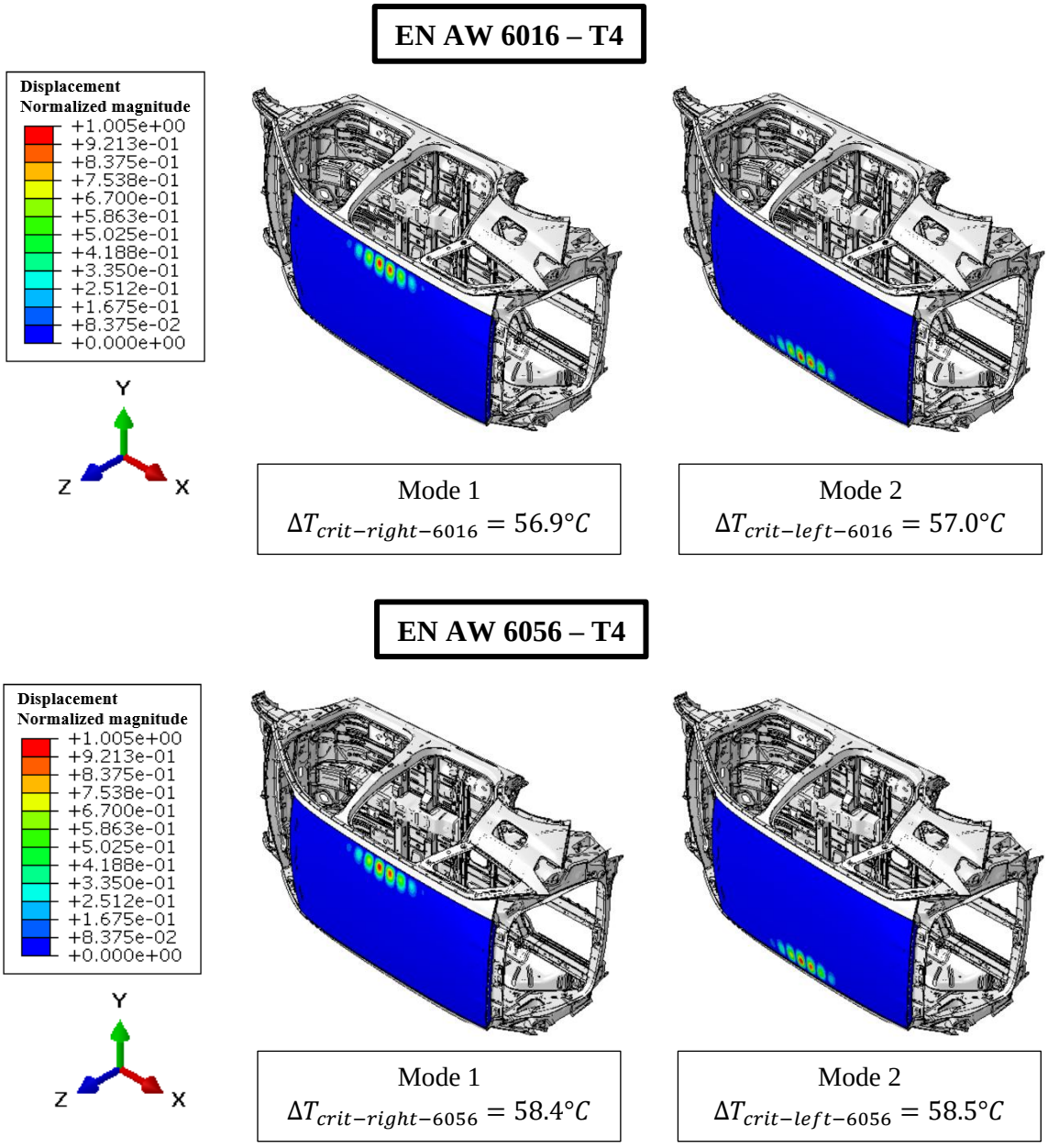

Figure 94 *Result of the thermal buckling analysis through Finite Element simulation.* $\Delta T_{crit-right}$ *and* $\Delta T_{crit-left}$ *represent, respectively, the temperature variation required to reach the first buckling mode on the right and left sides of the car roof.*

Upon analyzing figure 94, intriguing insights emerge. Notably, temperature variations of 56.9°C and 57.0°C are the critical points for inducing buckling on the right and left sides of the car roof, respectively, when constructed from EN AW 6016-T4. For the roof made of EN AW 6056-T4, the required temperature variations are 58.4°C and 58.5°C for inducing buckling on the corresponding sides. These findings unequivocally demonstrate that the first two modes constitute a singular symmetric mode, initiating practically at identical temperature variations. The relatively minor difference between the buckling temperatures for these two aluminum alloys can primarily be attributed to their slightly varying coefficients of thermal expansion, with values of $\overline{\boldsymbol{\alpha}_{\boldsymbol{th}_{6016}}} = 2.24 \,.\, 10^{-5}$ °C^{-1} and $\overline{\boldsymbol{\alpha}_{\boldsymbol{th}_{6056}}} = 2.23 \,.\, 10^{-5}$ °C^{-1}.

Additionally, the close proximity of the temperatures needed to induce buckling on the left and right sides of the roof suggests that buckling is likely to occur nearly simultaneously on both sides of the structure. An intriguing finding is that these buckling temperatures are relatively low when compared to the temperature variations encountered during the automotive industry's production process, which typically ranges from 140°C to 220°C (approximately 180°C in the studied case). Therefore, a post-buckling analysis becomes imperative to comprehensively assess the structural behavior beyond the buckling initiation stage.

2.2 Thermal post-buckle simulation: aluminum alloy car roof with geometry equivalent to a steel roof

Utilizing the same methodology as employed in the numerical simulations described in Chapter 3, the investigation of thermal post-buckling phenomena involved conducting simulations incorporating buckling mode shapes as geometric imperfections, introducing a factor of 0.01 within the model. To simulate the thermal effects encountered during the automotive painting phase, three temperature curve were employed as thermal loads (refer to figure 95). Given the substantial size of the structure, it is expected that temperature heterogeneities will manifest. For pragmatic purposes within an industrial context, the application of temperature is categorized into three distinct groups of components: external parts (surrounding the vehicle externally), internal parts (located in the vehicle's interior paint), and intermediate parts (between the external and internal components).

In light of the observations made in Chapter 3, wherein the thermal loads are progressively applied over time, the influence of acceleration in the post-buckling phase is deemed to be insignificantly consequential. Accordingly, an implicit analysis approach is deemed most appropriate for scrutinizing the problem. Moreover, considering that post-buckling deformations are not directly proportional to the applied loads, the simulation incorporates geometric nonlinearity.

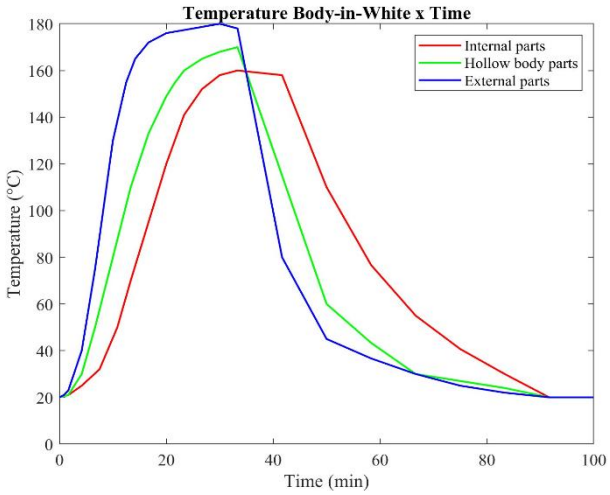

Figure 95 *Temperature graph used in numerical analysis. The structural components are divided into three groups: external parts (surrounding the vehicle externally), internal parts (located in the vehicle's interior), and hollow body parts (between the external and internal components).*

In Chapter 2, the mechanical properties of the aluminum alloys were examined during the heating phase. However, the thermal post-buckling analysis requires a comprehensive understanding of their behavior after the subsequent cooling phase. To achieve this, tensile tests were performed, with the same standards and test conditions (at least 3 valid tests per temperature condition) as those utilized in Chapter 2. Considering the isotropic nature of the material concerning Young's modulus and yield strength, the tensile tests were exclusively conducted with the aluminum alloys cut in the longitudinal direction (rolling direction). To avoid redundancy of information already presented in Chapter 2, this section will solely focus on presenting the curves of the average temperature cycles (figure 96) and the stress-strain relationships (figure 97) derived from the tensile tests.

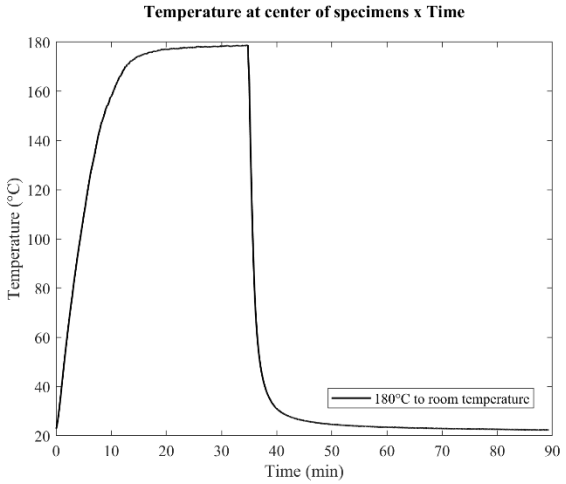

Figure 96 *Average temperature evolution measured by thermocouple located at the center of aluminum alloy specimens.*

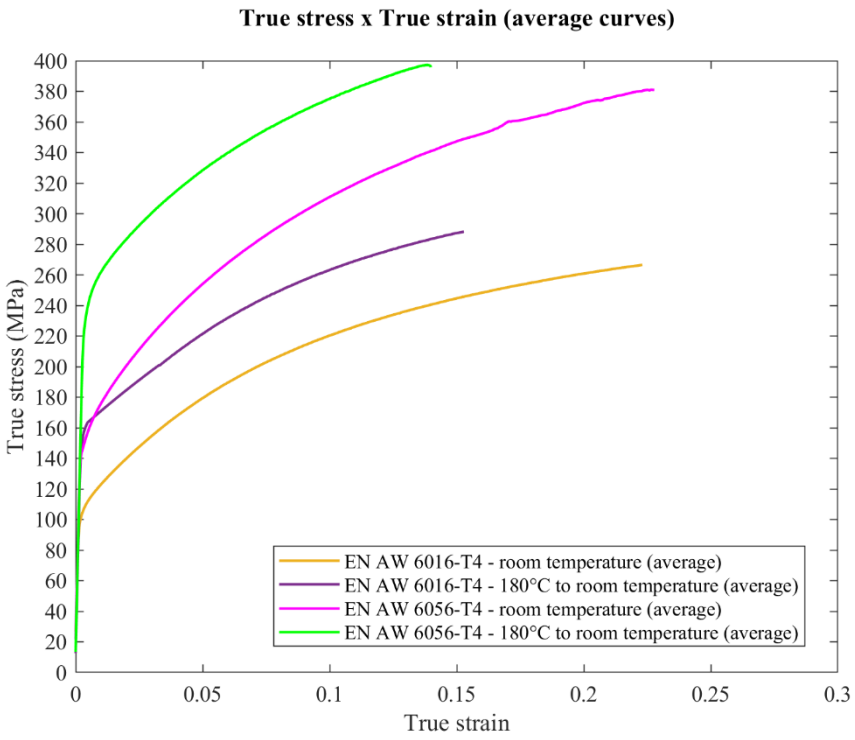

Figure 97 *Average true stress x strain curves obtained for the room temperature situation both before and after the heating process. The material's properties at room temperature before the heating process were extracted from Chapter 2.*

Table 15 *Result of the analysis of the mechanical properties.* $\overline{Rp_{0.2}}$ *is the average of the elastic limits obtained with an offset of 0.2% from the elastic zone;* $\sigma(\overline{Rp_{0.2}})$ *is the standard deviation of the elastic limits;* $\overline{E}$ *is the average of the Young's moduli;* $\sigma(\overline{E})$ *is the standard deviation of Young's moduli.*

	Temperature	$\overline{Rp_{0.2}}$ (MPa)	$\sigma(\overline{Rp_{0.2}})$ (MPa)	$\overline{E}$ (GPa)	$\sigma(\overline{E})$ (GPa)
EN AW 6016-T4	Room Temp.	107.67	4.34	65.19	0.46
	180°C → Room Temp.	162.68	5.94	67.43	0.65
EN AW 6056-T4	Room Temp.	155.20	1.39	70.38	0.09
	180°C → Room Temp.	242.93	7.47	71.10	0.82

For the thermal post-buckling analysis, aluminum alloys aged for 3 months were specifically chosen due to their slightly lower yield strength in this condition compared to the natural aging state of 6 months. This deliberate selection ensures that the examination focuses on the most critical scenario, where the material's response is more susceptible to thermal effects and potential buckling.

Upon reviewing the data in table 15, a notable distinction is observed in the yield strength of EN AW 6016-T4 between the case before (107.67 MPa) and after (162.68 MPa) the heating cycle, exhibiting a substantial variation of 55 MPa between the two cases. Similarly,

the EN AW 6056-T4 alloy exhibits a notable difference of 70 MPa in the yield strength between its room temperature state before (155.20 MPa) and the state after (242.93 MPa) the 180°C heating cycle. Such differences in yield strength become crucial to consider in the post-buckling analysis.

On the other hand, despite the substantial variations in yield strength, the Young's modulus of both materials did not show significant differences between their states before and after the heating cycle at 180°C. This suggests that Young's modulus, while sensitive to changes in temperature during testing, remains relatively stable when tested at the same temperature, regardless of the specific heating cycle the material underwent after the T4 heat treatment. This result demonstrates that the Young's moduli of these alloys are primarily influenced by the current temperature conditions during the testing phase, rather than the historical thermal treatment history of the material.

Using the material properties obtained from both aluminum alloys, a post-buckling simulation was performed on the aluminum alloy car roof, designed to mimic the geometry of the steel roof. Given the intricate nature of vertical displacement curves, which deviate significantly from the simplistic hyperbolic shape typically encountered around the point of buckling, employing the Shariyat criteria becomes impractical. While effective for laboratory tests, it proves inadequate for the current scenario. Thus, an alternative methodology is essential to pinpoint the onset of buckling accurately. In light of this, the Budiansky method emerges as a more suitable approach [110]. This criterion relies on identifying a sudden change in the curvature of the load-displacement or temperature-displacement response curve.

To visualize and analyze the post-buckling behavior, figures 98-A and 99-A were generated. These figures respectively present the out-of-plane displacement curves for the EN AW 6016-T4 and EN AW 6056-T4 roofs. The data was derived from the results of post-buckling simulations performed along specific lines, as highlighted by the red lines in figures 98-B and 99-B. These analysis lines were strategically positioned at a distance of 62 mm from the right edge of the roofs, carefully chosen due to their alignment with the epicenter of the most significant out-of-plane displacements in a wavy format observed within the structure.

As depicted in figures 98-A and 99-A, the first pronounced changes in out-of-plane displacement manifest themselves at a temperature of 63.3°C, exhibiting a peak displacement magnitude occurring between the 1.2-meter and 1.4-meter positions along the length of the car roof.

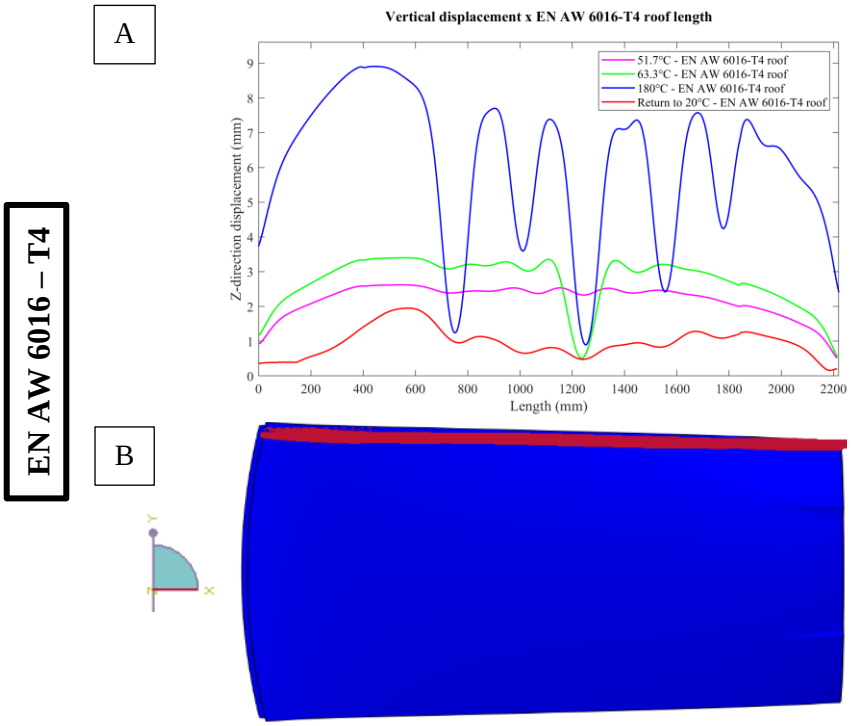

Figure 98 *EN AW 6016-T4 roof:* ***A)*** *Out-of-plane displacement curves derived from the results of post-buckling simulations along the red line highlighted in 98-B;* ***B)*** *Line at a distance of 62 mm from the right edge of the roof (epicenter of the most significant out-of-plane displacements).*

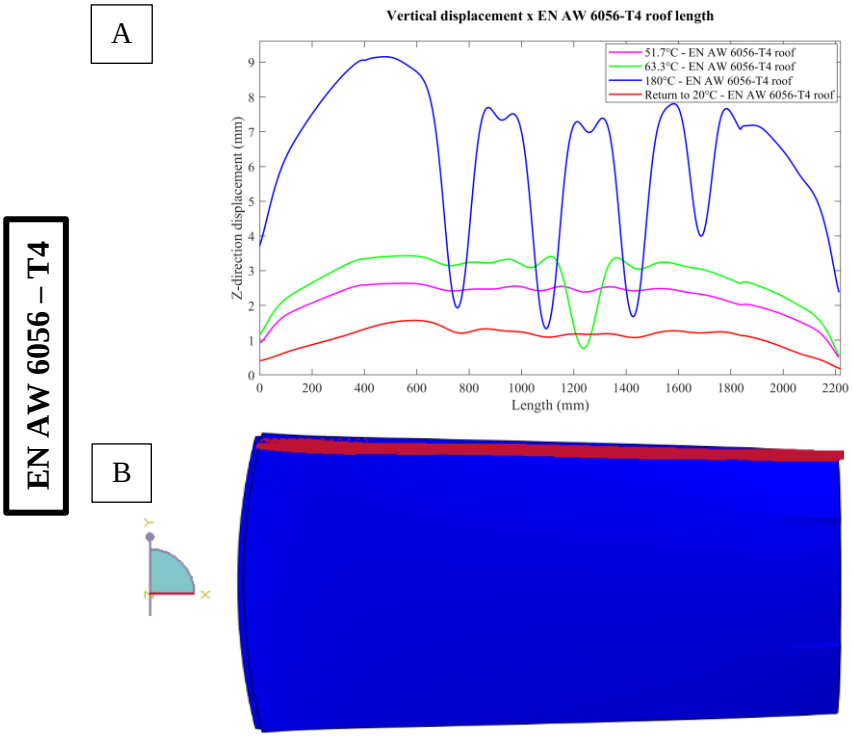

Figure 99 *EN AW 6056-T4 roof:* ***A)*** *Out-of-plane displacement curves derived from the results of post-buckling simulations along the red line highlighted in 99-B;* ***B)*** *Line at a distance of 62 mm from the right edge of the roof (epicenter of the most significant out-of-plane displacements).*

To highlight and facilitate the comparison of the behavior between car roofs made of EN AW 6016-T4 and EN AW 6056-T4, the displacements in the Z-direction of the structures were isolated in figure 100. The comparison is carried out under two specific conditions: at 180°C (figure 100-A), representing the maximum displacement due to appearance defects, and at return to 20°C after the heating cycle (figure 100-B - displacement resulting from post-buckling).

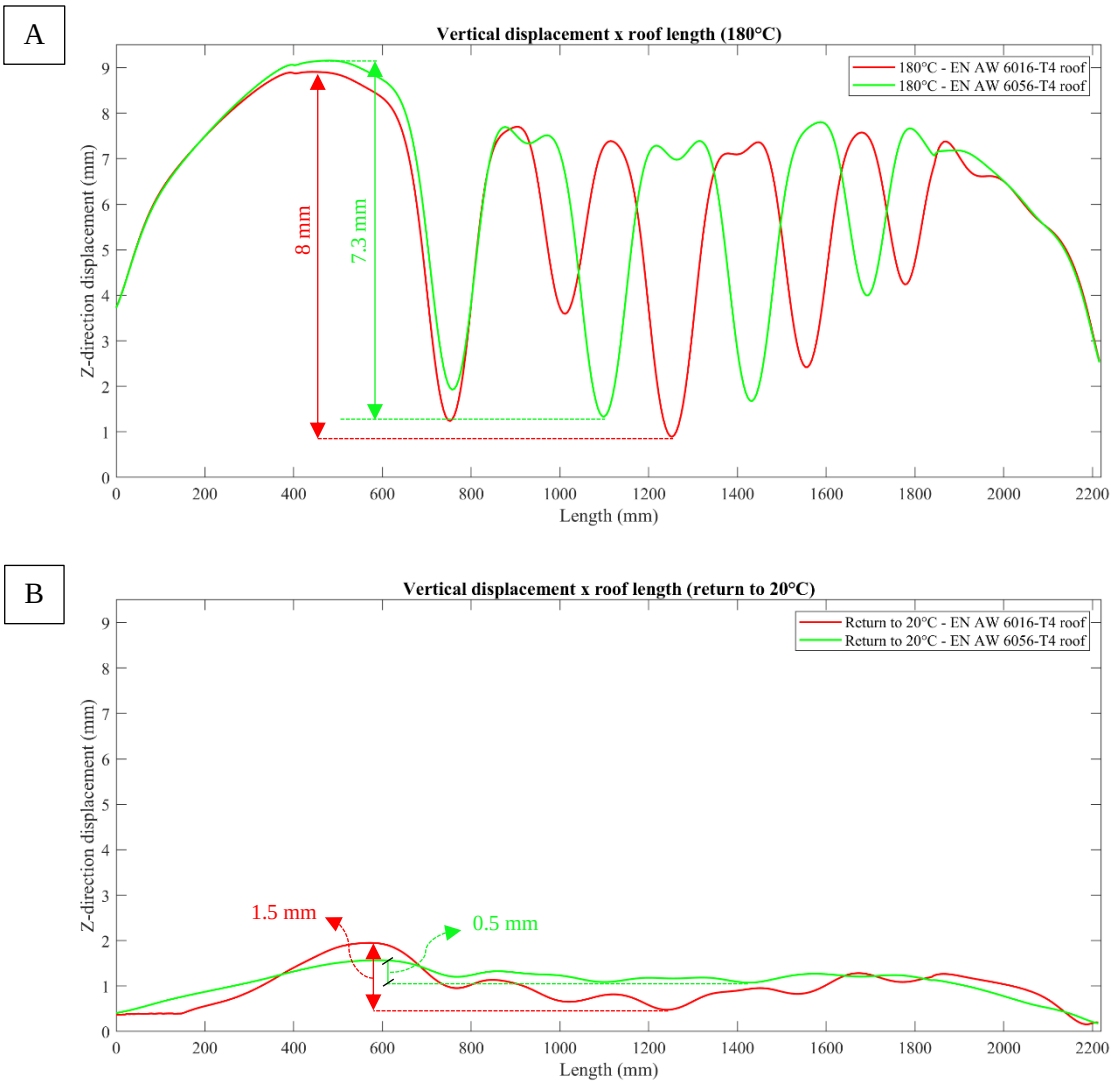

Figure 100 *Comparative transverse displacement curves of the car roofs made of EN AW 6016-T4 and EN AW 6056-T4 are illustrated for two specific conditions:* ***A)*** *At 180°C;* ***B)*** *At 20°C after the heating cycle.*

For the EN AW 6016-T4 roof, at 180°C, the Z-directional displacement reaches a maximum value of 8.9 millimeters, with a minimum displacement of 0.9 millimeters, resulting in a maximum difference of 8.0 millimeters. On the other hand, the EN AW 6056-T4 roof exhibits a Z-directional displacement with a maximum value of 9.2 millimeters and a minimum displacement of 1.9 millimeters, resulting in a maximum difference of 7.3 millimeters. In summary, when comparing the behavior of car roofs made of EN AW 6016-T4 and EN AW

6056-T4 at 180°C, the EN AW 6056-T4 roof shows a maximum difference of 7.3 millimeters in Z-directional displacement, which is 0.7 millimeters less than that of the EN AW 6016-T4 roof. This variance stems primarily from variations in thermos-mechanical properties, notably differences in expansion coefficients, rigidity, and elastic yield characteristics.

Upon returning to a temperature of 20°C, the displacement curves exhibit subtle undulations in response to the structure's behavior. These undulations pose a potential challenge to the structure's visual conformity, introducing irregularities and deviations from the desired aesthetic standards. Once again, the EN AW 6056-T4 outperforms the EN AW 6016-T4, with a residual displacement of 0.5 mm between the maximum and minimum displacement in the undulated region, compared to 1.5 mm for the latter, indicating a value three times lower.

In order to confirm the accuracy of the displacements obtained in the post-buckling simulation, a scan analysis was conducted within a designated insulated area, as depicted in Figure 101 – A. This analysis aimed to scrutinize the car roof made of the material with the poorer performance in the post-buckling situation between the two chosen materials: the EN AW 6016-T4.

Regarding the scans, they were conducted using laser scanning technique. The scan analysis employed the HandySCAN BLACK™|Elite scanner [111] (figure 101 – B). This scanner possesses an accuracy of 0.03 mm and operates on the principle of triangulation [112]. Additionally, this device gets the depth information of the scene through stereo vision methodology. In this process, a laser projects a structured pattern onto the surface of the object being scanned. The structured light pattern is reflected off the surface of the object. The geometry of the object causes distortions in the pattern's shape and position. The cameras captures images of the reflected light pattern. These images contain information about the distortions caused by the object's surface geometry. By analyzing the captured images, the system calculates the 3D coordinates of points on the object's surface based on the observed distortions in the light pattern. This calculation is achieved using trigonometric principles, hence the term "triangulation." The calculated 3D coordinates are combined to form a point cloud, which represents the surface geometry of the scanned object. Each point in the point cloud corresponds to a specific location on the object's surface.

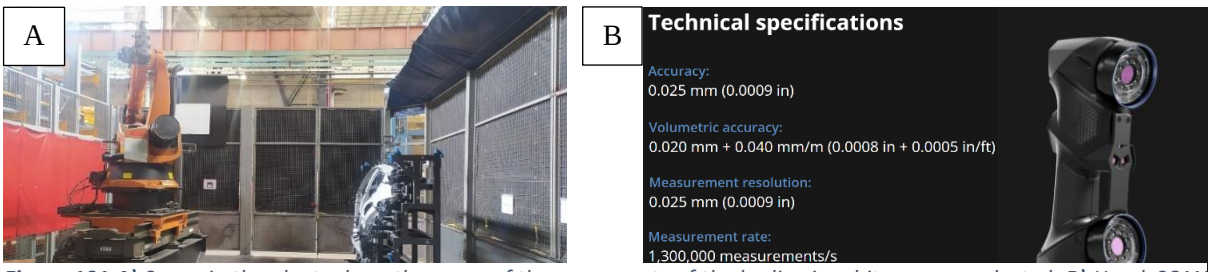

Figure 101 A) *Space in the plant where the scans of the upper parts of the bodies-in-white were conducted;* ***B)*** *HandySCAN BLACK™|Elite scanner [111].*

The virtual post-processing analysis was carried out using the Polyworks software [113] and the scan results are depicted in figure 102. Upon examining the results, it becomes evident that the lateral areas of the car roof display severe appearance defects, with the most significant displacement variation occurring in the Z-direction within the undulated region, measuring 1.3 mm. To corroborate the validity of the post-buckle simulation findings, a comparison was made between this measurement and the 1.5 mm displacement value obtained from the numerical analysis. The notable alignment between these values confirms the correlation in terms of the order of magnitude of the displacements, thereby fortifying the reliability and accuracy of the simulation model.

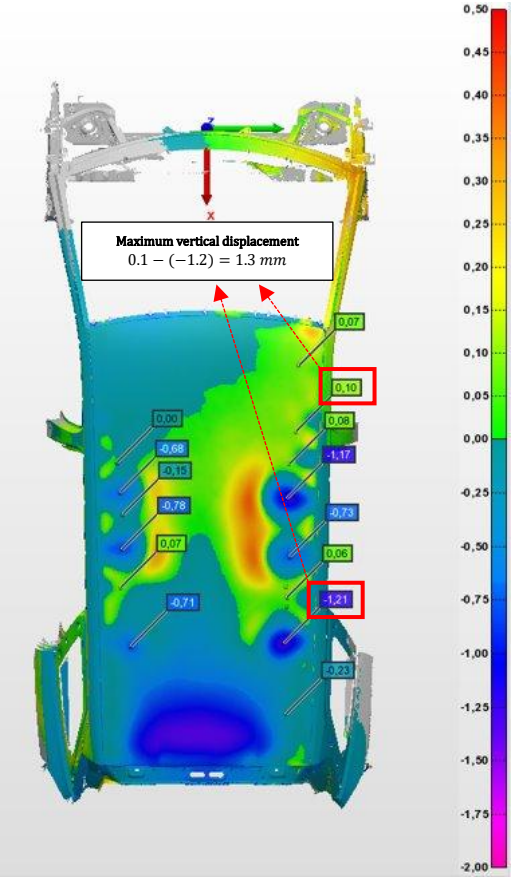

Figure 102 *Vertical displacement results obtained through the scan conducted with the car roof made of EN AW 6016-T4. Measurements are in millimeters.*

After correlating the displacements of the real structure with those obtained from the numerical simulation, it is possible to take a step further to complement the analyses. Figure 103 and figure 104 illustrate the outcomes of the numerical simulation analysis conducted on the z-directional displacement field, plastic deformation patterns, and principal compressive stresses, providing insights into the mechanical behavior of the car roof made of EN AW 6016 and EN AW 6056, respectively, at different temperatures. The chosen temperature points

included 20°C, 63.3°C, 180°C, and the return to 20°C. These results offer a comprehensive understanding of how the car roof responds to thermal loading conditions, aiding in optimizing its design and material selection for enhanced performance. At the initial condition for the post-buckling simulation (20°C), the structure exhibited stability. Then, at 63.3°C, buckling initiation was observed for both materials. In figure 103 and figure 104, the circled red regions in the displacement field and principal compression field indicate the appearance of displacement and stress peaks. This signifies the onset of buckling. Additionally, analyzing the plastic strain field revealed that, for both materials, the structure experienced buckling while still within the elastic strain domain.

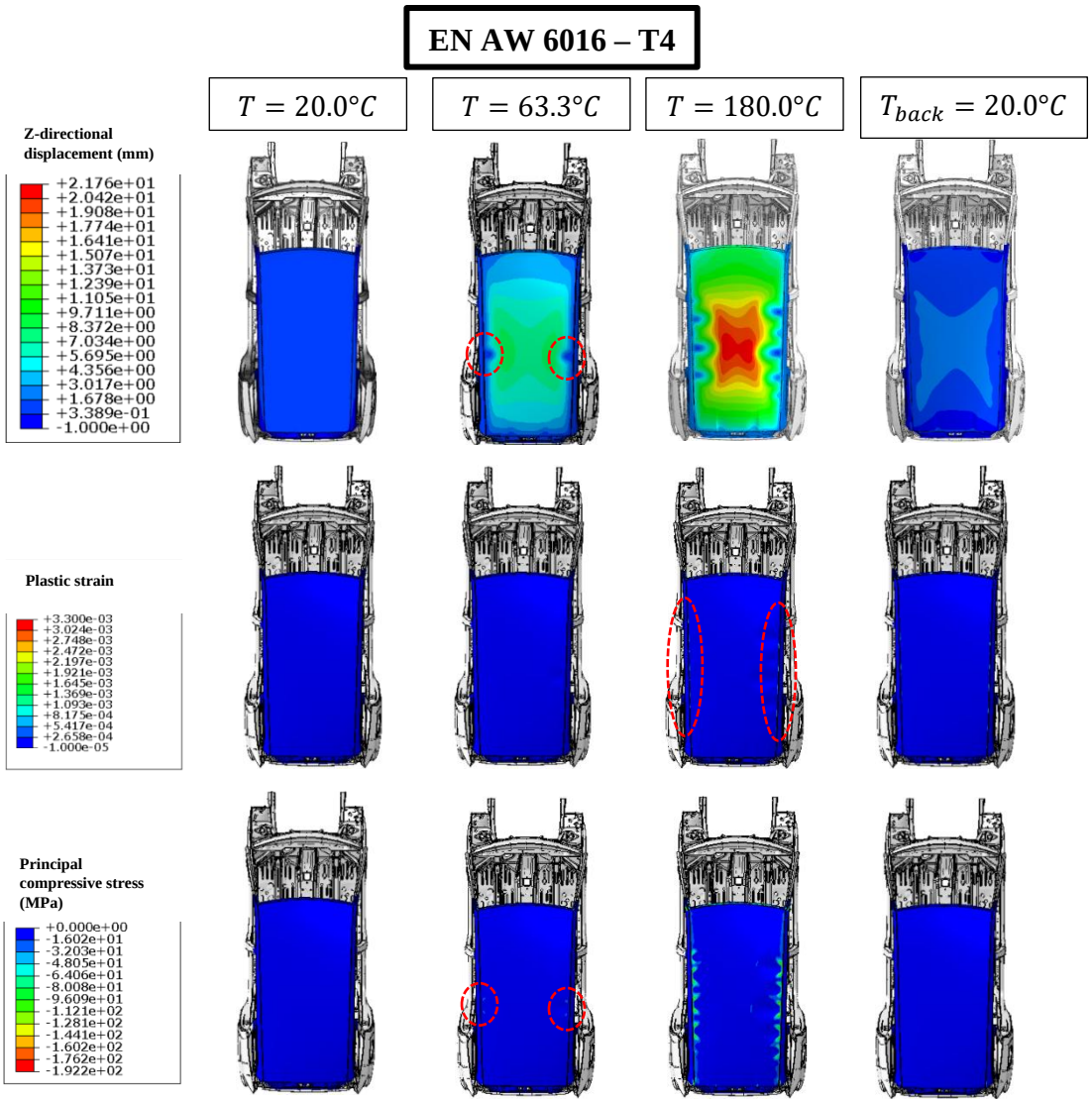

Figure 103 *Body-in-white analysis of Z-directional displacement, plastic strain, and principal compressive stresses fields at 20°C, 63.3°C, 180°C and return to 20°C. Material: EN AW 6016-T4.*

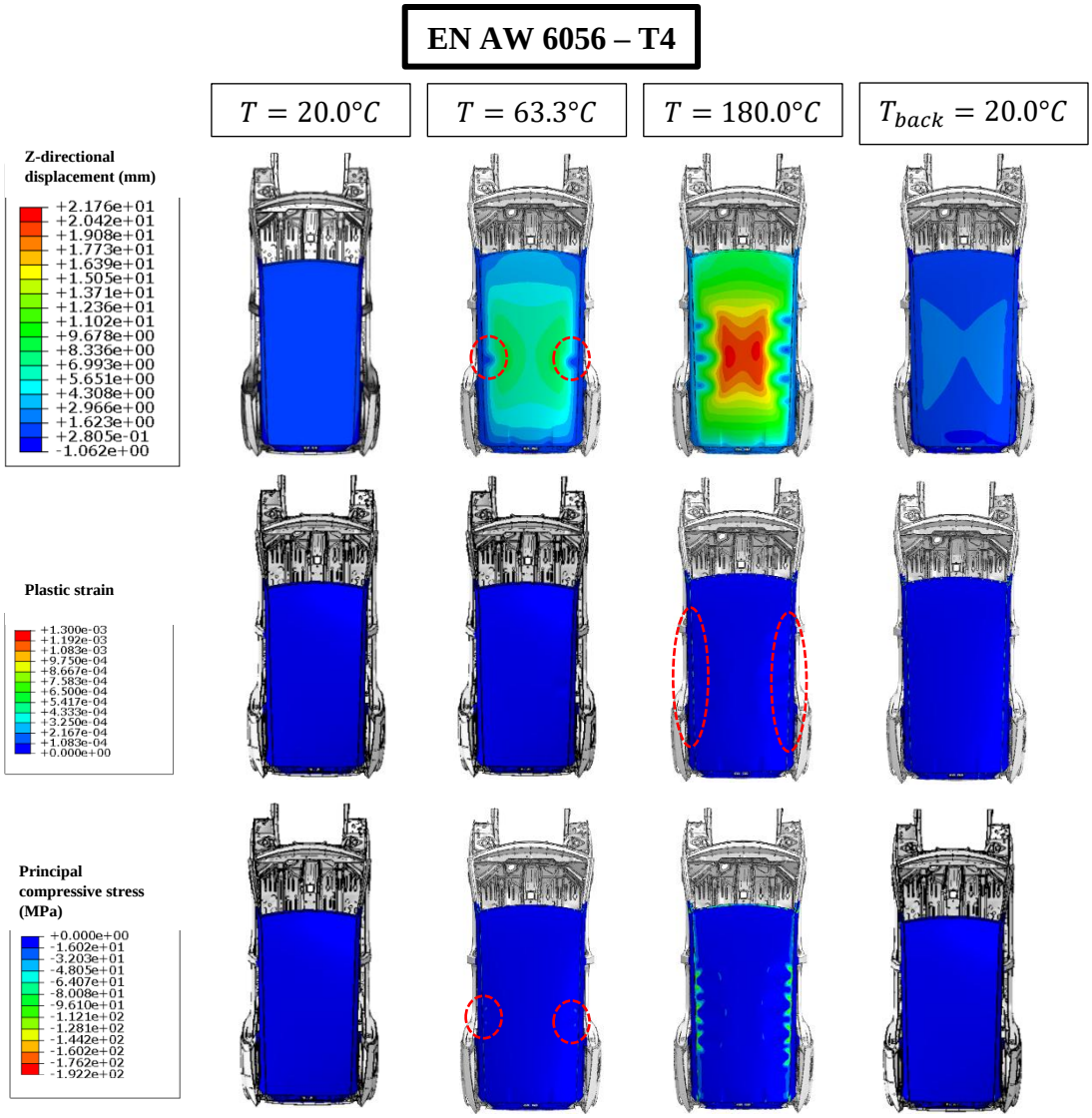

Figure 104 *Body-in-white analysis of Z-directional displacement, plastic strain, and principal compressive stresses fields at 20°C, 63.3°C, 180°C and return to 20°C. Material: EN AW 6056-T4.*

At 180°C, the displacement and stress analyses clearly revealed that the car roof had undergone buckling. The presence of numerous local peaks in these fields indicated significant displacement variations and the occurrence of plastic deformation. Particularly noteworthy was the circled red region in the plasticity analysis at the lateral borders of the roof, showing evidence of a plastic strain of 0.33% for the car roof made of EN AW 6016-T4 and 0.13% for the car roof made of EN AW 6056-T4. As observed, the car roof made of EN AW 6056-T4 demonstrated better results in terms of plasticity compared to the EN AW 6016-T4. This plastic strain resulted from the boundary condition imposed to represent the welding operations between the roof and the body side of the body-in-white. Since the plastic strain directly causes the structure to remain deformed even after the cooling process back to 20°C, it is logical to find more pronounced undulations in the car roof made of EN AW 6016-T4 compared to EN AW 6056-T4 after the cooling phase.

Finally, by comparing the results of the physical test with those of the simulation, as presented in figure 105, a satisfactory correlation is observed in terms of the manner in which the structure buckles and the location of the buckling-induced undulations, which are predominantly found near the lateral edges of the roof. Hence, the visual conformity issues highlighted by the simulation were validated through the physical test.

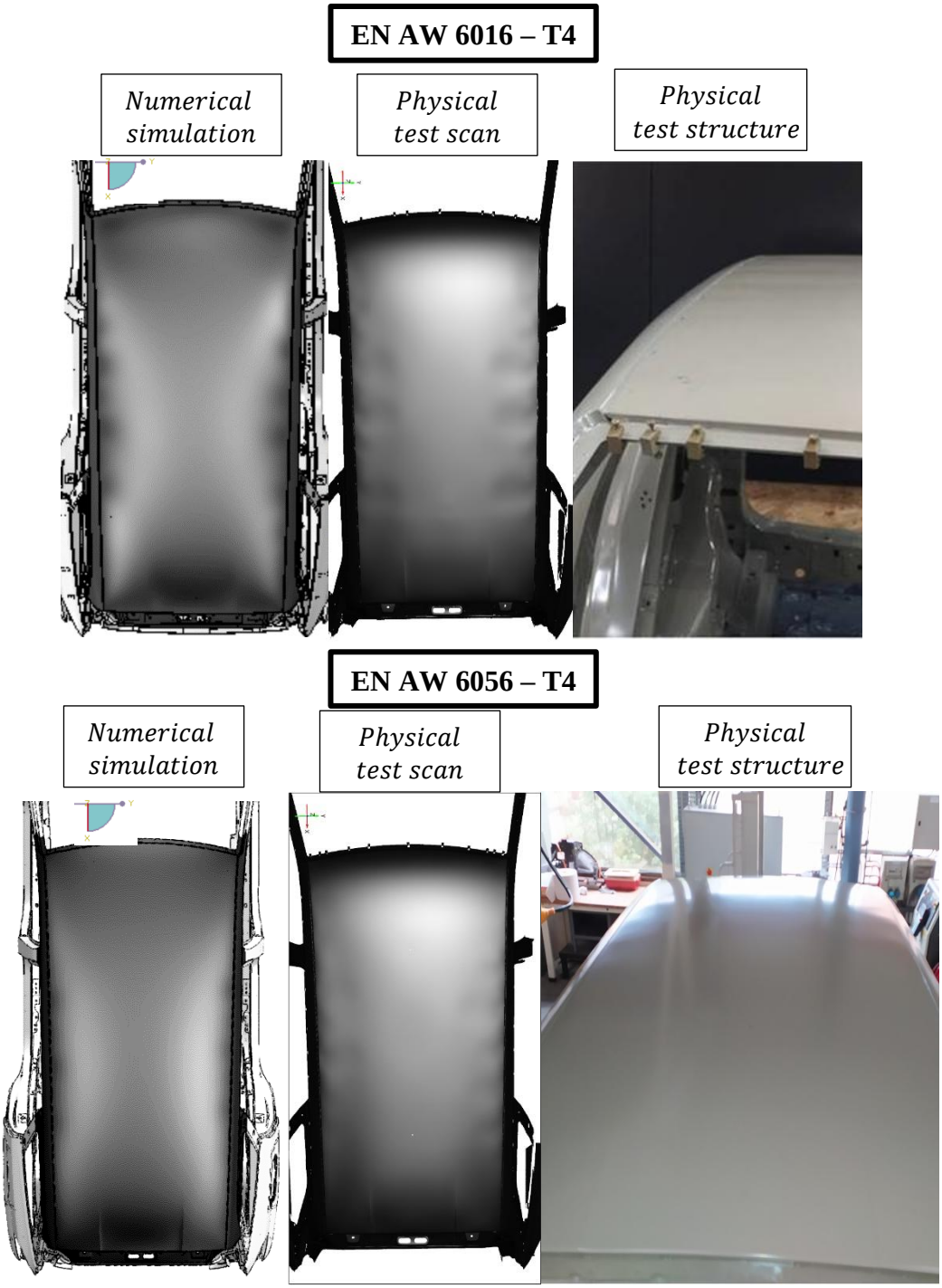

Figure 105 *Comparison of appearance results for the roof: numerical simulation, real structure scan, and photographic analysis (respectively, from left to right).*

2.3 Conclusive insights from analyzing aluminum alloy car roof with steel roof geometry

The current section presented an investigation into the instability issue faced by a car roof made of aluminum alloys EN AW 6016-T4 and EN AW 6056-T4 when assembled with a predominantly steel body. Due to the complexity and cost associated with conducting full-scale tests, a numerical methodology was developed to predict the thermal buckling behavior of the structure.

In accordance with the material properties of the two alloys, as detailed in Chapter 2, the tensile test analysis uncovered substantial disparities in yield strength between the room temperature state before and after the heating cycle at 180°C. For EN AW 6016-T4, the yield strength transitioned from 108 MPa at ambient temperature to 163 MPa at ambient temperature after the heating cycle, marking an increase of 55 MPa in the elastic limit or a 51% rise in comparison to the pre-heating cycle value. In the case of EN AW 6056-T4, this difference is even more pronounced, with the yield strength escalating from 155 MPa at ambient temperature before the heating cycle to 243 MPa at ambient temperature post-heating, indicating a disparity of 88 MPa or a 57% increase relative to the ambient temperature yield strength prior to heating. This emphasizes the critical importance of accounting for thermal effects in post-buckling analyses. Additionally, the Young's modulus of both materials exhibited sensitivity to testing temperature variations (information in Chapter 2) but remained relatively unaffected by the specific heating cycle applied after the T4 heat treatment.

Structurally, it was observed that buckling issues arise at a temperature difference of approximately 63°C while the structure is still within its elastic regime. Such temperature variations are relatively small compared to the maximum temperatures experienced during production (180°C), making it crucial to account for post-buckling behavior to predict the final appearance of the roof. In this section, the consideration of buckling modes for post-buckling simulation was accomplished by introducing imperfections with an amplitude factor of 0.01 into the model.

Based on the results obtained from the simulations, it was observed that the car roof structure exhibits undulations at the conclusion of the heating phase. These undulations manifest as deviations from a smooth and uniform displacement pattern. Specifically, the maximum amplitude of these undulations near the lateral edges of the roof was measured to be 1.5 mm for the case where the material used was EN AW 6016-T4. This outcome aligns closely with real-world scan results of the car roof, where a maximum vertical displacement of 1.3 mm was recorded. Furthermore, the location of these undulations corroborates the numerical simulation, validating the numerical model as sufficiently representative of reality.

In contrast to the observations with the roof composed of EN AW 6016-T4, when using EN AW 6056-T4 material, the maximum amplitude of undulations decreased to 0.5 mm. This notable discrepancy in the magnitude of undulations between the two materials underscores the impact of material selection on the post-buckling behavior of the car roof under thermal loading conditions. The superior performance of EN AW 6056-T4, evident from the reduced amplitude of undulations, highlights its potential to enhance the visual conformity and structural integrity of the car roof. Hence, the primary optimization derived from the study with the standard roof geometry is the selection of the material for further improvements. Since EN AW 6056-T4 demonstrated a superior response in terms of plastic deformation and residual displacement in the post-buckling analysis, the focus will be, from now on, exclusively on conducting structural analyses using this material, as depicted in figure 106.

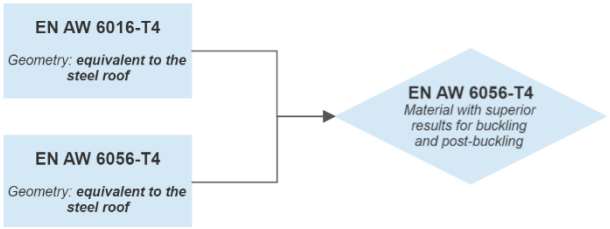

Figure 106 *Decision flowchart illustrating the selection of EN AW 6056-T4 as the material for optimized structural analysis.*

Based on the findings, it is evident that a cost-effective and timely solution is imperative. Considering the limitations of the production process, making substantial alterations to the production line may not be a feasible option. Instead, a viable approach involves implementing design modifications to enhance the critical buckling temperature. These modifications can be achieved by updating the modular stamping die to improve the car roof's resistance to buckling under thermal loading conditions. By optimizing the design utilized in the car roof, it becomes feasible to enhance its structural stability and overall performance when subjected to thermal stresses. This approach will help mitigate the instability issue faced by the car roof and ensure its visual conformity, without causing significant disruptions to the production process.

Hence, the forthcoming section will delve into a comprehensive study to analyze how alterations in the car roof's geometry can impact its critical buckling temperature. By scrutinizing these effects, the aim is to gain a deeper understanding of how design modifications can influence the roof's thermal behavior, thereby enhancing its resistance to buckling.

3. Influence of the car roof's geometry parameters on the critical buckling temperature

In order to investigate the influence of the car roof's geometry parameters on the critical buckling temperature, the analysis will commence with an analogous and straightforward case - a rectangular plate with clamped boundaries subjected to heating. This choice is based on the

similarities between this geometric shape and the car roof's structure. Subsequently, the current analysis will focus on examining the impact of introducing curvatures in both the width and length of the rectangular plate on its resistance to thermal buckling. This study aims to gain valuable insights into how design modifications can affect the car roof's thermal behavior and enhance its ability to withstand buckling under thermal loading conditions.

3.1 Influence of curvature of a fixed rectangular plate on the thermal buckling

3.1.1 Flat rectangular plate (without curvature)

Analytically, the thermal buckling equations developed by Ko and Jackson [114 - 116] for uniformly heated and constrained rectangular panels using the Rayleigh–Ritz method, written in terms of temperature rise (ΔT) for each set of integral values $\{m, n\}$ (or mode shape), have the following form when the coefficient of thermal shear distortion is zero:

$$\sum_k \sum_l [\frac{M_{mnkl}}{\Delta T} + P_{mnkl}] \, . A_{kl} = 0 \quad (93)$$

Where M_{mnkl} is the bending-stiffness parameter, P_{mnkl} the extensional stiffness parameter and A_{kl} Fourier coefficient of trial function for out-of-plane displacement *w*. As the objective of this chapter is to explore geometric modifications to enhance the car roof's resistance to thermal buckling, the focus will be on comparing the results of the analytical model developed by Ko [115] with the numerical model. This comparison will allow observation of how variations in shape influence the critical buckling temperature and the structural buckling behavior. Therefore, the equations of the terms in equation (93) will not be developed in this report but are shown in reference [114]. When equation (93) is reduced to the isotropic case with no transverse shear effects, the buckling temperature will be independent of the material's modulus of elasticity [117]. The first-order solution for the constant temperature case, where the number of buckle half waves in the *x*-direction (m) and number of buckle half waves in *y*-direction (n) and the index l and k are equal to one, gives:

$$\Delta T_{crit} = \frac{\pi^2 . t^2}{9 . \alpha . (1+\upsilon)} \, . \frac{\frac{3}{a^4} + \frac{2}{a^2 . b^2} + \frac{3}{b^4}}{\frac{1}{a^2} + \frac{1}{b^2}} \quad (94)$$

Where a is the length, b is the width, t is the thickness, υ is the Poisson's ratio, α is the thermal expansion coefficient of the material (in this case, of EN AW 6056-T4), and ΔT_{crit} is the critical temperature variation. Figure 107 graphically depicts the geometric parameters of the studied plate.

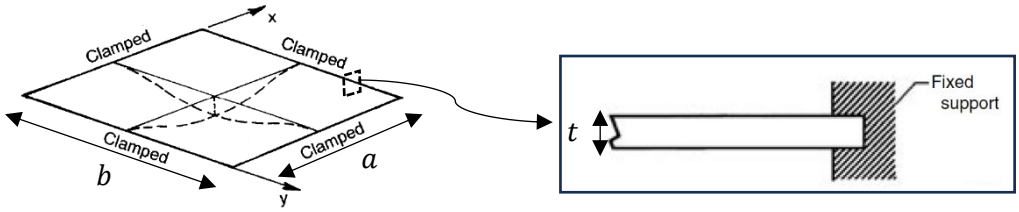

Figure 107 *Geometric representation of the case studied for thermal buckling of a rectangular plate with fixed boundaries. Figures taken from [114] and [115] - adapted.*

For the study, a rectangular plate with dimensions similar to those of the car roof but in a completely flat structure will be selected. Geometric measurements will be as follows: a = 2300 mm, b = 1000 mm and t_s = 1.1 mm. The properties of EN AW 6056-T4, as presented in Chapter 2, will be utilized. Through equation (94), it is possible to observe that the analytically calculated critical temperature variation for the study plate is $\Delta T_{crit} = 0.12°C$.

After obtaining the analytical result, a numerical buckling simulation was conducted for the rectangular plate clamped with the same geometric parameters used in the theoretical calculation. As in previous cases, here too, the imposed temperature variation for calculating the critical temperature variation was 1°C with a uniform temperature profile heating. The mesh criteria were the same as those chosen for the vehicle's roof, meaning that the mesh was S4 with global size elements of 5 mm, totaling 92,000 elements for the plate simulation. Through numerical simulation, a critical temperature of $\Delta T_{crit} = 0.13°C$ was obtained. The result can be seen in figure 108, and the comparison between the temperatures obtained analytically and numerically is shown in table 16.

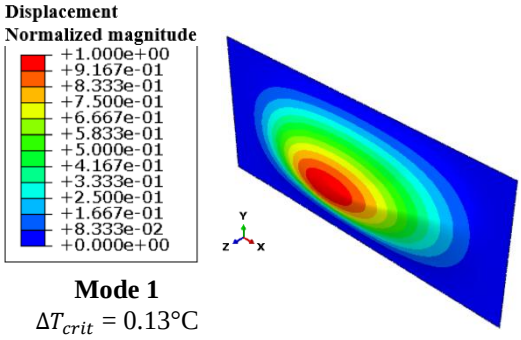

Figure 108 *Result of the thermal buckling analysis through Finite Element simulation for a rectangular plate with clamped boundaries.*

Table 16 *Comparison of critical buckling temperatures obtained analytically and numerically for the first mode of buckling for a rectangular plate with clamped boundaries.*

CRITICAL TEMPERATURE VARIATION – CLAMPED RECTANGULAR PLATE		
ΔT_{crit} analytical	ΔT_{crit} numerical	ΔT_{error}
0.12°C	0.13°C	8.3%

The primary conclusion drawn from the thermal buckling analysis for the rectangular plate with clamped edges is the remarkably low critical buckling temperature required to initiate the first buckling mode. Additionally, it is noteworthy to observe that the shape of the first mode exhibits half waves both in the x-direction and y-direction, significantly differing from the shapes of the first two modes of the car roof. Subsequently, the analysis will examine a case more closely aligned with the geometry of the car roof: a curved rectangular plate with clamped edges. Initially, the focus will be on cases where the curvatures are present in only one direction (either along the length of the plate or along its width). This approach allows for a concentrated examination of the influence of these unidirectional curvatures on the critical buckling temperature.

3.1.2 Curved rectangular plate along the length or width

As in the previous section, since the buckling simulation yielded good results compared to theoretical equations, the study of the behavior of unidirectionally curved rectangular plates will be conducted solely through numerical means. This approach will expedite the acquisition of results and the analysis of how the structure buckles.

For the purpose of comparison with the results obtained from the rectangular plate without curvature, the analysis of curvatures will also be conducted with a plate of length (a) of 2 300 millimeters and width (b) of 1 000 millimeters. The introduction of a radius of curvature in the length direction (r_{length}), or a radius of curvature in the width direction (r_{width}) will then commence. Initially, the focus will be on observing independently the longitudinal and transverse radii of curvature, with the latter having an infinite radius, i.e., remaining flat on one side, as illustrated in figure 109.

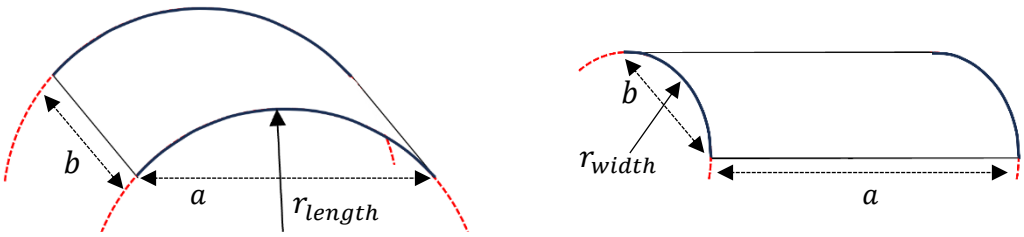

Figure 109 *Radii of curvature for the study of thermal buckling of a rectangular plate with fixed boundaries.*

The results of the analysis of the influence of curvature on the critical buckling temperature are shown in figure 110. It is observed that the critical buckling temperature for the first buckling mode evolves inversely with the radius of curvature.

Curvature radius (mm)	ΔT_{crit} – width direction (°C)	ΔT_{crit} – length direction (°C)
2 500	11.74	11.68
5 000	5.92	5.83
7 500	4.00	3.88
10 000	3.02	2.92
15 000	2.03	1.97

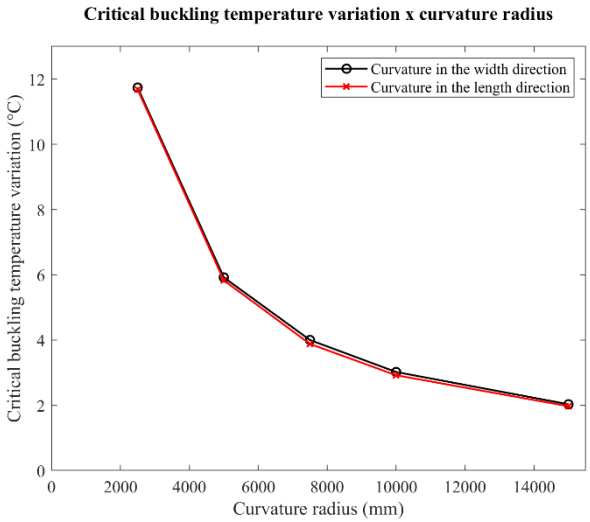

Figure 110 *Evolution of the critical buckling temperature in relation to the curvature radius (analysis to reach the first buckling mode).*

Therefore, in order to optimize the critical buckling temperature, a smaller radius of curvature proves to be the most favorable condition. Figure 110 underscores that, given the chosen geometry, the application of curvature to either the longitudinal or transverse radius yields a similar temperature outcome. This observation is clearly depicted in the graph section where the curvatures for transverse and longitudinal radii coincide. The extension of both curves further emphasizes that, irrespective of alterations to the radius of curvature, the impact on the buckling temperature remains consistent as long as its value remains constant. Finally, it is worth noting that the undulations disperse uniformly across the surface of the rectangular plate, whether the curvature is along the length (figure 111 - A) or width (figure 111 - B).

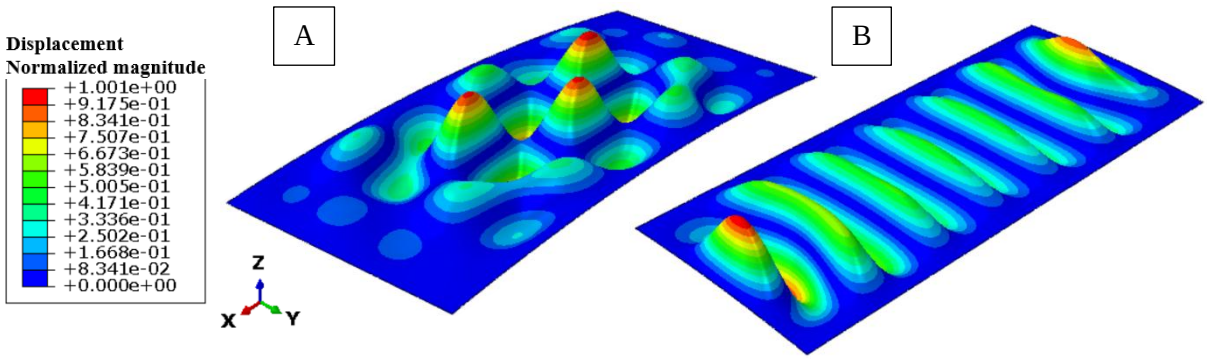

Figure 111 A) *Buckling with a dispersed shape throughout the rectangular plate when the curvature is longitudinal* ($r_{length} = 7500\ mm$)*;* ***B)*** *Buckling with a dispersed shape throughout the rectangular plate when the curvature is applied in the transverse direction* ($r_{width} = 7500\ mm$).

With these conclusions drawn, it is now intriguing to examine intermediate cases with two different curvatures imposed on the plate.

3.1.3 Curved rectangular plate along the length and width

The car roof has a geometry that is curved both in the width and length directions. For this reason, two distinct cases will be compared to better illustrate how the rectangular plate takes shape once it thermally buckles: the first case involves the rectangular plate having a much smaller radius of curvature in the length direction compared to the curvature radius in the width direction; the second case is the opposite, where the curvature in the length direction is much larger than in the width direction.

For the first case, r_{length}= 1 500 mm and r_{width} = 7 500 mm were chosen. For the second case, r_{length}= 7 500 mm and r_{width} = 1 500 mm. The numerical result for both cases is shown in figure 112. These selections were deliberate to underscore the profound influence of two distinct curvatures, thereby generating two markedly different scenarios: the former characterized by a width curvature radius significantly greater than that of the length curvature, while the latter features a width curvature radius substantially smaller than that of the length curvature. It is noteworthy that opting for a larger curvature radius value, such as 10 000 mm instead of 7 500 mm, would result in the side with this curvature radius approximating more closely to a planar surface, making it less intuitive to discern the impacts of the curvatures.

Certainly, contrary to the singular curvature plate with folds distributed across the entire plate, the scenario where the curvature in the length direction significantly exceeds that in the width direction exhibits localized folds. This configuration closely resembles the deformation pattern observed in the car roof simulation's buckling mode.

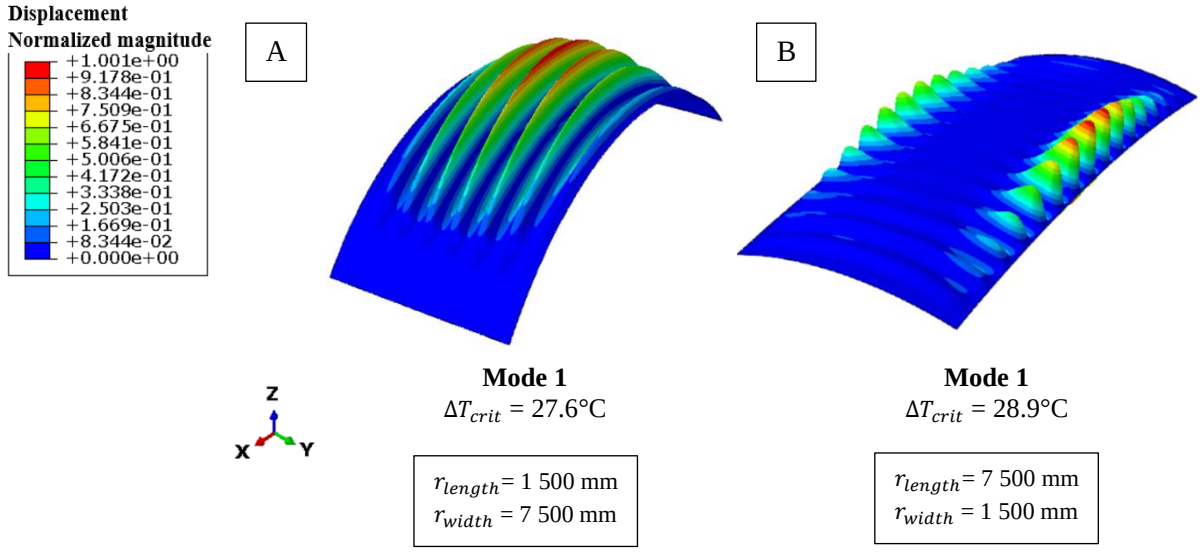

Figure 112 A) *Buckling result of the rectangular plate when the curvature is* r_{length} = 1 500 *and* r_{width} = 7 500 *mm;* ***B)*** *Buckling result of the rectangular plate when the curvature is* r_{length} = 7 500 *mm and* r_{width} = 1 500 mm.

The study conducted to understand the influence of curvatures in the width and length directions of a rectangular plate is valuable for drawing conclusions that contribute to the

comprehension of how the plate buckles and how the buckling temperature varies in each case. However, the body-in-white is the result of connecting various pieces with well-defined positions in the assembly and welding process. Therefore, making a significant change in the curvature of the roof would generate numerous connection issues with the parts connected to it. Consequently, it would be necessary to make changes to the steel components of the body-in-white, which, due to impracticality, is not an ideal solution.

Considering this, in addition to changing the curvature of the roof, another approach was studied to provide an efficient solution for increasing the stability of thin components: the addition of plastic deformation in a way that the car roof design is not compromised. The goal is to introduce local stiffening to the areas where the structure first undergoes buckling.

3.2 Influence of adding ribs on thermal buckling of a rectangular plate

The use of stiffeners has proven to be an effective method for increasing local stiffness in components, especially in areas susceptible to buckling. A numerical analysis conducted by (H. Layachi & Y. M. Xu, 2015) [118] , comparing three types of stiffened panels, concluded that the use of stiffeners generally enhances the stability performance of panels against mechanical loading. Additionally, (A. Pritykin, I. Kirillov, 2015) [119] reported an increase in the critical stresses of a clamped rectangular plate with an installed inclined stiffener through finite element analysis and experimental procedures.

In the case of the car roof, adding an attached structure would significantly compromise the brand's design, which is also a crucial consideration. Instead of reinforcing the structure locally with stiffeners, an alternative approach is to directly modify the roof design to induce local deformation, creating stiffer zones in the form of steps or grooves.

These localized design changes are referred to as ribs, and the goal is to position them mainly in areas that show initial signs of buckling, essentially at the epicenter of the maximum vertical displacement due to buckling. The study will proceed to investigate the influence of geometric parameters on thermal buckling, with a specific focus on assessing how the addition of ribs can impact the shapes of modes and the critical buckling temperature.

The addition of ribs will serve as an example on the same structure studied previously in figure 112 - B, which exhibits a mode shape similar to the first buckling mode of the car roof. As depicted in figure 113, two rectangular-shaped ribs will be considered, positioned equidistantly from the lateral edge of the rectangular plate. The design alteration was implemented 100 millimeters from the lateral edge of the rectangular plate, aligning with the epicenter of vertical displacements for the first buckling mode. Various values for the modification height (parameter h_{ribs}) were tested during the analysis. The parameter h_{ribs} was tested with both positive values (rib with upward prominence) and negative values (rib with downward prominence).

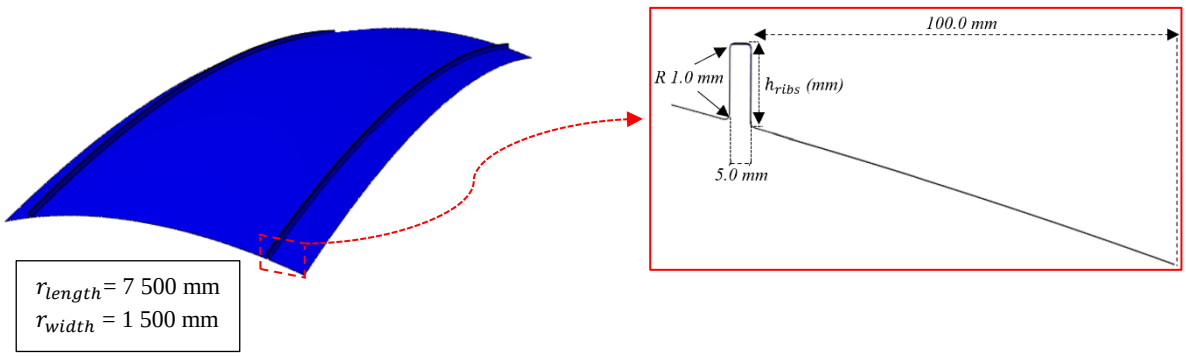

Figure 113 *Alteration on the curved rectangular plate of figure 112-B through the introduction of two rectangular-shaped ribs positioned 100 millimeters from the lateral edges of the rectangular plate.* h_{ribs} *represents the maximum height of the ribs.*

Additionally, the case where this parameter has a value of zero is considered the scenario without ribs in the structure, meaning the case of the unreinforced structure that has been previously studied and showed ΔT_{crit} = 28.9°C. The obtained values for the variations in critical temperature, where the reinforced structure reaches the first buckling mode, are shown in table 17. Based on the results obtained, a graph is plotted (see figure 114) to provide a visual representation of the evolution of the critical buckling temperature as a function of the reinforcement height.

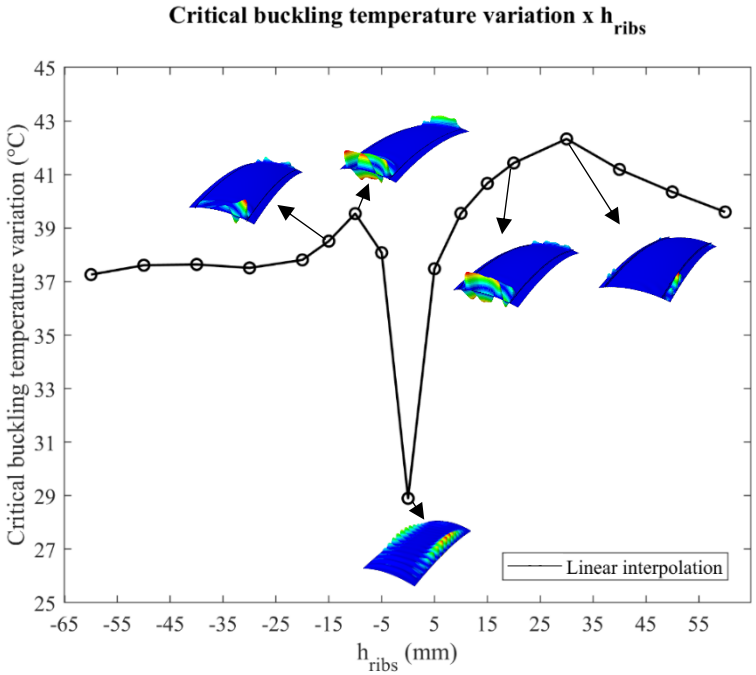

Figure 114 *Critical buckling temperature as a function of the chosen reinforcement height. The selected points for representation with images of the structure were points where the structure exhibited significant changes in the buckling mode.*

Table 17 *Results of ΔT_{crit} as a function of the parameter h_{ribs}.*

h_{ribs} (mm)	ΔT_{crit} (°C)	h_{ribs} (mm)	ΔT_{crit} (°C)
0	28.9	30	42.3
5	37.5	40	41.2
10	39.6	50	40.3
15	40.7	60	39.6
20	41.4		

h_{ribs} (mm)	ΔT_{crit} (°C)	h_{ribs} (mm)	ΔT_{crit} (°C)
0	28.9	-30	37.5
-5	38.1	-40	37.6
-10	39.5	-50	37.6
-15	38.5	-60	37.3
-20	37.8		

Observing the information shown in table 17, several conclusions can be drawn. The first is that the presence of reinforcements with a well-chosen height or depth allows for an increase in the buckling temperature. In the studied case, it is notable that the critical buckling temperature increased from 28.9°C in the case without reinforcements to 42.3°C when the ribs had a height of 30 mm and to 39.5°C when the ribs had a depression of 10 mm. This confirms that the design change for the addition of localized reinforcements is a viable solution that presents a good possibility of increasing the critical temperature.

The second conclusion is that up to a rib height or groove depth of 10 mm, the buckling temperatures increase in a generally symmetrical manner compared to the case without reinforcements.

Finally, it was noted that from a certain value of h_{ribs}, there is a sudden change in the way the structure buckles. In the configuration studied, each time the structure is stiffened, meaning each time the absolute value of h_{ribs} is greater, it becomes more resistant to the initially avoided mode, but it starts to facilitate the formation of another mode with a different shape. According to the points in figure 114, these values, in the studied case, are when the reinforcement has a height of 30 mm, in the case where the h_{ribs} parameter is positive, and -10 mm when h_{ribs} is negative.

The conclusions drawn from the addition of reinforcements to the longitudinally and transversely curved rectangular plate are highly complex, given that each case represents a unique scenario. In addition to height, there are several parameters that can be varied, potentially leading to different conclusions. These parameters include the quantity and positioning of reinforcements, the geometry of reinforcements, the geometry of the piece, boundary conditions of the problem, and the manner and intensity of how the load generating the disturbance is applied, among others. To obtain conclusions that are more closely aligned with reality at the scale of the vehicle, the study will continue by directly adding reinforcements to the structure of the car roof. This approach will enable the selection of the most suitable car roof design for the industrial context in which this study is situated.

4. Simulations: proposal for a new roof geometry

Advancing further in the investigation, the study will now delve into actual structural configurations for the car roof. As highlighted in the preceding section, incorporating ribs directly into the roof design has the potential to delay the onset of the first buckling mode. However, as emphasized earlier, the efficacy of this reinforcement is contingent on its specific form. Armed with this understanding, the focus shifts to an examination of various shapes for potential enhancements in structural appearance.

4.1 Ribs in the roof geometry

Three different reinforcement geometries were tested to be compared with the car roof without reinforcements initially studied. The same principle used for the rectangular plate was applied. In other words, the choice of the car roof that will be assembled into the body-in-white will be based on the buckle simulation result for a car roof with completely clamped edges, as show in figure 115 . Therefore, the higher the critical temperature to activate the first buckling mode, the better to avoid this problem and thus have fewer appearance defects.



Figure 115 *Fixed boundary condition applied to simulate the thermal buckling analysis of the isolated car roof.*

The disturbance load is induced by a temperature increase of 1°C, and the mesh predominantly consists of S4 elements with a global size of 5 mm. This mesh configuration mirrors the one used in the case of the roof with geometry equivalent to a steel roof, saw previously in this chapter. Figure 116 illustrates the different rib geometries tested and their respective results for the first buckling modes on each side of the car roof. The proposed geometries have been given specific names for easy reference. The geometry equivalent to the steel roof is named "standard," and the others are named "V2," "V3," and "V4," where "V" stands for "Version." Each proposed geometry was designed in collaboration with teams responsible for brand styling and stamping. This was done to verify the feasibility of each proposed solution. Initially, the ribs for each version were based on geometries from past Stellantis models. Due to the limitations of the modular stamping die developed for the aluminum alloy roof, designs with only two ribs, one on each side of the car roof near the lateral edges, in the length direction, could be proposed.

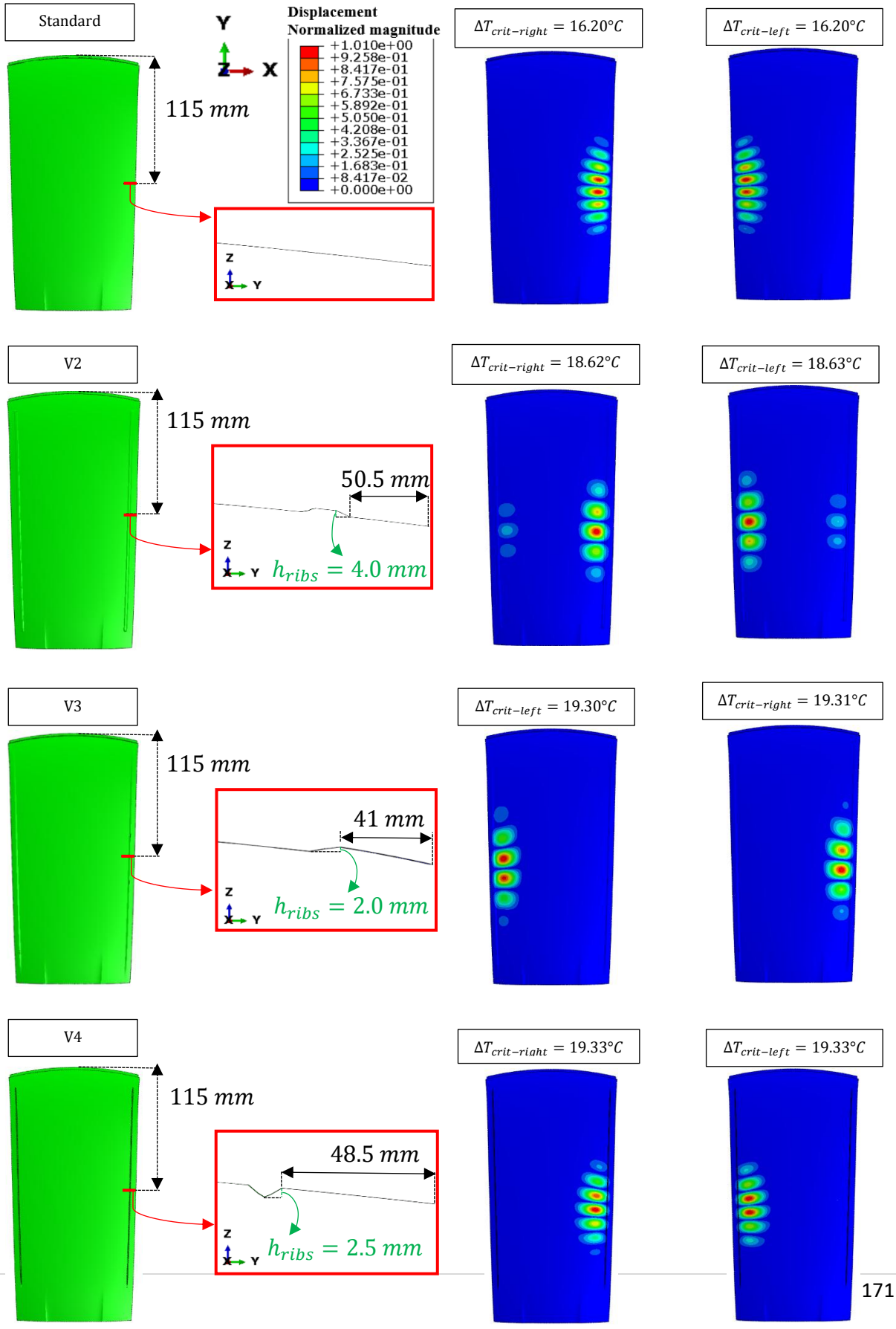

Figure 116 *Different rib geometries tested and their respective results for the first buckling modes on each side of the car roof.*

As shown by the results in figure 116, the proposed versions that achieved higher critical buckling temperatures were versions V3 and V4, with very similar ΔT_{crit}, measuring 19.30°C for the V3 roof and 19.33°C for the V4 roof to reach the first buckling mode. The fourth version (V4) was deemed more challenging to manufacture by the stamping team due to the presence of more pronounced curvatures in the stiffening geometry.

Moreover, the design team considered it aesthetically less appealing for SUV customers. For these reasons, the decision was made to proceed with improvements by incorporating modifications in line with the third version (V3). Figure 117 illustrates the choices made thus far for the car roof.

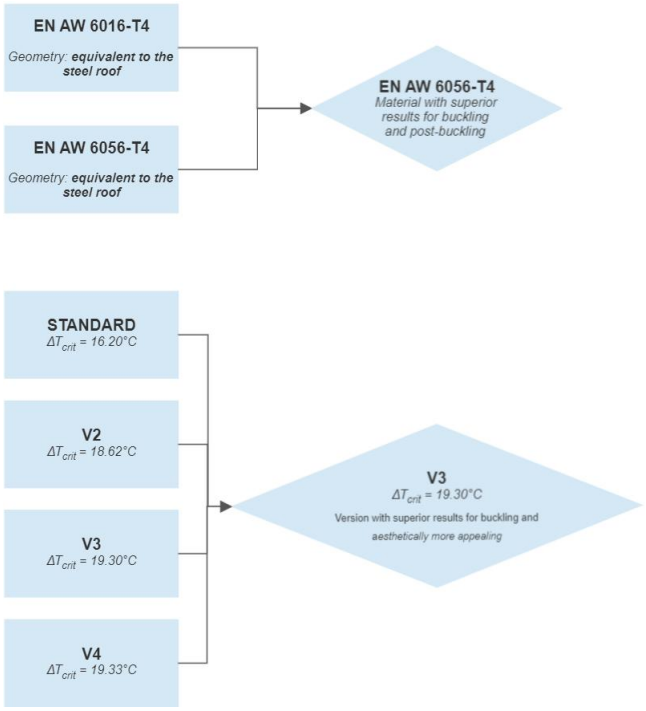

Figure 117 *Decision diagram used to illustrate the most favorable final decisions regarding the choice of the car roof choice.*

After version V3 of the car roof was chosen, it was improved based on conclusions drawn from the study of the influence of the height and position of the ribs. Thus, the ribs were positioned 97 mm from the lateral edges of the middle of car roof (at the midpoint along the length), passing through the epicenter of the displacement peaks in the corrugated region due to the occurrence of the first buckling modes on each side of the structure. To facilitate machining and enhance feasibility, it was decided to incorporate ribs parallel to each other, running straight and not conforming to the curvature of the lateral section of the car roof along its length. Then, as it was observed that increasing the height of the ribs up to 10 mm certainly favored the increase in the critical buckling temperature, the height of the ribs was increased

from 2 mm to 5.8 mm in the section at 115 mm from the front of the roof. Figure 118 shows the comparison between the initial V3 model and the modified V3.

The reason for choosing the parameter $h_{ribs} = 5.8\,mm$ is due to limitations regarding the machining of the modular stamping die for the production of the V3 – modified roof and also due to stamping limitations of the aluminum alloy to avoid fissures during the operation. However, as can be seen, the results of the modifications made to the V3 roof were satisfactory enough to more than double the temperature of the first buckling mode, previously $\Delta T_{crit-left} = 19.30°C$, and now $\Delta T_{crit-mode\,1} = 41.03°C$.

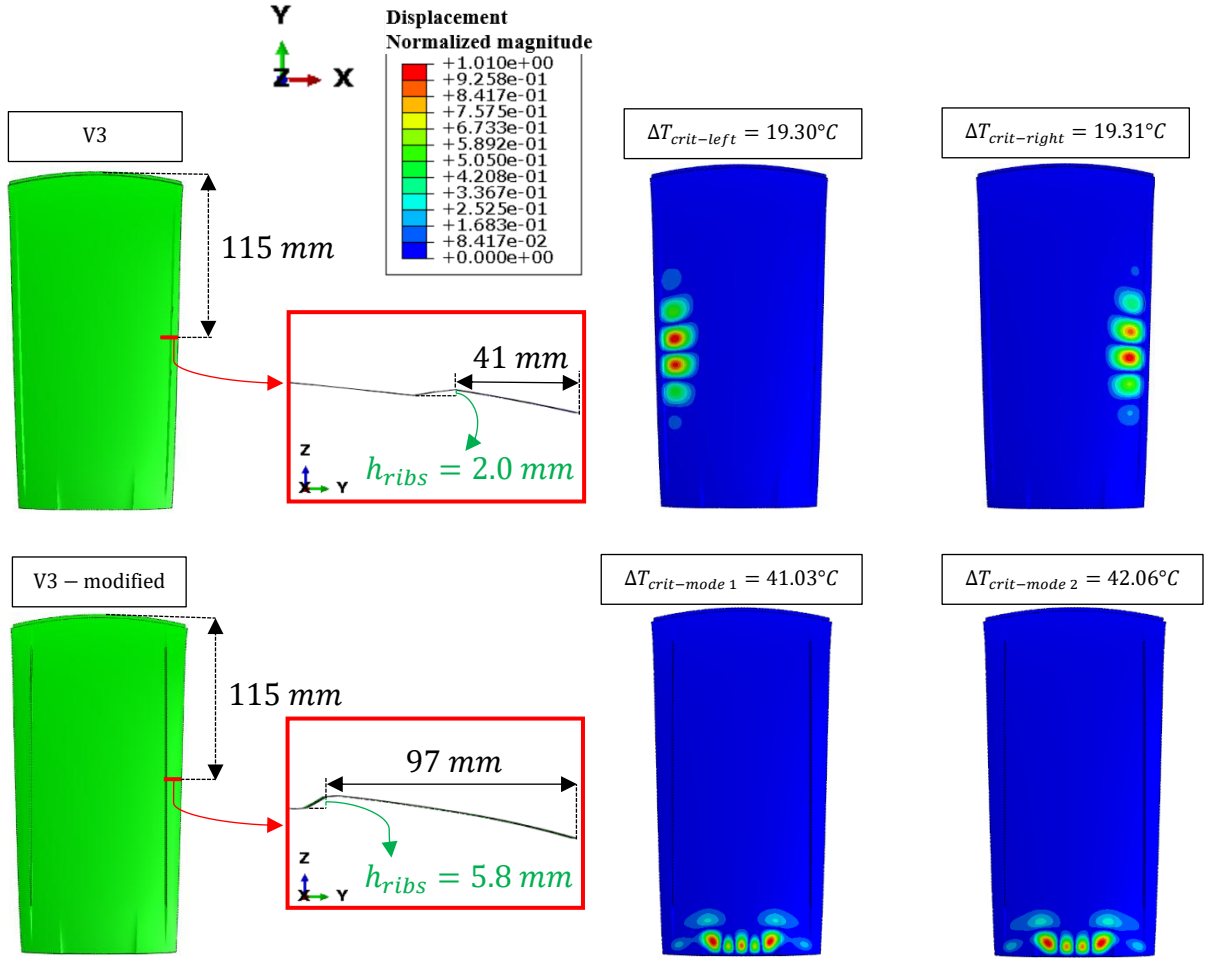

Figure 118 *Comparison between the initial V3 model (ribs at 41 mm from the lateral borders of the roof) and the modified V3 (ribs at 97 mm from the lateral borders of the roof).*

It can also be observed from the results presented in figure 118 that, with the boundary conditions of fixation around the roof, the region that was stiffened is no longer where the first

modes of the car roof are located, but rather in the rear region of the structure. This observation highlights the significance of the improvements made to the car roof design.

As a consequence of these findings, the decision has been made to select this modified structure for attachment to the body-in-white. This strategic decision is depicted in the decision flowchart provided in figure 119, which outlines the rationale behind the choice.

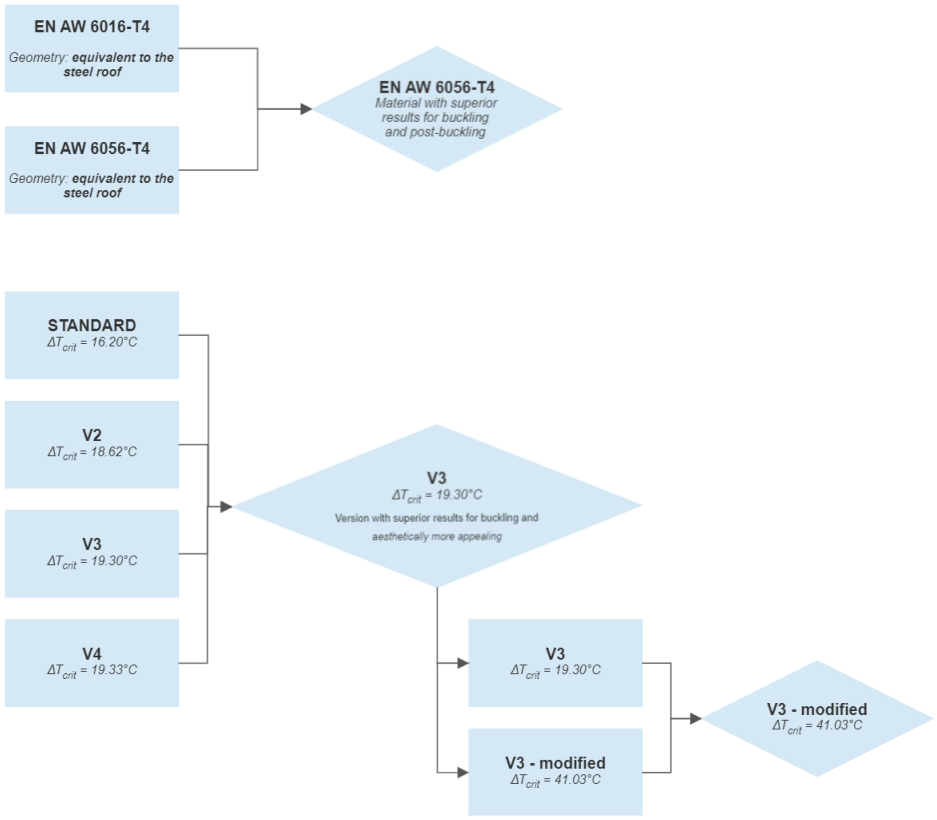

Figure 119 *Flowchart showing the choices made that led to the final selection of the roof with V3 – modified geometry due to the higher buckling temperature when the roof is analyzed in isolation with fixed edges.*

4.2 Thermal buckle simulation: aluminum alloy car roof with proposed geometry

Using the same numerical simulation artifacts as those used for the aluminum alloy roof with the geometry equivalent to the steel roof, the entire body-in-white simulation was conducted with the EN AW 6056-T4 roof in the V3-modified format. Thus, the first analysis performed was the buckle simulation, and the results are shown in figure 120.

As observed, the way the structure buckles changed compared to the simulation of the fully encased roof. This is because, in the case of the roof assembled to the body-in-white, the surrounding structures have a certain flexibility as they deform.

Consequently, the variation in critical temperature to reach the first buckling mode also changes, going from $\Delta T_{crit-mode\,1} = 41.03°C$, in the case where the roof is encased at its edges, to $\Delta T_{crit-mode\,1} = 125.8°C$, when the car roof is assembled to the body-in-white.

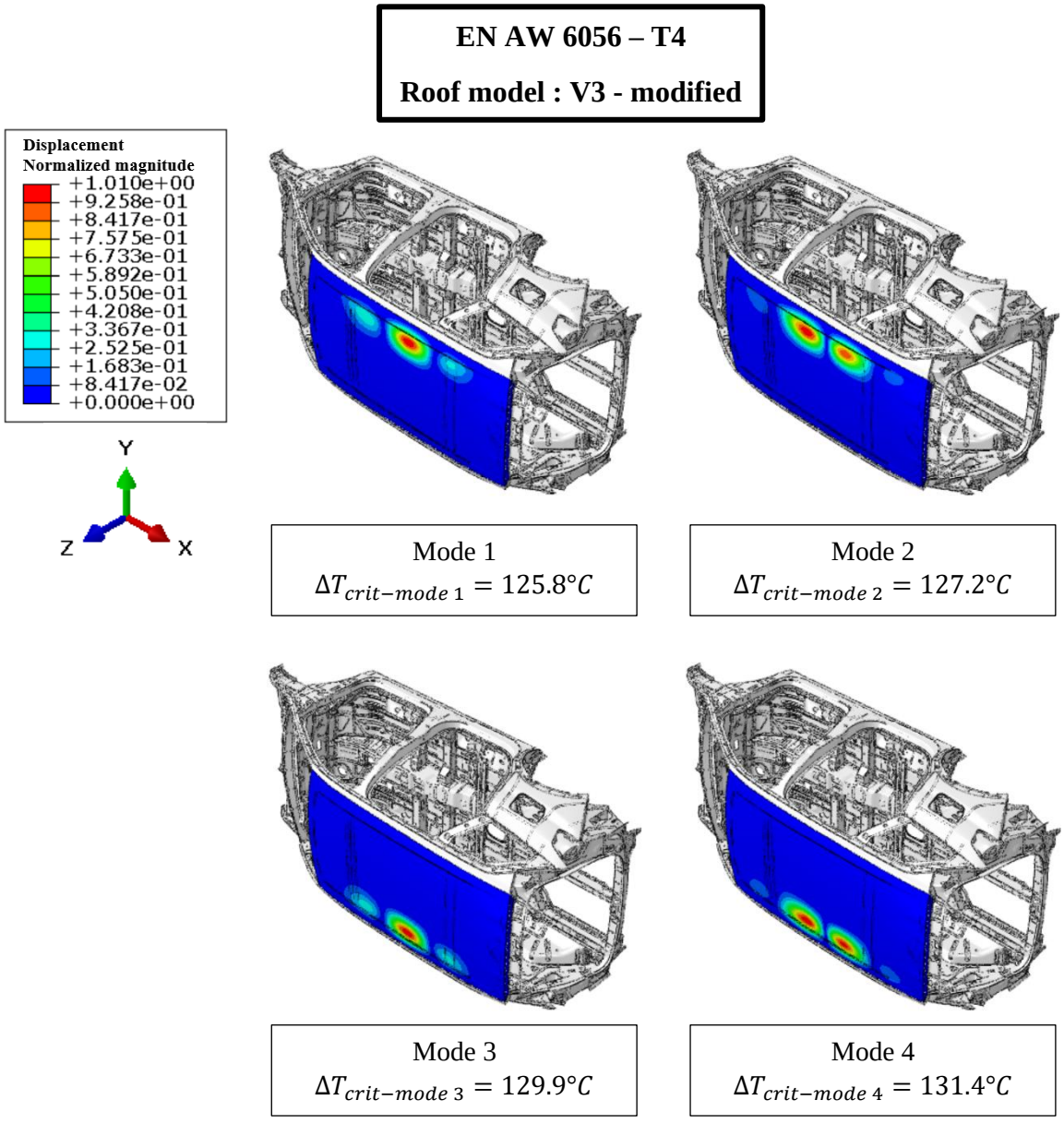

Figure 120 *Results of the thermal buckling for the first four modes using Finite Element simulation analysis. $\Delta T_{crit-mode}$ represents the temperature variation required to reach the buckling mode of the car roof.*

The comparison of buckling simulations between the initially designed roofs and the proposed roof yields valuable insights into the effectiveness of the design modifications. As illustrated in figure 121, strategic alterations to the geometry in specific locations have led to a significant enhancement in the critical buckling temperature variation for the first mode. Specifically, the critical buckling temperature has increased from 56.9°C to 125.8°C, representing a notable rise of 68.9°C required for the activation of the first buckling mode.

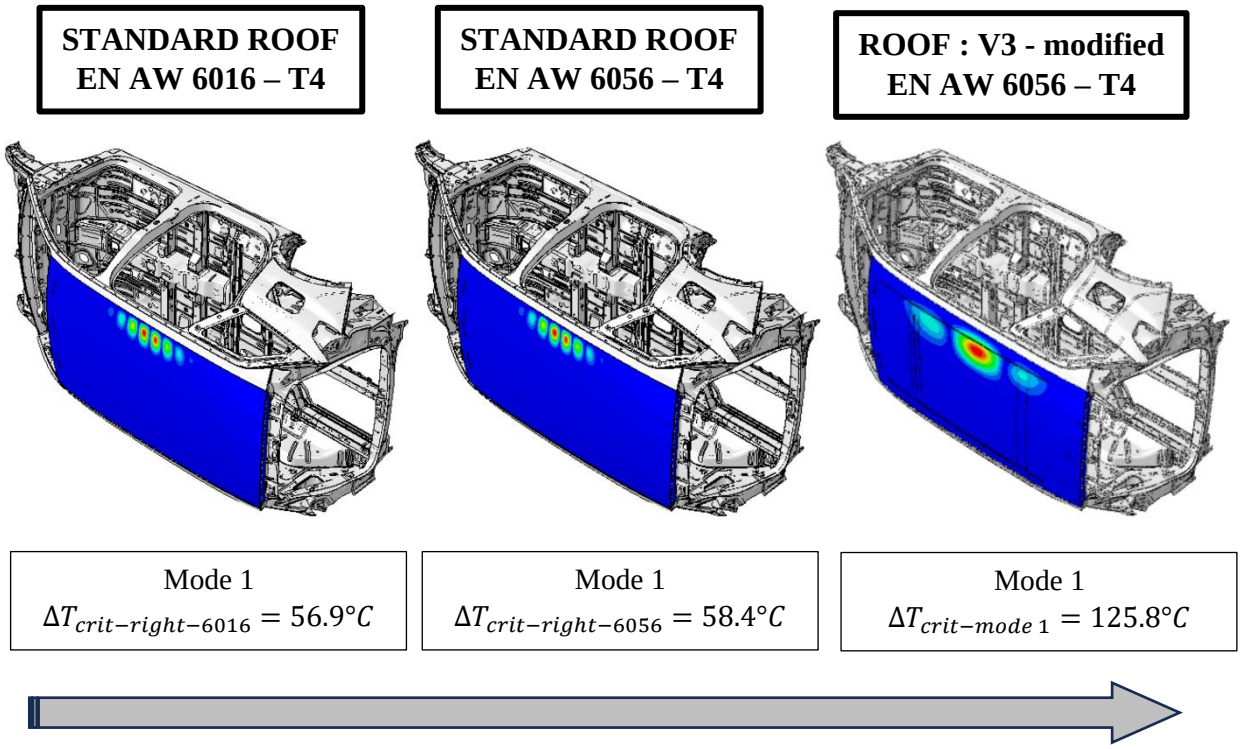

Figure 121 *Comparison of the results obtained through the buckling simulation with the complete body-in-white, including the initially designed roofs and the proposed roof.*

With the results of the comparative analysis using the thermal buckling temperatures of the roofs, a flowchart was created, as shown in figure 122, illustrating all the decisions leading to the choice of the V3-modified roof version for numerical and experimental testing. Following the same steps taken for the standard geometry roof analysis, a post-buckling analysis was conducted after the thermal buckling analysis.

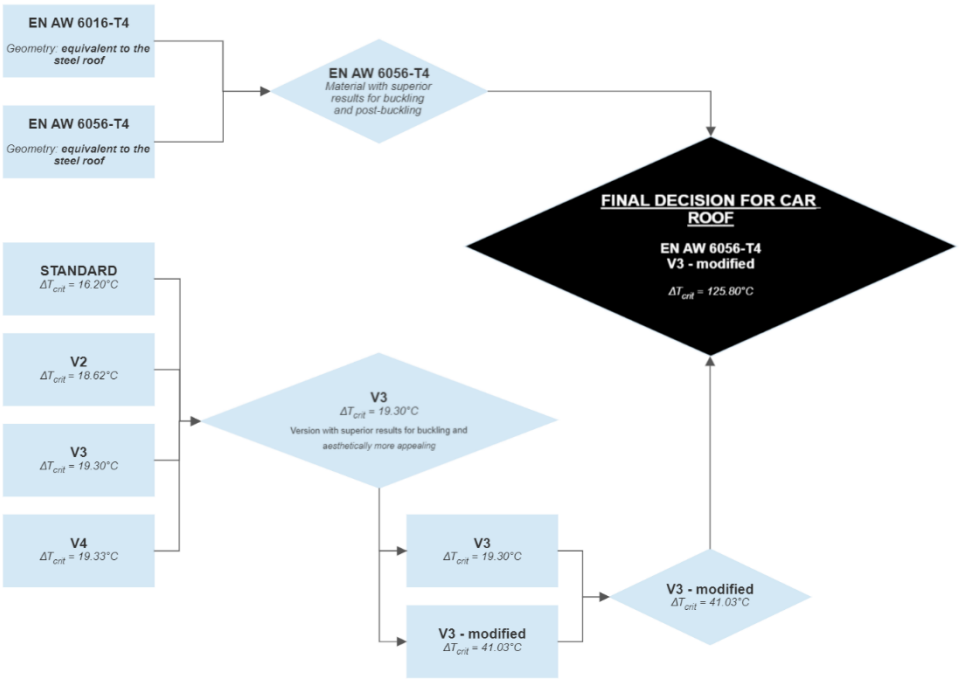

Figure 122 *Flowchart showing the justifications for choosing the material EN AW 6056-T4 and the geometry of the roof version V3-modified.*

4.3 Thermal post-buckle simulation: aluminum alloy car roof with proposed geometry

For the post-buckling analysis of the V3-modified roof, the same temperature curves utilized for the standard roof case will be employed. Additionally, the Budiansky criterion will be applied similarly to identify any sudden changes in the curvature of the load-displacement

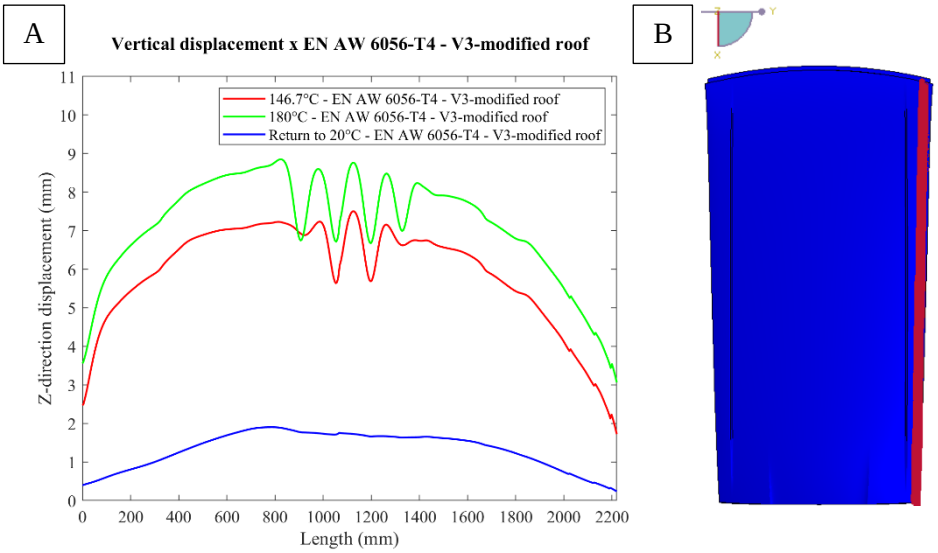

Figure 123 *EN AW 6056-T4 – V3-modified roof:* ***A)*** *Out-of-plane displacement curves derived from the results of post-buckling simulations along the red line highlighted in figure 123-B;* ***B)*** *Line at a distance of 58 mm from the right edge of the roof (epicenter of the most significant out-of-plane displacements in wavy format).*

or temperature-displacement response curve. Unlike the standard roof case, with the V3-modified model, the epicenter of the most significant out-of-plane displacements in a wavy format observed within the structure was located at 58 mm from the right edge of the roof. In this way, displacement graphs in this region were plotted, as shown in figure 123.

For comparison purposes, it was juxtaposed the performances obtained between the V3-modified roof and the conventional automotive roof made from the EN AW 6056-T4 alloy, as evidenced in figure 124 – A and B. The findings in this figure are of remarkable interest, given that in figure 124 – A, a substantial disparity in maximum vertical displacements between the peaks and valleys of the wavy regions of the roofs is evident. While, in the case of the conventional roof, such displacement discrepancy reached 7.3 mm, in the proposed roof, this difference was reduced to 2.2 mm, representing a reduction of 5.1 mm or 70% of amplitude reduction between the two situations. Furthermore, the outcome becomes even more notable when comparing the results obtained after the cooling process (figure 124 - B), where residual ripples are discernible in the standard roof, whereas in the proposed roof, such undulations become practically nonexistent, thus resulting in a substantial aesthetic improvement.

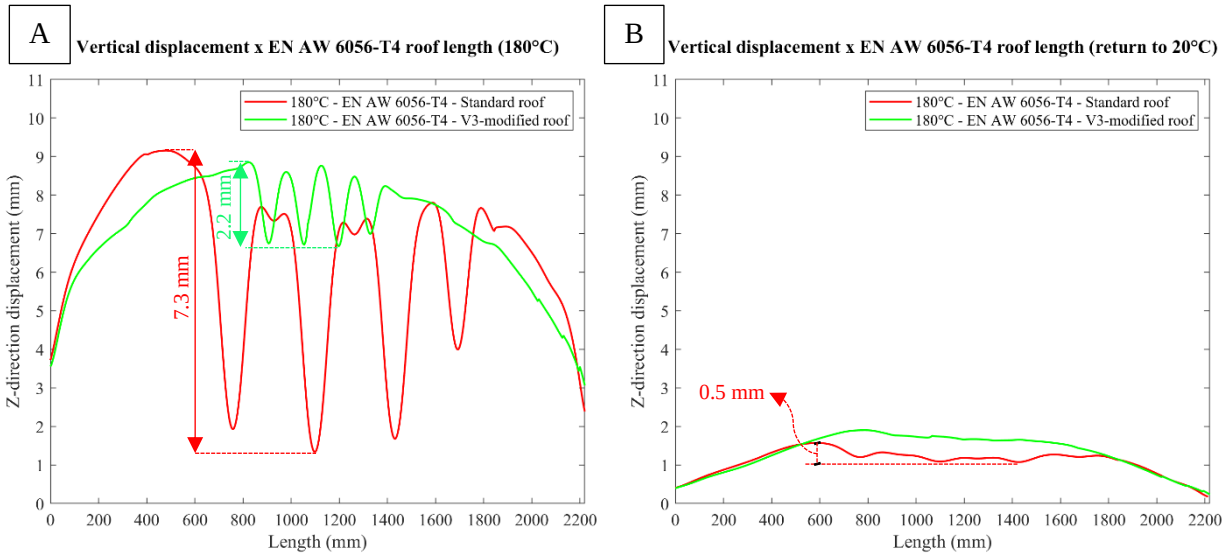

Figure 124 *The comparative vertical displacement curves of the standard car roof and the V3-modified roof made of EN AW 6056-T4 are illustrated for two specific conditions:* ***A)*** *At 180°C;* ***B)*** *At 20°C after the heating and cooling cycle.*

In the same manner as done with the standard roof geometry, figure 125 illustrates the outcomes of the numerical simulation analysis conducted on the z-directional displacement field, plastic deformation patterns, and principal compressive stresses, providing insights into the mechanical behavior of the V3-modified car roof made of EN AW 6056 at different temperatures.

At the initial condition for the post-buckling simulation (20°C), the structure exhibited stability. Then, at 146.7°C, buckling initiation was observed, with the circled red regions in the

strain field and principal compression field indicating the appearance of displacement and stress peaks. This signifies that the onset of buckling for the V3-modified roof happens at a temperature which is more than twice higher when compared to the EN AW 6056-T4 standard roof case (which showed a buckling temperature of 63.3 °C).

At 180°C, the stress analyses clearly revealed that the car roof had undergone buckling, but what is interesting to highlight is the comparison in displacement at this temperature with the case of the standard roof. In the standard roof, localized undulations in the displacement field were typically observed, whereas in the case of the V3-modified roof, the displacement is distributed more evenly. Additionally, when examining the principal compressive stress

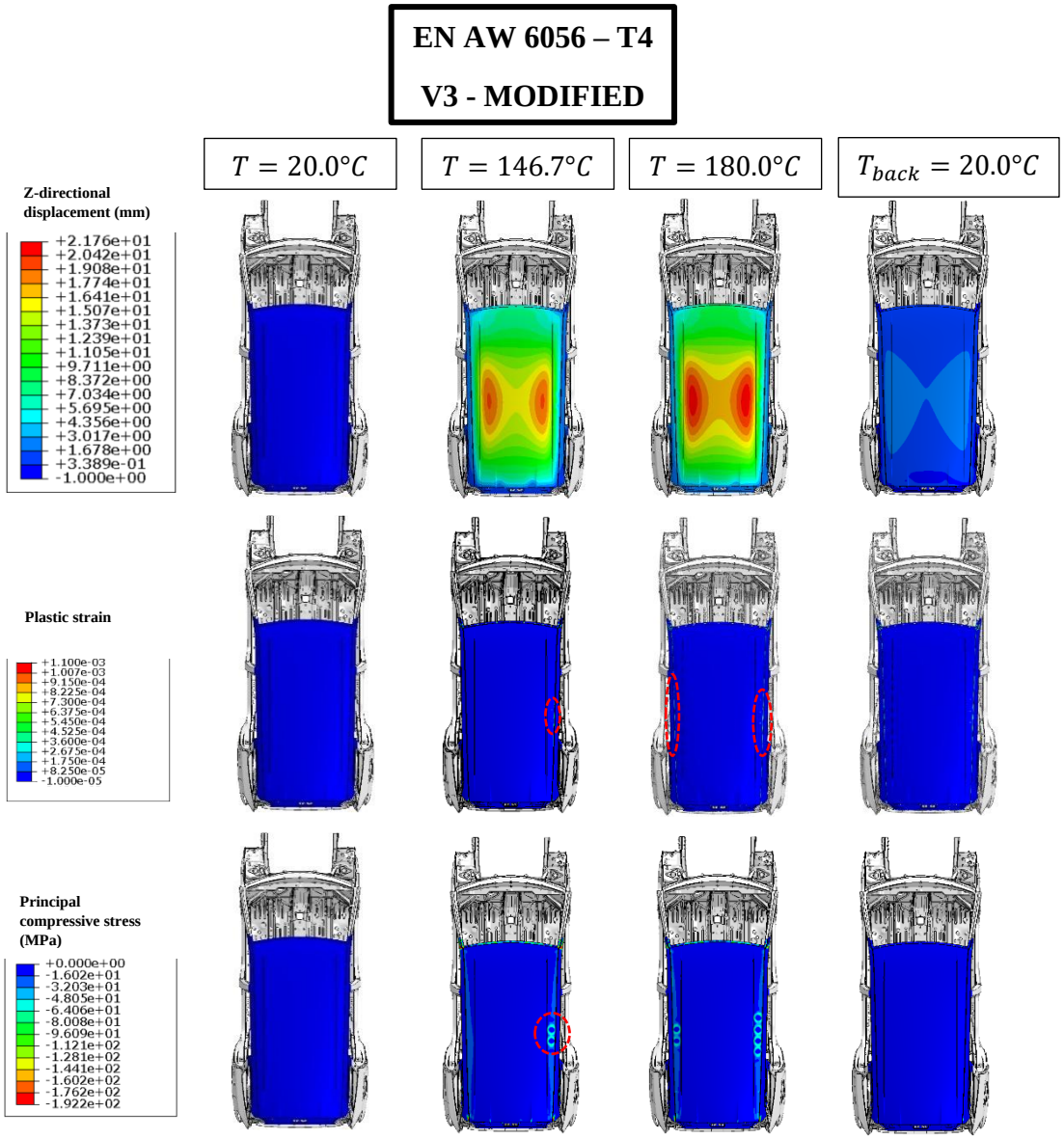

Figure 125 *Body-in-white analysis of Z-directional displacement, plastic strain, and principal compressive stresses fields at 20°C, 63.3°C, 180°C and return to 20°C. Material: EN AW 6056-T4 / Roof style: V3-modified.*

distribution, it becomes apparent that stress peaks tend to be more localized, primarily confined to the area between the beginning of the rib and the lateral border of the roof.

Given that the proposed roof structure shows a delayed onset of buckling compared to the standard roof and exhibits more localized compressive stresses in the modified case, the structure demonstrates superior performance in terms of deformation after the cooling process back to 20°C. This outcome represents an enhanced result in terms of the final appearance compared to the other roofs tested.

The comparative visual results of numerical simulation, scanning, and testing conducted with the V3-modified version of the car roof are found in figure 126. The amplitudes observed in the car roof were so small that they are visually imperceptible, revealing a viable solution for the industry, as it is possible to confirm in figure 127. Moreover, this underscores a reliable simulation methodology that can save time and money, considering that numerical analyses are less costly in various aspects than full-scale vehicle tests.

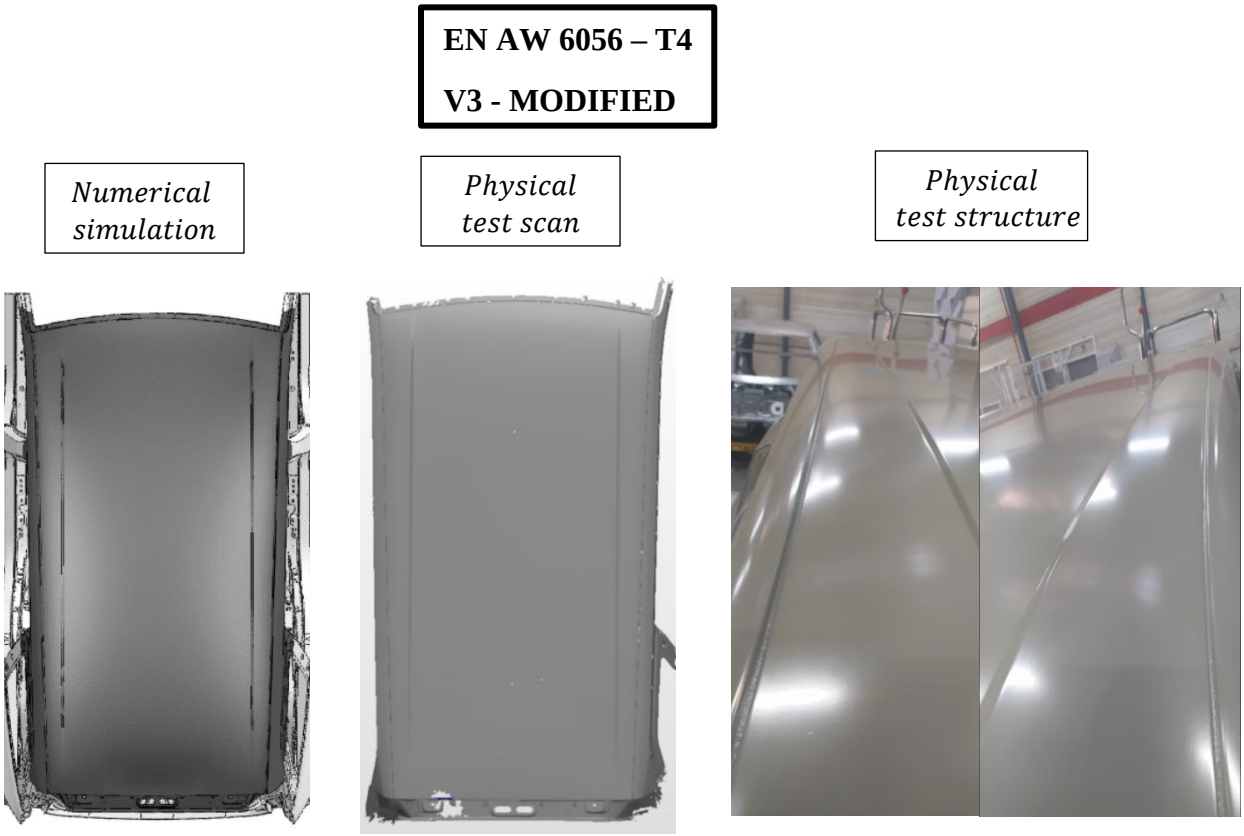

Figure 126 *Comparison of appearance results for the roof: numerical simulation, real structure scan, and photographic analysis (respectively, from left to right). Material: EN AW 6056-T4 / Roof style: V3-modified.*



Figure 127 *Modified roof after heating and cooling cycle. Material: EN AW 6056-T4 / Roof style: V3-modified.*

5. Conclusion – Chapter 4

In Chapter 4, the instability issue faced by the aluminum alloys EN AW 6016-T4 and EN AW 6056-T4 roof structure of an SUV vehicle when assembled with a predominantly steel body was addressed. Recognizing the complexities and limitations associated with conducting full-scale tests on such structures, a numerical methodology was developed to predict the mechanical behavior, specifically focusing on thermal buckling and post-buckling.

Upon analyzing the simulation results, it became evident that the car roof structure displayed discernible undulations upon completion of the heating phase. These undulations, characterized by deviations from a uniform displacement pattern, were particularly notable near the lateral edges of the roof. The findings revealed that issues related to the aluminum alloy car roof, with a geometry equivalent to a steel roof, arise at a relatively small temperature difference of approximately 63°C, while the structure is still within its elastic regime. Considering the post-buckling behavior becomes crucial for predicting the final appearance of the roof in the vehicle. To simulate post-buckling, imperfections with an amplitude factor of 0.01 were introduced into the model. In the scenario employing EN AW 6016-T4 material, the maximum amplitude of these undulations reached 1.5 mm after the heating cycle. Remarkably, this finding closely mirrors the real-world scan data of the car roof, which recorded a maximum vertical displacement of 1.3 mm. Moreover, the localization of these undulations aligns with the numerical simulation, thereby affirming the fidelity of the numerical model in representing real-world conditions. In the case of the roof made of EN AW 6056-T4, the results indicated that

the structure exhibits undulations at the end of the cooling phase, with maximum amplitudes of 0.5 mm. Such deviations from a smooth and uniform displacement pattern can significantly impact the aesthetic appearance and overall quality of the car roof.

Upon observing superior aesthetic outcomes, particularly in terms of reduced undulation amplitudes, associated with EN AW 6056-T4, this material was chosen for further investigation. Subsequently, the numerical model underwent validation through a physical test conducted on the full-scale structure. Findings from both cases exhibited congruent trends concerning the shape and positioning of roof surface defects. To address appearance defects, a study was conducted on the influence of car roof geometry parameters on critical buckling temperature. Instead of reinforcing the structure locally with stiffeners, an alternative approach was opted for modifying the roof design to induce local deformation, creating stiffer zones in the form of steps or grooves, referred to as ribs in this dissertation.

Following the evaluation of four distinct roof styles featuring varied rib geometries, the V3 proposal emerged as the preferred choice for further analysis. This selection was grounded in its ability to strike a harmonious balance between several criteria, including superior buckling outcomes, feasibility considerations, and alignment with the design ethos of the car brand. Positioning the ribs 97 mm from the lateral edges of the car roof based on improved conclusions drawn from the study, the proposed roof structure showed the first signs of buckle at 146.7°C in the post-buckle simulation. This onset of buckling for the V3-modified roof occurs at a temperature more than twice as high as the EN AW 6056-T4 standard roof case, which exhibited a buckling temperature of 63.3°C. At 180°C, the simulation results demonstrated a more homogeneous displacement pattern in the V3-modified roof compared to the standard roof, enhancing its aesthetic appeal.

In essence, the comparative findings underscore the superior performance exhibited by the proposed roof structure, distinguished by a delayed onset of buckling and more localized compressive stresses when juxtaposed with the standard roof. This structural superiority directly translates into an enhanced final appearance when contrasted against other roofs subjected to testing. Noteworthy is the virtually imperceptible minimal amplitudes observed in the modified car roof, thereby affirming the practicality and effectiveness of this solution for industry adoption. Moreover, this approach introduces a dependable simulation methodology capable of yielding substantial time and cost savings, given the inherently lower expenses associated with numerical analyses compared to full-scale vehicle tests across various dimensions. These results serve as a pivotal resolution to a longstanding issue dating back to 2010 within Stellantis. By embracing this approach, Stellantis can not only improve the performance of their car roofs but also streamline their design and testing processes, ultimately delivering greater value to consumers while maintaining competitive advantage in the automotive industry.

Bibliography – Chapter 4

[110] M. Shariyat, Thermal buckling analysis of rectangular composite plates with temperature-dependent properties based on a layerwise theory, Thin Walled Struct. 45 (2007) 469 439–452. https://doi.org/10.1016/j.tws.2007.03.004

[111] CREAFORM©. HandySCAN 3D|BLACK Series - Technical Specifications. Source: https://www.creaform3d.com/en/portable-3d-scanner-handyscan-3d/technical-specifications. [accessed 08.04.2023].

[112] G. Ye et al. Improving measurement accuracy of laser triangulation sensor via integrating a diffraction grating. Opt Laser Eng 143. (2021) https://doi.org/10.1016/j.optlaseng.2021.106631

[113] PolyWorks Europa. PolyWorks®: The Smart 3D Metrology Digital Ecosystem. Source: https://www.polyworkseuropa.com. [accessed 08.04.2023].

[114] William L. Ko. Predictions of Thermal Buckling Strengths of Hypersonic Aircraft Sandwich Panels Using Minimum Potential Energy and Finite Element Methods, NASA Technical Memorandum 4643 (1995). https://www.nasa.gov/centers/dryden/pdf/88372main_H-2009.pdf

[115] William L. Ko. Thermal Buckling Analysis of Rectangular Panels Subjected to Humped Temperature Profile Heating, NASA Dryden Flight Research Center, Edwards, California (2004). https://ntrs.nasa.gov/api/citations/20040021345/downloads/20040021345.pdf

[116] Ko, William L. and Raymond H. Jackson, Mechanical and Thermal Buckling of Rectangular Sandwich Panels Under Different Edge Conditions, NASA TM-4585, NASA Dryden Flight Research Center, Edwards, California (2004). https://ntrs.nasa.gov/api/citations/19940029198/downloads/19940029198.pdf

[117] Thornton, Earl A.. Thermal Buckling of Plates and Shells, Applied Mechanics Reviews 46 (1993), 10 pp. 485–506. https://doi.org/10.1115/1.3120310

[118] H. Layachi & Y. M. Xu. Performance and Stability Analysis of Sub-stiffening for Mechanical Buckling and Post Buckling: A Selective Study. Procedia Engineering, 109, 3-10 (2015). https://doi.org/10.1051/matecconf/20179501004

[119] A. Pritykin, I. Kirillov. "Critical rigidity of stiffener for increasing shear stability of rectangular plate." Mechanics of Advanced Materials and Structures, vol. 21, no. 3, 2014, pp. 219-225, doi: http://dx.doi.org/10.5755/j01.mech.21.3.9045

[120] ANSA pre-processor – Stellantis material library. Stellantis France, 2020.

General Conclusion

As outlined in Chapter 1, this thesis embarked on a comprehensive journey to address the intricate challenges associated with replacing a steel roof with aluminum alloy counterparts in the industrial context, particularly within the framework of the AM2 Project. The motivation originated from the critical issue of thermal loads during the post cataphoresis heating phase, significantly impacting the appearance, production, and sales of the vehicle roof. The urgency of this research is evident in the quest to control appearance defects arising from differential thermal expansion in an aluminum alloy roof assembled in a multi-material body-in-white. Three pivotal aspects guide the thesis: the solution must be applicable to the car's structure, respect existing production processes and tools, and adhere to the Peugeot brand's style identity. The acquisition of temperature data during the heating phase of the structure on the production line was particularly focused on the car roof, considering its significance for both the thesis's subject and the funding organization, Stellantis. Through temperature measurement testing, it was observed that the car roof undergoes a variation from ambient temperature to a value of 180°C, constituting the temperature range of interest. This data acquisition process not only aligns with the research objectives but also serves as a critical aspect in understanding the thermal behavior of the car roof, thereby informing subsequent analyses and design considerations. Utilizing the "*Projet V*" as the starting point for analyzing the problem to identify where in the physics the issue of appearance defects fit, it quickly became apparent that the problem was related to the occurrence of thermal buckling in the structure. This facilitated a focused study on the field of interest.

Recognizing this, Chapter 2 delved into the thermomechanical properties of two aluminum alloys (EN AW 6016-T4 and EN AW 6056-T4) under slow heating and natural aging conditions (3 and 6 moths). The study uncovered several key findings, including the isotropic mechanical behavior of the materials and the minimal influence of natural aging on their mechanical properties. Notably, significant temperature-dependent variations were observed in both yield strength and Young's modulus. Specifically, it was observed that as temperature increases, there is a pronounced non-linear rise in yield strength, attributed to the formation of β"-precipitates. This effect was most prominent in EN AW 6056-T4 aged for 3 months, exhibiting a substantial increase of 78 MPa between room temperature and 220°C. Conversely, while the elastic limit exhibited this non-linear behavior, Young's modulus values demonstrated a non-linear decrease with rising temperature. The most significant reduction in Young's modulus was noted in EN AW 6056-T4 aged for 6 months, experiencing a decrease of 20 GPa between room temperature and 220°C. These insights into the thermomechanical properties of the aluminum alloys provide valuable groundwork for understanding their behavior under different temperature conditions, crucial for subsequent analyses and design considerations in automotive applications. Thermal expansion and heat-related properties underwent meticulous

scrutiny, providing pivotal insights into material behavior across diverse temperature conditions up to 220°C. Both materials were subjected to thorough thermal analysis, revealing similar coefficients of thermal expansion ranging from 2.23 to 2.24 x 10-5 °C-1 when aged for 3 months and 2.11 x 10-5 °C-1 when aged for 6 months. However, EN AW 6016-T4 exhibited slightly higher values of specific heat capacity (Cp) and diffusivity compared to EN AW 6056-T4, resulting in a higher thermal conductivity for EN AW 6016-T4 relative to EN AW 6056-T4.These findings held significant importance for the subsequent analysis, given their absence in the company's material database in such detailed form. Moreover, these results laid the necessary groundwork for advancing numerical simulations and seeking a more robust correlation between simulation outcomes and physical tests. This alignment was the primary objective of the thesis and a key challenge faced by the company, which, until this study, struggled to establish strong correlations between tested cars and numerical simulations conducted using the aluminum alloy roof.

Following that, Chapter 3 delved into thermal buckling phenomena in circular plates and the coupling of different materials under thermal loading. The investigation thoroughly explored the influence of material and geometric parameters on critical buckling temperature, considering essential material properties like thermal expansion coefficient, Poisson's ratio, and Young's modulus, alongside geometric parameters such as radius, length, thickness, and imperfections. In the analysis of circular plates, modest temperature variations of approximately 5-6°C were found to lead to critical buckling temperatures for both aluminum alloys. The analysis emphasized the predominance of the first buckling mode and revealed noticeable differences in plastic deformation between the two alloys. Specifically, EN AW 6016-T4 exhibited a maximum plastic deformation of 3.0E-3, nearly double that of EN AW 6056-T4 (1.6E-3). Additionally, compressive stresses in the principal direction were significantly higher in the EN AW 6056-T4 plate (-173.2 MPa) compared to EN AW 6016-T4 (-140.1 MPa) at the maximum test temperature. Regarding the investigation into the coupling of different materials under thermal loading, it underscored the critical role of boundary conditions in buckling phenomena. Differential expansion analysis revealed compensation for buckling through imposed displacement, with numerical simulations demonstrating temperatures of less than 5°C for aluminum alloy buckling. Despite challenges, comparisons between numerical simulations and practical tests showed satisfactory correlations. For instance, the simulation for EN AW 6016-T4 alloy with an imperfection factor of 4.00 yielded a vertical displacement of 7.3 mm, closely aligning with the practical test result. Similarly, in the simulation for the EN AW 6056-T4 alloy with an imperfection factor of 5.00, the vertical displacement was 7.3 mm, mirroring the observed value in the practical test of 7.6 mm. Numerical simulations showcased the robustness of the model in simulating thermal buckling behavior, obtaining good correlation between laboratory tests and numerical studies. The numerical simulations also demonstrated remarkably low temperatures for aluminum alloy buckling, corroborating findings from

physical tests in the laboratory environment, thus raising concerns about potential issues in the real-scale analysis of vehicles.

The culmination of advancements and insights in this dissertation enabled the effective tackling of the instability challenge inherent in the aluminum alloy roof structure of an SUV integrated with a predominantly steel body, as discussed in Chapter 4. Recognizing the intricacies and limitations of full-scale testing, a focused numerical methodology was devised to predict mechanical behavior, with a specific emphasis on thermal buckling and post-buckling phenomena. Issues in the appearance of the aluminum alloy car roof were unveiled at a relatively modest temperature difference of approximately 63°C, still within the elastic regime. Recognizing the significance of post-buckling behavior in predicting the final roof appearance, imperfections were introduced in the simulations. This revealed undulations at the cooling phase's conclusion with maximum amplitudes of 1.5 mm and 0.5 mm for EN AW 6016-T4 and EN AW 6016-T4 roofs, respectively.

Choosing EN AW 6056-T4 for further investigation based on its superior appearance results, the numerical model was validated through physical testing. The results showed consistent trends in roof surface defects. To address appearance concerns, an exploration of the influence of car roof geometry parameters on critical buckling temperature was conducted, leading to a design modification approach. Four roof styles with different rib geometries were tested, and the V3 proposal was identified for further analysis. In the V3 proposal, where the rib was positioned 97 mm from the lateral edges, initial signs of buckling were observed at 146.7°C, more than twice as high as the standard roof case. At 180°C, simulation results showed a more homogeneous displacement pattern in the V3-modified roof compared to the standard roof, enhancing its aesthetic appeal.

In summary, the comparative results highlight the superior performance of the proposed roof structure, characterized by a delayed onset of buckling and more localized compressive stresses compared to the standard roof. This structural advantage translates into a superior final appearance when compared with other tested roofs. The minimal amplitudes observed affirm the viability of this solution for the industry, while the introduced simulation methodology proves to be a reliable and cost-effective alternative to full-scale vehicle tests. Notably, the example of the 300 k€ spent on fabricating the modular stamping for the modified roof underscores the significance of the developed numerical simulation in avoiding excessive costs associated with ineffective geometric proposals. This breakthrough offers a decisive solution to a persistent challenge that has troubled Stellantis since 2010. Embracing this method not only enhances the effectiveness of their vehicle roofs but also streamlines their design and testing procedures. This, in turn, promises to deliver enhanced value to consumers while solidifying Stellantis' competitive edge within the automotive sector.

Finally, the strides made in this research can lay the foundation for innovative avenues of exploration within the automotive industry. For instance, the creation of a patent during this

study opens possibilities for its integration with the RTI method (Reflectance Transformation Imaging) [121], providing a quantifiable measure for subjective assessments of appearance defects on car roofs. In today's context, where human judgment based on visual inspection determines the presence or absence of defects, these findings offer a more objective and standardized approach to evaluation. Furthermore, examining another perspective, appearance defects on large yet delicate structures like car roofs can sometimes be attributed to the use of expanding adhesives. These are employed to mitigate excessive vibrations between the car roof and the cross-members in the upper part of the body-in-white. This aspect suggests an expansion of research into the realm of thermally expansive materials, which has the potential to induce markings in the geometry of various structures. Consequently, this research can extend into a domain focused on the utilization of such materials, opening up new possibilities for enhancing structural design and appearance quality. Lastly, while this dissertation primarily concentrated on the analysis of car roofs, the versatility of the numerical simulation methodology employed in this research allows for its application in proactive calculations for diverse structures. This adaptability invites the exploration of preventive assessments for various components beyond car roofs, contributing to a broader spectrum of applications and advancements in structural engineering and design in the automotive field.

[121] G. LE-GOIC et al. HD-RTI: an adaptive multi-light imaging approach for the quality assessment of manufactured surfaces. Computers in Industry 132 (2021). https://doi.org/10.1016/j.compind.2021.103500

Appendices

PATENT

Title of the Invention: *Système de mesure optique, ensemble de caisse de véhicule automobile, utilisation dudit système de mesure optique et procédé de suivi de l'évolution d'un gradient de déformations d'un pavillon* – EN : Optical measurement system for automobile vehicle body assembly, utilization of the optical measurement system, and method for tracking the evolution of a deformation gradient in a roof.

INVENTORS

Name of the drafter and main inventor: *Leandro Maurício da Silva.*

Names of the other inventors: *Patrick Briend, Lionel Meslin, Olivier Ponte-Felgueiras, Sofia Sousa dos Santos, Daniel Fouillen, Lucas Michel, Peggy Broussaud Laloue, Romain Créac'hcadec.*

DESCRIPTION OF THE INVENTION

1 - Existing Technologies or Processes:

The proposed solution is part of the broader domain of welding assembly expertise, with a specific focus on joining an aluminum roof to a steel body-in-white (figure 1-1).

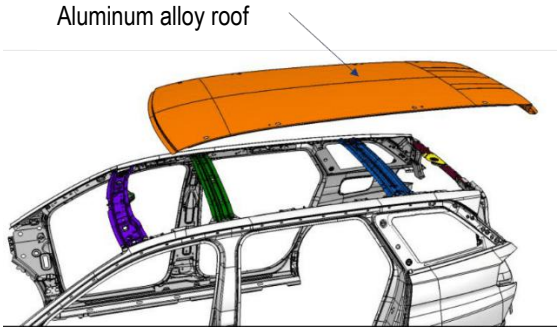

Figure 1-1 – Aluminum alloy roof assembly on a steel body-in-white.

It allows for the measurement of 3D displacement fields and then the estimation/quantification of deformation gradients, related to the differential expansion of aluminum compared to steel when this multi-material body-in-white is subjected to the thermal loading associated with the baking phase (around 180°C for 1h30 at the Rennes site) after cathodic electrodeposition (figure 1-2).

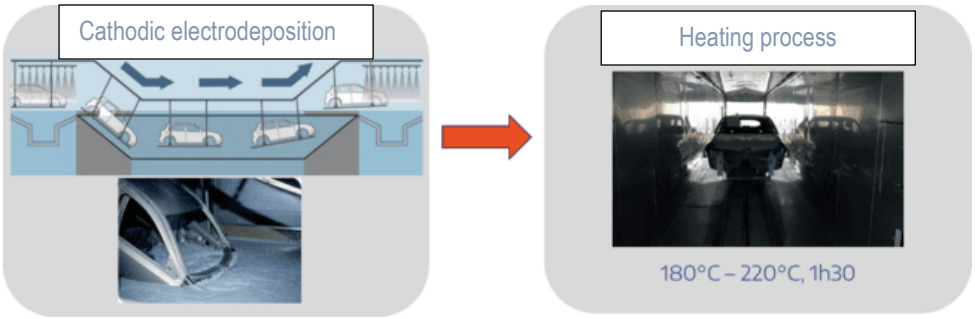

Figure 1-2 – Cathodic electrodeposition and heating processes.

As of today, there is no commercially available system that allows:

- access to a 3D displacement field;
- immersion inside a heating tunnel of several hundred meters, where the temperature (T) ranges between 180°C and 210°C, for a duration of 60 to 90 minutes;
- and guarantees complete energy autonomy concerning the used measurement system.

In summary, one envisions the use of an optical measurement system capable of measuring displacement fields (associated with the expansion phenomena experienced by a structure) in an environment subjected to high temperatures, around 200°C, if protected by an insulated thermal box (with an interior temperature not exceeding 45°C for 90 minutes to integrate the appropriate electronics), which would be attached to the body-in-white and energetically autonomous. Consequently, none of the commercialized systems fulfill all of these conditions.

- ***Defects and/or problems that make currently available solutions unsatisfactory***

Regarding current image stereocorrelation systems, they are insufficient on their own as they are not designed to operate in environments where the temperature exceeds 50°C. Their volume is often substantial, despite technological advancements. On the other hand, systems like High-Temperature sensors are directly usable but provide access to a point of measurement rather than a measurement field.

Considering optical systems specifically dedicated to high temperatures, it is not possible to quantify this physical quantity, and their cooling systems are too substantial to be integrated into a body-in-white. Lastly, the autonomy of the desired system must be total and minimized to carry the lightest possible battery, ensuring it does not hinder the proper progress of the heating process.

In summary, the problems or defects encountered by the available systems include:

- Electronics not supporting a working temperature exceeding 50°C;

- Cooling system too bulky and, above all, very energy-intensive;
- For some, the impossibility of quantifying a displacement field, like point-wise and wired High .Temperature sensors;
- System powered by the grid or low autonomy;
- Excessive mass and size of certain systems;
- Total absence of lighting in the heating tunnel.

2 – Technical Presentation of the Invention:

- ***The invention in a few words:***

- The invention focuses on developing an optical measurement system that quantifies geometric variations related to the differential expansion phenomena experienced by an aluminum roof (welded to a steel body-in-white) during the baking process in a 200m long tunnel for 1h30 at 180°C without illumination. This system captures pairs of images at regular intervals (every 5 seconds), from the tunnel entrance to the exit of the overhead conveyor, with the underside of the roof illuminated by a cold light source. This enables mapping of the roof displacement fields throughout this thermal loading, followed by a comparison of these experimental results with those obtained through simulation to optimize the numerical "post-buckling" model developed in Leandro Mauricio da Silva's thesis;

- In addition to optimizing this "predictive" numerical model, the system also validates local reinforcement solutions, such as grooving/ribs, proposed by this model to eliminate appearance defects (figure 1-3) present on the aluminum roof in an iso-steel configuration.

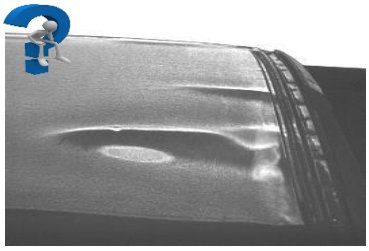

Figure 1-3 – Illustration of appearance defects present on an aluminum alloy roof.

- ***What problem(s) does this invention seek to solve?***

This invention seeks to quantify, in the form of 3D maps, the dimensional variations experienced by an aluminum roof during the baking process, as the body-in-white passes inside

a 200 m tunnel where the temperature ranges between 180°C and 210°C for 1h30, all in complete darkness.

- ***Detailed Description***

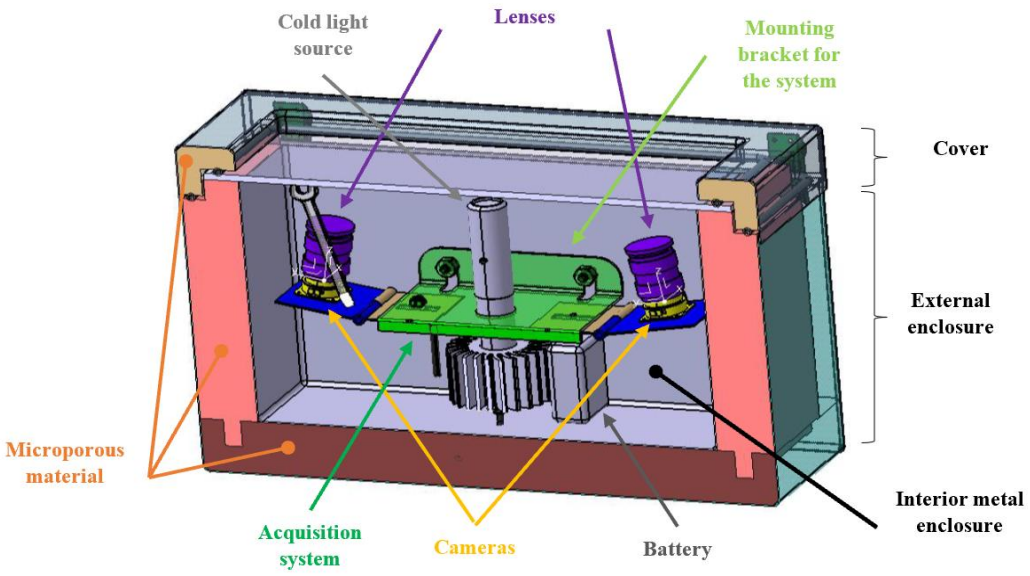

Figure 1-4 Descriptive illustration of the invention of the developed image acquisition system.

We developed a stereo vision sensor in the form of a micro-system for 3D digital image stereo-correlation using 2 HQ cameras, a control unit, and 2 lenses 24mm f/1.4, to acquire synchronous image pairs representative of the geometric state of the roof at time t. This system is sized to the strict minimum but with increased optical performance (figure 1-4).

- The stereo vision system is integrated into its thermal housing;
- Integration of a battery, with geometric characteristics minimized to the essential to avoid penalizing the final volume of the measurement system, ensuring the autonomy for 2 hours;
- Calibration of the complete system is then carried out;
- The complete system is then integrated and rigidly fixed inside the body-in-white;
- The vehicle body is presented at the entrance of the heating tunnel;
- From then on, the system acquires pairs of images at regular intervals (every 5s), from the entrance of the tunnel to the exit of the body. For this purpose, a program has been developed in Python to perform the acquisition of these image pairs and trigger the light flux from the cold source to illuminate the scene for 2s during each acquisition phase;
- A second calibration is carried out to ensure the relevance of the estimated parameters;

- At the end of this acquisition phase, the data is transferred to a remote PC, and then post-processed using specific software to characterize the displacement fields (along the X, Y, and Z axes) of a car roof and quantify the evolution of deformation fields throughout this heating process;
- These experimental results will then be compared to the results from numerical simulations. The primary goal is to optimize this model to predict appearance defects initially and propose/validate local reinforcement solutions, such as the presence of ribs, in a second step;
- Ultra-compact system to observe a surface on the roof of about $0.5m^2$ at approximately 77 cm away from it (figure 1-5).

It is always possible to increase the specifications of the cameras used to obtain higher resolution or increase the number of glasses constituting the shield to achieve a much later thermal equilibrium. However, considering the size, costs, mass, and technical requirements in terms of the observed surface and depth of field, the system we propose appears to be the most relevant at the time this document is written.

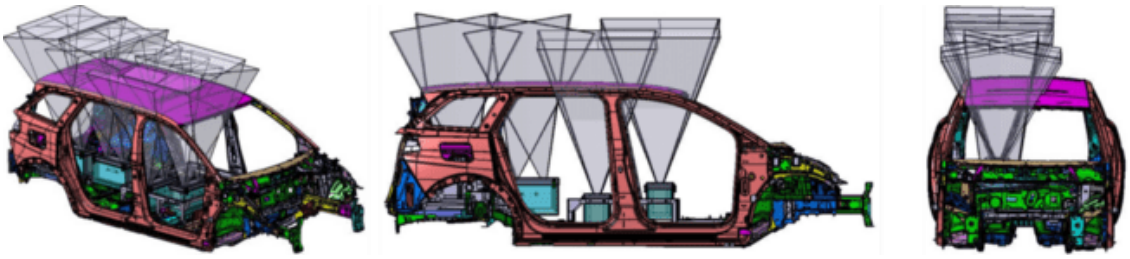

Figure 1-5 Illustration of the different observable zones depending on the sensor's position.

The invention also includes the association of a cold light source (figure 1-6) to illuminate the roof at the exact moment of the shots since the tunnel lacks lighting and to drastically reduce the thermal radiation in the housing.



Figure 1-6 – Cold source projector.

The insulation of the measurement system is ensured by a box made of metallic components and microporous insulation materials, and it features a triple glazing porthole on its cover (figure 1-7). The external glass is treated against thermal shocks, allowing the system to directly observe the roof while limiting thermal conduction.

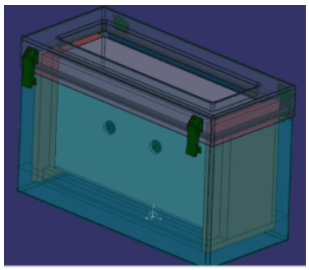

- **Figure 1-7** Illustration of the thermal housing topped with its cover equipped with the triple glazing porthole.

- ***Technical benefits created by the invention***

- The very compact size of this stereo vision sensor allows for an optimal depth of field (camera/roof distance) of 77 cm, providing a field of view (measurable roof surface) of approximately 0.5 m^2;
- The physical integration of the stereo vision sensor components into the thermal housing and the attachment of the thermal housing to the blank body meet the requirements of image correlation throughout the curing tunnel. This avoids introducing an additional error factor to the estimation of geometric variations due to parasitic movements between the housing and the blank body;
- The articulation of the plates supporting the cameras enables precise adjustment of the optical axis of each camera with the normal to the observation point. This ensures that the cameras rigorously observe the same scene, guaranteeing an optimal measuring volume. After locking the position of the plates, this stereoscopic system has a fixed triangulation base;
- The design of the walls and the porthole associated with the thermal housing, as well as the materials it is made of, maintain an internal temperature of the housing around 45°C for 1h30. Material and treatment choices for the porthole minimize reflection phenomena as the cold light flux passes through each glass plate.
- The use of a cold light source projector illuminates the underside of the roof for a duration of 2s, synchronized with the image pair acquisition phase.

- ***Economical Interest***

- Time savings on the validation of aluminum roof concepts;
- Cost savings on stamping tools as the shape of the aluminum roof, incorporating reinforcement ribs, will be numerically validated by the model (whose accuracy, robustness, and predictability have been confirmed by this optical measurement method);
- Expertise gain in addressing corrosion product runoff issues during the drying phase.

Title : Control of appearance defects generated by differential thermal expansion on an aluminum alloy roof assembled in a multi-material body-in-white

Keywords: thermal buckling, differential thermal expansion, aluminum alloy roof, multi-material body-in-white, automotive thermomechanics, numerical and experimental analysis.

Abstract: The new EU regulations on CO_2 emissions, Industry 4.0 advancements, and emerging energy sources are prompting the automotive sector to explore lightweight materials for future vehicles. In this context, Stellantis launched a project called "*Projet AM2*" in partnership with collaborators, with a primary emphasis on multi-material and multi-technology processes. This initiative involves integrating an aluminum roof into a body-in-white predominantly composed of steel. While the weight reduction potential of multi-material approaches is significant, challenges arise from temperature fluctuations during vehicle fabrication, leading to thermal buckling in thin structures like car roofs. This thesis addresses strategies to prevent and predict surface defects caused by thermal buckling while adhering to automotive industry standards. Despite the widespread use of aluminum alloys in the automotive industry, there is a lack of literature on the thermomechanical properties of aluminum alloys (EN AW 6016-T4 and EN AW 6056-T4) under slow heating conditions lasting 40-50 minutes up to 220°C, including natural aging effects. This study revealed a substantial non-linear increase in under slow heating conditions lasting 40-50 minutes up to 220°C, including natural aging effects. This study revealed a substantial non-linear increase in yield strength and a corresponding decrease in Young's modulus values with rising temperature. Furthermore, the plastic response varied notably depending on the heating cycle employed. The variations in diffusivity, specific heat, and conductivity were also studied with the increase in temperature. Regarding the instability phenomenon induced by differential expansion, comprehensive investigations were conducted using analytical, physical, and numerical analyses within a controlled laboratory environment. Two tests were devised to assess material behavior under different boundary conditions and geometries, revealing distinct stress states attributed to differing plastic regimes. A simulation method was developed to account for the evolving properties of aluminum alloys during temperature fluctuations, and the results were corroborated by the experimental tests. Additionally, thermal buckling onset was observed to occur within the material's elastic regime. Finally, numerical simulation models were developed to assess and predict the effects of differential expansions on the aluminum alloy roof at the scale of the body-in-white structure. Based on the analysis, a redesigned car roof was proposed, considering both industrial feasibility and brand-specific design criteria. Subsequently, an industrial-scale prototype featuring the proposed roof yielded promising outcomes, affirming the viability of the proposed design approach.

Titre : Contrôle des défauts d'aspect dus à la dilatation thermique différentielle sur un pavillon en alliage d'aluminium assemblé dans une caisse en blanc multi-matériaux

Mots clés : flambement thermique, dilatation thermique différentielle, pavillon en alliage d'aluminium, caisse en blanc multi-matériaux, thermomécanique automobile, analyse numérique et expérimentale.

Résumé : Les nouvelles réglementations européennes sur les émissions de CO_2 et l'essor de l'Industrie 4.0 poussent le secteur automobile à explorer des matériaux allégés. Dans ce contexte, Stellantis a lancé le Projet AM2 pour intégrer un toit en alliage d'aluminium dans une caisse en blanc multi-matériaux, principalement composée d'acier. Cette approche permet une réduction significative du poids, mais pose des défis liés aux variations de température durant la fabrication, entraînant un flambement thermique des structures fines comme les toits de voiture. Cette thèse propose des stratégies pour prévenir et prédire les défauts d'aspect dus à ce phénomène tout en respectant les normes automobiles. Malgré l'usage répandu des alliages d'aluminium dans l'automobile, peu d'études traitent des propriétés thermomécaniques des alliages EN AW 6016-T4 et EN AW 6056-T4 sous un chauffage lent (40-50 minutes jusqu'à 220°C), incluant les effets du vieillissement naturel. L'analyse a révélé une augmentation non linéaire de la limite d'élasticité et une diminution du module de Young avec la température, ainsi que des variations de la diffusivité, de la chaleur spécifique et de la conductivité thermique. L'instabilité induite par la dilatation thermique différentielle a été étudiée par des analyses expérimentales, analytiques et numériques en laboratoire. Deux essais ont permis d'évaluer le comportement des matériaux sous différentes conditions et géométries, révélant des états de contrainte distincts selon les régimes plastiques. Un modèle de simulation prenant en compte l'évolution des propriétés thermomécaniques a été développé et validé expérimentalement. Il a notamment mis en évidence que le flambement thermique se produit dans le régime élastique du matériau. Enfin, des modèles numériques ont été établis pour analyser et anticiper les effets de la dilatation thermique sur le pavillon en aluminium à l'échelle de la caisse en blanc. À partir de ces résultats, une nouvelle conception du pavillon a été proposée, conciliant faisabilité industrielle et critères esthétiques. Un prototype industriel a été fabriqué, validant la pertinence de cette approche et ouvrant la voie à son application en production.